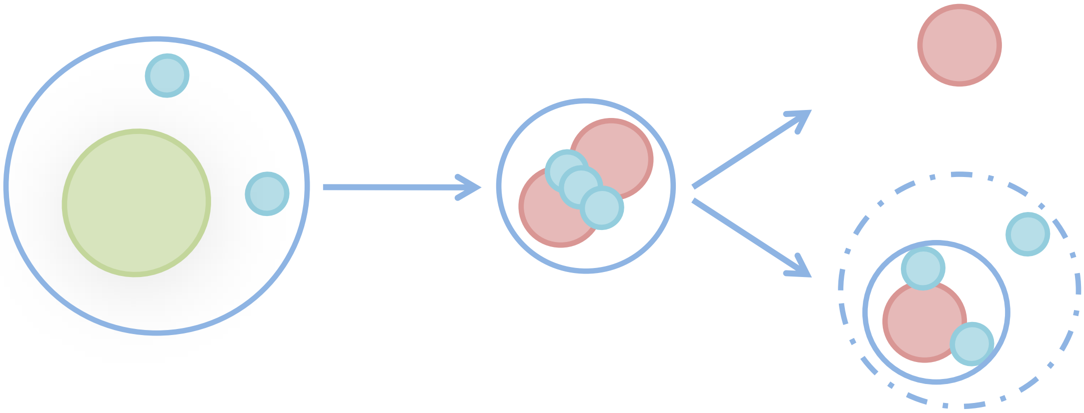

Study of the multi-fragmentation channels following the β-decay of the halo nucleus ^{11}Li and its core ^{9}Li

Miguel Madurga Flores

Instituto de Estructura de la Materia
CSIC

Departamento de Física Teórica.

UAM

Directora: Mª Jose Garcia Borge

November 2009

Study of the multi-fragmentation channels following the β-decay of the halo nucleus ^{11}Li and its core ^{9}Li.

MEMORIA PRESENTADA PARA LA OBTENCIÓN DEL
TITULO DE DOCTOR.

Miguel Madurga Flores

Director
Dra. María José García Borge

November 15, 2009

Contents

Dedicada a mi madre y mi tia Pilar,

Para AS, EM y ER, esta tesis también es vuestra.

Introduction

Light nuclei near the driplines

The exploration of nuclear matter under extreme conditions, which can be created in modern accelerator laboratories, is one of the major goals of modern nuclear physics. With access to exotic nuclei at the very limits of nuclear stability, the physics of the neutron and proton driplines has become the focus of interest. The driplines are the limits of the nuclear landscape, where additional protons or neutrons can no longer be kept in the nucleus– they literally drip out. In the vicinity of the driplines, the structural features of the nuclei change compared to nuclei closer to the β-stability line. The normal shell closures may dissapear and be replaced by new magic numbers. The gradual vanishing of the binding energies or clusters of particles may at the driplines give rise to β-delayed particle emission or even particle radioactivity. In some neutron rich nuclei a threshold phenomenon, nuclear halo states, has been studied extensively, both experimentally and theoretically, and is now a well established structural feature of many light dripline nuclei. Although there have allways been interest in studying the properties of exotic nuclei, the real breakthrough was the observation of halo states. An increased experimental effort was made to address the new problems that suddenly appeared, with new facilities built and new experimental techniques developed. On the theoretical side, the presence of halo states meant a new paradigm of physics at the driplines, which attracted theory to the driplines in a way unseen before.

The nuclear halo is purely a threshold effect, as, when approaching the driplines, the binding energy of the last nucleon, or pair of nucleons, decreases and the states come close to the continuum. This low binding energy results in a increased tunneling probability into the classical forbidden region. This extended spatial extension of the valence nucleons can be viewed as a halo surrounding the nucleus core. Of course, the height of the Coulomb barrier limits the spatial extension of the tunneling region of the valence proton of neutron deficient nuclei, and only one case is well established, ^{8}B. For both neutron and proton halos, on top of the binding energy condition, the valence nucleons have to have low relative angular momentum, which implies they only occur in either s or p single-particle states.

The first observation of the unusual matter distribution of light nuclei, latter interpreted as the neutron halo, was obtained by Tanihata and collaborators in the mid-eighties when measuring the matter radii of the heaviest bound helium isotopes, ^{6}He and ^{8}He [Tan85a]. Shortly after, they obtained the same results for Li isotopes where the matter radius of ^{11}Li was observed to be 30% bigger than that of the closest particle stable neighbor ^{9}Li [Tan85b]. Both ^{6}He and ^{11}Li are examples of two neutron halos, which are of great interest due to their Borromean character, where the three body system is unbound with its parwise subsystems unbound. The study of both nuclei in one neutron stripping reactions permitted to obtain the composition of the ground state wavefunction of both nuclei. The ^{6}He ground state wavefunction was shown to be mostly $0p_{3/2}$, as expected from shell model, with a small mixture of 7% of $0p_{1/2}$ [Chu97, CS97]. On the other hand, the ^{11}Li ground state structure was observed to be a contain a strong mixture of 45(10)% of $1s_{1/2}$ plus the $0p_{3/2}0p_{3/2}$ component expected from shell model [Sim99]. Although of great importance, this result was not completely surprising, as earlier theoretical calculations [IT94] predicted the p-wave and s-wave mixing in the ground state composition in order to explain the momentum distribution of ^{9}Li recoils after breakup of ^{11}Li [Kob88].

The other He isotope identified by Tanihata et al. as having a large spatial extension, ^{8}He, is more complicated than the two neutron halos mentioned above. First, the two neutron separation energy is found to be larger than that of ^{6}He. Second, it was observed that the sum of the two and four neutron separation cross section corresponds to subtracting the integral alpha cross section to the integral ^{8}He cross section. This clearly points in the direction of a α+4n structure of the ground state of ^{8}He. This interpretation was latter supported by the analysis of the ^{8}He β-delayed particle emission discussed below.

But the cases of particle halos observed in light nuclei include not only three body systems, but two body systems as well. As mentioned above, the only confirmed case of one proton halo is the ground state of ^{8}B, although the 495 keV excited state in ^{17}F is known to have an extended wave-function [Bor93a] . One neutron halos are found in ^{11}Be [For99], ^{15,19}C [Dat03, Mad01], and ^{23}O [Sau00]. All these halo cases were identified by measuring a large one neutron removal cross section and a narrow momentum width of the resulting fragments. This is consistent with a s-wave ground state, as expected to form a halo state. The case of ^{11}Be is more interesting, since the valence neutron in the ground state is not a filling the $p_{1/2}$ state as expected from shell model, but an intruder $s_{1/2}$. To understand this inversion most models require that the $[^{11}\mathrm{Be}(0^{+})\otimes 1s_{1/2}]_{1/2^{+}}$ configuration is mixed with the 2^{+} first excited state of ^{10}Be, $[^{10}\mathrm{Be}(2^{+})\otimes 0d_{5/2}]_{1/2^{+}}$, a hypothesis later confirmed experimentally [For99, Gei99, Aum00].

Although most of the recent information about dripline nuclei has been obtained from reaction experiments with radioactive nuclei, nuclear β-decay, the subject of this thesis, is a proven probe of the nuclear structure and it is of interest at the driplines. As we move closer to the driplines, the particle emission processes become more important, up to the point that the β-delayed particle emission will dominate over the decay to bound states. For halo nuclei close to the neutron dripline, the halo structure may have an effect on the beta-decay. The large spatial extension of the halo wavefunction might reduce the overlap with the daughter state, hindering the transition, or the halo neutrons might decay more or less independently from the core, giving rise to parent-core matching patterns in the beta decay [NNR00].

As mentioned above, the high energy available for the beta-decay, together with the low nucleon, or even cluster, separation enegies, make several beta-delayed processess possible. Close to the neutron dripline, the most basic beta-delayed process is the single or multiple neutron emission. Furthermore, more exotic beta-delated particle emission has been observed in dripline nuclei, such as deuteron and triton emission. The first experimental observation of beta-delayed deuteron emission was obtained in the decay of ^{6}He [Rii90], although this experiment was designed to observ the decay mode; later, the deuteron energy spectrum was obtained [Bor93a], indicating that the beta-decay occurs directly into the deuteron continuum, not through an intermediate state in the ^{6}Li daughter state.

A beta-delayed triton branch has been observed in ^{8}He [Bor93b], where R-matrix calculations indicate that the decay occurs thorugh a 1^{+} state in ^{8}Li, with a large $\mathrm{B_{GT}}$=5.18. This result indicates that the ground state of ^{8}He has a large overlap with an alpha particle and a neutron cluster configuration.

Other possible effect of the unusually large spatial extension of the halo is the hindrance or enhancement of the feeding of certain states in the daughter nucleus. The first forbidden transition of ^{17}Ne to the 495 keV state in ^{17}F has a branching ratio of 1.59(17)% [Bor93c, Oza97, Mor02], two times larger than the transition in the mirror nucleus ^{17}N to the 871 keV state in ^{17}O [Ajz86]. The shell model calculation presented in [Bor93c] explains this discrepancy due to the large spatial extent of the $1s_{1/2}$ proton orbit.

The enhancement of the feeding to states around 2 MeV below the Q_{β} value is a general trend observed in neutro rich dripline nuclei ^{6,8} and ^{9,11}Li. In the case of ^{9}Li, the $\mathrm{B_{GT}}$to the 11.8 MeV state is 5.3(1.0) [Pre03], much larger than the transition in the mirror nucleus ^{9}C to the 12.22 MeV state in ^{9}B of 1.20(15) [Ber01].

The beta decay of the nucleus of interest in this work, ^{11}Li, shows all the neutron rich decay characteristics mentioned above. Both beta delayed triton [Lan84, Bor97a] and deuteron emission [Muk96, Raa08] has been observed. The triton emission was determined to occur normally through a intermediate state in ^{11}Be. However, the deuteron emission hs been recently confirmed to occur directly to the deuteron continuum [Raa08], in similar fashion to the beta delayed deuteron emission in ^{6}He.

The unusual configuration of the halo ground state of ^{11}Li has been proposed to be responsible [Bor97b] of the small feeding to the $1/2^-$ ^{11}Be first excited state. A shell model calculation of the B_{GT}required a mixture of s and p wave components of the neutron ground state wavefunction of ^{11}Li, as later confimed in the neutron knockou data [Sim99]. Moreover, the beta decay strength feeding the state at 18 MeV in ^{11}Be has been proposed [Bor97a] to be as large as those found in other neutron rich halo nuclei, as mentioned above.

The effects of the halo wave function on the beta decay stress the importance of obtaing a complete picture of the B_{GT}decay strength. The decay to the first excited state and neutron emitting states has been extensively studied [Mor97, Bor97b, Fyn04, Sar04, Hir05]. However, the challenge in the case of the decay of ^{11}Li resides in the complexity of the decay channels above the charged particle thresholds. In this thesis I present the analysis of the beta-delayed charge particle emission channels in ^{11}Li, in order to obtain a more accurate description of the B_{GT}strength distribution to levels above the charged particle emission thresholds. Specifically, we are interested in comparing the strength distribution to that of the ^{9}Li core, searching for specific patterns indicating of independent core or halo decay.

This thesis will be divided in the following chapters:

- **Theoretical background**. In this chapter I present the theoretical foundations of the beta-decay process. After, I summarize general aspects of the β-delayed particle emission and known cases of particle precursos. Finally I summarize the previous knowledge about the beta decay of the two nuclei studied in this work, ^{9}Li and ^{11}Li.

- **Experiment.** In this chapter I describe the technical aspects of the setups used in the experiments described in this Thesis, as well as the production technique, isotope separation on-line, used at the facility where the experiments took place, ISOLDE.

- **Analysis techniques.** This chapter is divided in two sections concerning the two major analysis techniques used in this work. In the first section I describe the analysis techniques proper, necessary to extract and clean the necessary kinematical information. The second section deals with the models of the resonances and angular correlations used in the Monte-Carlo simulations. This simulations are compared to the data to better understand its features.

- **Study of the ^{9}Li β-delayed multiple particle emission from the 2.43 MeV state in ^{9}Be**. This chapter presents the results of the study of the breakup mechanism of the 2.43 MeV state in ^{9}Be. We compared the experimental alpha and neutron energy distribution with secuential and direct models of the breakup, obtaining a better match for for the drect model.

- **Study of the ^{11}Li β-delayed charged particle channels; Part I: 2003 experiment.** The results of the 2003 experiment on the ^{11}Li β-delayed charged particle emission are presented in this chapter. From the study of the charged particle energy correlations, we propose two new decay channels involving ^{A}He resonances and obtain new decay branching ratios.
- **Study of the ^{11}Li β-delayed charged particle channels; Part II: 2007 experiment**. In this chapter the results of the 2007 experiment on the β-delayed triton and ^{7}He+α channels are presented. Finally, we discuss the B_{GT}distribution obtain in this work compared to that of its core ^{9}Li, and compared to a shell model calculation.

Chapter 1

Theoretical background

This chapter presents a summary of the theoretical background related to the study dedicated to the β-delayed particle emission of neutron rich Li isotopes presented here. The beta decay is a well known process, which makes its study an ideal tool to determine the nuclear structure. Contrary to reaction experiments, which populate numerous excited states in the compound nucleus with many different dexcitation channels, the selection rules of β-decay are very selective, which makes easier to extract information on the parent and daughter nuclei.

The disadvantage of a reduced window to explore the daughter nuclear structure in nuclei near the valley of stability is reduced when going away from stability due to the quadratic increase of the mass difference between isobars. This increase in the Q_β window far from stability is accompanied by a reduction of the binding energy of the last nucleon. So often the β-decay of nuclei far from stability is followed by the particle emission, charged particles for the neutron defficient nuclei and neutron emission for the neutron rich. Only in the very neutron rich nuclei the Q_β-window is open to not only the βn decay mode but also to charged particle emission such as deuterons, tritons and alphas. These rare decay modes have the advantage of the very high efficiency for the detection of charged particles.

In this chapter I briefly review the β-decay formalism. In the particle emission section I discuss general aspects of β-delayed multi-particle emission and the known cases of β particle precursors. Finally I will summarize the current knowledge on the two nuclei studied in this Thesis, ^{9}Li and ^{11}Li.

1.1 The beta decay

The β decay is, in the β^- case, the decay of a neutron into a proton emitting an electron and an antineutrino, and in the β^+ case, a proton decays into a neutron emitting a positron and a neutrino. The β-decay of the free neutron is energetically favorable, with a half life of 885.7(8) s [Ams08]. In the nuclear medium, it is as well possible for a proton to decay into a neutron by capturing one of the electrons (EC, Electron Capture) of the most internal shells of the atom. Both electron capture and β^+ decay are possible except if the mass difference between the parent and daughter is lower than two electron masses. In the latter case there is not enough energy to create a positron and only the electron capture process is possible, as shown in eq. 1.5. The neutron decays into a proton in vacuum, while a proton can only decay in neutrons in nuclear matter. The β^+-EC decay mode, for neutron deficient nuclei, and the β^-, for neutron rich nuclei, are the most common way for unstable nuclei to decay into nuclei in the valley of stability. In summary, the β-decay types are:

$$A(N,Z) \rightarrow A(N-1,Z+1) + e^- + \overline{\nu_e} \qquad \beta^- \text{ decay} \tag{1.1}$$

$$A(N,Z) \rightarrow A(N+1,Z-1) + e^+ + \nu_e \qquad \beta^+ \text{ decay} \tag{1.2}$$

$$A(N,Z) + e^- \rightarrow A(N+1,Z-1) + \nu_e \quad \text{EC (Electron Capture)} \tag{1.3}$$

The energy available in the decay is given by the mass difference between the parent and daughter nuclei

$$Q_{\beta^-} = M_Z c^2 - M_{Z+1} c^2 \tag{1.4}$$

$$Q_{\beta^+} = M_Z c^2 - M_{Z-1} c^2 - 2m_e c^2 \tag{1.5}$$

$$Q_{EC} = M_Z c^2 - M_{Z-1} c^2 + B_e \tag{1.6}$$

where M_Z and $M_{Z\pm1}$ are the atomic masses of the parent and daughter nuclei respectively, and B_e is the binding energy of the electron in the inner shell where it was captured from. In electron capture X rays are produced when an electron from an upper shell occupies the hole left by the captured electron. In the β^- decay we do not take into account the binding energy of the produced electron. In $\beta^\pm$ decay processes the final state involves three particles, thus, the energy of the emitted electron or positron is continuous up to a maximum energy of $Q_{\beta^\pm}$.

In 1934, Fermi [Fer34] developed a successful theory of the beta decay based on the Pauli hypothesis of the existence of the neutrino. In that theory the decay probability per unit of time, $d\lambda_{i\rightarrow f}$, is given by the Fermi's Golden Rule:

$$d\lambda_{i\rightarrow f} = \frac{2\pi}{\hbar}|M_{if}|^2\rho(E_f) \tag{1.7}$$

where $\rho(E_f)$ is the available density of states in the daughter nucleus and $||M_{if}||$ is the coupling through the interaction operator of the wavefunction of the initial and final states, *i.e.* the matrix element. In the original formulation by Fermi, it was postulated that two vector currents are sufficient to describe the interaction. However in 1956, *strange* particles were discovered, with parity violating decay modes

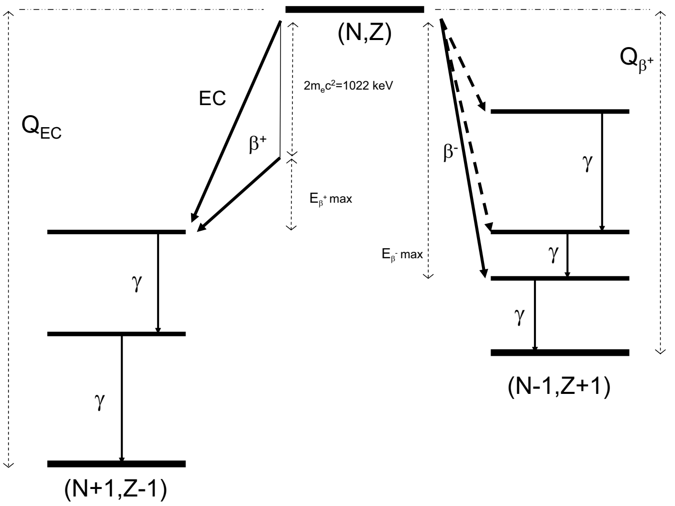

Figure 1.1: Schematic view of the β-decay populating states in the daughter nucleus, which in turn decay into the ground state of the daughter nucleus via gamma decay. The figure represents a particular case where both β^+-EC and β^- decay are energetically allowed, such as the case of ^{64}Cu, ^{74}As and ^{126}I.

observed. In 1956, Lee and Yang [LY56] developed a consistent theory of the weak interaction that violates parity, which was subsequently corroborated by the famous experiment by Wu and coworkers [Wu 57]. In the Lee and Yang theory the matrix element is described by the coupling of a vector and an axial-vector current

$$M_{if} = G_F \left(\overline{\psi'}_i \gamma_\mu \gamma_5 \psi_i\right) \left(\overline{\psi'}_f \gamma^\mu \psi_f\right) \tag{1.8}$$

where $G_F/\hbar c$=1.16637(1)$\times 10^{-5}$ GeV^{-2} [Yao06] is the Fermi coupling constant, $\psi_{i,f}$ are the initial and final wavefunctions, γ^μ are the Dirac matrices and γ_5 are the chirality matrices. To simplify the calculations, the wave function of the electron and the neutrino are considered plane waves, $exp\left(i\frac{\vec{p}\,\vec{r}}{\hbar}\right)$, which do not carry angular momentum. This approximation defines the *allowed* β-decay transitions. One advantage of this approximation is that we can factorize the interaction in hadronic and leptonic parts

$$d\lambda_{i\rightarrow f} = \frac{2\pi}{\hbar}|M_{if}^H|^2|\langle e^-,\overline{\nu}_e|J_\mu^L|0\rangle|^2\rho(E_f)^2 \tag{1.9}$$

where M_{if}^H is the hadronic matrix element and $\langle e^-,\overline{\nu}_e|J_\mu^L|0\rangle$ is the non-relativistic leptonic matrix element. The equation is written for β^- decay because this is the case for ^{9,11}Li, the nuclei studied in this work. The forbidden transitions of a given order can be calculated using the above expression by expanding the exponential terms of the electron wave function up to the desired order. A more detailed discussion on this formalism is given in [HM84, GK90].

The transition probability in the *allowed* approximation is thus given by integrating the above equation over the electron and neutrino states density

$$\lambda_{i\to f} = G_F^2 \frac{m_e^5 c^2}{2\pi^3 \hbar^7} | \left\langle f|\hat{O}_\beta|i\right\rangle |^2 \int_{m_e c^2}^{E_i - E_f} dE_e p_e^2 \left(E_i - E_f - E_e\right)^2 \mathcal{F}\left(Z_f, E_e\right) \tag{1.10}$$

where E_i, E_f are the energies of the initial and final state, respectively, the $\mathcal{F}\left(Z_f, E_e\right)$ factor takes into account the interaction between the nuclear charge and the emitted electron, and $\left\langle f|\hat{O}_\beta|i\right\rangle$ is the hadronic matrix element between the initial and final states in the non relativistic approximation. These matrix elements are explicitly dependent on the structure of the parent and daughter nuclei. The second part of the equation, the integral that depends on the energy and momentum of the emitted electron, is called the Fermi integral, $f\left(Z_f, E_{fi}\right)$, so we can rewrite the above equation as

$$\lambda_{i\to f} = G_F^2 \bar{K}^{-1} f(Z_f, E_{fi}) | \left\langle f|\hat{O}_\beta|i\right\rangle |^2 \tag{1.11}$$

where $\bar{K}^{-1} = \frac{m_e^5 c^4}{2\pi\hbar^7}$, $E_{fi} = E_f - E_i$ and

$$f\left(Z_f, E_{fi}\right) = \int_{m_e c^2}^{E_i - E_f} dE_e p_e^2 \left(E_i - E_f - E_e\right)^2 \mathcal{F}\left(Z_f, E_e\right) \tag{1.12}$$

is the Fermi integral, or Fermi factor. In the *allowed* approximation not only we can separate the hadronic and leptonic parts, but we can separate the vector and axial parts of the interaction

$$\hat{O}_\beta = \hat{O}_F + \hat{O}_{GT} \tag{1.13}$$

where $\hat{O}_F$ and $\hat{O}_{GT}$ are the vector and axial parts respectively. In the non relativistic approximation, valid for nuclear matter, they take the form

$$\hat{O}_F = \sum_j t_\pm(j) \tag{1.14}$$

$$\hat{O}_{GT} = \sum_j \sigma(j) t_\pm(j) \tag{1.15}$$

where the sum is over each nucleon of the final state in the daughter nucleus, J_i is the spin of the initial state in the parent nucleus, $t_\pm$ are the isospin raising and lowering operators (with $t_{\mp}$ for $\beta^{\pm}$ decay) and $\sigma(j)$ are the spin operators, the Pauli matrices. They are defined from the weak mixing angle θ_W as [Ams08]

$$\begin{aligned} g_A &\equiv \frac{1}{2} && (1.16)\\ g_V &\equiv -\frac{1}{2} - 2sen^2(\theta_W) && (1.17)\\ sen(\theta_W) &= 0.23149(13) && (1.18) \end{aligned}$$

With the axial-vector and vector, called Gamow-Teller and Fermi, parts of the interaction separated, we rewrite eq. 1.11 as

$$\lambda_{i \to f} = \frac{ln(2)}{D}[f_V(Z_f, E_{fi})\mathrm{B}_{\mathrm{F}}^{if} + f_A(Z_f, E_{fi})\left(\frac{g_A}{g_V}\right)^2 \mathrm{B}_{\mathrm{GT}}^{if}] \tag{1.19}$$

where $D = \frac{ln(2)\bar{K}^{-1}}{g_V^2}$=6144.2(13) s [HT09], g_A/g_V=-1.2695(29) [Yao06] and B_{F} and B_{GT} are defined as the Fermi and Gamow-Teller transition matrix elements:

$$\begin{aligned} \mathrm{B}_{\mathrm{F}}^{if} &= |\left\langle f|\hat{O}_F|i\right\rangle|^2 && (1.20)\\ \mathrm{B}_{\mathrm{GT}}^{if} &= |\left\langle f|\hat{O}_F|i\right\rangle|^2 && (1.21) \end{aligned}$$

For some calculations it is useful to define the Gamow-Teller transition element including the coupling constants

$$B(GT) = (g_A/g_V)^2\mathrm{B}_{\mathrm{GT}} \tag{1.22}$$

Finally, in order to obtain the transition probability one needs to calculate

- The leptonic part of the transition probability, the Fermi integrals f_A and f_V, represent the available final states density for the electron and neutrino, the phase space, that is completely determined by kinematics.
- The Fermi and Gamow-Teller transition elements, B_{F} and B_{GT}. The matrix elements depend only on the wave functions of the parent and daughter nucleus

Fermi integrals

The Fermi functions f_A and f_V are derived from the parameterization proposed by Wilkinson and Macefield [WM74]. They define a dimensionless Fermi function that can be divided in a charge independent part and a correction due to the nuclear charge

$$f_{WM} = \delta_{WM} f_{Z=0} \tag{1.23}$$

where $f_{Z=0}$ corresponds to the adimensional Fermi integral for Z=0

$$f_{Z=0} = \frac{1}{60}\left(2w_0^4 - 9w_0^2 - 8\right)p_0 + \frac{1}{4}w_0 ln(w_0 + p_0) \tag{1.24}$$

where $w_0 = (E_0 + m_e)/m_e$ is the relativistic Lorentz factor, E_0 is the electron end-point energy (*i.e.* the energy of the electron for 0 neutrino energy) m_e is the electron mass and $p_0 = \sqrt{w_0^2 - 1}$ is the electron momentum in electron mass units. The correction due to the nuclear charge is parameterized as

$$ln(\delta_{WM}) = \sum_{n=0}^{3} a_n (ln(Q_\beta - E_f))^n \tag{1.25}$$

where the a_n coefficients are tabulated in [WM74] for the different values of Z and $Q_\beta - E_f$. Finally, we obtain f_A and f_V from the parametrization of Wilkinson and Macefield as [CWB93]

$$f_A = \delta_R \delta_D f_{WM}; \qquad f_V = \delta_V f_A \tag{1.26}$$

where δ_R and δ_V are small ($\sim 10^{-5}$) corrections due to "outer" radiative processes and the distribution of nuclear charge respectively. The factor δ_V factor is the ratio between the f_V and f_A Fermi functions, which is around 1% for light nuclei.

Transition matrix elements

The transition matrix elements B_F and B_{GT} are the transition strengths for Fermi and Gamow-Teller decays respectively between the initial and final states. Therefore the strength depends on the overlap between the initial state in the parent nucleus and the final states populated in the daughter nucleus, which are eigenstates of the Fermi and Gamow-Teller operators. As indicated in equation 1.14 in the non relativistic *allowed* approximation of β-decay the Fermi operator contains only of the raising and lowering isospin operators. As the isospin is a good quantum number of the nuclear interaction, the eigenstates of the isospin operator are as well eigenstates of the daughter nucleus. Therefore the full Fermi strength, in the *allowed* approximation, goes to a single state in the daughter nucleus, called Isobaric Analog State (IAS), which is the image of the parent nucleus ground state. If the Coulomb force is neglected, then the IAS would be at the parent ground state energy relative to the daughter state. However, the relative position between the parent and the IAS in the daughter nucleus is determined by the coulomb energy shift due to the change in Z from the parent to the daughter nucleus. In β^- decay, adding one proton will move the IAS above the Q_β, whereas removing one proton, β^+ decay, will move it below the Q_β. This implies Fermi transitions only occur for β^+ decay, and for nuclei of Z>N.

The Gamow-Teller operator, shown in equation 1.15, contains the isospin raising and lowering operators as well as the spin operators, the Pauli matrices σ. This implies that the eigenstates of Gamow-Teller decay are simultaneously eigenstates of isospin and spin. As the nuclear force is spin dependent, the Gamow-Teller state is no longer an eigenstate of the daughter nuclei, but a distribution of states. The maximum of the Gamow-Teller strength , called the Gamow-Teller Giant Resonance (GTGR), is determined by the maximum overlap of the final states distribution with the initial parent nucleus wave function, so it is approximately centered at the IAS, with an equivalent Coulomb shift as the IAS.

Summarizing, the selection rules for *allowed* transitions are given by the Fermi and Gamow-Teller operators. For Fermi transitions no isospin or spin change are allowed, ΔT=0 and ΔJ=0. In the Gamow-Teller case, as both the spin and isospin operators are present, there can be change in isospin if there is change in spin simultaneously, ΔT=0,±1 and ΔJ=0, ±1. In both cases the operators in the *allowed* approximation are parity independent, thus the parity is conserved, $\Delta L = 0$. The transitions between two 0^+ states are a little bit different to classify. If the two 0^+ states are analog states, then the transition is very intense, of the Fermi type. If the two states have different isospin, the transition is greatly hindered, thus of the *forbidden* type [RG73]. In fact, the transition strength measured for isospin forbidden transitions is a measurement of the isospin mixing of the initial state [AF61].

The selection rules for transition non *allowed* transitions, called *forbidden*, are determined by the leptonic wave functions in the hadronic matrix elements. As mentioned above, the leptonic wavefunctions are treated in a multipolar expansion, where the order of the expansion, l, determines the selection rules. The parity change of *forbidden* transitions is always given by $\Delta\pi=\pi_i\pi_j=(-1)^l$. The spin change of *forbidden* Fermi transitions is $\Delta J=l-1$, whereas $\Delta J=l,l+1$ for *forbidden* Gamow-Teller transitions.

Experimental evaluation of the β-decay

In experiments, instead of the transition probability λ of eq. 1.19, the β decay strength is obtained from the decay rate ft,

$$ft = \frac{D}{\mathrm{B_F} + (g_A/g_V)^2\mathrm{B_{GT}}} \tag{1.27}$$

where f is the Fermi factor, $t = ln(2)/\lambda$ and $t = T_{1/2}/BR_f$ is the final state partial

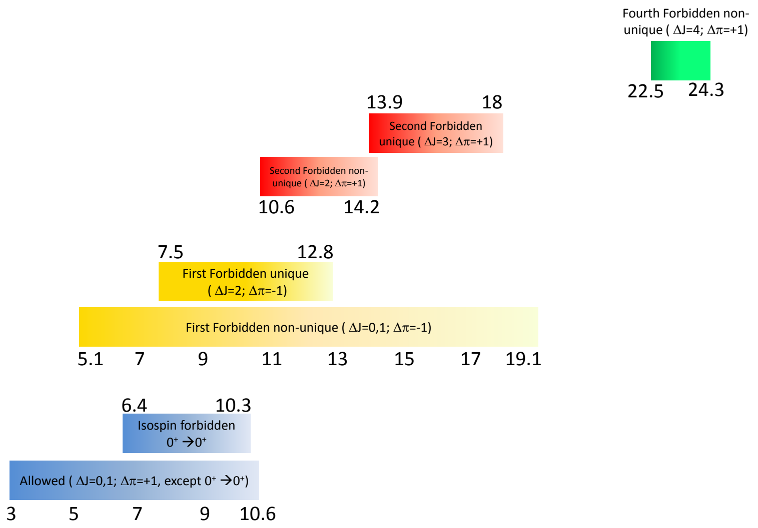

Figure 1.2: Observed ranges of $\log(ft)$ *values, ordered according to their degree of "forbiddenness", taken from [Sin98].*

half-life, where BR_f is the branching ratio to the final state. This allows to directly relate the B_F and B_{GT} matrix elements with the measured branching ratios, and therefore extract information on the wave function of the initial and final states.

Moreover, the strength of the transition, measured as $\log(ft)$, is related with the "forbiddenness" of the transition. As mentioned above, the degree of "forbiddenness" is related with the spin and parity change between the initial and final state, thus it can be used, if the initial parent state is known, to extract information on the spin and parity of the final states populated in the decay. B. Singh and coworkers [Sin98] have compiled the observed values (up to 1998) of different classes of *allowed* and *forbidden* transitions to obtain an empirical range of permissible $\log(ft)$ values, shown in Table 1.1. A graphical representation of the permissible ranges of the different orders of "forbiddenness" is shown in Fig. 1.2.

1.2 Particle emission

The beta decay process described in the previous section is by far the most common decay mechanism for unstable nuclei to reach the valley of stability. However, as one moves away from the stability valley, the binding energy per nucleon decreases, and thus the nucleon, or even clusters of nucleons (*e.g.* α particles), separation energy decreases. The particle ${}^{\mathrm{y}}_{\mathrm{x}}\mathrm{P}$ separation energy for nucleus ${}^{\mathrm{A}}_{\mathrm{Z}}\mathrm{X}$ can be calculated from

Table 1.1: List of observed $\log(ft)$ *values ordered by degree of "forbiddenness", compiled by B. Singh et al. [Sin98].*

β-decay transition type	$\Delta\pi$	ΔJ	$\log(ft)$
Superallowed	+1	$0 \approx 3.5$	
Allowed	+1	0,1	3.0→10.6
Isospin forbidden $0^+ \rightarrow 0^+$	+1	0	6.4→10.3
First forbidden non-unique	-1	0,1	5.1→19.1
First forbidden unique	-1	2	7.5→12.8
Second forbidden non-unique	+1	2	10.6→14.2
Second forbidden unique	+1	3	13.9→18.0
Third forbidden non-unique	-1	3	17.5
Third forbidden unique	-1	4	21.1
Fourth forbidden non-unique	+1	4	22.5→24.3

the mass differences as

$$S_P = -M(A,Z) + M(A-y, Z-x) + M(y,x) \tag{1.28}$$

defined positive for bound nuclei. Thus, $S_P = 0$ marks the limit of nuclear stability. In the case of neutron and proton separation energy, they are called the neutron and proton driplines, beyond which no more neutrons or protons can be kept bound to the nucleus. However, particle emission is not only possible for nuclei in the drip-lines. As the nuclei get closer to the drip-lines the particle separation energies become lower, thus making the β-feeding of states beyond the particle separation energy possible. This process is known as β-delayed particle emission.

In this section I will first summarize the experimental knowledge about direct and β-delayed particle emission. In a later section I will collect the current experimental and theoretical knowledge about the two nuclei studied in this work, ^{9}Li and ^{11}Li.

Direct particle decay

The proton dripline is closer to the valley of stability, as the coulomb repulsion prevents nucleus with a large proton excess to be bound. Thus, the observation of ground state proton radioactivity indicates that the proton dripline has been reached. The first evidence of proton radioactivity was observed in the study of a high spin, I^{π}=19/2^{-}, long lived isomeric state of ^{53}Co (see [BB08] and references therein). Since then, 28 nuclei emitting protons from their ground state are known [BB08]. It is interesting to note that no proton ground state emitters of Z below the 50 shell closure have been observed. This is due to the pure experimental requirement that the proton emission half-life has to be shorter than the β^+ decay half-life, but long enough to be detected, that, is the unbound proton travels through the potential barrier in a time long enough (t>μs) to observe the decay. The measurement of the decay half-life and proton energies has allowed experimentators to obtain conclusive information about the structure of many of these nuclei, which has been used to test the predictions of the shell model for spherical and deformed nuclei beyond the dripline.

Of even greater interest from the nuclear structure point of view is the case of two proton radioactivity, the last radioactivity mode observed. It was proposed by Zel'dovich [Zel60] for even-Z light nuclei, for which, due to the pairing force, one proton emission is energetically forbidden, whereas two-proton emission is allowed. The fact that it is easier to emit two protons simultaneously than to break the pair has the interesting consequence that by measuring the energies and angular distribution of these two protons one can learn about the decay mechanism and the correlations present in the parent nucleus wave-function. Several examples of two proton radioactivity of short-lived high excited states, populated in β-decay were early found [Cab83], the main interest was to find a "long"-lived ground state emitter. This was finally achieved in 2002 with the observation of two proton radioactivity from the ground state of ^{45}Fe [Gio02, Pfu02]. In 2004 a second ground state two proton emitter was observed, ^{54}Ni [Bla05].

On the neutron rich side, due to the difficulty in producing neutron rich nuclei, the neutron dripline has been reached only for nuclei of Z$\leq$10. The absence of any potential barrier for neutron emission makes the known neutron unbound nuclei short lived resonances, in the range of 10^{-20} s for light nuclei, such as $^{4-6}$H, ^{5,7,9,10}He or ^{10}Li, and in the range of 10^{-9} s for heavier nuclei such as ^{13}Be or ^{16,18}B [Til04].

β-delayed particle emission

The subject of this work is the use of the β-delayed particle emission process as a tool to study the structure of certain states. This process is possible for bound nuclei (S>0) near the driplines, since, while the isotopic mass difference (see equations 1.4 and 1.5) increases when approaching the driplines, the separation energies decrease, allowing for the β-feeding of states in the daughter nucleus above the separation energies. Beta delayed p, 2p, n, 2n, 3n, 4n, d, t and α emission has been observed [Poe96, JR01], with multiple particle emission also possible. Figure 1.3 shows an schematic view of β-delayed particle emission.

On the proton rich side, there are about 160 known βp emitting precursors today [BB08], which cover elements up to Hf (Z=73). The $\beta 2p$ decay mode has been confirmed for 10 proton rich nuclei (see [BB08] and references therein), ^{22}Al, ^{23}Si, ^{26}P, ^{27}S, ^{31}Ar, ^{35}Ca, ^{39}Ti, ^{43}Cr, ^{45}Fe and ^{50}Ni. Recently it has been claimed that ^{50}Ni is also a β-delayed two proton emitter [Dos07]. However, the measurement

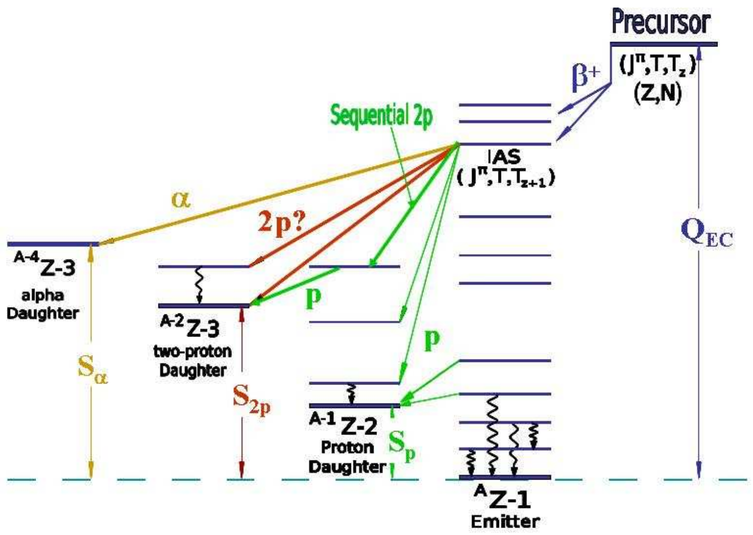

Figure 1.3: Schematic view of a β^+ precursor feeding states in the daughter nucleus that subsequently decay either emitting 1p, 2p, 3p and α particles, or by gamma de-excitation to lower energy states. Taken from [BB08].

was carried out by implanting the ^{50}Ni beam in a Si detector, so no proton-proton coincidences were measured. The two proton emission from the IAS was inferred from energetics. Finally, the β-delayed three proton radioactivity has been recently observed in ^{45}Fe [Mie07].

On the neutron rich side (see [Poe96] and references therein), 55 β-delayed neutron precursors have been observed (from ^{9}Be up to ^{94}Br), which include 15 $\beta 2n$ precursors, and three of them are three neutron emitters, ^{11}Li, ^{17}B and ^{31}Na. Finally, very exotic particle decay modes have been observed in β decay of nuclei near the neutron dripline, $\beta 4n$ in ^{17}B, βt in ^{6}He and ^{11}Li and βt in ^{8}He and ^{11}Li.

The large number of β-delayed precursors, as indicated above, makes the study of their particle emission a powerful tool to obtain information on both the β-decay of the parent nuclei and the nuclear structure of the particle emitting daughters. The β-delayed particle emission has been established for a long time, thus the decay mechanism is a well known process. The β-delayed proton emission in light nuclei occurs through states that are well separated, thus the energies are well defined and the β branching ratio can be obtained directly from the proton intensities. The particle emitting heavy nuclei are characterized by a high density of close narrow states in the daughter nuclei, resulting in a bell-shaped particle distribution. In these cases, it has been found that the fine structure of the particle distribution can be described by the statistical fluctuation due to the level density in the intermediate nuclei. Finally in some light nuclei close to the drip-lines, the daughter nuclei has only a few excited states, but usually broad, which complicates the analysis, specially if the final state includes the emission of two or more particles.

General features of the β-delayed particle emission in light nuclei

The features of the β delayed particle spectrum of light nuclei are dominated by the nuclear structure of the few states in the intermediate daughter nucleus. First, in light nuclei the states often have an appreciable fraction of the single particle strength and hence large widths, which may give rise to interference effects. Thus, special care has to be taken in the analysis of the experimental data and the interpretation of the results. Second, the combination of very large Q_β values and small separation energies for nucleons or clusters of nucleons results in relatively complicated spectra, due to the presence of channels with several particles in the final state.

Even in the simplest case, one particle emission from broad states, one has to take into account the effect of interference between states of the same spin. The effects of interference between states of the same spin can be either constructive, increasing the statistics in the energy region between the two interfering resonances, or destructive, giving rise to dips in the statistics. Thus, to properly estimate the beta feeding to interfering states from the observed statistics, it is not enough to simply count the area in the state energy region, a model that describes the interference between the states is needed. The R-matrix theory, originally developed to describe reaction mechanisms, has been adapted to describe the β-delayed particle emission of broad states, including interference effects.

In the cases where the final state includes more than two particles, the energy correlations between the emitted particles produce complicated spectra, that is the energy spectrum of the detected particles depends heavily in the energy and momentum correlations of the breakup mechanism. The possible break-up mechanism are:

- Directly into the final state continuum. The particles are emitted simultaneously into the final state, thus the kinematical relations between them and angular correlations depend uniquely on the phase space distribution and the properties of the initial state.

- Breakup through an intermediate resonance. In general, if one of the binary subsistems is a narrow resonance, and it is energetically available, that is, below the original state, the breakup will proceed sequentially. This can be understood by comparing the time the first particle needs to go through the potential barrier, which is inversely proportional to the Q value of the particle emission (the state energy minus the intermediate resonance energy), with

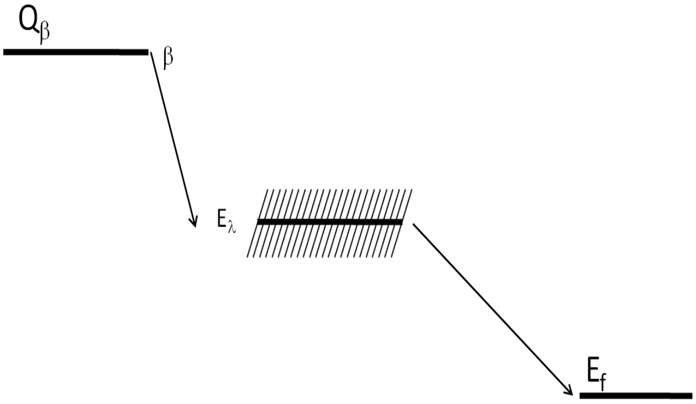

Figure 1.4: Schematic picture of the feeding of a single level decaying to a single channel of fixed energy E_f through an intermediate resonance of energy $E_{\lambda'}$. When the width of the λ and λ' intermediate states are equivalent the decay cannot be described as pure sequential ore direct breakup.

the half-life of the intermediate resonce, $\hbar/\Gamma$, where Γ is the resonance width. Therefore, when $Q \gg \Gamma$, the decay is purely sequential.

- Via a combination of both. However, if $Q \geq \Gamma$, the intermediate resonance is either broad or narrow but close to the original state, then the decay cannot be interpreted as sequential or direct breakup anymore (see Fig. 1.4).

Different formalisms are used to describe the breakup for direct or sequential mechanisms. In the sequential case, the energies of the different states and intermediate resonances completely determines the energy of the emitted particles. If the original state or the intermediate resonances are broad, then, as mentioned above, the R-matrix theory is applied to the decay of broad states through both narrow and broad resonances (see *e.g.* [BW88, Nym90, Ber01]).

In the case of multiple particle direct decay into the continuum, the simplest governing mechanism would be the distribution given by the phase space density integral of the particles momenta. Of course, in this formalism, all interactions and the initial state configuration between the particles are neglected. The first calculations that include the initial state information in the formalism, dubbed "democratic" decay, were carried by by Danilin [Dan87] for resonances in ^{6}Li and ^{6}He, Bochkarev [Boc89, Boc92] for ^{6}Be and ^{9}Be and ^{9}B [Boc90], Korsheninnikov [Kor90] for ^{12}C and

^{16}N, and Grigorenko for two proton radioactivity [Gri00, Gri01]. They postulate that the grand orbital momentum K is a good quantum number of the breakup, thus conserved.

$$K = L + 2n \tag{1.29}$$

, where L is the orbital angular momentum of the final three body system, and n=0,1,2,.... is the The final state configuration is then described in the basis of hyper-spherical harmonics of grand momentum K, and the particles spectrum is obtained by folding the phase space energy distribution with the energy distribution from "democratic" decay.

1.3 Previous knowledge of the ^{9}Li β-delayed particle emission

The ^{9}Li is a neutron rich nucleus with Z=3 and N=6. It decays via β^- to ^{9}Be, of $T_{1/2}$=178.3(4) ms [AW76] with a Q_β=13.6066(19) MeV [AWT03]. All excited states of ^{9}Be are above the neutron and alpha separation energies, S_n=1665.3(4) keV and S_α=2460(50) keV [AWT03]. The first experimental identification of ^{9}Li as a β-delayed neutron emitter was made by Gardner et al., [GKM51] by using the reaction ^{9}Be(d,2p)^{9}Li.

General knowledge of the ^{9}Li β-decay

Measurements of the energy spectra of delayed neutrons from ^{9}Li were performed by Macefield et al. and by [MWW69]Chen et al. [Che70] both using a time-of-flight technique. A feeding of 65(3)% to the ground state of ^{9}Be was found in [Che70], therefore a delayed neutron branching ratio P_n=35% was deduced. Björnstad et al. [Bjo81] determined a P_n=50(4)% by detecting beta-neutron coincidences. The beta particles were detected with a thick plastic scintillator and the neutrons with a 4π paraffin-moderated neutron counter.

As neither ^{8}Be nor ^{5}He are bound, all the ^{9}Be states that emit neutrons necessarily emit alpha particles at the same time. The first experiment was performed by Langevin et al. [Lan81]. Two silicon detectors were placed facing the carbon collecting foil, where the ^{9}Li was stopped, to measure α-α coincidences. It was established the role of states in ^{9}Be at 2.43, 2.78, 7.94 and 11.28 MeV. However, the lack of angular resolution prevented to obtain a firm conclusion about the decay mechanism. Nyman et al. [Nym90] measured the beta-delayed neutrons and alpha particles from the decay of ^{9}Li with a ^{3}He neutron spectrometer and a silicon surface barrier detector. In this work it was found that the main β-feeding to the high

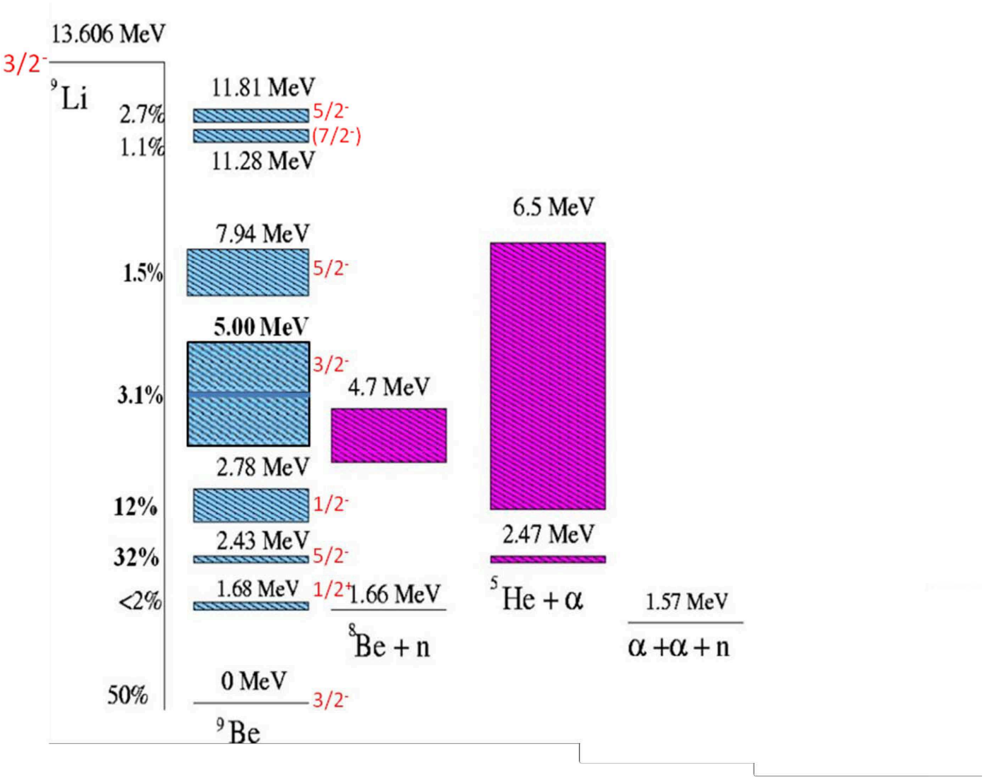

Figure 1.5: Schematic view of the β-decay of ^{9}Li and the intermediate resonances in ^{5}He and ^{8}Be that play a role in the breakup of ^{9}Be states. The states energies and spin and parities are taken from [Til04], the branching ratios and the spin and parity of the ^{9}Be 7.94 and 11.81 MeV states are taken from [Pre03, Pre05]. The ^{9}Be 5.0 MeV state energy, width, spin and parity are from [Pre05].

Table 1.2: Knowledge of the ^{9}Be states fed in the β-decay of ^{9}Li. The values are taken from [Pre05], otherwise stated. The B(GT) values include the $(g_A/g_V)^2$.

E(^{9}Be) (MeV)	I^{π}	Γ (keV)	BR (%)	B(GT)
g.s.	$3/2^-$	0	49.2(9)	0.0292(9)
1.684(7)	$1/2^+$	217(10)	<2	-
2.4294(13)	$5/2^-$	0.78(13)	29.7(30)	0.046(5)
2.78(12)	$1/2^-$	1080(110)	15.8(3)	0.011(5)
5.0(5)[a]	$3/2^-$ [a]	2000(500)[a]	3.2(10)[a]	-
7.94(8)	$5/2^-$ [a]	≈ 1000	1.5(5)	0.048(18)
11.81(2)	$5/2^-$ [b]	400(30)	2.7(2)	8.5(1.5)[b]

[a] Taken from [Pre05].

[b] Taken from [Pre03].

energy region in the daughter nucleus goes to the 11.81 MeV state in ^{9}Be, although a small β-feeding to the 11.283 keV state at the level of ~1% could not be discarded. This is in contradiction with [Lan81], which excludes any feeding to this state. This difference in the interpretation comes from different assumptions in the breakup mechanism: while Nyman et al fitted the alpha spectrum by assuming sequential decay through the ground state and the first excited states of ^{5}He and ^{8}Be [Nym90], Langevin et al., assumed instead that the breakup occurs as a mix of direct emission to the $2\alpha n$ continuum and through states in ^{8}Be. None of the two experiments contained enough information to determine the breakup mechanism unequivocally.

A series of experiments were performed in order to carefully determine the breakup mechanism, the branching ratios and the B(GT) values [Pre03, Pre05]. The charged particle spectrum was studied using full kinematical analysis, which allowed for the study of the different breakup scenarios, obtaining the branching ratios of each. The role of the ^{9}Be 11.81 MeV state proposed in [Nym90] was confirmed, it spin and parity were determined to be $5/2^-$ and a B(GT) value for this level of 5.3(9) was obtained [Pre03]. This implies the B(GT) to this state in the ^{9}Li β-decay its 4.4(10) times bigger than its counterpart in the mirror decay of ^{9}C measured in [Ber01], or 10.6(20) times bigger than that measured in [Buc01]. This is the largest asymmetry determined for a allowed beta transition.

Following the work on the high energy states, the low energy states in ^{9}Be were investigated [Pre05], with special care in studying the breakup through the ground state of ^{5}He. The branching ratios for the ^{9}Be states at 2.43, 2.78, 7.94 MeV were obtained, and the β-feeding of a $3/2^-$ state at 5.0(5) MeV and 2.0(5) MeV width was proposed. This state corresponds well with a state previously observed at 5.59 MeV in the ^{9}Be(p,p')^{9}Be* reaction, with tentative spin and parity assignment of

3/2$^-$ [Dix91]. A recent study [Bro07] of the breakup mechanism of states in ^{9}Be, populated in the ^{9}Be(^{6}Li,^{6}Li)^{9}Be, reaction confirmed the role of the ^{5}He resonances in the breakup of high excited states proposed by Prezado et al. [Pre05]. Table 1.2 and Fig. 1.5 show the current knowledge of the ^{9}Be states fed in the ^{9}Li β-decay.

Theoretical approach

On the theoretical side, the structure of ^{9}Be has been studied using a wide variety of models. Cohen and Kurath [CK65] used two different potentials (general two body matrix elements, 2BME, and a potential in LS representation, POT) for the two-body part of the shell model Hamiltonian, in order to solve the full p-shell interactions. The resulting excitation scheme of ^{9}Be reproduced well the known experimental knowledge of the time, and correctly predicted a 1/2 state below the first 5/2$^-$ and a 3/2$^-$ state at ∼5.0 MeV. Moreover, the calculated log(ft) are in excellent agreement with the experimental results for the low energy levels in ^{9}Be.

More recently Mikolas et al. [Mik88] summarized the different shell model prediction in the A=9 system within the full p-shell model space using the shell model code OXBASH. Four interactions were considered, two of them, (6-16)2BME and (8-16)POT, from the previous work by Cohen and Kurath [CK65] and the other two from Millener [Mil] and Kumar [Kum74]. As in the previous work [CK65], the calculated B(GT) of the low energy states in ^{9}Be agree well with the experimental results, although a discrepancy was found for the B(GT) values of the two 5/2$^-$ states at 7.94 and 11.81 MeV. They also calculated the spectroscopic factors for ^{8}Be+n and ^{5}He+α breakup, showing that the ratio between them follows the same trend observed in the experiments [Pre03, Pre05, Bro07], that is, at higher excitation energies in ^{9}Be the ^{5}He+α channel becomes more prominent.

Forssén et al [For08] have recently obtained the ^{9}Be excitation scheme in the *ab initio* No Core Shell Model (NCSM) formalism. The NSCM approach is based in solving the Schroedinger equation in a Harmonic Oscillator basis with a Hamiltonian including a realistic nucleon-nucleon interaction for the two body part. They reproduce remarkably well the ^{9}Be excitation spectrum, reproducing the ordering of the negative parity states. The cannot, however, reproduce the energy of the 1/2$^+$ first excited state, which was attributed to the lack of three body interactions in the Hamiltonian they used.

Another theoretical approach to model ^{9}Be consists in using microscopic simulations of the interactions of the components that form ^{9}Be. Kanada-En'yo [KEHO95] used the Antisymmetrized Molecular Dynamics (AMD) approach, which has the advantage that it does not assume intrinsic cluster configurations. Instead, it works with a set of wave functions that can develop into cluster states. the calculated excitation scheme reproduces well the ordering of the first three states in ^{9}Be, and again correctly predicts a 3/2$^-$ state in the 4-6 MeV region. Arai et al. [Ara96] and

Descouvemont [Des01] used a microscopic α+α+n cluster formalism to calculate the excitation scheme of ^{9}Be, in excellent agreement with the experimental values. Descouvemont [Des01] also investigates the overlap of the different excites states with ^{8}Be+n and ^{5}He+α configurations. The contribution of the ^{5}He+α channel is determined to increase as the excitation energy in ^{9}Be augments, a similar result as that of [Mik88].

Breakup of the ^{9}Be 2.43 MeV state

The subject of this thesis is the breakup mechanism of the ^{9}Be 2.43 MeV state. The breakup mechanism of this resonance has been a contentious subject for the past couple of decades. The proximity of this state (2.43 MeV) to the ^{5}He ground state ($E_{^5He}$=2.467(1) MeV [Til04]) and the tail ^{8}Be2^{+} first excited state ($E_{^8Be(2^+)}$=4.66(1) MeV, Γ=1.515(15) MeV) makes difficult to assign a purely direct of sequential character to the decay (see previous section).

The first study of the breakup of the ^{9}Be 2.43 MeV state by Bochkarev et al. [Boc89] and Vasil'ev et al. [Vas89] used a direct decay formalism described in hyperspherical coordinates, dubbed "democratic decay", along standard R-Matrix formalism to describe the breakup of the ^{9}Be 2.43 MeV state. The results of the analysis of the alpha spectrum support that most of the breakup occurs directly to the continuum with a sequential contribution of ~20% of decay through the ^{8}Be(gs). Grigorenko and Zhukov [GZ05] adapted the S-matrix formalism to include simultaneous scattering of three particles. Once applied to the photodisintegration of the ^{9}Be 2.43 MeV state it favors direct decay into the continuum, with a small contribution of sequential decay through the ground state of ^{5}He.

In a recent theoretical work by Alvarez-Rodriguez et al. [Alv08] on the distinction of direct and sequential three body decays. They studied the breakup of the ^{9}Be 2.43 MeV state using a three body α-α-n model of ^{9}Be. The method involves using Faddeev equations and the hyperspherical expansion method combined with complex scaling to obtain the resonance wave-functions. They found that the structures present at short distances, early in the breakup, are conserved once the particles move away, therefore, the initial configuration of the system determines the breakup mechanism. The results indicate that the majority of the breakups occur directly into the continuum, without any involvement of the ^{5}He(gs) or ^{8}Be(2^{+}) resonances, although there is a small contribution of sequential decay through the ground state of ^{8}Be.

A recent experiment by Papka et al., [Pap07] used a highly segmented setup to study the kinematics and angular correlations of the breakup of the 2.43 MeV state populated in the ^{9}Be(^{6}Li,^{6}Li)^{9}Be reaction. The main contributing channel was found to be the breakup through the 2^{+} first excited state of ^{8}Be, with a branching ratio of $86.5^{+4.5}_{-2.0}$%. A 11(2)% contribution from the ground state of ^{8}Be and a small contribution of <2.5% of the ground state of ^{5}He were also proposed. This results are in agreement with the theoretical calculations by Descouvemont [Des01]. It predicts contributions of 92.7%, 0.8% and 6.5% from the ^{8}Be(2^{+}), ^{8}Be(gs) and ^{5}He(gs) resonances, respectively. The sequential breakup of the ^{9}Be 2.43 MeV state was also considered by Buchmann et al. [Buc01] when studying the breakup of the mirror state in ^{9}B at 2.34 MeV. They determined from kinematics that the breakup of the ^{9}B 2.34 MeV state occurs largely via sequential decay through the ground state in ^{5}Li, which may indicate the mirror state in ^{9}Be decays sequentially through the ground state of ^{5}He.

Finally, determining the breakup mechanism of the ^{9}Be 2.43 MeV state is not only interesting from a nuclear structure point of view, but there is an extra motivation in regards of the ^{9}Be nucleosynthesis in neutron rich stellar environments. The α+α+n radiative capture process, ^{4}He(αn,γ)^{9}Be, plays an important role in the production of ^{12}C, and subsequently as a seed of the r-process (rapid capture of neutrons), in neutron rich stellar environments, such as supernova cores. The radiative capture reaction rate was first calculated for the ground state of ^{9}Be and assuming only a sequential reaction through the intermediate ^{8}Be ground state resonance [CF88]. Görres et al. [Gor95] improved the calculation of the reaction rate by taking into account the first excited state of ^{9}Be at 1.684 MeV, and by including the possibility of s-wave direct capture of a neutron after the first step of the reaction. Nevertheless, only the sequential reaction through the ground state of ^{8}Be was contemplated.

More recently, Angulo et al. [Ang99] performed a new calculation including more excited states in ^{9}Be. However, again, only the sequential reaction through the ground state of ^{8}Be was taken into account and the 2.43 MeV state in ^{9}Be was not considered, due to its small branch through ^{8}Be(gs). Given the importance of breakup of ^{9}Be excited states through ^{5}He observed in [Pre03, Pre05, Bro07], and the role of sequential breakup through ^{5}Li observed in the mirror states in ^{9}B, Buchmann et al. [Buc01] performed a new calculation of the ^{4}He(αn,γ)^{9}Be reaction rate, including the sequential reaction through the ground state of ^{5}He. This process was found to be more important at high temperatures, when there is enough energy available so that the most highly excited states in ^{9}Be can play role in the reaction rate, i.e. states known to have large decay branches through ^{5}He [Pre03]. This highlights the importance of determining the breakup mechanism of the ^{9}Be 2.43 MeV state, as a large breakup branch through the ground state of ^{5}He, is proposed from the study of the 2.34 MeV mirror state in ^{9}B, would have to be included in the present calculations of the ^{4}He(αn,γ)^{9}Be reaction rate, and modify the reaction rate at lower temperatures than previously expected.

1.4 Previous knowledge of the ^{11}Li β-decay

The ^{11}Li was first observed by bombarding an uranium foil with 5.3 GeV protons from the Bevatron cyclotron at Lawerence-Berkeley laboratory [Pos66]. In this experiment it was determined that ^{11}Li is particle bound even being so far away from the stable ^{6,7}Li isotopes. Although it is bound, its mass excess has been determined to be 40.72828(64) MeV [Smi08], and using the ^{9}Li mass of 24954.3(1.9) keV [AWT03] results in a neutron separation energy S_n=378(5) keV. The small separation energy indicates that the energy single particle states of the two last neutrons is so close to the boundary of the nuclear potential that new phenomena can occur.

Indeed, Tanihata and colaborators [Tan85b] measured the matter radii of Li isotopes, where they observed a largeincrease, 30%, of the ^{11}Li matter radii over that of the closest bound neighbour ^{9}Li. This was the first confirmation of a a new phenomenon, the neutron halo, where the wavefunction of the last bound particles extends in the classicaly forbidden zone of the nuclear potential, due to the low binding energy of the halo neutrons. A simple consecuence of this interpretation is that the halo wavefunction requires no signifcant potential barriers present, i.e. the largest spatial extensions will be obtained when the halo wavefunction is either s or p wave. In the case of the two neutron halos, as in ^{11}Li, s-wave will be favored as has increased simmetry [JR98]. The first evidence of a s-wave component of the ground state the ^{11}Li was indirectly obtained in the study of the β-decay of ^{11}Li [Bor97b]. They measured with high precission the branching ratio to the only bound state in ^{11}Be at 320 keV, and compared the result with a calculation using shell model. They found that the ^{11}Li ground state required a large 50% contribution of the $1S_{1/2}$ single particle state to match the feeding to the ^{11}Be 320 keV state. This result was later confirmed in a study of the momentum distribution of the halo neutrons in a striping experiment performed by Simon et al [Sim99]. The fit to the observed transverse momentum distribution indicated a contribution of 45% of the $1s_{1/2}$ single particle state.

^{11}Li β-decay to states in ^{11}Be below the charged particle thresholds

One of the most defining characteristics of the ^{11}Li β-decay is th large Q_β=20.54(3), which can be obtained from the ^{11}Li mass excess, 40.72828(64) MeV [Smi08] and comparing it to ^{11}Be mass excess, 20.171(4) MeV. [Bac05] The large Q_β combined with the low particle thresholds of ^{11}Be opens a pletora of decay channels, the largest number in any known nuclei. Experimental results have been reported for βn [Roe74], β2n [Azu79], β3n [Azu80], βt [Lan84] and βd [Muk96].

The first experimental efforts on the ^{11}Li beta-decay invoilved the determination of the neutrn emission probabilities [Roe74, Azu79, Azu80]. In the last expriment by Azume et al. [Azu80] an extensive study of the β-delayed neutron emission probabilites was performed using a ^{3}He proportional counter. Values of P_{1n}=82(7)%, P_{2n}=3.9(5)% and P_{3n}=1.8(2)% were reported.

Morrissey et al. measured the β-delayed neutron energy spectrum for the first time, using the time-of-flight technique. They obtained the branching ratio to a series of states in ^{11}Be previously observed only in the ^{9}Be(t,p) reaction. The ^{11}Li β decay to neutron unbound states ^{11}Be was addres using a new experimental technique developed by Fynbo et al. [Fyn03, Fyn04] based on stuying the dlopper broadenning of gamma lines in ^{10}Be to deduce the energy of the recoiling neutron. They obtained two new gamma transitionsin ^{10}Be and the beta branching ratios to states in ^{11}Be. An interesting result is that they found up to 6% of β feeding to an excitation energy region in ^{11}be around 16 MeV where no states have been seen before.

A similar study of the β-decay of ^{11}Li analysing the doppler broadening of gamma rays in the neutron-daughter was performed by Sarazin and colaborators [Sar04]. They obtained precise values of the decay branches and of the states in ^{11}Be and ^{10}Be involved. Furthremore, they observe a strong transition of the ^{11}Be 8.82 MeV state to states of spin in 2^+ and 2^-, proposed to have a ^{9}Be+n structure from shell model calculations (B.A. Brown, unpublished). They suggest that this effect points to a ^{9}Be core and 2n structure of the ^{11}Be 8.82 MeV state, which is of great interest to study the effects of the halo in the β-decay.

A recent β-γ-n coincidence experiment using polarized ^{11}Li [Hir05] determined the spin and parity of several levels fed in ^{11}Be (E<11 MeV). They used the time-of-flight technique to obtain the neutron energies and measured, in coincidence with neutrons, the assymetry of the emission of β-particle with respect of the polarizaion of the ^{11}Li beam, which is related to the spin and parity of the state populated in ^{10}Be. This techinique allowed them to obtain the spin of every level below the charged particle thresholds populated in the beta decay of ^{11}Li.

Fig. 1.7 shows schematically the ^{11}Li β-fed states in ^{11}Be and the decay channels discussed above as established prior to this experiment.

^{11}Li β-decay to states in ^{11}Be above the charged particle thresholds

The established channels involving charged particles involve the emission of α particles (2α+3n), ^{6}He (^{6}He+α+n), tritons (^{8}Li+t), deuterons (^{9}Li+d) and the emission of 1n and 2n feeding states in ^{10}Be and ^{9}Be, respectively. The β-delayed charged particle emission of ^{11}Li has been the subject of several previous studies [Lan81, Lan84, Muk96, Bor97a]. The two channels involving coincident α particles were studied only once prior to this work [Lan81]. The 2α3n channel was established to have contributions from the breakup of two states in ^{11}Be, one at 10.59 MeV and the other at around 18.5 MeV. The ^{6}Heαn channel was established as the ^{6}He+α breakup of a state at about 9.4 MeV in ^{10}Be fed in the neutron decay of the 10.59 MeV state in ^{11}Be.

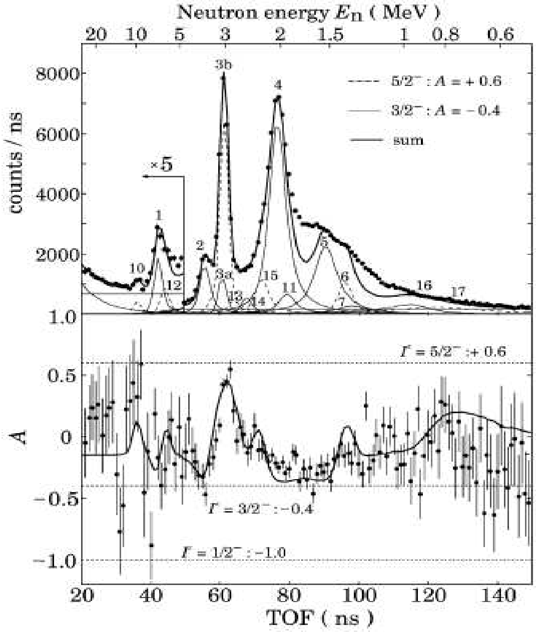

Figure 1.6: The upper panel shows the time of flight spectrum of ^{11}Li β-delayed neutrons, and the lower panel the assymetry in the beta emission, in coicidence with neutrons of the given energy. The dashed lines mark the expected values of the assymetry for a given spin of the ^{11}Be state. Taken from [Hir05].

By means of a gas-detector telescope for particle identification, the different ^{6}Heαn, 2α3n, ^{10}Be+n, ^{9}Be+2n, ^{8}Li+t and ^{9}Li+d decay channels of the ∼18.5 MeV state in ^{11}Be and its branching ratios were determined [Bor97a]. An R-matrix analysis established the energy of this state to be 18.15(15) MeV. The large reduced width of the ^{9}Li+d channel with respect to the Wigner limit [Mac60] was interpreted as evidence of the ^{11}Li(gs) β-decaying directly into the ^{9}Li+d continuum.

In the study of Hirayama et al.[Hir05] of the β-delayed neutron emission the 10.59 MeV level was found to contribute to the neutron spectrum via transitions to the ^{10}Be(gs) and tentatively to the first 2^+ state at 3.4 MeV and to the unresolved doublet at ∼9.27 MeV (4^-) and 9.4 MeV (2^+). The β-decay asymmetry of these three neutron transitions consistently determines the spin and parity of the 10.59 MeV level in ^{11}Be as $5/2^-$. Its 210(40) keV width was determined from the reaction ^{9}Be(t,p)^{11}Be [Ajz78].

Additional information about the decay of the 10.59 and 18.15 MeV states in ^{11}Be is obtained from three-neutron emission probability, which is equal to the branching to the five body (2α3n) final state. From the average branching ratio to the only bound state in ^{11}Be, and the P_{2n}/P_{1n}, P_{3n}/P_{1n} ratios determined by Azuma et al. [Azu80] a value of P_{3n}=1.9(2) % is obtained.

The different experiments summarized above paint a fairly complicated picture of the β-delayed charged particle breakup of ^{11}Li. It is neither well understood which levels in ^{11}Be are contributing to the charged particle channels nor their breakup mechanisms.

On the theoretical side there is one previous calculation of Gamow-Teller transitions in ^{11}Li [SO97] that involves states above the charged particle thresholds. Starting from a previous work [SO94], where they established the importance of *sd* shell mixing in the halo neutrons wavefunction, they studied the ^{11}Li Gamow-Teller distribution. They found that not only there is significant strength in the unknown region between 10 and 18 MeV, but the Gamow-Teller strength peaks at an energy between around 16 MeV. Moreover, they found the peak position to be sensitive to the *sd* mixing of the halo neutrons in ^{11}Li. This only remarks the importance of studying the high energy region of the ^{11}Li β-decay

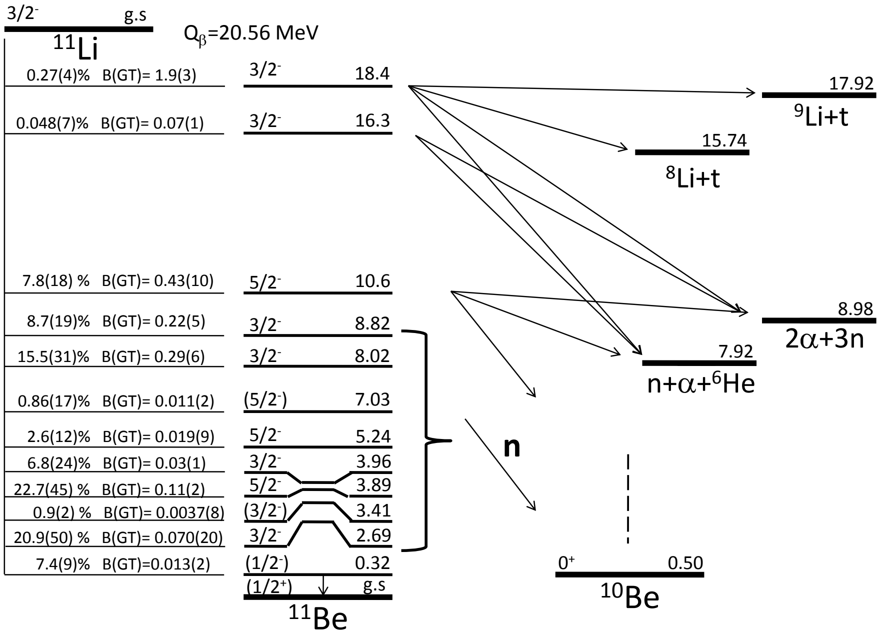

Figure 1.7: *Level scheme of the ^{11}Be states fed in the β-decay of ^{11}Li. The open breakup channels are shown, with each state decay channels indicated by arrows. The branching ratios for the 10.6 MeV state and states above are from the work presented in this Thesis.*

Chapter 2

Experiment

In this chapter, I will describe the experimental apparatus used in the two experiments performed in 2003 and 2007. Both runs were held at the ISOLDE facility at CERN. Radioactive nuclei are produced in this facility by bombarding a thick target with the proton beam from the PS-booster cyclotron. The ^{11}Li isotope was selected among the reaction products of a Ta target. The ^{11}Be beam was then implanted in the center of our experimental setup in a thin carbon foil, in order to measure the decay at rest.

The basic principles of the facility, ion production and how particle detection was carried out in our setup will be discussed. A slightly different setup was used in each experiment, as we tried to optimize the measurement of the ^{11}Li β-delayed charged particle channels. Both experiments used Double Sided Silicon Strip Detectors as the main detection unit, mounted in telescope configuration backed by thick Silicon pads. Furthermore, the neutron time-of-flight detector TONNERRE was mounted in 2003's experiment.

2.1 The ISOLDE facility

The production of radioactive nuclei at the ISOLDE-CERN facility is based on the on-line separation (Isotope Separation On-Line) of the reaction products after bombarding a heavy target with the proton beam of the PS-Booster cyclotron. The cyclotron produces a 2.4 μs long, 1.2 s interval pulsed beam, each proton pulse has $3{\cdot}10^{13}$ pps at 1.4 GeV. The cyclotron super-cycle is 14.4 s long, spanning 12 pulses, among which ISOLDE typically takes seven. The main drawback of using a pulsed cyclotron is the great energy dissipation out of the target, which reduces its useful life due to mechanical stress.

The reactions produced by the impact of the proton beam in the target are divided in three categories. In spallation reactions the target nucleus dissipates

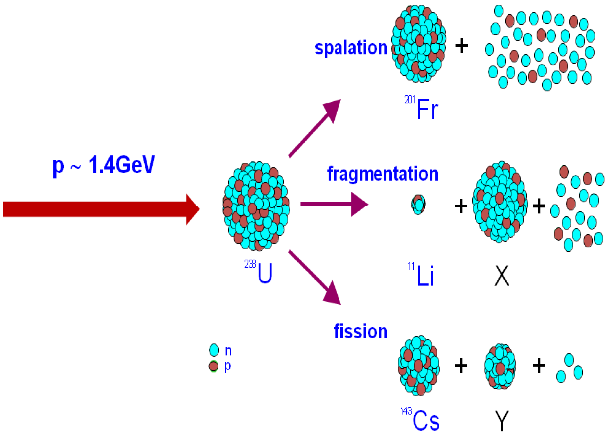

Figure 2.1: Example of the different reactions occurring on a ISOLDE target after the 1.4 GeV PS-Booster proton beam impacts om a UC_x target. In spallation the excess of energy is dissipated by evaporating neutrons and protons, resulting in nuclei of mass number close to ^{238}U, such a ^{201}Fr. The fragmentation process involves the fission of the uranium in two nuclei where one is much lighter than the other, such as ^{11}Li. Finally, when the two fission fragments have similar masses, like when ^{143}Cs is produced, the process is simply known as fission.

the energy excess by neutron and proton evaporation. Thus, the resulting nuclei have mass number A that is close to the one of the target. An alternative process is when the target nucleus fissions due to the proton impact. Symmetric fission occurs when the two fission fragments have roughly half of the target nucleus mass. Otherwise, if one of the fragments is much lighter than the other, the process is known as fragmentation, which allows to produce neutron rich light nuclei out of heavy targets. Fig 2.1 shows the three possible reactions after proton impact.

Diffusion and ionization of the reaction products

The reaction products escape the target via diffusion processes. The ISOLDE targets consist of a cylinder of about 20cm long and 2cm in diameter of a highly resilient material such as Tanthalum and containing typically: small cylinders, as in the case of the Ta and Nb targets, or pressed powder pellets, such as the Uranium Carbide (UC_x) target, and liquid targets as the PbBi or Sn targets. The target is kept at a high temperature (1000°-2000° C) to facilitate the diffusion of the reaction products, as diffusion follows the Arrhenius law for most materials:

$$D = D_0 \cdot e^{\frac{-Q}{kT}} \tag{2.1}$$

Where Q is the activation energy and T is the temperature. In most materials whose diffusion does not follow the Arrhenius law, its diffussion can be described as a sum or product of Arrhenius terms.

Once the reaction product arrives at the target's surface it effuses out the target chamber into the ionization source. This process occurs as random path. There are several ionization sources available at ISOLDE, each one tailored for the ionization of a certain type of nucleus.

- The surface ionization source is based on the electron interchange that occurs between an atom and certain materials when the atoms passes close to their surface. Materials whose work function is low (around 2 eV) will easily give electrons to the passing-by atoms, therefore negatively ionizing them [Rav]. This source is the most efficient positive ion source, with as much as 90% of atoms ionized for most of the elements into their 1^+ charge state.

- Another commonly used ion source is the FEBIAD plasma ion source (Forced Electron Beam Ion Arc Discharge). This source consists of a cathode heated up to ~2000° C in order to emit electrons. The electrons are then confined in a chamber whose entrance is a perforated foil acting as an anode, and the cathode is the extraction electrode of the produced positive ions. The chamber contains a gas, Ar-gas usually, that is ionized when it gets in contact with the cathode's electrons, resulting in a plasma state gas. The electron cloud of the plasma ionizes the reaction products by impact as they pass through the FEBIAD chamber. One electron removal probability is very high for this source, making it the most efficient way of ionizing noble gases into their 1^+ charge state [SRI92].

- Finally, a laser ionization source is also available at ISOLDE. Two or three lasers with different frequencies are used, one of them tuned to a first atomic transition that selects the chemical element we are interested in. The remaining two lasers are tuned to frequencies that excite the element to the ionization continuum. This method allows the laser ion source to be the most selective source in the ISOLDE catalogue [Rav].

Beam extraction

In order to extract the ions from the target-ion source system, these two elements are placed inside a container kept at a 60 kV potential, while the exit of the target-ion source system is connected to ground. This potential propels the ions into the mass separator. There is a problem in using this extraction method along a pulsed cyclotron. The proton beam impacting in the target creates a very short and intense current, ionizing the surrounding air. If the extraction potential were to be active at that moment, there would be a discharge destroying the high voltage source.

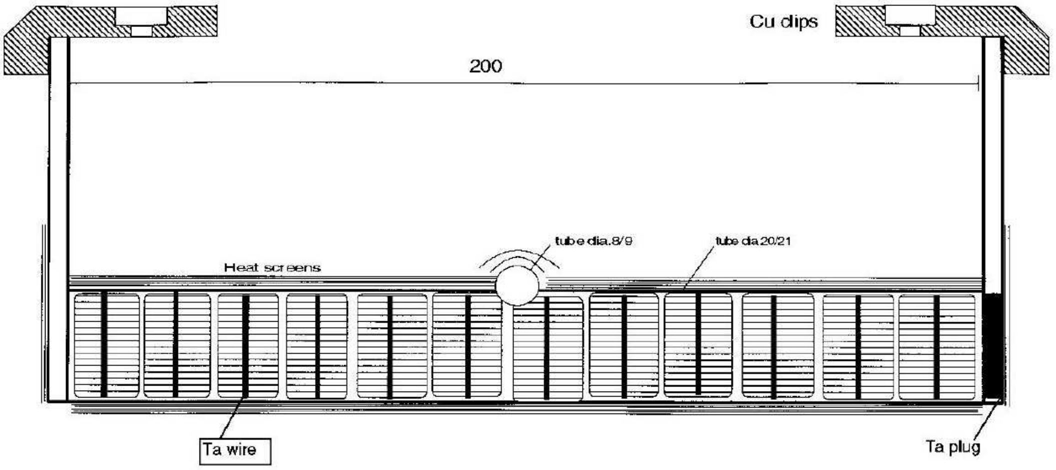

Figure 2.2: Cross section of the target container, consisting of a 20.21 cm W tube heated up to 1720° C. The cylinders inside are the target itself, in our case Ta.

In order to avoid this problem the extraction voltage is set to 0 V 35 μs before the proton impact, and restored 5 ms after. This is achieved by superimposing a negative polarity pulse to the extraction voltage, during the desired period [Kug00]

Mass separation

There are two mass separators available at the ISOLDE facility, GPS (General Purpose Separator) and HRS (High Resolution Separator). The former consists of a series of magnetic lenses focusing the ion beam coming from the ion source, a magnetic dipole separator of 55°and a second series of magnetic lenses after the separator. The GPS separator's resolution power is around $m/\Delta m=2400$, where Δm is the mass difference between the selected nucleus and the neighboring nuclei masses. The series of magnetic lenses after the separator focus the selected ions and distributes them in three different beams. Two magnetic dipoles form the separator core of HRS, with a series of magnetic quadrupoles and magnetic lenses correcting high order optical aberrations. The full HRS system's maximum resolution power is $m/\Delta m=15000$ [Kug00]. But due to the low optimization of the emmitance of the beam the maximum mass resolution observed was 7000 in an experiment where ^{37}Ca was separated using the HRS from ^{37}K [Gar91].

2.2 Production of ^{11}Li

The nuclei of interest in this work are ^{9}Li and ^{11}Li. The two isotopes were produced bombarding a Ta target with protons from the PS-booster cyclotron, in the frag-

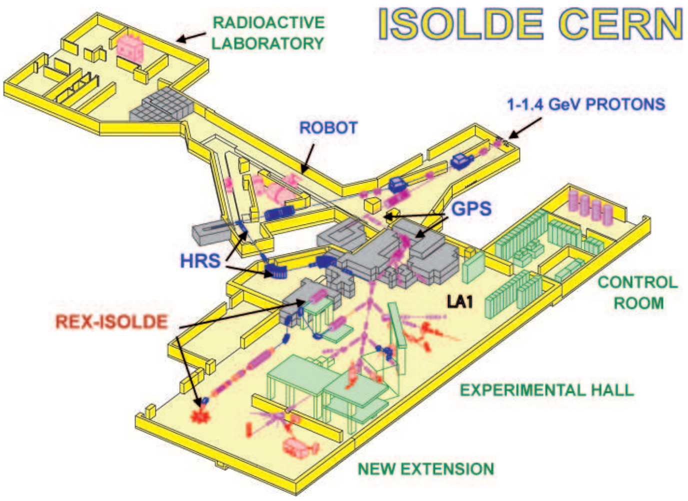

Figure 2.3: Schematic drawing of the ISOLDE experimental Hall. The experiments described in this work took place at beam line LA1.

mentation reaction ${}^{181}_{73}\mathrm{Ta}_{108}+\mathrm{p}\rightarrow{}^{9,11}_{3}\mathrm{Li}_{6,8}+\mathrm{X}$. The electronic affinity of the chemical element Li is very low, so it is easy to ionize to positive charge. The tungsten surface ionization source was used, as is the most effective positive ionization source, in combination with the HRS mass separator in 2003 and the GPS mass separator in 2007. Although for light elements such as Li there is no need of the high resolution separator HRS, GPS was not available in 2003. In both experiments in 2003 and 2007 the extraction voltage was set to 30 kV, in order to use the thinnest carbon foil stopper possible.

The number of ^{11}Li ions implanted in the experimental setup was estimated from the observed intensity of the $\beta\alpha$ decay channel of the ^{11}Be daughter nuclei (see 5.4, 6.3.3). We obtained 100 ions/s in the 2003 experiment and 800 ions/s in the 2007 experiment. The transmission probability through the ion source-mass separator system was estimated to be around 50% in both experiments, which implies a production rate in the target of 2000 ions/s in 2003 and 1600 ions/s in 2007.

2.3 Time distribution of the recorded events

The pulsed nature of the PS booster helps β-decay experiments of short lived species, as nuclei decay freely between pulses and one measure on-line . In some cases, like ^{11}Li, the daughter nucleus^{11}Be is long lived ($T_{1/2}$=13.81(8) s [Ajz88]) compared to the mother ($T_{1/2}$=8.5(2) ms [Ajz88]), and a charged particle emitter as well. Thus, daughter activity is an undesired background to the mother's delayed particle emission. By gating in a adequate time interval we can enhance the decay of the desired nucleus

Figure 2.4 shows the number of triggers plotted versus time after the proton impact, for all the ^{11}Li data in the 2003 experiment. The full scale spans 4 s after the proton impact. The histogram shows a small peak at very short times, shown in the inset, and a stepped structure at fixed time intervals. The continuous distribution corresponds to the β-decay of the daughter ^{11}Be, as the decay rate of ^{11}Be saturates the production rate due to the similarity of the half-life ^{11}Be (13.81(8) s) and the PS-Booster supercycle of 14.4 s. The stepped structure of the ^{11}Be activity is due to the pulsed nature of the PS-booster, with the interval height determined by the number of times two proton pulses have occurred within this given time interval during the data taking run.

The inset of Figure 2.4 shows the triggers structure for the first 150 ms after the proton impact. There is a very short spike at the very first channels, related to the neutron flash after the protons impact on the Ta target. Then, after 5 ms, the curve reflects the competition between the release of ^{11}Li from the source and its β-decay. Given that the curve is the activity of all active nuclei in the source, A_{total}, multiplied by a scaling factor, S given by the number of pulses we took during the experiment [Tur08]:

$$S{\cdot}A_{total}(t) = S\left(\frac{1}{\tau_{^{11}Li}}N_{^{11}Li} + A_{^{11}Be}(t) + A_{noise}\right) = S{\cdot}\left(I_0(1-e^{-t/\tau_{^{11}Li}}) + A_{^{11}Be}(t) + A_{noise}\right) \tag{2.2}$$

where $\frac{1}{\tau_{^{11}Li}}N_{^{11}Li}$ is the ^{11}Li activity, I_0 is the ^{11}Li production rate and $A_{^{11}Be}$ is the daughter ^{11}Be activity. $A_{^{11}Be}(t)$ becomes constant and equal to the production rate after a short period, taking into account that, as mentioned before, $T_{1/2}(^{11}\mathrm{Be})$=13.81(8) s. A$_{noise}$ is the activity due to recorded noise in the ADC, which is time independent. I_0 is determined by the release function of ^{11}Li, and it is a function of time only for $t < t_f$, where t_f is the mean life for the fast falling component of the release [Tur08]. Therefore, for $t > t_f$ the curve in Fig. 2.4 is dominated by the free decay of ^{11}Li and its daughter nucleus ^{11}Be. The red line in the inset of Figure 2.4 shows a chi squared fit of the β-decay dominated part of the histogram to the formula above. The resulting ^{11}Li half-life, 11(2) ms, is a bit larger than the literature value of 8.5(2) ms [Til04]. One has to take into account that this experiment was not designed to properly measure the half-life of the ^{11}Li decay, so no specialized equipment was used to calibrate the time spectrum. Certainly small errors in the diffusion formula will affect this very short half-life.

In the ^{9}Li case, the daughter nucleus ^{9}Be is stable, and the only delayed particles emitted are α's, so the only expected component is ^{9}Li decay plus the time-independent activity coming from electronic noise in the DAQ system. Figure 2.5 shows the time structure for ^{9}Li data in 2003's experiment. The fit yields a half-life

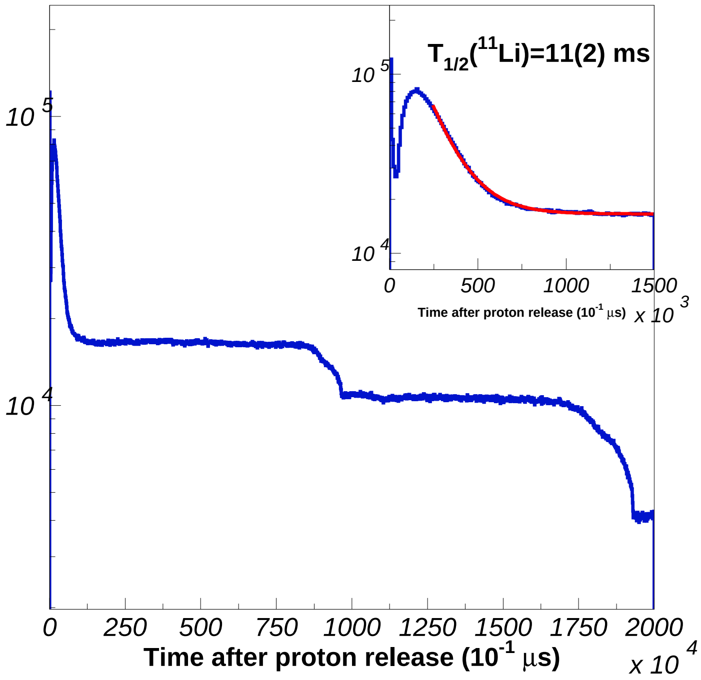

Figure 2.4: Time structure of triggers measured in the 2003 experiment. The peak at the start of the histogram corresponds to decay events of the short lived mother ^{11}*Li (*$T_{1/2}$*)=8.5(2) ms [Ajz88]). The continous distribution corresponds to decays of the daughter* ^{11}*Be. The* ^{11}*Be activity saturates after a few cycles and becomes constant because of the longer half life of 13.81(8) s [Ajz88], . The heights of the stepped structure of the* ^{11}*Be activity is determined by the ocurrence oftwo proton pulses occured within a given time interval. We can see in the picture that 46% of the time the interval is 1.2 s, 27% of the time is 2.4 s and the remaining 27& longer than 3.6 s or longer. The inset shows the* ^{11}*Li activity peak, fitted to a exponential plus constant function. The result of 11(2) ms is within error bars of the literature value.*

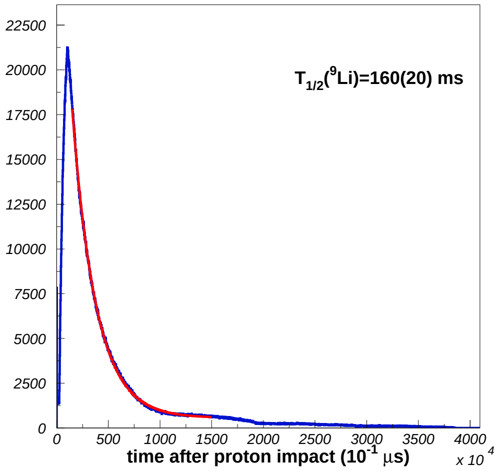

Figure 2.5: Time distribution of triggers in the ^{9}*Li* β*-decay measurement in the 2003 experimental run. The peak extending to the first second (channel 1000×*10^4*) corresponds to* ^{9}*Li decay activity, of* $T_{1/2}$*=178.3(4) ms [AW76]. The red line corresponds to a exponential decay plus constant fit, obtaining* $T_{1/2}$*=160(20) ms, consistent, within error bars, with the literature value.*

of 160(20) ms, which is compatible with the literature value of 178.3(4) ms [Til04].

2.4 Experimental setup

The work discussed in this thesis corresponds to two experiments, in 2003 and 2007. Each experiment had different a setup, as the setup of the 2007 experiment was optimized to efficiently detect the charged particle channels we were interested in. However, both setups can be described as a number of main detector units, telescopes consisting of Double Sided Silicon Strip Detectors (DSSSD) stacked with thick silicon pads, surrounding a carbon foil were the radioactive beam was implanted. The telescope configuration is an excellent tool for β-decay experiments, as the DSSSD's combine high charged particle detection efficiency with high granularity, for momentum reconstruction and pile up suppression. The silicon pads are used for β triggering and beta suppression. In the 2003 experiment, apart from the telescopes, we used the neutron time of flight detector TONERRE, consisting of 12 plastic scintillator pads in a pseudo-cylindrical configuration. First, I will describe the setups used in both experiments, and later I will briefly characterize the properties of the detectors and the electronic data acquisition system used

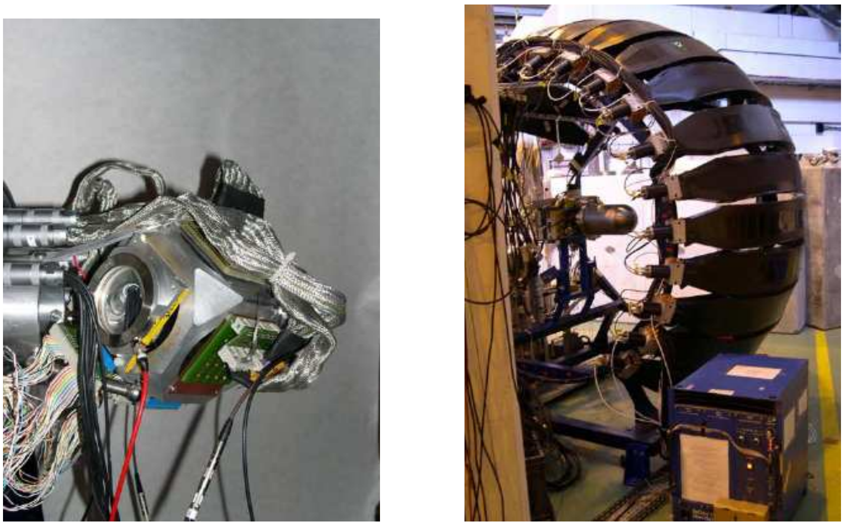

Figure 2.6: Left: Picture of the cubic frame with particle telescopes mounted in 2003 experiment. . Right: image of the detector array TONNERRE surrounding the 2003 experimental setup at ISOLDE. The vacuum chamber was the cone-shaped aluminum tube at the end of the beamline.

2.4.1 Setup of the 2003 experiment

The setups designed for the measurement of β-delayed particle emission in radioactive ion beam facilities have some common features. First, the beam is stopped in a thin foil, normally carbon, in order to measure the emission of β decay products at rest. Second, as normally one is interested in measuring in coincidence small branches of scarcely produced isotopes, such as ^{11}Li, a large amount of detectors are used. The isotope of interest is collected in a carbon-foil were is left to decay, and the foil is surrounded by detectors to obtain an angular coverage as close to 4π as possible. In some cases three, four or up to six telescopes are mounted, and taking into account that each DSSSD correponds to 256 pixels, it amounts to up to 1300 individual detection elements.

The setup of 2003 experiment consisted in a section dedicated to the measurement of charged particles, four DSSSD detectors backed by Si pads, mounted on the surfaces of an cubic aluminum frame (see Fig. 2.6(a), and a section for measuring neutrons, consisting of the neutron time-of-flight detector array TONNERRE (see Fig. 2.6(b)). Following, I will describe each detection device in detail.

Charged particle detection

The charge particle section of the experiment consisted in four particle telescopes, each consists of a DSSSD backed by a Si pad, mounted on the surfaces of a cubic

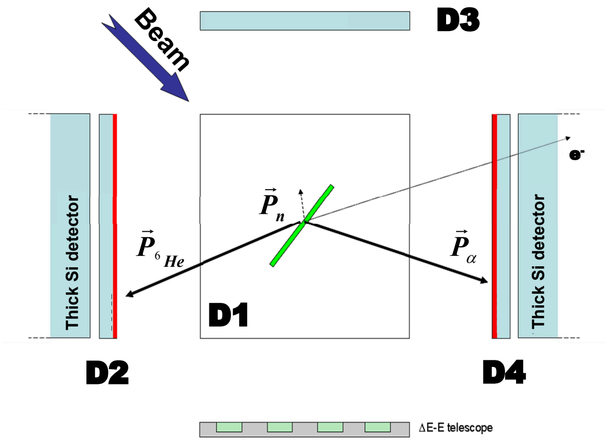

Figure 2.7: Schematical view of the relative positions of the particle telescopes in 2003 experiment. Detector D1 is placed on the surface of the page. The Δ*E-E telescope in the bottom is an experimental solid state telescope, which was placed for testing purposes, and not used in the analysis presented here.*

aluminum frame. Two of the DSSSD's, D2 and D4 (see Fig. 2.7) were of the new ultrathin design and, the remaining, D3 was of the 600 nm deadlayer type Design W, and all backing Si pads were 1.5 mm thick. The trigger of DSSSD D1 did not work properly during the experiment, so we did not used the data from D1 it in the analysis.

The angular efficiency of the telescopes was determined by the geometrical properties of the cubic frame the telescopes were mounted on. The dimensions of the cubic frame are 10×10×10× cm^3, and the carbon foil was mounted on a stick, placed in the bottom vertex of the cube. The stick was adjusted so that the carbon foil stopper was on the geometrical center of the cube. Therefore, each detector center was 5 cm away from the decaying source, which defines the angular coverage of each telescope at ∼4% of 4π.

The incident angle of the beam on the carbon foil stopper is an important parameter of the setup to determine the implantation depth, the amount of matter the particles traverse before reaching the detectors (for details see the following chapter). The impinging depth in the carbon foil is only determined by the charge of the beam ions and their energy. However, the depth is defined perpendicular to the foil surface, thus by tilting the foil the effective depth changes. The beam entered through one of the vertex of the cube, and the carbon foil was placed with its surface along one of the diagonal planes of the cube, see Fig. 2.8). Using the reference frame of Fig. 2.8 the beam, $\overrightarrow{B}$, and the carbon foil stopper surface direction, $\overrightarrow{S}_F$, are

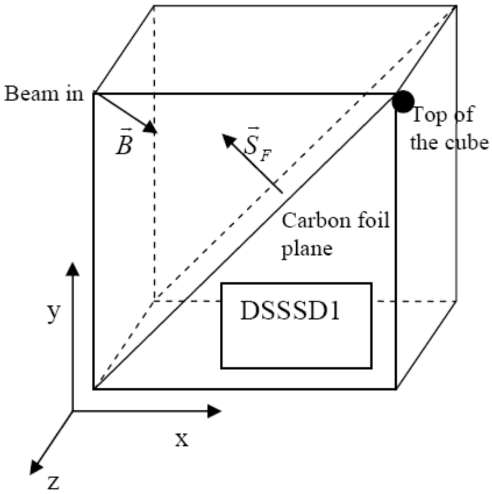

Figure 2.8: Relative directions of the beam and the carbon foil stopper surface vector in 2003 experiment. All detectos were mounted on the center of the surfaces of the cube.

$$\overrightarrow{B} = (\cos\frac{\pi}{4}, -\sin\frac{\pi}{4}, -\cos\frac{\pi}{4}) \tag{2.3}$$

$$\overrightarrow{S}_F = (-\cos\frac{\pi}{4}, \sin\frac{\pi}{4}, 0) \tag{2.4}$$

From which the incident angle, θ_B , is calculated as

$$\theta_B = \arccos\frac{\overrightarrow{S}_F \cdot \overrightarrow{B}}{\left|\overrightarrow{S}_F\right|\left|\overrightarrow{B}\right|} = 144.73°(35.26°) \tag{2.5}$$

Taking into account that the *Li* ions were extracted with a 30 kV voltage, the resulting impinging depth in carbon is 1408 Å. A carbon foil of 60 $\mu g/\mathrm{cm}^2$ thickness (2663 Å) was chosen, in order to implant the beam roughly at the middle of the foil. By implanting the beam in the middle of the beam we minimize the amount of matter the β-delayed particles traverse, as thus the energy losses, before hitting the detectors placed in both sides of the carbon-foil.

From Fig. 2.7 we see there are three types of coincidence geometries for the three DSSSD, D2, D3 and D4. Hits in D2 and D4 were classified as *180^o* coincidences, and covered angles from 127^o to 180^o between the detected particles. Hits in D3 and either D2 or D4 were classified as *90^o* coincidences and covered angles from 37^o to 143^o between the detected particles. Finally, coincidences detected in the same detector, classified as *0^o* coincidences, covered angles from 0^o to 50^o between the detected particles.

Neutron detection

The neutron detection was carried out by the neutron time-of-flight detector TONNERRE. We used a single layer configuration consisting in 16 pads, thus covering 25.7% of 4π. TONNERRE can be setup with a maximum of 28 pads (see section 2.5.2), althoug due to the low height of the ISOLDE beam-line, hte bottom pads could not be mounted. However, TONNERRE in the full 28 pad configuration has a high probability of cross-talk and neutrons out-scattering (see section 2.5.2). Thus, a side benefit of the 16 pad configuration used in the experiment presented in this thesis is a low cross-talk and neutron out-scattering probability of $\lesssim$0.15% (from 0.39% with the full configuration) [But00] Taking into account the intrinsic efficiency of the pads of ~25%, the neutron detection efficiency in 2003 experiment was ~6%.

The start signal for the time of flight measurement was provided by the trigger from the thick silicon pads in each telescope. As the alpha particles are stopped in the front DSSSD's this ensues the Si pad trigger is from a β particle hit in the detector. The stop was given by any signal in one of the of the TONNERRE pads.

Signal processing and data acquisition

The preamplifier-amplifier chains of the DSSSD detectors were composed of integrated modules, 16 channels each, thus requiring two chains per DSSSD, one for each side of the detector. Moreover, each amplifier integrated both the slow shaping amplifier, a fast timing amplifier and a Leading Edge Discriminator to obtain the trigger. This allowed us to keep the amount of modules to a manageable number. The electronic chain for the back Si pads was composed of a chain of preamplifiers-fast amplifiers of standard NIM modules.

The electronic chain of TONNERRE was designed for timing, therefore the output signal of the pre-amplifiers was directly coupled to constant fraction discriminator with ECL-type output signal for fast timing. the ECL signals were directly plugged in the TDC to record the timing information.

The main aquisition trigger was produced combining the DSSSD and Si pads triggers. Each integrated amplifier module used in one side of the DSSSD produced its own trigger signal, an or of the 16 input channels. The front and back triggers of each DSSSD were combined in a main DSSSD trigger with an logic OR in a Fan In/Fan Out module. Finally the four DSSSD triggers were combined in a *alpha* trigger. The Si pads triggers were produced using the CFD technique on the fast amplifier signal, and were combined with a logic OR into a main *beta* trigger. The main acquisition trigger consisted of the *alpha* and *beta* triggers combined with a logic OR. The main acquisition trigger was fed into a gate generator to produce a 4 μs acquisition window. The acquisition window defines the coincidence window, as the ADC's and TDC's are designed to digitize only during this window.

The data acquisition was handled by a VME crate. The data were stored in listmode (each event in the data cointains a list of the modules that fire in coincidence), which was subsequently converted into PAW format for their analysis. PAW (Physics Analysis Workstation [cer]) is a collection of software and Fortran libraries designed for the analysis of high statistics and high number of channels recorded in coincidence in nuclear physics and high energy physics experiments.

A schematic view of the electronics used in 2003 experiment is presented in Figs. 2.9, 2.10, 2.11.

2.4.2 Setup of the 2007 experiment

The setup in the 2007 experiment was similar to that of the 2003 experiment. We stopped the Li ions in a thin carbon foil, and the charged particle detection was done by particle telescopes consisting of DSSSD detectors backed by thick Si pads. In this experiment the neutron time-of-flight detector TONNERRE was not installed, so there was no neutron detection.

The goal of the 2007 experiment was to study low intensity exotic β-delayed charged particle decay branches, so we optimized the setup. In order to achieve this goal two improvements were designed: (i) a new aluminum table was designed to support the detectors, which allowed us to reduce the distance to the carbon foil stopper; (ii) improvement of the acquisition electronics and the trigger to reduce at the maximum the triggering noise.

Charged particle detection

The charged particle detection was provided by three particle telescopes, all of them with new ultrathin windowless DSSSD stacked with 1.5 mm thick Si pads for beta signal and veto. The angular acceptance of the detectors was given by their distance to the carbon foil. Detectors D1 and D3 (see Fig. 2.12) were placed 5 cm away from the carbon foil, thus covering $\sim$4 of 4π, whereas detector D2 was placed 3.7 cm away from the foil, covering $\sim$7% of 4π. We can make a rough estimate of the improvement over the 2003 experimental run by using the angular acceptance of measuring two isotropically emitted particles in coincidence, $2\Omega_1\Omega_2$. In 2003 we obtained a 0.3% of 4π whereas in 2007 we obtained a 0.6% of 4π, a factor of 2 increase.

The geometry of the setup, as in the previous experiment, defined three possible types of two-particle coincidences. Hits in D2 and D3 (see Fig. 2.12), classified as

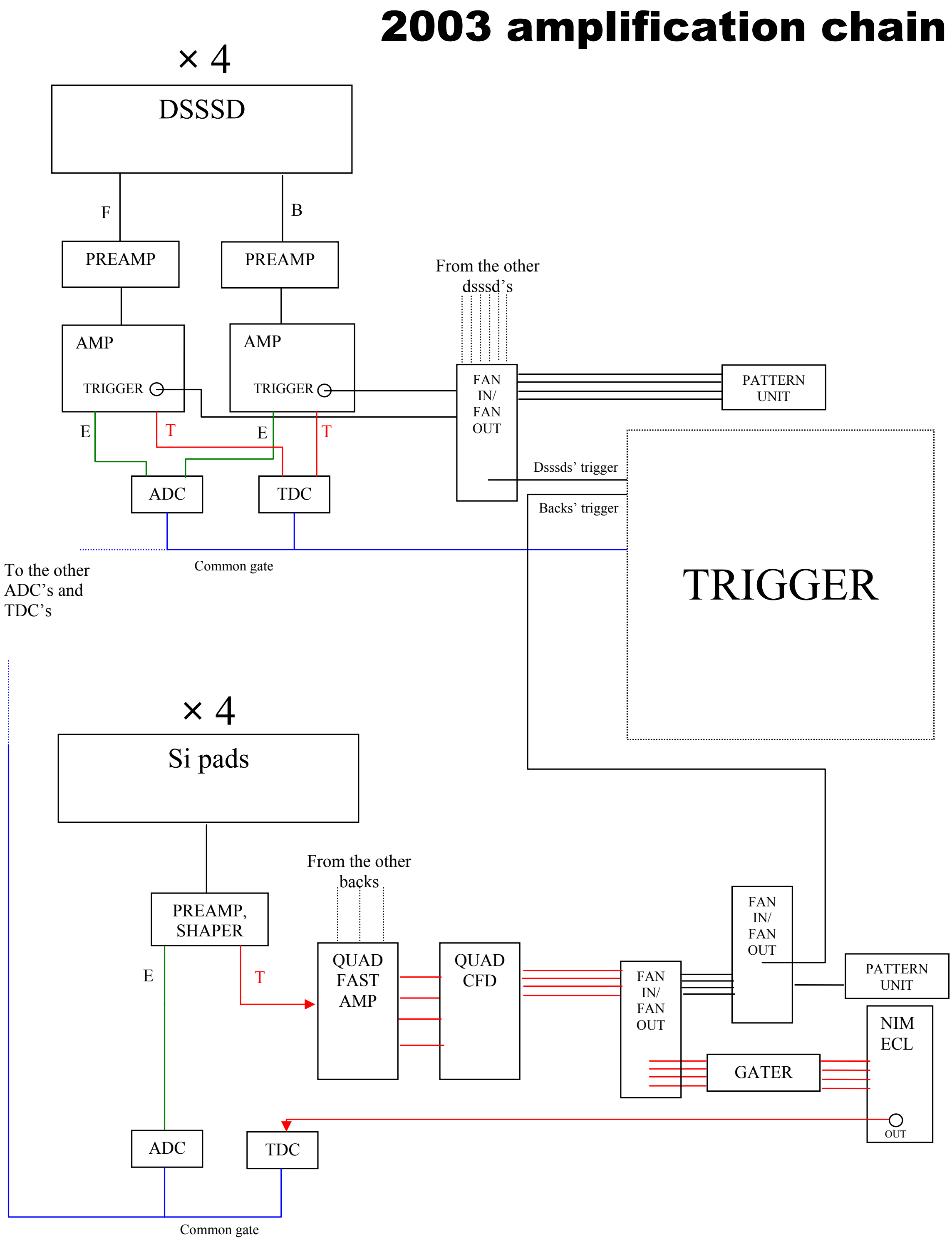

Figure 2.9: Schematic drawing of the electronics in 2003 experimental setup. The NIM/ECL modules are used to transform regular NIM signals into fast ECL signals. The trigger section is shown in Fig. 2.10

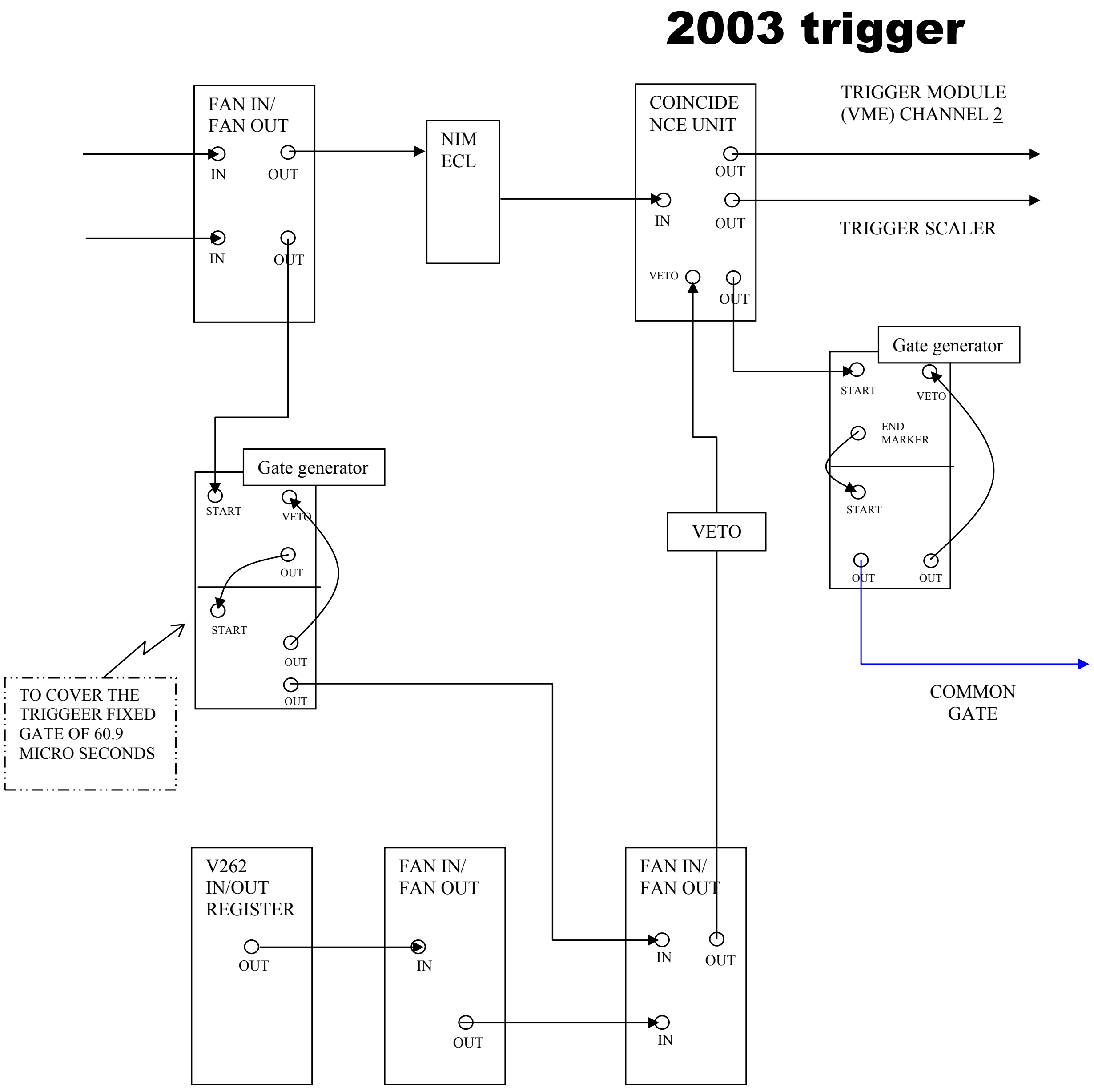

Figure 2.10: Schematic drawing of the modules used to define the trigger in 2003 experimental setup.

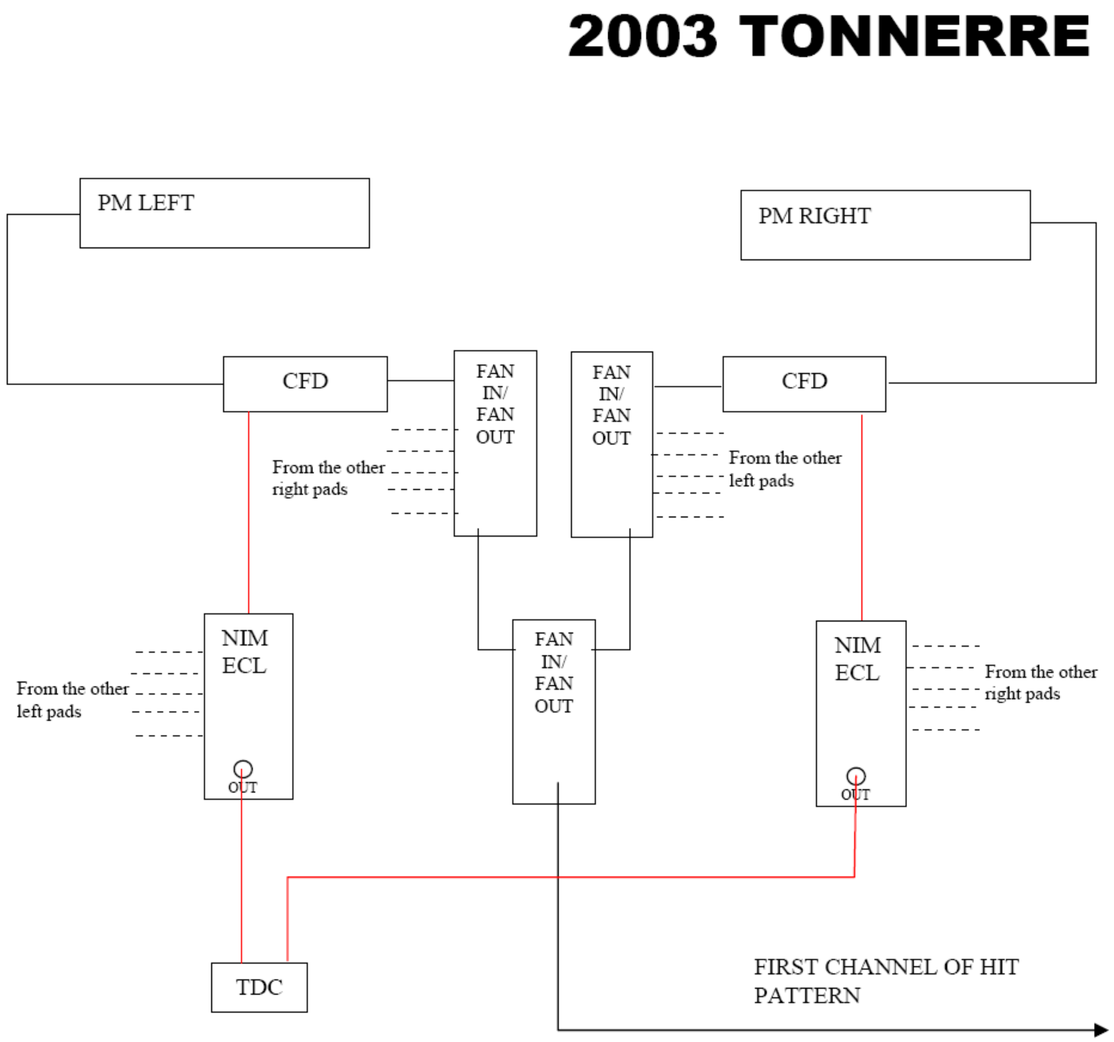

Figure 2.11: Schematic drawing of the TONNERRE electronics in 2003 experimental run.

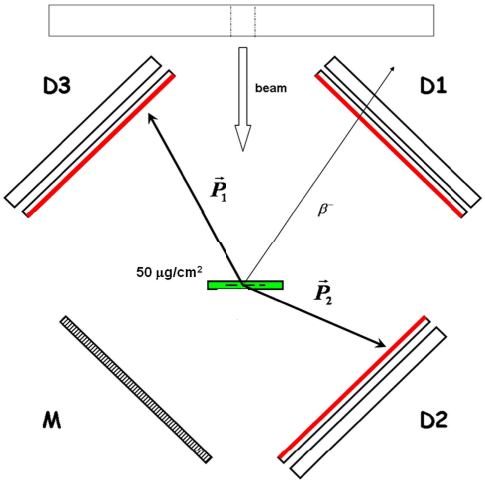

Figure 2.12: Schematic view of the 2007 experiment. Detector M corresponds to a prototype silicon telescope mounted for testing purposes.

180^o coincidences, covered angles from 120^o to 180^o between the detected particles. Hits in D1 and either D2 or D3, classified as *90*^{o} coincidences, which covered angles from 31^o to 149^o between the detected particles. Finally, coincidences detected within the same detector, classified as *0*^{o} coincidences, covered angles from 0^o to 50^o between the detected particles for detectors D1 and D3 and between 0^o and 68^o for D2.

We used a 50 μg/cm^2 (2127 Å) thick carbon foil, placed in the center of the aluminum table. The carbon foil was mounted directly facing the beam and nontilted, so that all the detectors faced the carbon foil at a 45°angle. As the ^{11}Li beam was extracted with a 30 kV voltage, the impinging depth was 1408 Å, therefore particles leaving the carbon foil from one side will go through double the matter than from the other.

Signal processing and data acquisition

In 2007 experiment both the DSSSD detectors and Si pads preamplifier-amplifier chains used integrated modules. This kept the electronics to the minimum, and as the 16 amplifiers had integrated leading edge discriminators, which made easy to integrate the signal in the trigger time window.

As in the 2003 experiment each trigger from the preamplifers was combined with a logic OR to produce a DSSSD trigger. The three DSSSD triggers were combined in a Fan In/Fan Ou with a logic OR to produce the main trigger of the experiment.

The data acquisition was handled by a VME crate, controlled by a Motorola microprocessor for VMEbus control newly bought before the experiment, controlled by the MIDAS software. As in 2003 experiment, the listmode files (in this case MIDAS listmode) were converted into PAW ntuples for subsequent analysis.

The improvement in trigger control and processor speed, combined by the increased angular acceptance, allowed us to record ∼10 times more particle coincidences than in 2003 experiment. An schematic view of the electronics setup is shown in Figs. 2.13, 2.14.

2.5 Description of the experimental equipment

In this section I will briefly discuss the physical properties of the detector systems used in the two experiments presented in this thesis, and the working principles of the data acquisition used. As mentioned in the previous section the main detection component in both experiments was Si Double Sided Strip Detectors, a type of semiconductor detectors. Moreover, the neutron time-of-flight detector TONNERRE was used in 2003 to measure neutrons in coincidences woth charged particles. TONNERRE detector elements consists in plastic scintillator pads, thus the properties of plastic scintilators will be discussed as well. More details about the working principles of radiation detectors can be found in [Kno79].

2.5.1 Semiconductor detectors

The double sided silicon detector's and silicon pad's detection principle rely in their properties as semiconductors. In a semiconductor material the valence electrons band is completely full and located a few eV below the conduction band. A particle moving inside the material will easily excite electrons from the valence band to the conduction band and produce an electrical current. Therefore, the energy of the impinging particle is proportional to the voltage produced by the particle induced current. The advantage of semiconductor detectors relies precisely in the large number of charged carriers, the electron-hole pairs, produced due to the low excitation energy increases greatly the resolution compared to ionization based detectors.

One might naively think that the charge collection might be carried out by using metal conducting contact. However, this approach is not convenient as the electrons or holes produced near the contacts would be substituted by charge from the conducting material, establishing a stable current in the circuit. This leakage current is responsible of an electronic noise that can even mask the particle signal we want to observe, thus it has to be avoided. In order to prevent this leakage current the charge collection is performed in a region of the semiconductor crystal where the charge concentration has been modified. This region has been doped with atoms of higher valence than that of the semiconductor (p side) or lower (n side). In the typical case of crystals of group IV elements, such as Si or Ge, elements of the group

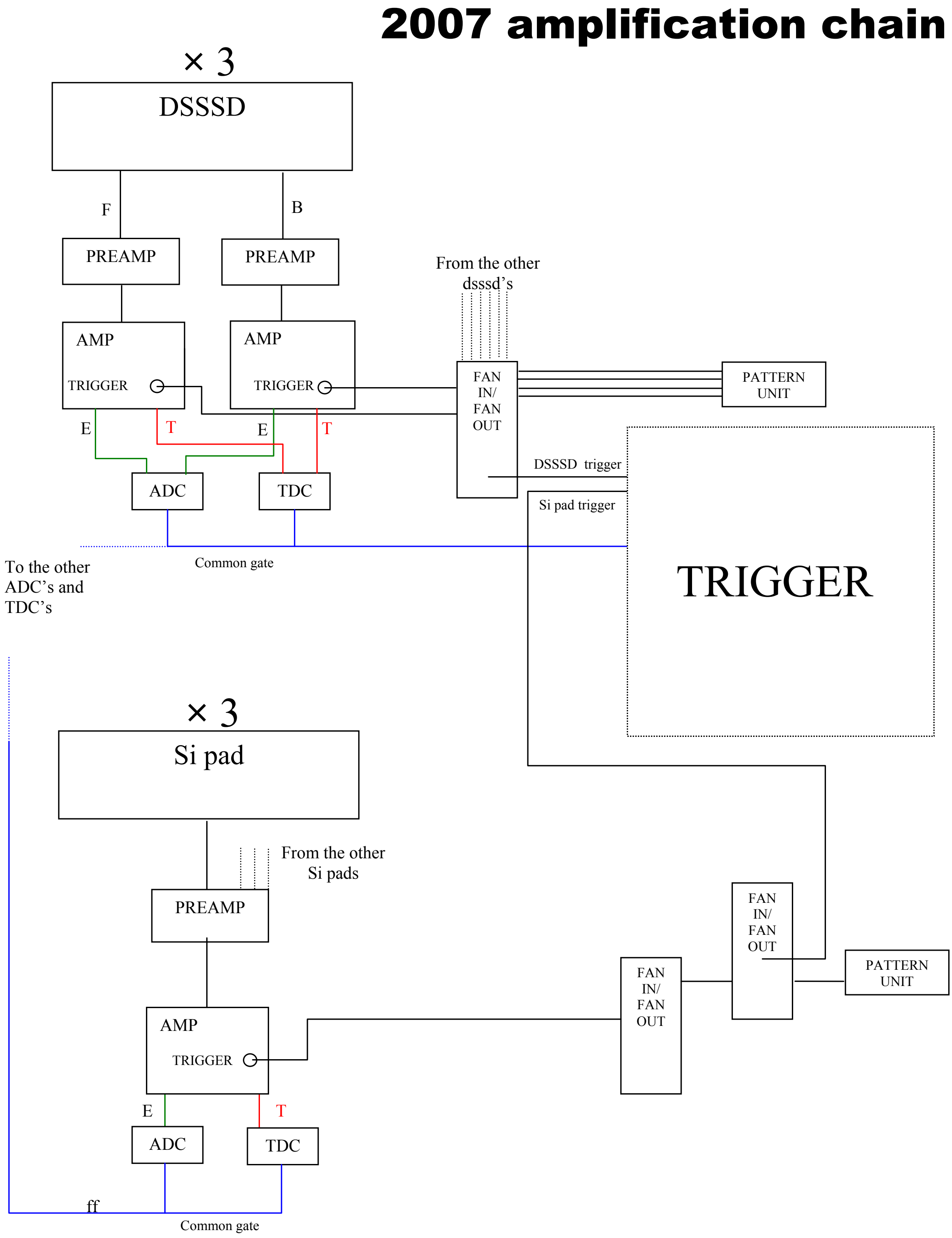

Figure 2.13: *Schematic drawing of the electronics setup in 2007 experimental setup. The NIM/ECL modules are used to transform regular NIM signals into fast ECL signals. The trigger section is shown in Fig. 2.14*

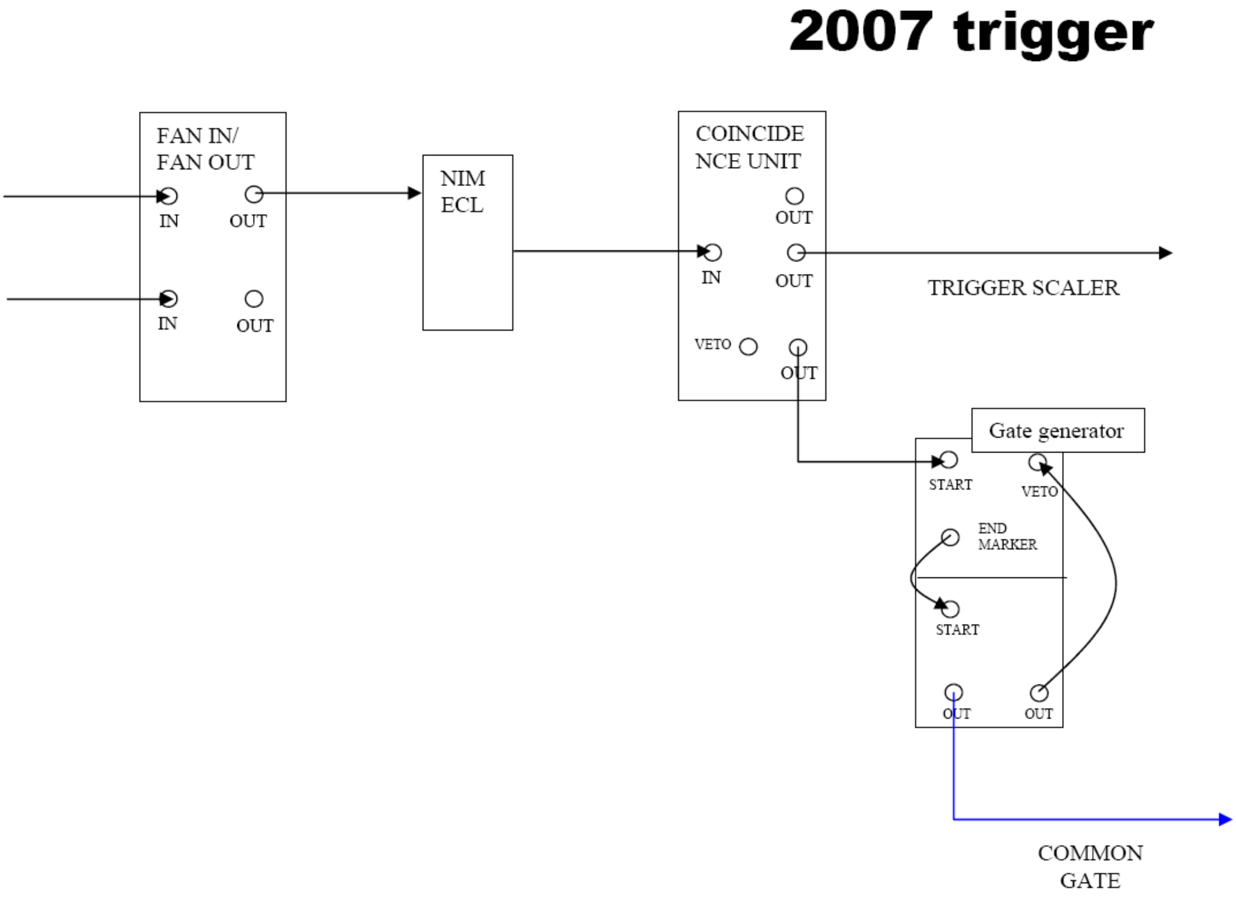

Figure 2.14: Schematic drawing of the modules used to define the trigger in 2007 experimental setup.

V (Bi) or higher are used for n side doping, and elements of the group III or lower (Li) for n side doping. The charge imbalance between the p and n side produces a net diffusion of electrons from the n side to the p side, and holes in the opposite directions. The combined effect is to build up a net negative space charge on the p side and positive space charge on the n side of the junction. The accumulated space charge creates an electric field that diminishes the tendency for further diffusion. The electric field can be calculated from Poisson equation

$$\nabla^2\varphi = -\frac{\rho}{\epsilon} \tag{2.6}$$

where ρ is the charge density and ϵ is the dielectric constant of the material. In the region over the which the potential extends, called the depletion region, exhibits some very attractive properties as a medium for the detection of particles. An electron-hole pair created by an impinging particle in the depletion region will be immediately swept out from the depletion region by the electric field, and their motion constitutes a basic electrical signal. This makes convenient to use a detector where a voltage is applied in the same direction of the field of the depletion region, thus extending the transition region d to

$$d \cong \left(\frac{2\epsilon V}{eN}\right)^2 \tag{2.7}$$

calculated from eq 2.6 and imposing the continuity of the potential in the boundaries, where N is the dopant concentration on the side of the junction that has the lower dopant level, V is the applies voltage, ϵ is the dielectric constant of the material and e is the electron charge. The equation implies the depletion region extends to the side with the lowest dopant level.

The silicon diode detectors operated at room temperature are excellent for charged particle detection. The detection efficiency is essentially 100% over a certain energy interval, defined by the entrance window and the electronic amplification used. Moreover the ideal intrinsic resolution due to the number of charge carriers produced is between 3 and 4 keV. In large detectors, like those used in our experiments, the resolution is significantly lower, around 30-35 keV. This reduced resolution can be attributed to several effects, such as incomplete charge collection, electronic noise, etc.

Double Sided Silicon Detectors and Silicon pads

The silicon detectors used in our experiments are doped by exposing the surface of the material to a beam of ions produced by an accelerator, a method known as ion implantation. At a fixed accelerator voltage, typically around 10 keV, monoenergetic ions are produced which have a well-defined range in the semiconductor material.

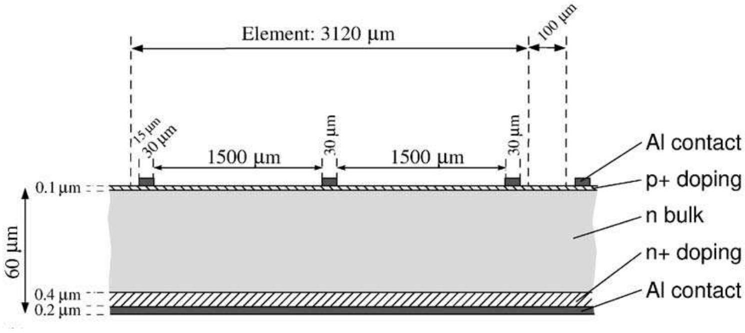

Figure 2.15: Cross section of the DSSSD designed for an ultra thin entrance window [Ten04].

Following exposure to the ion beam, an annealing step is normally carried out to reduce the effects of radiation damage caused by the incident ions, although the temperature required (<500°C) is lower than that needed for the thermal diffusion of dopants. This makes, compared to silicon surface barriers, ion-implanted detectors more stable and less dependent of enviromental conditions. Also, they can be made with entrance windows fairly thin. In the case of the detectors used in our experiments, boron ions were implanted to form a p^+ side of 100 nm range.

In the simplest detectors we used, the silicon pads, the charge collection is carried out by a single aluminum contact on top of the p^+ side, thus making the total entrance window as thick as 600 nm silicon equivalent, 400 nm of B implantation plus 200 nm of aluminum contact. This detectors were manufactured with thick silicon wafer, 1.5 mm, in order to use them as the back detector in charged particle telescopes. In our β-decay experiments, the energy of the emitted alpha particles is so low that they do not go through the front detector, so the silicon pad's were used for β-trigger and β filtering in anti-coincidence mode.

The main detector unit in our experiments was the double sided silicon strip detectors (DSSSD). The DSSSD were developed with the aim of improving the performance in low energy charged particle detection following β-decay. The detectors used in the experiments presented in this thesis were 60 μm thick, in order to reduce as much as possible the energy deposited by the β particles emitted in the decay. The detector is doped in 16 individual strips in the front p^+ side and 16 orthogonal strips in the back n^+ side of the diode. The charge induced by the impinging particles in each strip is collected by an aluminum layer that covers completely the strips, thus adding an extra layer of no active mataerial to the entrance window. The high segmentation achieved by the individual 32 strips has two advantages.

- First, the probability of β-summing (charged particle + β) is proportional to the solid angle subtended by the detector. By Subdiving the detector surface in

16×16 elements (pixels) we get the reduction factor in the summing probability

- Second, by dividing the area of the detector in strip the impinging particle position can be deduced, which is necessary to perform certain techniques as deadlayer energy reconstruction and momentum reconstruction (see next chapter).

Finally, a great effort in reducing the entrance window of the DSSSD's has been carried out within our group over the years, as the energy loss in the entrance window limits the minimum energy detectable. The first type of DSSSD used in our group had an entrance window similar to that of the silicon pad, 600 nm thick. A new design was proposed, replacing the aluminum contact with an metal grid placed over the p^+ entrance of the detector [Ten04] (see Fig. 2.15). The grid pitch is 1500 μm and 30 μm thickness over a 3120 μm separation between strips, thus covering only 2% of the detector surface. This reduces the entrance window for the remaining 98% of the detector surface to the thickness of the implantation layer, which was reduced to 100 nm with a new implantation technique. The new detector proved to have a low energy cut-off up to 250 keV for alpha particles [Ten04], compared to the 650 keV for alphas of the Design W DSSSD [Ber01].

2.5.2 Plastic scintillators

The neutron time-of-flight detector TONNERRE consists in plastic scintillator pads, so I will briefly describe their particle detection properties. Plastics scintillators are based on the natural fluorescence of certain materials. Ionizing radiation traveling through the material excites the molecules up to higher levels, which in turn decay through low energy transitions. The de-excitation of the material typically occurs though a cascade of transitions in the visible energy range. The fluerescent materials used in plastic scintillators are polymers of organic molecules. The advantage of this type of materials is that its response is fairly linear with the energy of the incident particle, that is, the amount of photons emitted is linearly proportional to the energy of the particle. In general, the luminosity, L, is determined by the energy loss of the incident particle, following Birk formula [Kno79]

$$\frac{dL}{dx} = \left(S\frac{dE}{dx}\right)\left(1 + kB\frac{dE}{dx}\right)^{-1} \tag{2.8}$$

where S is the material intrinsic parameter, and the second term takes into account the energy loss due to material molecules non-radiative excitation modes. The two parameters k and B are fitted to each material. The second term can only be ignored for fast electrons, and in that case the light output will be truly linearly related to the initial particle energy E. This term cannot be ignored for neutrons, but TONERRE is designed to measure the neutron energy from the time-of-flight information, rather than the light output in the plastic scintillators.

Once the light signal has been produced inside the plastic, the emitted photons have to be extracted out the material. In the plastic scintillators case, the distance at which the intensity is diminished a factor of two is in the order of meters. Thus, in general there will not be intensity loss due to the intrinsic opacity of the plastic material. It is enough, then, to have good light confinement inside the plastic, by wrapping the material in a reflective layer and avoiding losses in the connection of the plastic with the photomultiplier tube.

The photomultiplier tube transforms the light output of the plastic scintillator into an electrical signal that can be measured by the data acquisition system. The transparent photocatode that forms the entrance window produces electrons when hit by a photon. A voltage accelerates the electrons in vacuum towards the first dinode. An electron hitting the dinode extracts one or more electrons from it, a process called secondary electron emission. By putting a series of dinodes in the photomultiplier tube, dependig on the number of dinodes up to 10^6 electrons per single incident electron can be produced, a signal high enough to be studied.

TONNERRE

In the 2003 experiment we had the neutron time-of-flight detector array TONNERRE (TONneau pour NEutRons REtardes) installed in collaboration with the Laboratoire de Physique Corpusculaire from Université de Caen. The detector array consists of up to 32 plastic scintillator paddles, each 160 cm long, mounted in a barrel geometry achieving a constant radius of 120 cm [But00], see Fig. 2.16.

Each detection paddle of TONNERRE consists of a single plastic scintillator element, with photomultiplier tubes in both ends of the element. The plastic scintillator material chosen is BC400, which has a decay time of 2.4 ns, in the typical range for fast neutron detection, and a light output of 65% of anthracene, the reference plastic scintillator. The plastic scintillator paddles are of 160 cm length, 20 cm width and 4 cm thickness. The paddle thickness, 4 cm, was chosen to achieve a compromise between the time-of-flight resolution, which increases with decreasing thickness, and good light transmission in the plastic scintillator, which decreases as the thickness decreases. The energy resolution is $\delta E/E \approx \delta d/d$, which for δd=4cm, the thickness, and d=120 cm, the total distance, results in relative error of 8%, or 80 keV for 1 MeV neutrons. The transmission for 4 cm thick pads was estimated to be around 80%.

There are two advantages in using two photomultiplier tubes per individual detector instead of one. First, requiring a coincident signal in both tubes significantly reduces the noise contribution. Second it simplifies obtaining the time-of-flight. A single event has two time measurements from each photomultiplier tube, t_1 and

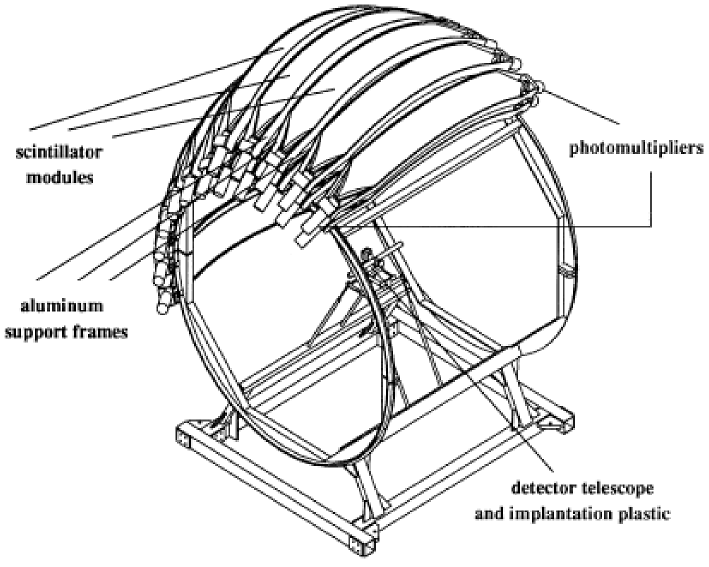

Figure 2.16: Schematic view of the detector array TONERRE (taken from [But00]).

t_2, which is the time-of-flight,TOF, plus the time the signal takes to reach each photomultiplier, τ_1 and τ_2

$$t_1 = \text{TOF} + \tau_1; \quad t_2 = \text{TOF} + \tau_2 \tag{2.9}$$

where τ_1 and τ_2 should follow

$$\tau_1 + \tau_2 = \frac{l}{v} \tag{2.10}$$

where l=160 cm is the length of the detector paddle and v is the speed of light in the scintillator material. The speed of light in the plastic was calculated by measuring a source very close to the plastic, imposing TOF=0, obtaining 16.3 cm/ns. Finally one can calculate the TOF as

$$\text{TOF} = \frac{t_1 + t_2}{2} - \frac{l}{2v} \tag{2.11}$$

From a practical point of view the offset, $\frac{l}{2v}$, is individually adjusted for each detection paddle in order to fix the TOF of prompt gamma rays at 4 ns, as the speed of light in air is 30 cm/ns. A more detailed description of the geometry and time calibration of TONERRE is given in section 3.1.5.

Finally, the intrinsic efficiency of TONNERRE was estimated using a ^{252}Cf neutron source, obtaining a ~25% efficiency for a single detector and ~42% for two detectors stacked one top of the other [But00]. The good intrinsic efficiency, combined with the barrel geometrical disposition, which can cover up to 45% of 4π when 28 pads are used in a single layer, results in a total detection efficiency of ∼12%. However, in this configuration the probability of cross-talk, a neutron being detected by two pads, and neutron out-scattering between pads are rather high, 0.10% and 0.29% respectively. In our experiment a intermedium configuration of 16 paddles was used, covering 25% of 4π and with a total detection efficiency we can extrapolate from the values in [But00] of 7%, and an estimated cross talk $\lesssim$0.03%.

2.5.3 Electronics setup and data acquisition system

In the previous section we saw the main detectors used in our experiments, the DSSSD, produce a voltage signal whose amplitude is proportional to the energy of the incident particle. In the case of the detector array TONNERRE, the information is given by the difference in time between the starting signal of the trigger and the signal coming from the photoamplifier tubes. The goal of the electronics setup and of the data acquisition system is processing and recording those signals for later analysis. The modules in charge of digitizing the voltage pulses coming from the detectors are the ADC (Analog to Digital Converter), and the modules recording the time differences are the TDC (Time to Digital Converter). The information is then stored in a computer via a micro-processor controlled VME data bus. The preamplifiers and amplifiers have two different tasks. First, producing a signal proportional to the original detector signal and high enough to be digitized by the ADC, which have a 0 to 8 volt range. Second, releasing a fast signal once a user-defined threshold is overrun, used to define the setup trigger and for timing purposes.

Although it may seem inadequate, separating the detector signal in two different signals after the amplification stage is necessary due to the physical response of the amplifiers. The amplification process requires shaping and amplifying steps, which are normally rather slow, making these signals unsuitable for timing purposes. Instead, the fast signal delivered by the amplifiers has a raising time (the time required to go from 10% to 90% of the pulse height) of a few ns, perfect for timing between different signals. The signals used in the timing part are of the Emitter-Coupled Logic (ECL) type. This signals are of the differential type, that is, instead of using a single signal and ground, two signals of opposite polarity are send through a pair of copper wires twisted tight together. By having the two cables close together the electronic noise is expected to affect both in a similar way, orif not identical, thus vanishing when the two signals are added.

The signal processing used in nuclear physics are built following the NIM (Nuclear Instrumentation Module) standard. The standard defines the mechanical and electrical characteristics of the modules, with the objective of easily working with different modules of different companies. There are two signals specified in the NIM standard:(i) analog signals, whose amplitude and shape are proportional to the incident particle energy and collected charge; (ii) logic signals of pre-defined shape and amplitude, corresponding to logic 1 or 0. The advantage of logic signals is that they are easy to transport between modules, as they are rather insensitive to electronic noise or distortion.

Following, I present a brief description of the modules used in our experiments: preamplifiers, amplifiers, ADC, TDC, CFD, Fan in/Fan out, gate generators and the VME data acquisition system. For detailed information see [Kno79, Leo87].

Preamplifiers

The basic function of a preamplifier is to amplify weak signals from a detector and to drive it through the cable that connects the preamplifier with the rest of equipment. Since the input signal at the preamplifier is generally weak, preamplifiers are normally mounted as close as possible to the detector so as to minimize cable length. In this way, pickup of stray electromagnetic fields is reduced and cable capacitance, which reduces the signal to noise ratio, minimized. There are three basic types of preamplifiers: voltage sensitive; current sensitive; and charge sensitive. Charge sensitive preamplifiers are based on collecting the detector charge in a capacitor. This makes them ideal for solid state detectors, such as DSSSD's, as the output voltage does not depend on the detector capacitance, which in general might vary due to the detector leakage current. The main drawback of the charge sensitive preamplifiers resides in the release of the capacitor, which produces an exponential-tail type of pulse.

Amplifiers

The amplifier not only has to amplify the signal delivered by the preamplifiers, but it has to shape it to a convenient form for further processing. In both cases the amplifier must preserve the information of interest, depending of the detector we are analyzing. If time information is required, such as for TONERRE, a fast response is necessary. If pulse height information is desired, a strict proportionality between input and output (linear amplifier) must be preserved. Shaping is a crucial step to correctly integrate the full signal from the preamplifier and avoid pile-up by shaping the end of the signal. As stated above, one of the drawbacks of charge sensitive preamplifiers is the exponential tail of the signal, which might be up to 50 μs long. If another signal is produced in this time range, the amplitude (and thus the energy information) of the new signal is increased by the tail of the previous signal. This is the so called pile-up effect. To avoid pile-up, one must either restrict the counting rate or re-shape the signal to remove the exponential tails. Another benefit of shaping the signal is optimizing the signal to noise ratio. The most widespread pulse shaping technique is the use of CR differentiators and an RC integrators. The CR differentiator filters the low frequencies whereas the RC integrator filters the high frequencies. Combining both in cascade filters substantially the electronic noise present.

ADC (Analog to Digital Converter)

The ADC converts the information of an analog signal into an equivalent digital number. There are two types of ADC depending on the type of signal one wants to digitize. The peak-sensing ADC's digitize the maximum amplitude of the pulse, whereas the charge sensitive ADC's digitize the full pulse integrated current. The former are used in detectors where the amplitude of the signal contains the physical information, such as in slow integrated signals from amplifiers for solid state detectors.

The most widely used technique is the successive approximation method. Here, the incoming pulse is compared to a series of reference voltages to determine the height of the pulse. If the signal is greater or lower than certain reference voltages, then the bit is set to 1 or 0, and half of the previous reference is added for the next bit. In our experiments the ADC were of 12 bit resolution, a number that converted from binary is in the range between 0 and 4095 (2^{12}-1). The time required the digitization, called conversion, is generally long, in the range of μs (2.5 μs in the case of the ADC used in the experimetns pesented in this thesis), which constitutes the major source of dead time when measuring high rate processes. This has to be carefully taken into account in high rate experiments, such as reaction experiments with intense stable beams, or high frequency experiments, such as measurements with short-pulsed beams.

CFD (Constant Fraction Discriminator)

The discriminator is a device which responds only to input signals with a pulse height greater than a certain threshold value. If this criterion is satisfied, the discriminator responds by issuing a standard logic signal; if not, no response is made. If the signal is quickly released it will be convenient for timing study, as the logic signals are easy to manipulate. There are several methods to define what shoots the trigger signal, such as a simple threshold over the leading edge of a signal. The most efficient method is the constant fraction triggering technique. In this method, the logic signal is generated at a constant fraction of the peak height. The basis for this idea arose from empirical tests which showed the existence of an optimum triggering level at a certain fraction of pulse height independent of the amplitude. This optimum level depends on the shape of the incoming signal, so it is convenient that the discriminator has an adjustable level. The constant fraction technique is based on splitting the incoming V_a signal in two signals. One is delayed a time τ_d equal to the time it takes for the pulse to rise from the constant fraction level to the pulse peak. The other part is inverted and attenuated by a factor k, $V_b = -kV_a$. The two are then summed to produce a bipolar pulse that cancels at a fraction k of the original signal height. Finally, the zero-crossing point is used as the trigger of the logic signal.

Fan In/Fan out

The Fan In/Fan Out modules have two different purposes, the Fan In or fast coincidence mode combines several input signals into the sum signal, and the Fan Out mode multiplies a single input signal into several identical signals of the same height and shape. It is common to use fast coincidence mode for logic signals, normally including Boolean logic operators in the input signals. The signal through time for this modules is in the order of 10 ns, which is negligible compared to the 2 μs shaping time of the amplifiers.

Gate generator

The gate generator delivers a logic signal (equivalent to a logic 1) of a determined duration and frequency. It is generally used to define the time interval for acquisition when using several detectors in coincidence. In this case the module does not produce gates of a determined frequency, instead, the module is activated using a START signal. The START signal is therefore the acquisition trigger. The trigger is produced by combining the CFD signals from the different detectors using Fan In/Fan Out modules with Boolean AND or OR to control the detectors in the trigger.

VME data acquisition crate

The VME data acquistion crate contains the control hardwared necessary to run and record the ADC and TDC data. The backplane (back connectors) is the VMEbus, which essentatially maps the VME cpu pins. This makes the ADC and TDC connected to the VMEbus an exptension of the VMEcpu itself. Thus, the VME cpu operating system is responsible of the acquisition operations, such as data bus management, data structure and data recording, ethernet connections for remote input/output etc. In the experiments presented in this thesis the VME cpu did not come with an operating system on card, in ROM or flash format. Instead the operating system was loaded from a remote computer at startup. The acquistion operating systems used were the GSI developed MBS (Multi Branch System), or the UK-STFC (Science and Technology Facilities Council) developed MIDAS (Multi Instance Data Acquisition System).

Chapter 3

Analysis techniques

In this chapter I summarize the different analysis techniques necessary to process the raw data into useful information to address the physics case under study, such as: energy, momentum or in some cases the mass of the particles.

The information relevant to the decay properties of states in particle emission processes is the kinematical properties of the emited particles. Therefore, the raw data recorded by the data acquisition system has to be filtered and processed to obtain the energy and momentum of the emitted particles. Energy loss corrections are applied to compensate for the detector non sensitive layers and the carbon-foil thickness. However, in β-delayed particle emission processes such as the one presented in this thesis, it is not enough to study the kinematical properties of the emitted particles to characerize the states in the daughter nucleus. Simulations of the decay mechanism using a formalism that describes the resonances involved in the decay are compared with the data. This allows us, by testing different hypotheses, to obtain the resonances parameters, energy, width and spin. The R-matrix formalism, developed to describe nuclear reactions, was used in this thesis to obtain the energy spectrum of the emitted particles from the daughter's resonances parameters. Finally, the analysis of the angular correlations detected in the decay channels where the particles are emitted sequentially allows to study the spin of the resonances involved.

This chapter is divided in two sections. First I discuss the series of analysis procedure necessary to process the raw data into the desired obsrvables, that is position and energy of the detected particle. A brief subsection at the end of the calibrations section summarizes the usage of TONNERRE. Second I present the kinematical calculations used in the analysis of particles detected in coincidence, and a summary on the formalisms used in the simulations of the data, the R-matrix formalism and the angular correlations between particles emitted in cascade.

3.1 Analysis procedures

The first step in the data analysis consists of obtaining the position and energy of the detected particles from the raw data stored by the MBS or MIDAS data acquisition in a event by event basis, which permits to re-run the experiment using different analysis techniques (see chapter 2). Moreover, there are checks necessary to ensure that the data being analyzed are free of background sources such as noise triggering, β-summing or incorrect energy deposition in the detector. The different analysis procedures are:

- Electronic noise cuts: The low amplitude noise in the acquisition system appears as a peak in the low energy part of the ADC spectrum, which has to be cut off in the data analysis. These thresholds have to be determined individually for each strip of each detector, for a total number of 96 channels,32 per detector, in both 2003 and 2007 experiments.

- Geometry calibration: The hit position of the detected particles can be obtained from the strip information stored in the data, as the DSSSD strips are arranged on the detector in a known way. However, in order to obtain the trajectory of the particle in the setup one needs to calibrate the geometry of the detectors with respect of the carbon foil stopper.

- Energy calibration: It correlates the energy of the particle to the pulse height data digitized by the ADC. In order to increase the precision of the calibration for low energy β-decay experiments one has to take into account the energy losses in non-active layers, *i.e.* the detectors dead layer and the carbon foil.

- Event filters: These filters are applied to the calibrated data in order to ensure that the event corresponds to a charged particle hitting the detector. These include matching between the energy recorded in the front and the back sides of the DSSSD and suppressing the effect of β background in the detectors.

3.1.1 Electronic noise cuts

The first step of the analysis is to define the low energy thresholds in the software. In principle this step does not have to be the first, but as the noise might correspond to a large percentage of the recorded data ($\sim$96% of the spectrum shown in Fig 3.1), cutting this noise saves processor time.

As indicated in the previous chapter, the amplifiers have built-in discriminators to cut as much electronic noise as possible. However, these thresholds are set as low as possible, in order to increase the detection efficiency as much as possible without getting a too high trigger rate and leaving electronic noise in the low end part of the

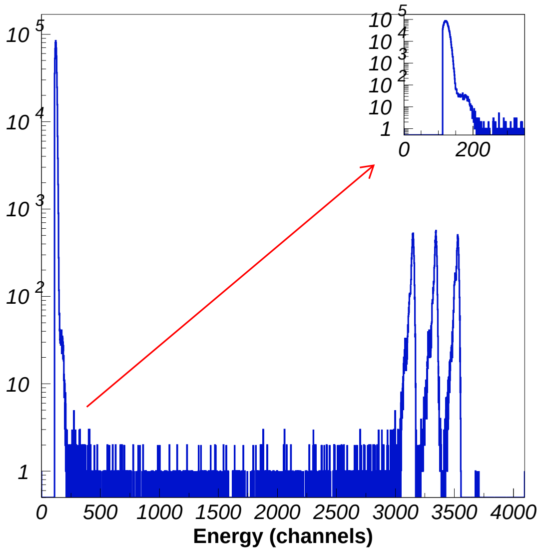

Figure 3.1: Triple alpha spectrum recorded in strip twelve of DSSSD D3 in 2007 experiment. The inset shows a zoom of the first 250 channels for a clear view of the electronic noise present in the spectrum.

spectra. Removing this noise in the analysis implies defining a software threshold that represents the absolute low energy detection threshold of the analysis. It is therefore very important to set these thresholds as close to the end tail of the noise as possible. Calibration data are used typically, as the calibration data appears at much higher energy than the noise and leaves the low end of the spectrum clean of real events. Fig. 3.1 represents a typical example of a triple alpha source where we can see the noise in the low energy end of the spectrum (the noise part of the spectrum is shown in the inset).

The procedure was applied to every strip of the detectors used in the analysis.

3.1.2 Geometry calibration

The calibration of the geometry of the setup consists in determining the relative position of the beam spot, or calibration source, with respect to a coordinate system centered in each detector. This allows for the reconstruction of the trajectory of the particle. This calibration is typically performed before the energy calibration, as it is necessary for dead layer corrections, as these depend on the particles angle of incidence.

The front and back strip information of a DSSSD gives the direction of a vector for the impinging particle, $\overrightarrow{r}^{int}_{part}$, which describes its position in the intrinsic frame

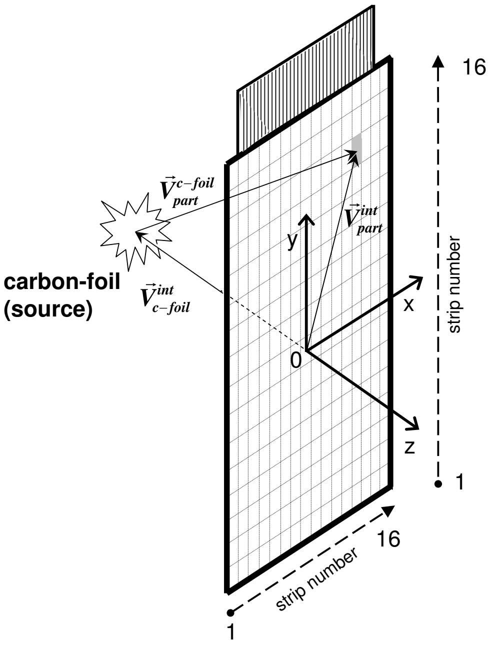

Figure 3.2: Schematic view of the relation between the direction of a particle described in the intrinsic reference frame of the detector and the reference frame of the carbon foil. The vector labeled $\boldsymbol{V}^{int}_{part}$ is the position of the impinging particle in the detector intrinsic reference frame, $\boldsymbol{V}^{c-foil}_{part}$ is the position of the particle with respect of the carbon foil and $\boldsymbol{V}^{int}_{c-foil}$ is the position of the carbon foil in the detector reference frame.

of the detector, as shown in Fig. 3.2. The surface of the DSSSD is divided in 16 3×50 mm^2 vertical and horizontal strips (see section 2.5.1). Thus, the particle coordinates can be obtained from the front and back strip numbers, NS$_f$ and NS$_b$ as

$$\begin{aligned}
\overrightarrow{r}^{int}_{part}(x) &= NS_f * 3 - 25\ mm \qquad (3.1)\\
\overrightarrow{r}^{int}_{part}(y) &= NS_b * 3 - 25\ mm \qquad (3.2)\\
\overrightarrow{r}^{int}_{part}(z) &= 0 \qquad (3.3)
\end{aligned}$$

The direction of the particle from the beam spot in the carbon foil reference frame, $\overrightarrow{r}^{c-foil}_{part}$, is obtained from the direction of the particle in the intrinsic frame, $\overrightarrow{r}^{int}_{part}$, and the direction of the carbon foil in the intrinsic frame of the detector, defined normal to the surface of the c-foil plane, $\overrightarrow{r}^{int}_{c-foil}$ as

$$\overrightarrow{r}^{c-foil}_{part} = \overrightarrow{r}^{int}_{part} - \overrightarrow{r}^{int}_{c-foil} \qquad (3.4)$$

Therefore, the geometry calibration is reduced to obtain the direction of the carbon foil in the intrinsic frame of the detector. The direction of the carbon foil with respect to the detector is obtained by taking advantage of the fact that the intensity observed in a given pixel depends on the solid angle covered by the pixel. This underlines the importance of removing the electronic noise before any analysis, as the intensity of the noise in a given pixel depends only of the hardware thresholds of the strips. This noise would add a level of background to the DSSSD intensity distribution that would make very difficult, even impossible, to obtain a correct distribution.

A DSSSD pixel is defined, for a detected particle, as the overlapping area of the front strip and the back strip hit, thus covering 3×3 mm^2. Assuming that the surface of a pixel is small compared to the distance to the source, ~50 mm, the solid angle Ω covered by a pixel is

$$\Omega = \frac{A\cos\theta}{4\pi\left|\overrightarrow{r}^{c-foil}_{part}\right|^2} \qquad (3.5)$$

where $\theta = \frac{\overrightarrow{r}^{c-foil}_{part}(z)}{\left|\overrightarrow{r}^{c-foil}_{part}\right|}$ and A is the area of a pixel, 9 mm^2. Figure 3.3 shows the triple α source intensity distribution for detector D2 from 2003 setup. It shows the cosine behavior depending on the spherical coordinate, θ, expected from eq. 3.5. The beam spot, or the source, position vector, $\overrightarrow{r}^{c-foil}_{part}$, is finally obtained from a χ^2 fit of the experimental distribution.

The geometry calibration has to be performed for each detector and each time a new source, or the carbon foil is changed in the setup. Table 3.1.2 summarizes the

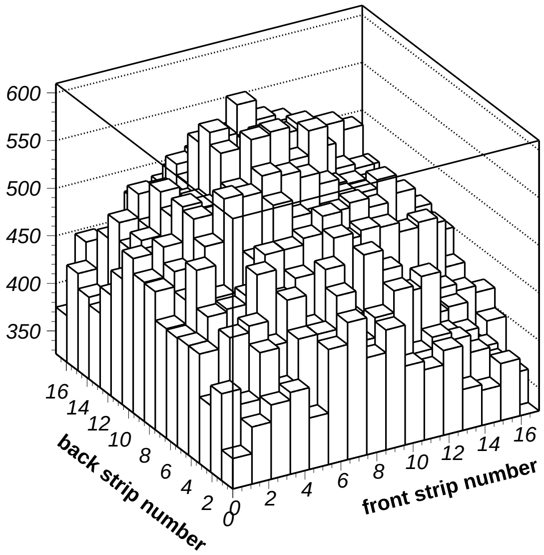

Figure 3.3: Intensity distribution recorded for the triple α source for detector DSSSD D2 in 2003 experiment. The distribution follows the expected cosine shape in θ.

sources and beam spot obtained for 2003 and 2007 experiments. However, in our case, the carbon foil stopper was not touched during beam time, so a single geometry calibration is needed in each experiment. The triple α and ^{148}Gd calibration sources were fixed one on each side of an empty carbon foil holder.

3.1.3 Energy calibration

The energy calibration relates the ADC information stored in the data with the energy of the detected particle. The ADC's convert the height of the voltage pulse, produced by the electron-hole pairs created by the impinging particle, into a 12 bit digital number, which is finally recorded in the data. Both the response of the detector and the ADC are expected to be linear, E=A·Ch+B, in a wide range of energies. A peculiarity of the DSSSD's is that each 32 strips have their own preamplifier-amplifier-ADC chain, which means that in terms of data acquisition each strip is an individual detector. This implies that each of the 32 strips of each detector has to be calibrated separately.

Calibration sources are measured in the experiment to optimize the energy range, normally before and after the data taking, in order to check the stability of the calibration. In both the 2003 and 2007 experiment we used the calibrations done after the data taking. In 2003 experiment both set of calibration files match, althoug the calibration taken after data taking were of higher statistics, thus more precise.

Table 3.1: Source and beam spot positions as seen from the detectors point of view in 2003 and 2007 experiments. During the calibration run, each time the sources were mounted in the setup the stick where they were mounted was taken apart and put back facing in each detector individually, which explains the divergent positions between each source. The stick holding the carbon foil was mounted in with a different angle with respecto to the sources, again changing its relative position with the detectors.

Run	Detector	Source	$\overrightarrow{r}^{int}_{c-foil}(x)$ (mm)	$\overrightarrow{r}^{int}_{c-foil}(y)$ (mm)	$\overrightarrow{r}^{int}_{c-foil}(z)$ (mm)
2003	D1	^{148}Gd	0.0(1)	0.0(1)	50.0(5)
		3-α	3.29(2)	-3.38(3)	46.6(2)
		beam spot	0.0(1)	0.0(1)	50.0(5)
	D2	^{148}Gd	-1.52(1)	-5.19(4)	55.3(3)
		3-α	2.58(2)	-2.45(2)	55.3(3)
		beam spot	2.08(2)	-2.02(2)	52.7(3)
	D3	^{148}Gd	-2.00(2)	-2.16(2)	53.0(4)
		3-α	2.65(2)	-2.00(2)	55.9(5)
		beam spot	1.96(2)	-0.227(2)	65.0(4)
	D4	^{148}Gd	3.29(3)	5.63(4)	53.0(2)
		3-α	0.0590(5)	2.12(2)	53.1(3)
		beam spot	0.871(7)	0.963(9)	60.0(3)
2007	D1	^{148}Gd	-0.531(4)	-4.89(4)	45.7(2)
		3-α	-0.446(4)	0.450(3)	47.1(3)
		beam spot	0.0	0.0	51.5
	D2	^{148}Gd	-0.268(2)	-1.01(1)	35.6(1)
		3-α	-2.01(2)	-2.91(2)	37.9(3)
		beam spot	0.0	0.0	37.1
	D3	^{148}Gd	-4.36(3)	-5.47(4)	45.7(3)
		3-α	-1.81(1)	-1.13(1)	50.9(2)
		beam spot	0.0	0.0	50.0

In 2007 the gain of the amplifiers was changed just before the ^{11}Li started, thus the set of calibration files taken before beam cannot be used. The sources used in both experiments were ^{148}Gd (only in the 2003 experiment) and the triple alpha source (triple α). This gives calibration points of energies [Fir99]:

	Source	E_α (keV)	I_α (%)
	^{148}Gd	3182.787(24)	100
3-α	^{239}Pu	5156.59(14)	73.3(8)
		5144.3(8)	15.1(8)
		5105.5(8)	11.5(8)
	^{241}Am	5485.6(12)	85.2(8)
		5442.90(13)	12.8(2)
		5388(1)	1.4(2)
	^{244}Cm	5804.82(5)	76.4(2)
		5762.70(3)	23.6(2)
		5664(3)	0.022(1)

The alpha decay of the three nuclei present in the triple α source are fairly close, and in some cases, as the three alphas from the ^{239}Pu or the two closest of the other two source are within the resolution of the detectors of ~40 keV. One normally would do a gaussian fit of the highest peak and match it to the strongest transistion. However, this procedure adds an error due to the unresolved alphas. To avoid this problem, for each nucleus of the triple α source we used the average of the three alpha energies weighted by their intensities respectively.

$$E_{source} = \frac{1}{\sum I_{\alpha_i}} \sum_{i=1,3} E_{\alpha_i} \cdot I_{\alpha_i} \tag{3.6}$$

resulting in 5148.9(1) keV, 5478.72(8) keV and 5794.85(3) keV, for the ^{239}Pu, ^{241}Am and ^{244}Cm sources. Of course, using the weighted average of the tabulated energies implies we use the weighted average of the peak in the data, instead of a gaussian fit.

$$E_{data} = \frac{1}{\sum_{k=i}^{f} w(k)} \sum_{i}^{f} k \cdot w(k) \tag{3.7}$$

where the sum is over the channel index k and $w(k)$ is the weight of a given channel k, the number of counts. The averaging region, channels i and f, is selected so that it spans the three peak considered for each nucleus in the triple alpha source.

In the regular procedure, one would calibrate directly matching the data with the weighted averages of the tabulated energies, calculated above. However, as described in the previous chapter, one unavoidable characteristic of silicon detectors is the presence of a non-active entrance window called dead layer. This dead layer effect has to be taken into account before performing the calibration, as the energy loss of particles in matter is non-linear. This means that the calibration correlates the deposited energy of the source, instead of the tabulated energy. Of course, this explains why the geometry calibration is performed before the energy calibration, as it is needed to determine the path of a detected particle through the detector dead layer.

The energy loss of a given type of particle traversing through a length L of silicon is obtained integrating the stopping power of the particle in silicon

$$\Delta E = \int_0^L dx \left(-\frac{dE}{dx} \right)_{Si} \tag{3.8}$$

where $\left(\frac{dE}{dx}\right)_{Si}$ is the stopping power of a given particle in Si. Of course, in the data analysis we perform the inverse operation, adding the energy loss to the calibrated energy. This integral is difficult to solve, as the stopping power depends on the energy of the particle, and this dependency is not allways known analytically.

The stopping power for α particles, our calibration sources, is obtained interpolating SRIM (Stopping and Range of Ions in Matter) tables, and the integral is solved numerically. SRIM is a software package [BH80] for windows which allows to calculate the stopping power and range for any ion in any target composed of a single chemical element, or layers of different elements. In its current form, it allows, with 10% accuracy, to reproduce 89% of the experimental results of stopping power of He ions in matter.

The interpolation is obtained using the interpolation subroutine *polint* from the *Numerical Recipes* [WHPF01]. *Polint* is a rather flexible subroutine that is designed to perform a polinomial interpolation of order N-1 for N points, based on *Neville's algorithm. Neville's algorithm* is based in a recursive relation between polinomials that go between a pair of numbers in the given set of $n + 1$ numbers. Starting with polynomial of order zero, that is the set of numbers themselves, one construct polinomials of orden one between pairs, and recursively obtain the polinomial of order $\leq n$ that fits the entire set [WHPF01]. In our case we used a three-point interpolation.

$$L = \frac{D}{\cos\theta} \tag{3.9}$$

$$\theta = \arccos \frac{\overrightarrow{r}^{source}_{part}(z)}{\left|\overrightarrow{r}^{source}_{part}\right|} \tag{3.10}$$

where D is the thickness of the dead layer, which is 0.6 μm silicon-equivalent for the old w-design detectors, detector D3 in 2003 experiment, and 0.1 μm of silicon

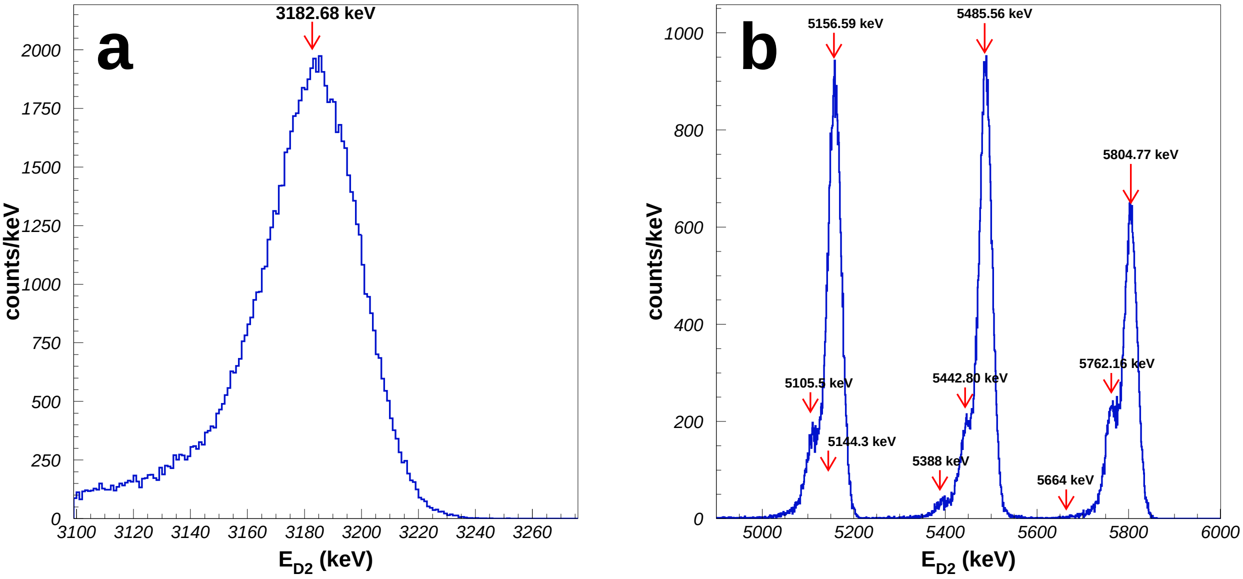

Figure 3.4: Left: (a) shows the 3182.68 keV alpha transition as seen from detector D2 in 2003 experiment The ^{148}*Gd source used was a strong, 3 kBq. The arrow points the exact energy of the source. Right: triple* α *source as seen from detector D2 in 2003 experiment. The triple alpha source used was of 300 Bq intensity. Again the arrows mark the exact energies of the different alphas of the calibration source.*

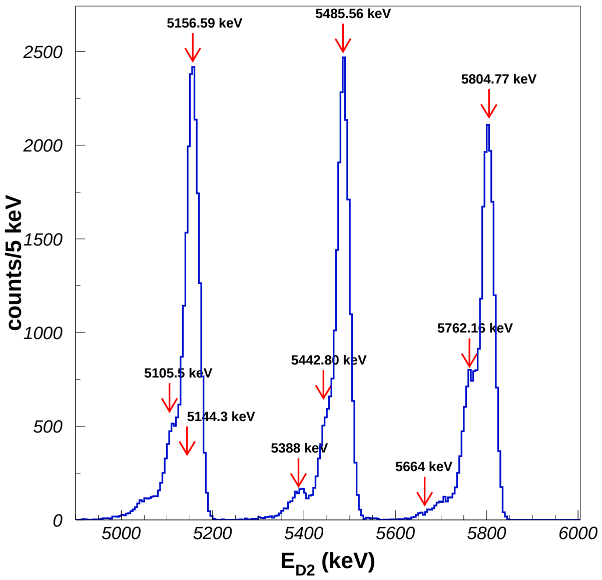

Figure 3.5: Triple alpha source as seen by detector D2 in 2007 experiment. As in Fig 3.4 the arrows mark the exact energies of the source alphas.

for the new ultra-thin detectors, all the remaining detectors used, and all detectors used in 2007 experiment. The resulting deposited energies, for a typical hit in the center strip of 8 of the ultra-thin detectors 50 mm away from the source, are 3145.41 keV for the ^{148}Gd source and 5120.84, 5451.80 and 5768.75 keV for each averaged alpha energy of the triple α source.

Once the energy losses for the sources are taken into account, the calibrations of each 32 individual strips of each detector can be performed. As mentioned above, the detector and ADC behavior is expected to be linear, so the calibration is just a simple linear function relating the channel number to the deposited energy

$$E_{deposited} = A \cdot channel + B \tag{3.11}$$

The parameters A (keV/channel) and B (keV) are obtained from a χ^2 fit of the 4 calibration points. Figures 3.4(a),(b) show the ^{148}Gd and triple alpha sources seen in detector D2 in the 2003 experiment and Fig. 3.5 shows the triple α source seen in D2 in 2007 experiment. The energy of the different alphas from the sources are indicated by the arrows in the three figures. As an example of the effect of the dead layer Fig. 3.6 shows the triple α source as seen from detector D3, in red the deposited energies and in blue the emitted energies.

The calibrations were checked measuring online the β-delayed alpha emitter ^{20}Na

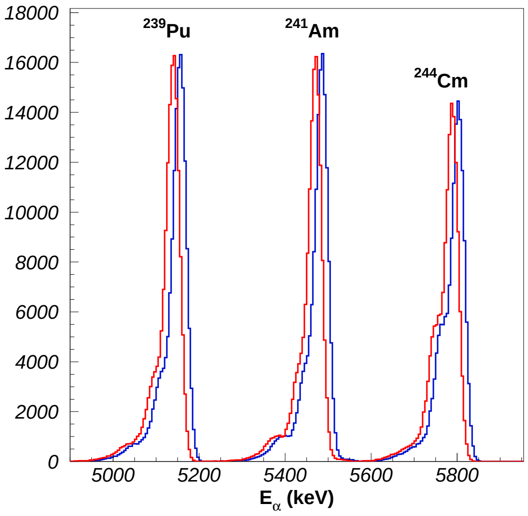

Figure 3.6: Triple alpha source as seen by detector D3 in 2007 experiment. The deposited energy is shown in red and the corrected energy, the original source energy, in blue.

($T_{1/2}$)=447.9(23) ms [Til98]). Figure 3.7 (taken from [Cli89]) shows the ^{20}Ne states fed in the β-decay of ^{20}Na, where we see there are 16 states in ^{20}Ne above the alpha separation energy of 4.72985(1) MeV [AWT03]. The nominal alpha particle energies [Cli89] observed in our detectors are:

E_α (keV)	I_α (relative %)
2150(5)	100
2479.6(21)	3.652(43)
2659(7)	0.074(6)
3799(3)	1.510(27)
4432(5)	17.31(9)
4675(3)	0.553(15)
4885(3)	1.09(3)
5106(7)	0.055(7)
5249(4)	0.165(11)

The main advantage of using the internal source ^{20}Na is that it comes directly from the target and separator. In this way the positioning and size of the incoming beam is reproduced within 1 or 2 mm, which allows us not only to check the goodness of the calibrations done with external sources, but to check if the energy loss effect of the carbon foil is properly taken into account. The energy loss in the carbon foil is

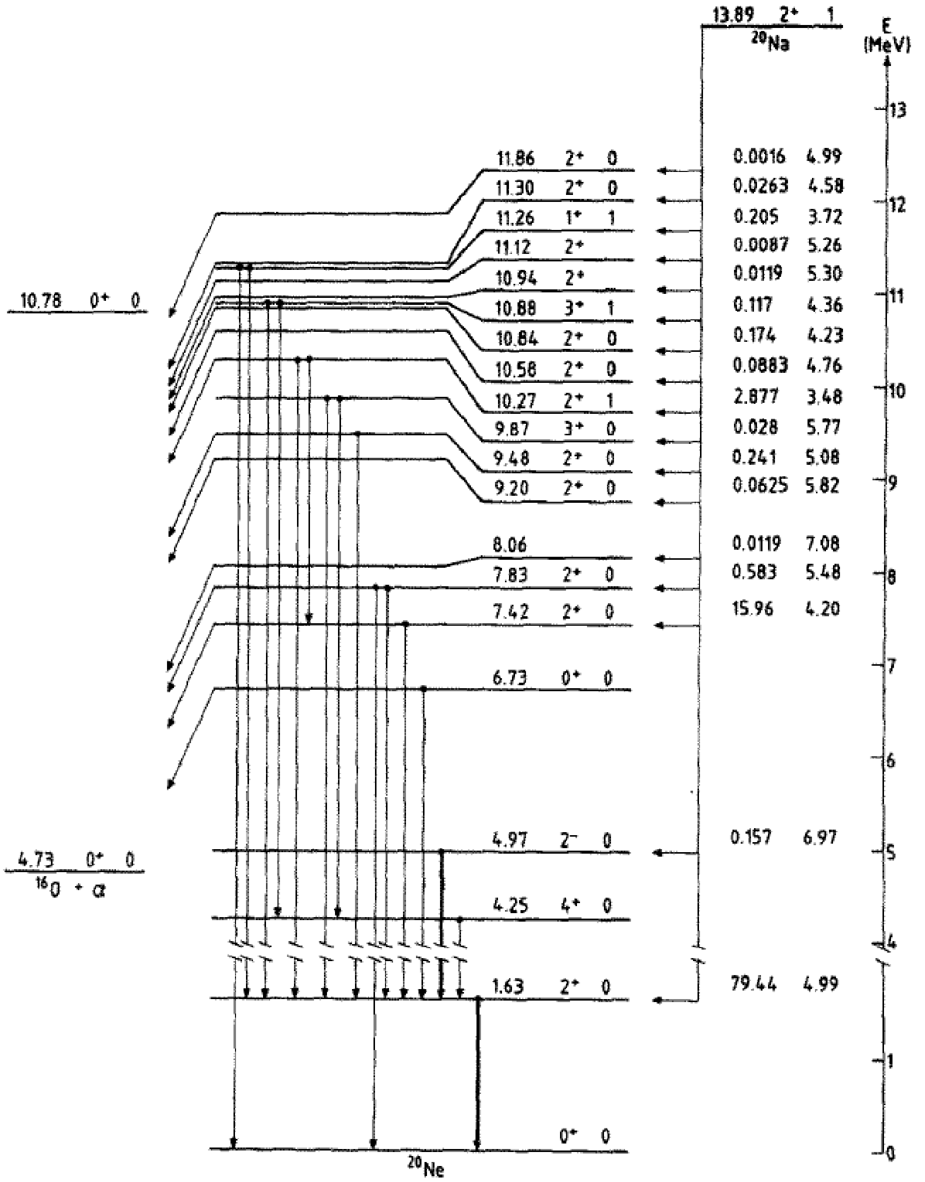

Figure 3.7: ^{20}Na β decay scheme, taken from [Cli89].

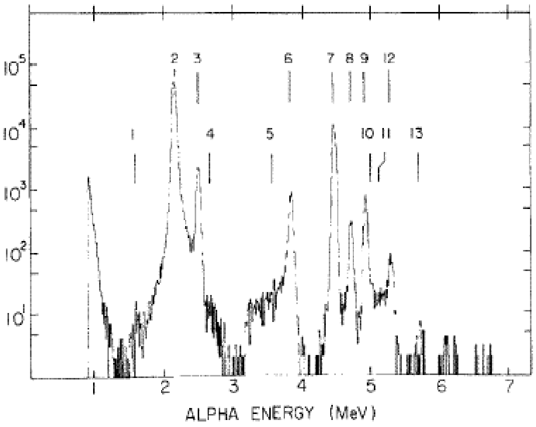

Figure 3.8: Energy spectrum of ^{20}Na β-delayed particles, taken from [Cli89]. The transitions observed in this work, listed in the text, are 2,3,4,6,7,8,9,10,11,12.

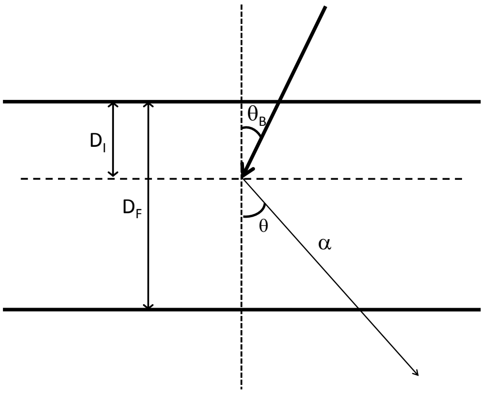

Figure 3.9: Schematic view of the different lengths and angles necessary to calculate the path of an emitted particle inside the carbon foil.

added to the dead layer-corrected energy in the same way, integrating the stopping power in the path inside the foil, which depends on the carbon foil thickness and the impinging depth of the ^{20}Na ions, as shown in Fig. 3.9.

For the detectors facing the impinging side of the foil, D in eq. 3.10 is replaced by the impinging depth (D_{I}). In case the detector is facing the opposite side, D is replaced by the foil thickness (D_{F}) minus the impinging depth. The impinging depth of the ^{20}Na, and ^{8,9,11}Li, ions, is obtained from the TRIM (TRansport of Ions in Matter) part of the SRIM package, which calculates the range and straggling of ions in matter via a Monte-Carlo calculation. In both 2003 and 2007 experiments the beam energy was set to 30 keV, thus the impinging depths depend only on the angle between the beam and the carbon foil θ_B, defined in spherical coordinates (see Fig. 3.9). The impinging angle θ_B was 35.26°in 2003 and 0°in 2007, thus obtained impinging depths:

	D_{I} (Å) (2003)	D_{I} (Å) (2007)
^{20}Na	398	483
^{8}Li	—	1654
^{9}Li	1374	1674
^{11}Li	1408	1714

The carbon foil thickness, D_{F}, was chosen so that the ^{11}Li ions stopped approximately in the middle of D_{F}. A 60 μg/cm^2, correspoding to 2663 Å, foil was used in 2003, and a 50 μg/cm^2 (2127 Å) foil in 2003.

Finally, the angle θ in spherical coordinates from equation 3.10 is not the same for the carbon foil, as by construction of the reference frame of eq. 3.4, the unitary vector $\hat{z}$ is the same as in the reference frame of the detector. We need to do a coordinate change to the carbon foil surface reference frame. The most general way of implementing this coordinate change is using the CERNLIB subroutine *polrot* [cer], which rotates a reference frame into another given a rotation axis $\overrightarrow{a}$ and a rotation angle ϕ. Both the rotation axis and the angle can be easily obtained from the carbon foil surface vector, $\overrightarrow{S}_{cf}$, and the detector surface vector, $\overrightarrow{S}_D = \hat{z}$ both defined in the detector reference frame, as

$$\overrightarrow{a} = \hat{z} \times \overrightarrow{S}_{cf} \tag{3.12}$$

$$\phi = \arccos \frac{\hat{z} \cdot \overrightarrow{S}_{cf}}{\left|\overrightarrow{S}_{cf}\right|} \tag{3.13}$$

Combining the dead layer energy loss correction with the carbon foil energy loss correction we obtain the proper alpha energies. Figures 3.10(a) and (b) show the

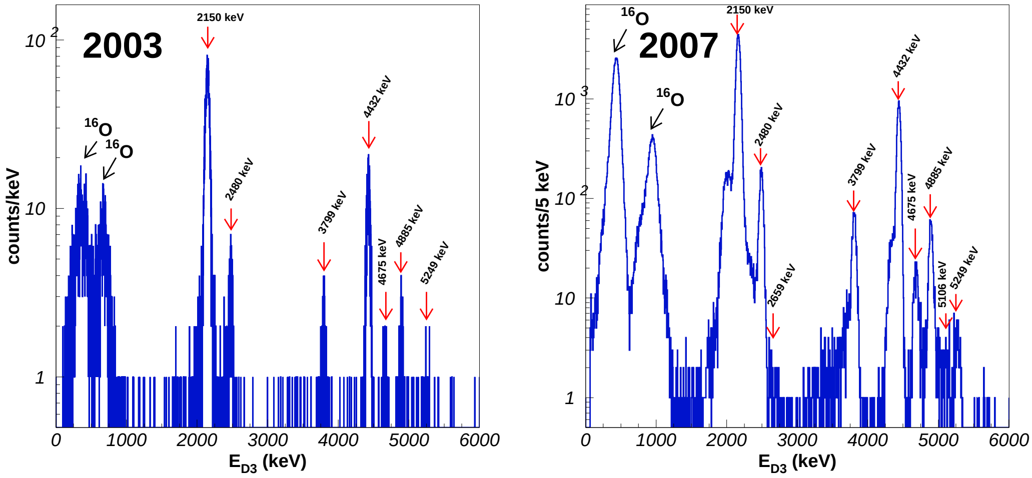

Figure 3.10: Left: ^{20}*Na energy spectrum, with carbon foil and DSSSD dead layer energy losses taken into account, as seen by detector D3 in 2003 experiment. The arrows mark the exact alpha energies. The two low energy peak correspond to the recoil ions,* ^{16}*O, from the two most intense alphas at 2150 and 4432 keV. Right:* ^{20}*Na spectrum as in the left picture for 2007 experiment. The difference in statiscs are due to the longer* 20*Na beam time dedicated in 2007.*

dead layer and carbon foil corrected ^{20}Na spectrum as seen from detector D3 in 2003 and 2007 experiment, respectively. The arrows in both figures mark the tabulated alpha energies [Cli89]. Figure 3.8 shows the ^{20}Na alpha spectrum from [Cli89] for comparison. Finally, Fig. 3.11 shows the typical effect of dead layer and carbon foil corrections on the ^{20}Na spectrum, shown for detector D1, all strips combined, of 2007 experiment. Not only the energy losses are corrected, but the resolution is increased by removing the energy spread due to different entrance angles for each strip

After carbon foil correction, there was still a discrepancy in the energy of the ^{20}Na alphas of around 70 keV for detector D4 in 2003 experiment. This discrepancy was corrected using an effective carbon foil thickness of 92 μg/cm^2 (4200 Å). This correction exploits the fact that the detector D4 was placed in the side of the foil behind the beam spot. As the energy after dead layer and carbon foil correction of the ^{20}Na alphas in D2 and D3 was correct, that would indicate a problem in the carbon foil thickness D_F, not the impinging depth D_I.

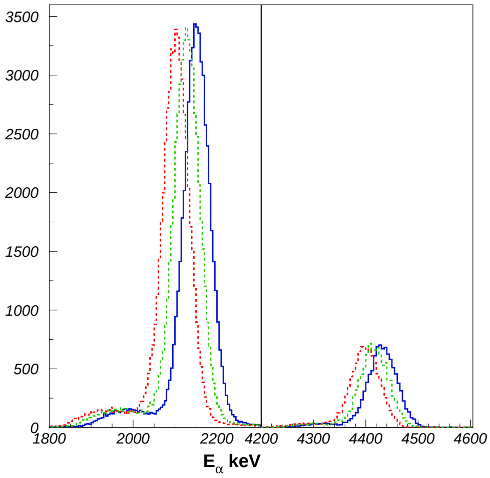

Figure 3.11: Effect of dead layer and carbon foil corrections for the two most intense alpha particles of ^{20}*Na as seen by detector D1, all strips combined, of 2007 experiment. The red histogram shows the deposited energy, the green histogram the energy corrected of energy losses in the dead layer of the detector and the blue histogram shows the energy with full dead layer and carbon foil corrections.*

3.1.4 Event filters

Once the geometry of the setup and the detectors have been calibrated, there are still some checks necessary to be done to improve the quality of the data. The quality is reduced by several sources, among them, beta background in the detectors and beta-pileup. These problems are less relevant today, as the new generation of detectors are highly segmented, which considerably reduces these effects. There are still, however, benefits doing further analysis to reduce them, as it gives an insight of the goodness of the response of the detector.

As mentioned in the previous chapter the charge collection in double sided silicon strip detectors (DSSSD) is carried out by not one, but 16 individual strips in each side of the silicon wafer. As mentioned in the previous chapter, a strip is the defined by the boron implantion region, which is collected by an aluminum contact (or grid in the new ultrathin detector), and finally connected to a single wire, thus corresponding to a single channel in the electronics. This means the DSSSD detectors do not have proper pixels, but the information associated to the front strip(s) and back strip(s). Of course, a physical event (that is, a voltage surge produced by a particle, not by noise in the detector) should have the same information for both front and back strips, but this does not allways happen in practice.

Fig. 3.12a shows the calibrated energy recorded in the front strips of DSSSD

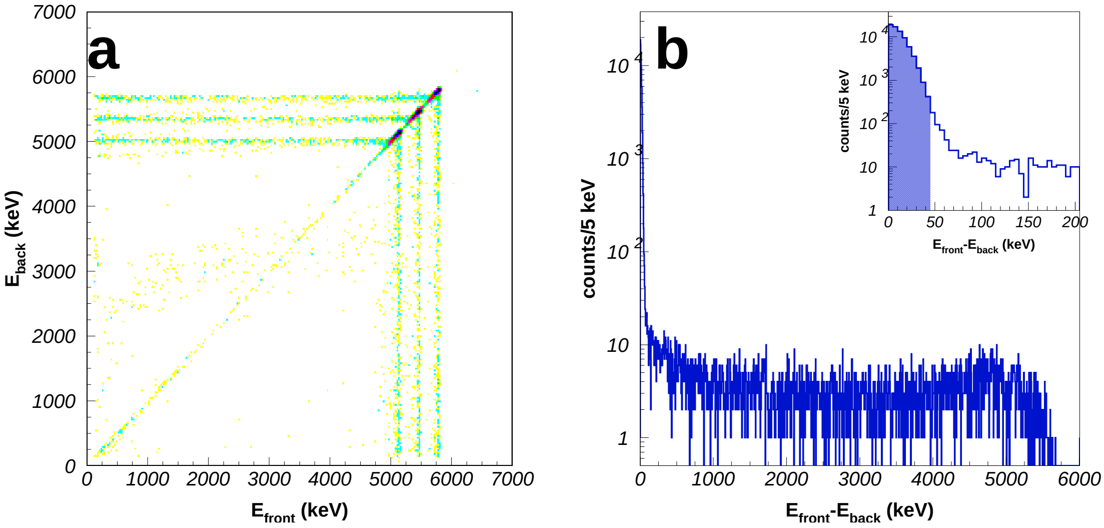

Figure 3.12: Left: figure a shows the energy recorded, for the triple α source, in the front strips of DSSSD D2 versus the energy recorded in the back strips, for the 2007 experiment. The diagonal line corresponds to good events, were the energy recorded in both strips in the front and back is the same. The horizontal and vertical lines extending from the three points of the source indicate events were one of the sides recorded less energy than the other. Right: figure b shows the energy difference between front and back for the triple α events shown in the left figure. The inset shows the first 200 keV, the peak corresponding to the diagonal line. The shadowed area in the inset shows the area below the energy difference cut of 40 keV used in this detector, corresponding to 93.3% of all recorded events.

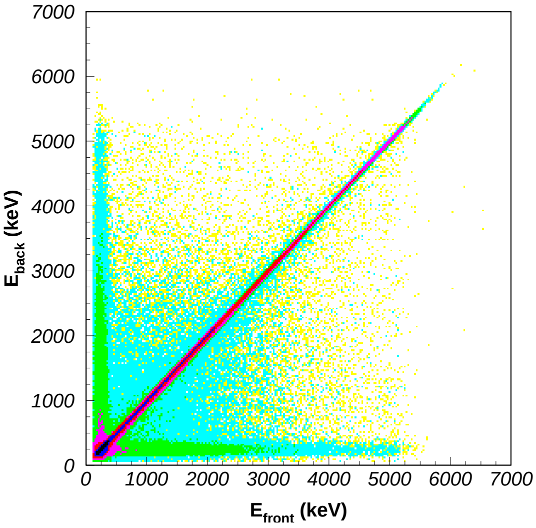

Figure 3.13: energy recorded in the front strips of DSSSD D2 for the ^{9}Li β-decay versus back energy. The two main features are the two lines extending from the low energy point to higher energies. These lines correspond to events of multiplicity two where we couple the energy recorded in one of the front strips of a given particle with the energy recorded in one of the back strips of a different particle.

D2 against the energy recorded in the back strips, for the triple α source, in 2007 experiment. It shows, that even for a simple case such as an α event of well defined energy, and where the maximum multiplicity of an event is 1, not all events are recorded with the same front and back energies (corresponding to the diagonal line, the three dots being the three peaks of the source), but there are horizontal and vertical lines extending to lower energies from the three dots of the triple α source. These extending lines correspond to an event where the proper energy was recorded in one of the sides of the detector but not in the other. These events indicate incomplete charge collection in the strip of the offending side, due to charge sharing between neighboring strips. Fig. 3.12b shows the front energy minus the back energy for the same triple α data set of Fig. 3.12a. The diagonal line in the latter plot corresponds to the low end peak in Fig. 3.12b, which contains, for instance, for the first 75 keV, $\sim$94% of the recorded statistics.

Fig. 3.13 shows the front energy against back energy scatter plot for DSSSD D2, for ^{9}Li data from the 2007 experiment. In this case, the multiplicity in a detector of a given event can be either one or two, as there are two α particles emitted per each β-delayed neutron emission (BR=50.8(9)% [Til04]).

In this case, apart from the events extending to lower energies from the diagonal line, there are two lines extending to higher energies from the concentration of events in the low part of the scatter plot. These two lines correspond to events of multiplicity two where we pair the energy recorded in one of the front strips of a given particle with the energy recorded in one of the back strips of a different particle. There are four different combinations of front and back strips for a multiplicity two event, of which only two are correct. Selecting front-back pairs whose energy difference is below the given threshold partially solves that problem, as only the correct pair will have energy difference close to zero, for ^{9}Li events where the difference of the emitted energies of the two alpha particles is higher than the chosen threshold. The threshold used for DSSSD D2 was 40 keV, meaning that 95% of the double coincidences were recorded with a difference of the emitted energies higher than the chosen threshold. In the remaining 5% of the coincidences, where the two alpha particles are emitted with a difference of energies below the threshold, the correct front-back couple can only be chosen by pairing the energy measured in a given front strip with the closest energy recorded in the back strips.

The energy difference cuts used for the DSSSD's in 2003 and 2007 experiment where

	DSSSD	E$_{cut}$(keV)	number of events $\|E_f - E_b\| < E_{cut}$ (%)
2003	D2	40	85.7
	D3	50	79.2
	D4	80	87.8
2007	D1	60	94.3
	D2	40	93.3
	D3	50	94.5

The second problem mentioned in the introduction of this section is the effect of beta particles in the detectors. Traditionally in β-decay experiments, one has to deal with both beta background in the low end of the detector and beta pileup. Beta pileup which occurs when a beta particle goes through the detector at the same time as one of charged the particles we are interested in measuring, resulting in a event of energy E$_{part}$+E$_\beta$. In principle, thi problem is much reduced by using very thin highly segmented detectors, such as the DSSSD's.

If a β particle hits a silicon detector, it will deposit a small amount of energy depending on the stopping power of electrons in silicon and the thickness of the detector. For ^{11}Li (Q$_\beta$=20.54 MeV [Bac08, AWT03]), the electron will be emitted in a range between close to zero and Q$_\beta$, with a maximum at 1/3(Q$_\beta$-E*), where E* is the energy of the state in the daughter nucleus. In the case presented in this thesis, the upper limit of the deposited energy would be given by the electrons emitted at Q$_\beta$, as they have the higher stopping power [SPS91]. For 20 MeV electrons, the energy deposited in silicon is 5.7194 MeV/cm [SPS91]. As the DSSSD's used in our experiment were 60 μm thick, the energy deposited by electrons emitted at

Q_β is ~34 keV, below the hardware thresholds in the amplifiers and well below the software threshold used in the analysis.

In the case of beta pileup we have to look into the probability that a beta particle hits the same strip at the same time as one of the particles we are interested in. The probability of measuring both particles in coincidence in a given strip, for isotropic emission, is given by the square of the solid angle covered by the strip. As the solid angle depends linearly on the surface of the detection element, the probability of beta pileup in a given detector consisting of N_s strips is given by:

$$P_{pileup} = N_s \Omega^2(\text{strip}) \approx N_s \frac{A(\text{strip})^2}{r^4} \tag{3.14}$$

As A(strip)=A(DSSSD)/N_s and Ω(DSSSD)≈ A(DSSSD)/r^2

$$P_{pileup} \approx N_s^{-1} \Omega^2(\text{DSSSD}) \tag{3.15}$$

The pileup probability for a stripped detector is reduced compared to a non stripped detector by the inverse of the number of strips squared. In the typical case of having the DSSSD's 5 cm away from the beam spot, as in both 2003 and 2007 experiments, each strip covers approximately a 16^{th} of 4% of 4π, 0.25% of 4π. This means that the beta particle has a 6.25 10^{-4} % probability of simultaneously hitting a strip, or 0.01% per detector. In practice this means that for an experiment consisting in 3 DSSSD's and measuring 7000 coincidences, as in 2003 experiment, 2 events may suffer of beta pileup, or 18 events out of 60000 coincidences, as in 2007 experiment.

In summary, beta pileup and beta background have little effect in the quality of the data in a experiment of low statistics such as the study of the β-decay of ^{9}Li and ^{11}Li presented here, as the beta background is well below the low energy thresholds set in the analysis and just 0.01% of the events per detector may show beta pileup. On the other hand, the effect of incomplete charge collection on one of the sides of the detector might be more important, as ~20% of the events recorded in the 2003 experiment were rejected by selecting events with an energy difference between front and back strips closer than the selected thresholds. Finally, this front-back energy difference technique is also necessary to properly couple front energy with back energies in events of multiplicity greater than one, as only the correct pairs will have matching energies.

Is important to mention that in both experimens in 2003 and 2007 the DSSSD detectos were stacked with thick (1.5 mm) Si pads for beta detection. This were used to test the beta summing in our experiment, as we studied the DSSSD spectrum in both anti-coincidence mode with its Si pad (no event analyzed if there is hit in the pad), and coincidence mode with other pads (event analyzed only if the beta is

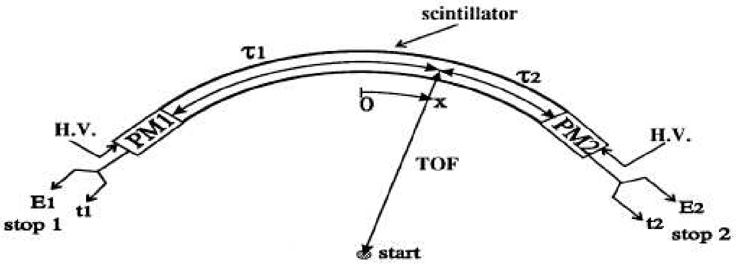

Figure 3.14: Schematic view of the different time measurements in a single TONNERRE pad.

detected in on other pad but the one behind the given DSSSD). The results confirm the lack of beta summing in the spectra presented in this work.

3.1.5 TONNERRE

The neutron-time-of-flight detector array TONERRE derives the energy of the detected neutrons from the time difference between the starting trigger and the STOP signal given by the photomultiplier tubes (for more details see section 2.5.2). Of course, this implies the calibration and analysis of TONNERRE events is done in a completely different way from that of a double sided silicon strip detector. In this section I will briefly describe the energy and geometry calibration techniques used in the analysis of TONNERRE. For a more detailed description see [But00, Tim01]

Time of Flight calibration

As we saw in section 2.5.2, TONERRE consists in 16 pads in our experiment with photomultiplier tubes at both ends of each detector pad. This means that for a single event there are two time measurements for the right and left, t_1 and t_2

$$t_1 = \mathrm{TOF} + \tau_1; \quad t_2 = \mathrm{TOF} + \tau_2 \tag{3.16}$$

where, t_1 and t_2 are the times between the trigger signal and the signal from each photomultiplier tube of TONNERRE, TOF is the particles time of flight, and τ_1 and τ_2 are the time the light need to travel between the hit point and the photomultipliers. Of course, $\tau_1+\tau_2$ should be the time the light output travels throught the whole detector (see Fig. 3.14)

$$\tau_1 + \tau_2 = \frac{l}{v} \tag{3.17}$$

where l is the pad length, 160 cmin our case, and v is the speed of light in the scintillator material, 16.3 cm/ns [But00]. From both equations we see

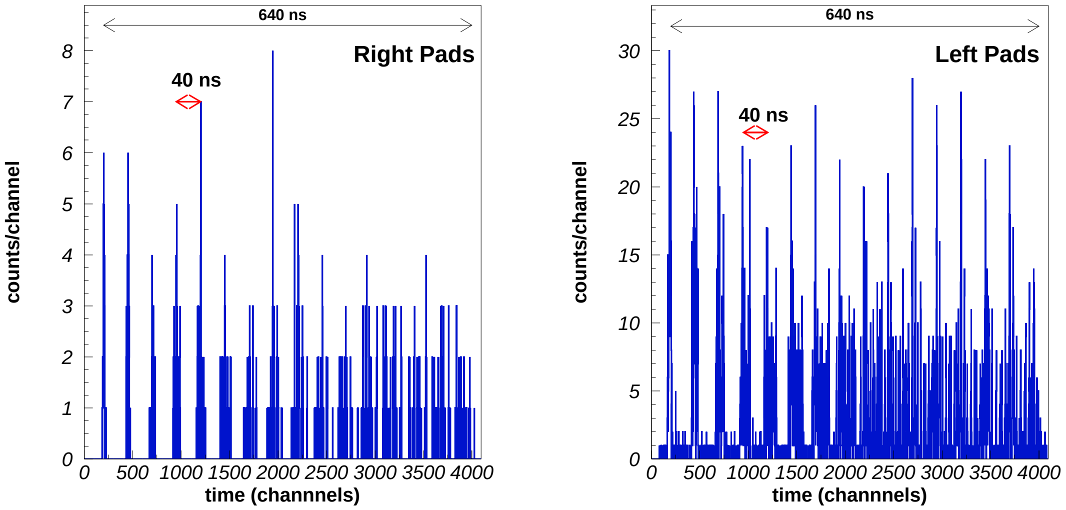

Figure 3.15: Left: Pulse calibrator time spectrum seen in the TDC's corresponding to the right photomultipliers of TONNERRE. The full range corrsponds to 640 ns and the distance between peaks to 40 ns. Right: same pulse calibrator seen in the TDC's of the left photomultipliers of TONNERRE. The time calibrator was used in different measurements for each set of photomultipliers, thus the different statistics.

$$\mathrm{TOF} = \frac{t_1 + t_2}{2} - \frac{l}{2v} \tag{3.18}$$

In general, when analyzing TONNERRE, t_1 and t_2 are given in channels, so we substitute this equation by

$$\mathrm{TOF} = \frac{a_1 t_1(channels) + a_2 t_2(channels)}{2} - B \tag{3.19}$$

where a_1 and a_2 are the TDC calibrations, and, as $\frac{l}{2v}$ is a constant, it is subsistituted by an adjustable offset. The TDC calibration were obtained using a time calibrator on the TDC input. A time calibrator is a pulse generating device, whose pulse range and frecuency can be adjusted. The two panels of 3.15 show the pulse calibrator time spectrum in the TDC's of the right photomultipliers of TONERRE and left photomultipliers of TONNERRE respectively. The full range corresponds to 640 ns and the period to 40 ns. The distance between peaks corresponds to 250 channels. Taking into account that the time calibrator period is 40 ns, results in a_1 and a_2 equal to 0.16 ns/channel.

The offset B is directly determined from the gamma rays emitted in the β-decay. The gamma rays fly at the speed of light, 30 cm/ns, thus requiring 4 ns to fly the 120

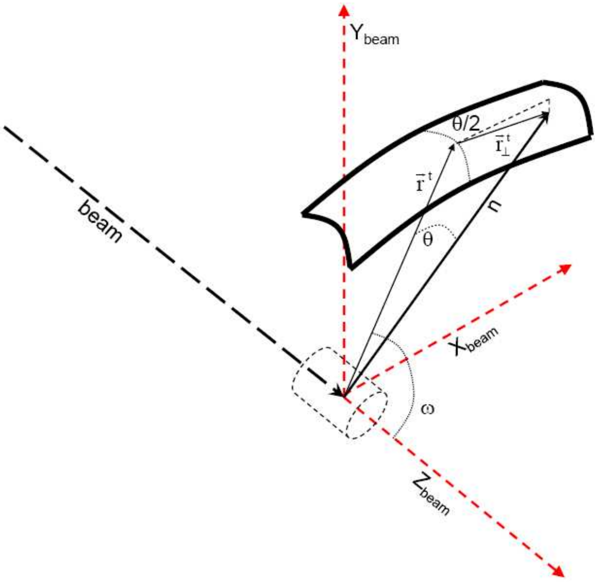

Figure 3.16: Schematic view of the axis used to calculate the neutron direction from a TONNERRE hit. The dotted cylinder represents the experimental chamber

cm of TONERRE radius from the setup to the scintillator pads. We will therefore adjust B so that the prompt gamma peak corresponds to 4 ns in the final spectrum.

Finally the energy of the detected neutron can be obtained from the time of flight (TOF), and using the mass of the neutron at rest, m_n=939.6 MeV/c^2, and the speed of light in vacuum $c = 30$ cm/ns:

$$E_n = \frac{1}{2} m_n v_n^2 = \frac{0.5227 d^2}{\mathrm{TOF}^2} \tag{3.20}$$

where TOF is defined in ns and d is the radius of TONNERRE, 120 cm.

Geometry calculation

From figure 3.14 we can extract the hit position along the TONNERRE pad, x, from the subtraction of the times measured in the left and right photomultipliers

$$t_1 - t_2 = \tau_1 - \tau_2 = \frac{2x}{v} - \frac{l}{v} \tag{3.21}$$

where v is the speed of light in the scintillator, 16.3 cm/ns, and L is the pad length, 160 cm. Therefore the hit position depends only of the time difference:

$$x = \frac{l}{2} + \frac{v}{2}\left(t_1 - t_2\right) \tag{3.22}$$

where we can remove the $l/2$ term if we center the reference frame in the center of the pad. Now, if we want to calculate the neutron direction vector from the x distance along the pad we have to take into account the spatial disposition of the detector array with respect to our experimental chamber. We define an external reference frame where the $\hat{z}$ corresponds to the ISOLDE beam direction and $\hat{x}$ to the top of the experimental chamber, shown in Fig. 3.16. In this reference frame, the direction of TONNERRE hit will be defined by two angles, the pad angle ω with respect to the $\hat{x}_{beam}$, and the angle θ between the direction vector and the direction to the center of the pad, in the following way:

$$\overrightarrow{r}_n = \overrightarrow{r}^t + \overrightarrow{r}^t_\perp \tag{3.23}$$

where $\overrightarrow{r}^t$ and $\overrightarrow{r}^t_\perp$ are defined from the reference frame as

$$\begin{aligned}
\overrightarrow{r}^t &= d\cos\omega \cdot \hat{Z}_{beam} + d\sin\omega \cdot \hat{Y}_{beam} && (3.24)\\
\overrightarrow{r}^t_\perp &= 2d\sin\frac{\theta}{2}\cos\frac{\theta}{2} \cdot \hat{X}_{beam} - 2d\sin^2\frac{\theta}{2} \cdot \hat{Y}_{beam} && (3.25)
\end{aligned}$$

where d is TONNERRE radius and x is te calculated distance along the scintillator pad. Finally, the angle θ is calculated (in radians) from the distance along the scintillator pad

$$\theta = \frac{x}{d} \tag{3.26}$$

and we approximate ω as the center axis position of each pad, measured during the experiment

Pad	ω ($\pm$0.2) (degree)
1	-46.74
2	-34.69
3	-23.04
4	-11.45
5	0
6	11.8
7	24.57
8	38.53
9	51.24
10	65.96
11	77.184
12	89.36
13	100.48
14	111.74
15	125.89
16	137.54

3.2 Kinematical Analysis

The β-delayed decay channels of the nuclei studied in this work, ^{9,11}Li, often include the simultaneous emission of multiple particles. The decay channels observed range from two body breakup, to a five particle final state:

- β-delayed two body breakup of ^{11}Li: There have been observed two different two body breakup channels ^{11}Li$\rightarrow^{8}$Li$+t$ [Lan84] and ^{11}Li$\rightarrow^{9}$Li$+d$ [Muk96]. The triton emission has been linked to the breakup of a high energy excited state in ^{11}Be [Muk96], whereas the deuteron emission has been recently confirmed to occur directly from ^{11}Li to the ^{9}Li$+d$ continuum.

- Three body ^{9}Li$\rightarrow 2\alpha+$n: The final state of the breakup of ^{9}Be is allways the three body channel, as none of the two body subsystems, ^{5}He and ^{8}Be are bounded. However, the breakup has been confirmed to proceed sequentially through both intermediate two body systems [Nym90, Pre03, Pre05].

- Three body ^{11}Li$\rightarrow^{6}$He$+\alpha+$n: This three body decay channel has been proposed to occur sequentially through an intermediate state in ^{11}Be [Lan81].

- Five body ^{11}Li$\rightarrow+2\alpha+3$n: This decay channel was assumed to be the direct breakup of a state in ^{11}Be to the five body continuum.

The different decay channels, and the different possible breakup mechanisms for each decay channels indicate the importance of studying the full kinematical properties of the final state. That is, it is not enough to individually measure the energy of the emitted particles. In order to determine the breakup mechanism, it is necessary to detect all the emitted fragments in coincidence. However, this is normally very difficult in the β-delayed breakup of ^{9,11}Li isotopes, as most of the channels include the emission of at least one neutron, which is hard to detect in coincidence with the other two charged particles (and it was not possible in the 2007 experiment, as there were no neutron detectors present). This means one has to extract all the information possible out of the energy correlations and momentum correlations between the charged particles detected.

All the multiple particle emission channels in ^{9,11}Li involve the simultaneous emission of two charged particles, wether they are emitted alone or in combination with neutrons. The lack of coincidence detection of all charged particle and neutrons simultaneously implies that proper kinematical analysis can only be performed for two-body channels (*i.e.* ^{8}Li+t, ^{9}Li+d), where all the emitted particles are detected, and three-body channels (*i.e.* 2αn, nα^{6}He), where the missing momentum corresponds to one neutron. Thus, from now on I am going to concentrate in techniques used to detect in coincidence 2-body and 3-body channels.

In the simplest case of two body breakup, energy and momentum conservation impose a relation between the energy of the two emitted particles

$$\overrightarrow{P}_A + \overrightarrow{P}_B = 0 \tag{3.27}$$

$$E_A + E_B = Q \tag{3.28}$$

where Q is the available energy for the breakup. In general Q will be distributed according to the resonance shape w(E). In a coincidence experiment, we can take advantage of these relations by plotting the energy detected in one detector against the energy detected in the other. The first equation implies that $\left|\overrightarrow{P}_A\right| = \left|\overrightarrow{P}_B\right|$, which we simplify to $\boldsymbol{P}$. Taking into account that $\mathrm{E}_{A,B}=\frac{\boldsymbol{P}^2}{2m_{A,B}}$

$$E_A = \frac{m_B}{m_A} E_B \tag{3.29}$$

Fig. 3.17 shows a typical example of two body breakup, the β-delayed ^{8}Li+t breakup of the 18.4 MeV state in ^{11}Be We see that the breakup appears as two lines of slopes $\mathrm{m}_{^8Li}/\mathrm{m}_t$ and viceversa. The two lines appear in the scatter plot depending on which particle hit one detector or the opposite, and the line length depends of the distribution of Q. The sum energy, corresponding to Q, is shown in the inset panel.

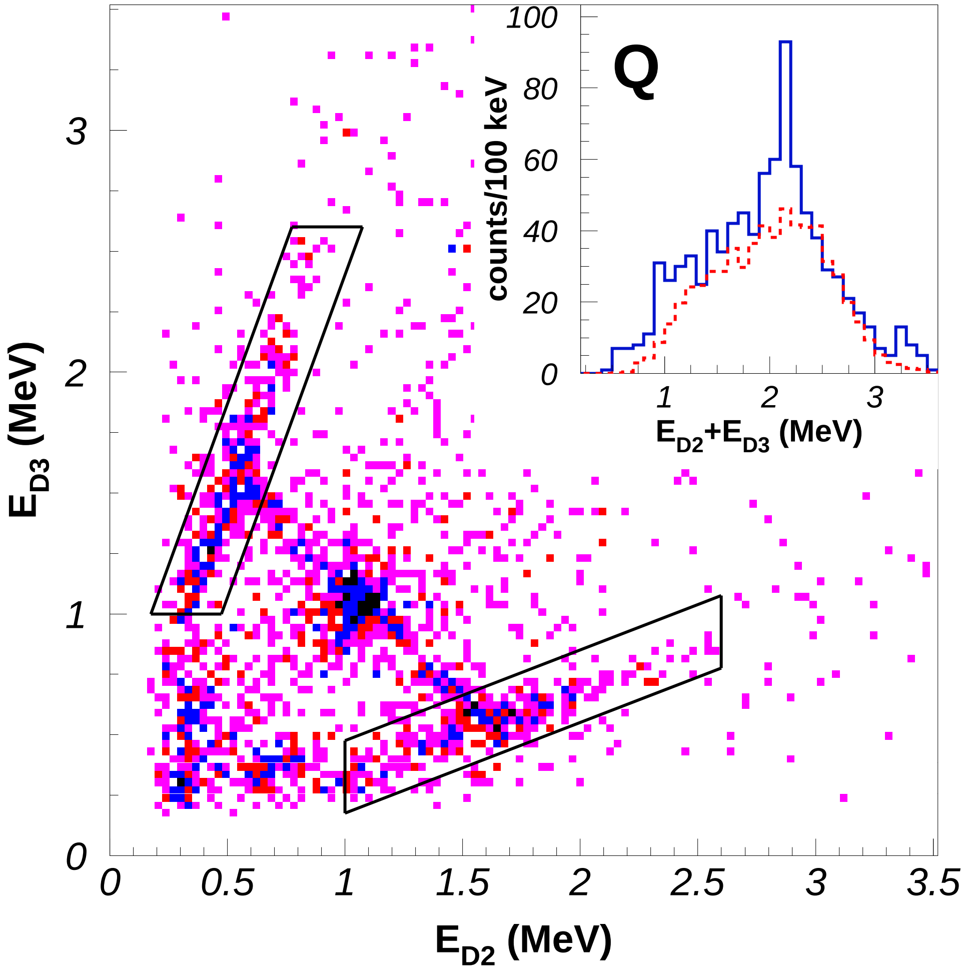

Figure 3.17: Energy recorded in DSSSD D2 against energy recorded in DSSSD D3 in 2007 experiment. The two lines of data, surrounded by boxes, correspond to the β-delayed 2-body ^{8}Li+t breakup of the 18.4 MeV state in ^{11}Be. The slope of each line correspond to the mass ratio between tritons and ^{8}Li, 8/3 and 3/8. The sum energy, shown in the inset, corresponds to the Q of the breakup, the 18.4 resonance in ^{11}Be. The group of data between the lines, corresponding to the peak in the inset, comes from the 3-body breakup of states in ^{11}Be. The red dashed line in the inset shows the resonance distribution decaying into ^{8}Li+t, modeled using R-matrix formalism.

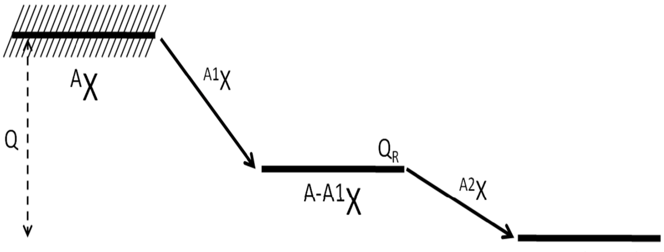

Figure 3.18: Schematic view of the sequential breakup of a broad resonance at energy Q over the channel threshold. The breakup proceeds via the emission of a ^{A1}X *fragment through an intermediate resonance at energy* Q_R *over the channel threshold.*

The case of characterizing the breakup mechanism in three body channels is more complicated. The first question one has to consider is wether the three particles are directly emitted into the three body continuum or the breakup proceeds sequentially through an intermediate resonance. In the former case, the breakup is characterized only by the sum energy of the three emitted particles, as it corresponds to the breakup Q value, the energy of the original resonance. The case of sequential breakup not only involves obtaining the Q value, but characterizing the order of emission of the different particles and the intermediate resonance. Fig. 3.18 shows schematically a level diagram of a three body breakup occurring through an intermediate resonance.

In the three body breakup case, the energy vs energy scatter plot between the two detected particles is less informative about the breakup than in the two body case. However, there is still some properties of the breakup mechanism that can be obtained from it. In general, if the three body breakup occurs directly into the continuum the shape of the scatter plot will be a featureless homogeneous distribution, delimited by the phase space restrictions. In the sequential case, one has to consider if the two detected particles were emitted from the intermediate resonance or each one in a different step of the breakup. In the former case, the sum energy of both particles corresponds to the energy of the intermediate resonance plus the energy boost from the first emitted particle. This implies the particles group along an antidiagonal line, which is the graphical representation of pairs of particles of the same sum energy. Fig 3.19 shows an example of this mechanism for the ^{11}Li β-delayed three body nα^6He channel, the breakup of the 10.6 MeV state in ^{11}Be through the ^{10}Be 9.5 MeV resonance, for 2003 data.

In the case where the two detected particles were emitted from a common resonance we can obtain the resonance energy from energy and momentum conservation. Defining $\overrightarrow{P}_{23}$ as the momentum in the center of mass system of the 2 and 3 particles, Q$_A$ (see Fig. 3.18) is obtained as [Ohl65]

$$
\begin{aligned}
Q_A &= \frac{\left|\overrightarrow{P}_{23}\right|^2}{2\mu_{23}} && (3.30)\\
\overrightarrow{P}_{23} &= \frac{\mu_{23}}{m_2}\overrightarrow{P}_2 + \frac{\mu_{23}}{m_3}\overrightarrow{P}_3 && (3.31)
\end{aligned}
$$

where $\mu_{23}=\frac{m_2 m_3}{m2+m_3}$ is the reduced mass of the 23 system.

Further information can be extracted if the full kinematics of the three emitted particles are obtained. In the particular case that concerns this work, one of the emitted particles in the three body breakup is a neutron, which is not detected in coincidence with the other two. The energy and momentum of the missing particle can be obtained from energy and momentum conservation

$$
\begin{aligned}
0 &= \overrightarrow{P}_1 + \overrightarrow{P}_2 + \overrightarrow{P}_n && (3.32)\\
\overrightarrow{P}_n &= -\left(\overrightarrow{P}_1 + \overrightarrow{P}_2\right) && (3.33)
\end{aligned}
$$

and

$$E_n = \frac{\left|\overrightarrow{P}_n\right|^2}{2m_n} \qquad (3.34)$$

However, one has to keep in mind that the precision on this calculation depends of the precision of the momentum of the two detected particles. This momentum is calculated from the energy of the particle and the hit position

$$\overrightarrow{P}_{1,2}(i) = \sqrt{2m_{1,2}E_{1,2}}\left(x^i_{1,2}\right) \qquad (3.35)$$

The error in the momentum thus depends in the pixel width as Δx^i=1.5 mm, the error in the determination of the sources distance, Δz$\approx$0.5 mm and the detectors resolution ΔE, which is around 35 keV for the DSSSD used in this experiment.

Once we have obtained the energy of the three particles involved in the breakup, we can go back to the problem of determining the breakup mechanism. As there are three particles involved, it is not enough to plot the energy of one of them against

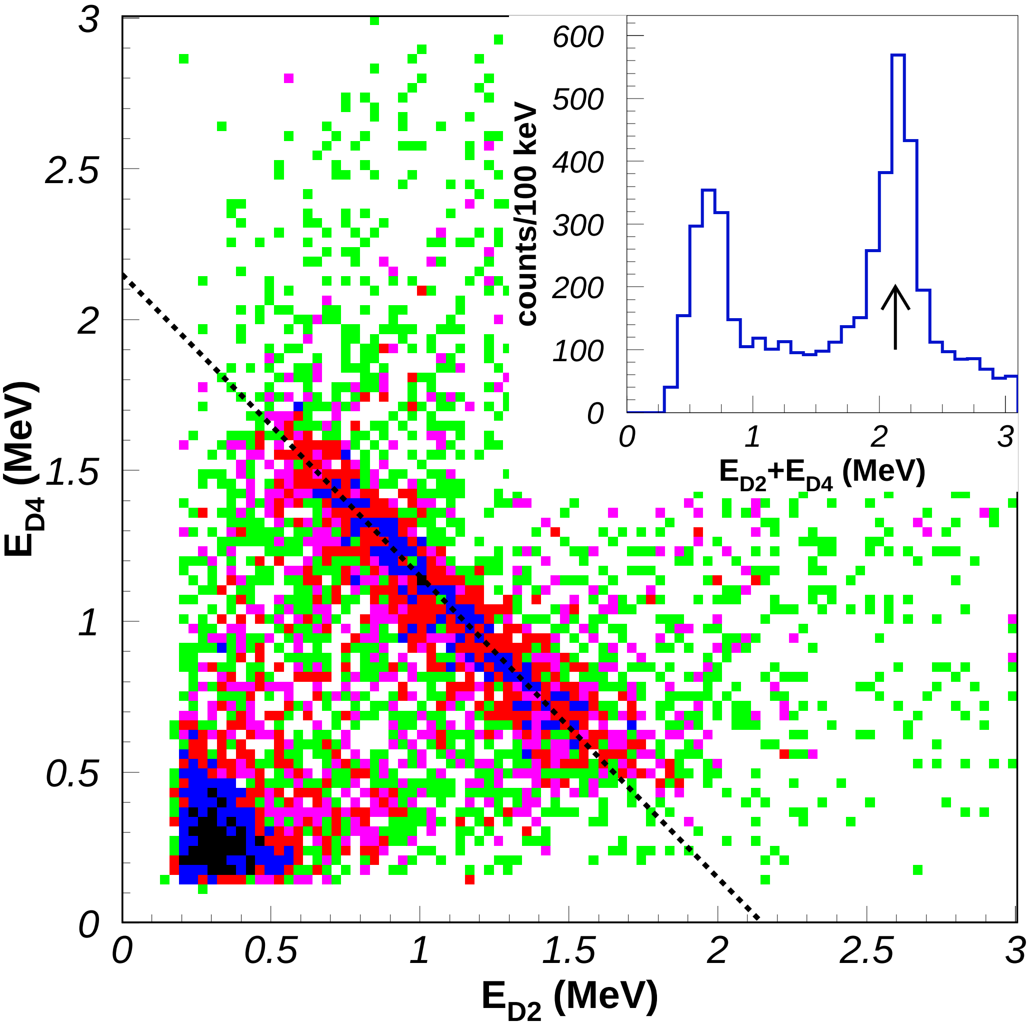

Figure 3.19: Energy versus energy scatter plot of events recorded in opposite detectors D2 and D4 in 2003 experiment. The antidiagonal line correspond to ^{6}*He+*α *events from the three body channel n*α^6*He. The antidiagonal line correspond to a fixed sum energy, as shown by the peak at 2.15 MeV in the inset (mark by the arrow). The low energy peak in the inset corresponds to the grouping of data at lower energies in the scatter plot. The lack of distinct features in this zone indicates direct breakup to the continuum, proposed to be the five body 2*α*3n channel [Lan81].*

the other. What we do instead is plotting the individual energy of each particle in the breakup against the sum energy of the three. This takes advantage of the fact that, in case of sequential decay, the first breakup is a two body process, so the first particle will be emitted with a fixed energy defined by the channel Q value and the intermediate resonance energy Q_R (see Fig. 3.18).

$$Q - Q_R = E_1 + E_{23} \tag{3.36}$$

Where E_{23} is the energy of the recoiling compound system. From momentum conservation, P_1=$P_2$3, we get

$$E_{23} = \frac{m_1}{m_{23}} E_1 \tag{3.37}$$

so the previous equation is rewritten as

$$Q = Q_R + \left(1 + \frac{m_1}{m_{23}}\right) E_1 = Q_R + \frac{M}{m_{23}} E_1 \tag{3.38}$$

where M is the mass of the initial breakup. This equation implies that for decay of broad resonances through an intermediate state of relative energy Q_R, if we plot the three particles against the total energy Q, the first emitted particle appears as a line of slope given by the ratio of the mass of the initial nucleus and the intermediate resonance and an offset determined by Q_R. Fig. 3.20 shows an example of this plot for the β-delayed two proton emission in ^{31}Ar. In this case the total energy is determined by the sum of the two emitted protons, as the energy of the recoiling ^{29}. This figure illustrates how we can selectively study the breakup mechanism. As the initial states fed in te β-decay, ^{31}O are very narrow the identification of the decay mechanism using the scatter plor is more easy to explain, but in fact itis really crucial to use it when the levels are broad, as in the case under study.

for each state in ^{31}Ar there are part of the decays occurring directly into the continuum, corresponding to the horizontal lines, and another part through an intermediate state in ^{30}S, the diagonal line.

3.3 Monte-Carlo simulations

Monte-Carlo simulations are used in this work to model the decay channels studied and link their observed kinematical properties with the properties of the resonances in the nuclei involved. As we saw in the previous section, the study of the kinematical properties of the decay is useful to determine the decay mechanism. However, a model of the breakup mechanism is needed to relate the observables, the particles energies and angular distributions, with the non-observable resonances in the involved nuclei.

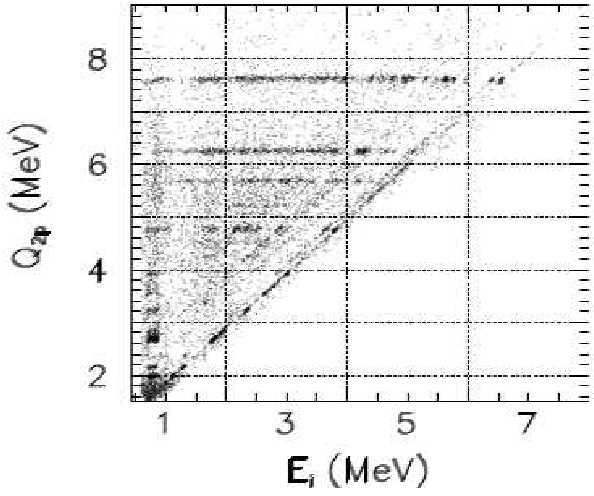

Figure 3.20: Example of a the individual energy versus sum energy spectrum used to determine the breakup mechanism of the β-delayed two proton emission of ^{31}Ar. The diagonal line corresponds to the first emitted proton through an intermediate resonance in ^{30}S, following equation 3.38. For each proton in the diagonal line there is another in the horizontal line close the y axis.

Event by event Monte-carlo simulations of the breakup were performed using the phase space integral for direct decay and the R-matrix formalism and angular correlations in the case were the breakup occur sequentially.

In the following sections I will briefly describe the phase space and R-matrix models used in this work. The phase space was necessary to describe the multiple neutron emission from states in ^{11}Be, and as basis for the "democratic" decay calculations in the breakup of the ^{9}Be $5/2^-$ 2.43 MeV state. Details on the "democratic" formalism used in the breakup of the ^{9}Be $5/2^-$ state can be found in section 4.4.2 and [Boc89, Vas89]. The R-matrix formalism was extensively used in order to describe the β-delayed sequential emission of charged particles and neutrons from states in both nuclei studied in this work, ^{9}Li and ^{11}Li. I will end with a description on the theory behind the angular correlations in sequential emission of particles.

3.3.1 The phase space

This section describes the role of the phase space integral to describe many body breakup systems, and a brief discussion on how it is calculated in the Monte-Carlo code GENBOD. For a more detailed discussion see [SS58, Kre61, Jam68].

The phase space integral was developed from a statistical approach to describe the production of multiple particles after high energy nucleon-nucleon collisions. The idea consisted in separating, in the transition probability σ, the nuclear and spin dependent interaction between the particles from the kinematic factors, in the following way

$$\sigma \propto |M_{fi}|^2 \rho_n \tag{3.39}$$

where M_{fi} is the matrix parameter that describes the interactions between the particles and ρ_n is the phase space integral of n particles. Thus, we can obtain the spectrum of any kinematic parameter f as

$$f(\alpha) = \frac{d}{d\alpha}(|M_{fi}|^2 \cdot \rho_n) \tag{3.40}$$

In this approximation, the production of particles (equivalent to the breakup into particles) is described as occurring in a small space region. The energy available results in a large number of possible final states, and each one can be arrived in a great many different ways. This circumstance suggests that statistical equilibrium will be attained, so that the system reaches a state where the n particles could be considered a gas of free particles. The importance of the phase space integral lays on the fact that it accounts not only for the kinematics of the system, but for the statistical description as well. The phase space integral, in Lorentz invariant form, is defined as

$$\rho_n = \int^{4n} \delta^4 \left(\mathbf{P} - \sum_{j=1}^{n} p_j \right) \prod_{i=1}^{n} \delta(p_i^2 - m_i^2) d^4 p_i \tag{3.41}$$

where $\mathbf{P}$ is the total four-vector of the n-body system, p_i are the four-vector of the individual particles and m_i are the masses of the particles. As mentioned above, the phase space integral contains the statistical and kinematical information of the system.

- The statistical factor is the density of states. The probability of finding an event in a given region is related with the number of available states in that region, i.e. the density of the phase space in that region. This comes into the expression in the product of $d^4 p_i$, which, with the energy conservation delta function, can be expressed in spherical coordinates as

  $$\delta(p_i^2 - m_i^2) d^4 p_i = \frac{|p_i|^2}{E_i} d|p_i| d\cos\theta_i d\phi_i \tag{3.42}$$

  where $|p_i|$ is the absolute value of the three momentum. Thus, the equation expresses the fact that the available phase space volume, the number of possible states that end up in the same final configuration, depends on the magnitude of the momentum itself.

- The kinematical factor is expressed by the delta functions that assure that momentum and energy are conserved. Of course, one in principle should include delta functions for all the known conservation laws, such as conservation of isospin, parity and angular momentum. Some of these conservation laws are implicitly taken into account, as one normally would not calculate the phase space integral for a forbidden transition.

  The angular momentum, however, poses a special problem because it leads to kinematic effects which are difficult to handle. In general the problem lays on the difficulty of finding variables that express the linear and angular momentum in a separable way. For two and three body systems the problem of angular momentum can be solved. However, for higher number of particles, the possibility of an exact solution appear hopeless and the effects of angular momentum conservation are normally included in the matrix elements, instead of the phase space integral.

Calculation of the phase space integral

Although a simple brute-force approach using the Monte-Carlo technique might be able to solve the phase space integral, it is normally impractical for a large number of particles in the final state. One normally takes advantage of recurrence relations in the Lorentz invariance form of the phase space integral. The first idea of using a recurrence relation to speed up the calculation of the phase space integral was proposed by Srivastava and Sudarshan [SS58], which allowed to calculate the phase space integral of the system of n particles depending on the system of $n-1$ particles. However, Monte-Carlo generators based on this recurrence relation are inefficient due to the fact that the components of the initial particle momentum have to be chosen randomly, which would often get momenta that violate conservation laws.

Further development by Kopylov [Kop60], and Raubold and Lynch (unpublished) defined a different recurrence relation, for a subset of particles ℓ of the total system of n particles. They start rewriting the momentum conservation delta functions in the form

$$\delta^4\left(\sum_{j=1}^{n} p_j - p\right) = \int \delta^4\left(p - p_\ell - \sum_{j=\ell+1}^{n} p_j\right) \delta^4\left(p_\ell - \sum_{j=1}^{\ell} p_\ell\right) d^4p_\ell \qquad (3.43)$$

Applying 3.43 in 3.41 we obtain

$$\rho_n(\mathbf{P}; m_1 \ldots m_n) = \int \delta^4 \left(\mathbf{P} - p_\ell - \sum_{j=\ell+1}^{n} p_j \right) \prod_{j=\ell+1}^{n} \delta(p_j^2 - m_j^2) d^4 p_j$$
$$\times \int \delta^4 \left(p_i - \sum_{j=1}^{\ell} p_\ell \right) \prod_{j=1}^{\ell} \delta(p_j^2 - m_j^2) d^4 p_j d^4 p_\ell \qquad (3.44)$$

which starts to look like the desired recurrence for a subset of ℓ particles. However, the delta function for the momentum conservation of the ℓ subsystem, $\delta(p_\ell^2 - M_\ell^2)$ is not present. We include taking into account that

$$1 = \int_0^\infty \delta(p_\ell^2 - M_\ell^2) \qquad (3.45)$$

Which gives us the desired expression

$$\rho_n(\mathbf{P}; m_1 \ldots m_n) = \int_0^\infty \int \delta^4 \left(\mathbf{P} - p_\ell - \sum_{j=\ell+1}^{n} p_j \right) \prod_{j=\ell+1}^{n} \delta(p_j^2 - m_j^2)$$
$$\times \delta(p_\ell^2 - M_\ell^2) d^4 p_j d^4 p_\ell \int \delta^4 \left(p_\ell - \sum_{j=1}^{\ell} p_j \right) \prod_{j=1}^{\ell} \delta(p_j^2 - m_j^2) d^4 p_\ell dM_\ell^2 \qquad (3.46)$$

where M_ℓ is the square of the four momentum of the ℓ particles, their invariant rest mass. The above equation can be written as the splitting relation of the n system in the subset ℓ and the remaining particles,

$$\rho_n(\mathbf{P}; m_1 \ldots m_n) = \int_0^\infty \rho_{n-\ell+1}(\mathbf{P}; M_\ell, m_{\ell+1} \ldots m_n) \rho_\ell(\mathbf{P}_\ell; m_1 \ldots m_\ell) dM_\ell^2 \qquad (3.47)$$

which can be applied repeatedly starting with ℓ=2

$$\rho_n = \int dM_{n-1}^2 \cdots \int dM_2^2 \prod_{i=1}^{n-1} R_2(M_{i+1}; m_i, m_{i+1}) \qquad (3.48)$$

and

$$\rho_2(M_{i+1}; M_i, m_{i+1}) = \frac{2\pi}{M_{i+1}} \sqrt{M_{i+1} + \left(\frac{M_i^2 - m_{i+1}^2}{M_{i+1}} \right)^2 - 2(M_i^2 + m_{i+1}^2)} \qquad (3.49)$$

Finally, the phase space integral is calculated with the Monte-Carlo method using equations 3.48 and 3.49. The limits of integration impose the possible value of the random invariant masses M_j of the Monte-Carlo. They are defined inside the available energy range

$$\sum_{i=1}^{j} m_i < M_j < M_n - \sum_{i=j+1}^{n} m_i \tag{3.50}$$

The Monte-Carlo code GENBOD [cer] (used in this work) is based on this method to calculate the momentum n particles distributed according to the phase space integral, given number of particles, the masses of the particles and the initial available energy.

3.3.2 R-matrix theory

The R-matrix theory was developed in the 1930's to describe the cross section of nuclear reactions in a simple way [Wig46]. Later, it has been adapted to a broad spectrum of applications, including obtaining cross sections of reactions of astrophysical relevance, Coulomb displacement energies and the β-delayed emission of particles. In the analysis of β-decay processes, the R-matrix method is necessary to describe known quantities such as the particles energy distribution or the total branching ratios with the parameters of the resonances involved. This approach solves the problem of describing the complicated particle spectra arising from the several decay channels present in some nuclei, such as the two nuclei studied in this work ^{9}Li and ^{11}Li, outlined above.

The R-matrix approach involves "poles", which correspond to bound states or resonances. The method is based on the assumption that we can define the interaction space in two regions:

- the internal region, where the nuclear force takes place, and where the physics of the problem is derived from the properties of the resonances;
- the external region, where only the Coulomb force remains.

The radius of the internal region is called the R-matrix radius and is denoted as a. Of course, up to the numerical accuracy the final result must be insensitive to its choice. A general prescription for $a = a_o\sqrt{A_1^{1/3} + A_2^{1/3}}$, being A_1 and A_2 the mass numbers of the two interacting nuclei (or the two fragments after breakup), and a_o is a parameter taking values between 1.4 and 1.5 fm. In the following section I will first describe the basic formulation of the R-matrix theory, in the single-channel zero-spin approximation. After, I will summarize the formalism used in the most common applications for the study of β-delayed particle emission.

General formalism

As mentioned above, we limit the formalism to the scattering (emission) of one particle in the single-channel zero-spin approximation. The generalization to multiple-channel is straightforward, and it will briefly discussed. As we are neglecting the role of spin, the wave functions are characterized by the relative angular momentum ℓ. The goal of the R-matrix method is to obtain an approximate solution of the Schrödinger equation

$$(H-E)\Psi^{\ell m}=0 \tag{3.51}$$

where $\Psi^{\ell m}$ is the two-body wave function. Let us consider a basis of wave functions

$$\phi_i^{\ell m}=\frac{u_i^\ell(r)}{r}Y_\ell^m(\Omega_r) \tag{3.52}$$

where $u_i^\ell(r)$ is the radial part of the wave function and $Y_\ell^m(\Omega_r)$ are the spherical harmonics. The radial part wavefunctions are supposed to be orthonormal over the internal region (r<a), and to have zero derivative at the surface (r=a). They are the solution of the Schrödinger equation in the internal region:

$$(H-E_i^\ell)\phi_i^{\ell m}=0 \tag{3.53}$$

where E_i^ℓ are the eigenvalues. Thus, the total wave function can be factorised as

$$\Psi^{\ell m}=\frac{g^\ell(r)}{r}Y_\ell^m(\Omega_r) \tag{3.54}$$

with

$$\begin{aligned} g^\ell(r) &= \sum_{i=1}^{N} A_i^\ell u_i^\ell(r) \text{ for } r\leq a \\ &= i^{\ell+1}(\pi(2\ell+1)/v)^{1/2}\left[I_\ell(kr)-U^\ell O_\ell(kr)\right]/k \text{ for } r>a \end{aligned} \tag{3.55}$$

where the unknown parameters are the expansion coefficients A_i^ℓ in the internal region and the collision matrix U^ℓ in the external region, the scattered wave function. The external part depends of the incoming and outgoing Coulomb functions, $I_\ell(kr)$ and $O_\ell(kr)$, which are expressed as combinations of the regular (F_ℓ) and irregular (G_ℓ) solutions of the Coulomb equation

$$\frac{d^2g_\ell}{dx^2}+\left(1-\frac{2\nu}{x}-\frac{\ell(\ell+1)}{x^2}\right)g_\ell=0 \tag{3.56}$$

where $\nu = \frac{Z_1 Z_2 e^2}{\hbar v}$ is the Sommerfeld parameter (v is the relative velocity between the particles). The incoming and outgoing functions are then

$$I_\ell(x) = O^*_\ell(x) = e^{i\omega_\ell}(G_\ell(x,\nu) - iF_\ell(x,\nu)) \tag{3.57}$$

In order to obtain the expansion coefficients A_i^ℓ we multiply 3.51 by $\phi_i^{\ell m *}$ and 3.53 by $\Psi^{\ell m *}$, and subtract both equations

$$A_i = \frac{\hbar^2}{2\mu m_N} \frac{u_i(a) g'(a)}{E_i - E} \tag{3.58}$$

where we dropped the index ℓ. In order to obtain the collision matrix we need to study the continuity of the wave function 3.55 at the surface. First, we have

$$g(r) = \frac{\hbar^2}{2\mu m_N a} \sum_i \frac{u_i(a) u_i(r)}{E_i - E} a g'(r) = G(r,a) a g'(a) \tag{3.59}$$

where $G(r,a)$ is the Green function, defined above. The R-Matrix is defined as the Green function at the surface

$$R = G(a,a) = \sum_i \frac{\tilde{\gamma}_i^2}{E_i - E} = \frac{g(a)}{a g'(a)} \tag{3.60}$$

where $\tilde{\gamma}_i^2$ is the formal reduced width, defined as

$$\tilde{\gamma}_i^2 = \left(\frac{\hbar^2}{2\mu m_N a} \right)^2 u_i^\ell(a) \tag{3.61}$$

where we see the formal reduced width depends explicitly on the internal wave functions. Besides, both the R-matrix and the reduced radius explicitly depend on the choice of the surface radius a. Equation 3.60 shows that the R-matrix is the inverse of the logarithmic derivative of the wave function 3.54 at the surface. Using 3.55 provides the collision matrix

$$U = \frac{I(ka)}{O(ka)} \frac{1 - L^* R}{1 - LR} \tag{3.62}$$

where L is a constant defined from the outgoing wave from the solutions of the Coulomb equation as

$$L_\ell = ka \frac{O'_\ell(ka)}{O_\ell(ka)} = S_\ell(ka) + iP_\ell(ka) \tag{3.63}$$

where the penetrability, P_ℓ and the, shift factor, S_ℓ, are defined from the regular and irregular solutions of the Coulomb equation, F_ℓ and G_ℓ, as

$$\begin{aligned} P_\ell(x) &= x/[F_\ell^2 + G_\ell^2(x)] && (3.64)\\ S_\ell(x) &= [F_\ell(x)F_\ell'(x) + G_\ell(x)G_\ell'(x)]P_\ell(x) && (3.65) \end{aligned}$$

where the penetrability corresponds to the transmission probability of the colliding (or emitted) particles through the Coulomb and centrifugal barriers.

With equations 3.54, 3.55 and 3.62 we can obtain the scattering cross section from the external part of the wave function

$$\sigma_{SC} = |\Psi(r)_{ext}|^2 = \frac{4\pi^2}{k^2}(2\ell+1)|1-U^\ell|^2 \tag{3.66}$$

In general the scattering cross section is a complicated expression which depends on the energies of the poles of the R-matrix, E_i, the reduced widths $\tilde{\gamma}_i^2$, and so on. Approximations are made to simplify the calculations under certain circumstances. The Breit-Wigner approach imposes that the single-channel zero-spin R-matrix close the pole energy E_i can be written as

$$R \sim \frac{\gamma_i^2}{E_i - E} \tag{3.67}$$

where γ_i is no longer a formal parameter. Instead, it is called the "observed" width of the Breit-Wigner approximation. Using 3.67 with 3.62 one can write

$$1 - U^\ell = \frac{-2iP_\ell\gamma_i^2}{(E_i - E) - \gamma_i^2 S_\ell - iP_\ell\gamma_i^2} \tag{3.68}$$

and by using 3.68 in the cross section 3.66 we obtain the classical Breit-Wigner shape

$$\sigma = \frac{4\pi^2}{k^2}(2\ell+1)\frac{\Gamma_{i\ell}}{(E_i + \Delta_\ell - E)^2 + (\Gamma_{i\ell}/2)^2} \tag{3.69}$$

where $\Gamma_{i\ell} = 2\gamma_i^2 P_\ell(E_i)$ is defined as the "observed" resonance width, $\Delta_\ell = -\gamma_i^2(S_\ell - B)$ is the shift factor, which is the relation between the "observed" resonance energy and the R-matrix poles. If the boundary condition B is chosen as $S_\ell(E_i)$ then the "observed" resonance energy will match the formal E_i.

Generalization to a multiple channel formalism is straightforward for the R-matrix

$$R = \sum_i \frac{\tilde{\gamma}_{i,\alpha}^2 \tilde{\gamma}_{i,\beta}^2}{E_i - E} \tag{3.70}$$

where $\tilde{\gamma}_{i,\alpha}$ and $\tilde{\gamma}_{i,\beta}$ are the reduced widths of pole i in channels α and β respectively. Obtaining the cross section for multiple interfering levels, however, is not as simple, and it will discussed in detailed only in the β-delayed particle emission in the next section.

Application to the β-delayed particle emission

The R-matrix theory described in the previous section provides all the necessary tools to describe the particle emission following β-decay. The formalism is adapted to describe the β-decay by matching the cross section probability in the R-Matrix reaction fomalism to the β-decay transition probability. This implies that the regular transition strength, eq 1.27, can no longer be used to describe the transition strength. Instead the more general equation is defined as [BW88]

$$w = \int w(E)dE \tag{3.71}$$

where the differential probability distribution is given by the summation over the transition probability in each decay channel, $w_c(E)$,

$$w(E) = \sum_c w_c(E) \tag{3.72}$$

Each decay channel is defined by the final state products, which will define a unique penetrability. The most general formalism of the transition probability in a given decay channel is

$$w_c(E) = Cf_\beta P_c \sum_{x=F,GT} \left| \sum_{\lambda\mu} g_{\lambda x}\gamma_{\mu c}A_{\lambda\mu} \right|^2 \tag{3.73}$$

where λ and μ indicate all possible resonances fed in the β-decay and participating in channel c. The constants $C = \frac{ln2}{D}$ and f_β, the Fermi factor and $g_{\lambda F,GT}$ are implemented so that the integral transition probaility, w, matches the β-decay probability $\lambda = \frac{ln2}{t_{1/2}}$. Thus, the resonance constants can be expressed as

$$(g_\lambda^F)^2 = \mathrm{B_F}, \qquad (g_\lambda^{GT})^2 = \left(\frac{g_A}{g_V}\right)^2 \mathrm{B_{GT}} \tag{3.74}$$

The pentrability P_c and the channel reduced with $\gamma_{\mu c}$ are defined in the regular R-Matrix formalism. The matrix elements $A_{\lambda\mu}$ are defined by their inverse [BW88]

$$(A^{-1})_{\lambda\mu} = (E_\lambda - E)\delta_{\lambda\mu} - \sum_c (S_c - B_c + iP_c)\gamma_{\lambda c}\gamma_{\mu c} \tag{3.75}$$

where E_λ is the resonances eigenenergies, S_c, B_c and P_c are the channels shift factor, boundary condition and penetrability as defined in regular R-matrix theory, and $\gamma_{\lambda,\mu c}$ are the resonances reduced widths. The summatory is again over the possible decay

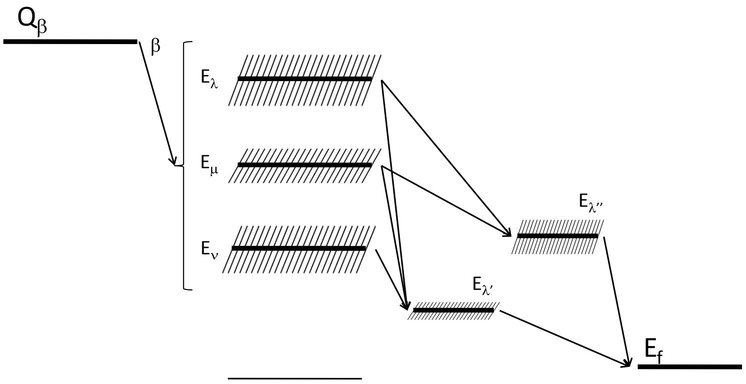

Figure 3.21: Schematic view of multiple broad levels being fed in the β-decay and decaying through several resonances into a final state. In this case the most general multiple level multiple channel formalism will be used to describe the decay probability.

channels c. This formalism is absolutely general, and describes the feeding of several resonances decaying through several decay channels, with interferences between the resonances in the same decay channel and the same spin and parity (see Fig. 3.21). However, this formalism is generally complicated to implement in a Monte-Carlo simulation due to the high number of free parameters which have to be fit.

In order to simplify the formalism a single level approximation is normally used, is a similar fashion to the reaction R-Matrix formalism. This approximation implies that the resonances are at enough energy from each other to make the effect of interferences negligible. In this work two variation of the single level approximation were used

- Single level, single channel.
- Single level, multiple channel

Single level, single channel R-matrix formalism

In this case each resonance is studied independently and decays through a single channel of fixed energy E_f (see Fig. 3.22). In this case, and assuming no Fermi transition (g_λ^F=0) equation 3.73 can be rewritten as

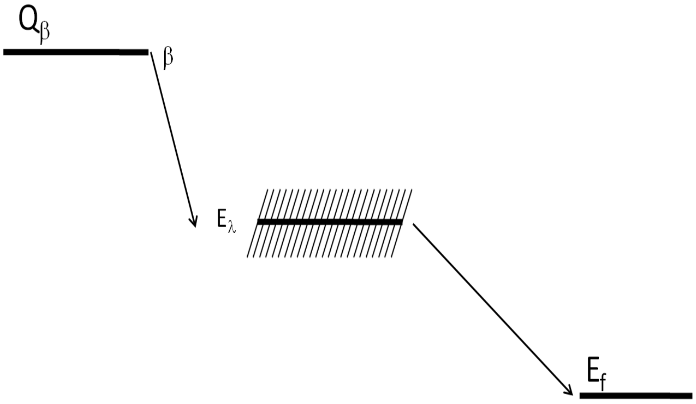

Figure 3.22: Schematic picture of the feeding of a single level decaying in a single channel of fixed energy E_f.

$$w(E) = Cf_\beta P_c(E-E_f)\frac{\left|g_\lambda^F\gamma_{\lambda c}/(E_{\lambda c}-E)^2\right|^2+\left|g_\lambda^{GT}\gamma_{\lambda c}/(E_{\lambda c}-E)^2\right|^2}{\left|1-\{S_c(E-E_f)-B_c+iP_c(E-E_f)\}\{\gamma_{\lambda c}^2/(E_{\lambda c}-E)\}\right|^2} \tag{3.76}$$

where C is defined as in the previous section, and the index c refers to the decay channel. In this case there is no Fermi feeding the equation can be rewritten as a simple Breit-Wigner form

$$w(E) = Cf_\beta\frac{g_{\lambda c}^{GT}P_c(E-E_f)\gamma_{\lambda c}^2}{(E_{\lambda c}+\Delta_{\lambda c}(E)-E)^2+\Gamma_{\lambda c}^2(E)/4} \tag{3.77}$$

where $\Gamma_{\lambda c}$ and $\Delta_{\lambda c}$ are defined as in the R-matrix single level case shown in the previous section

$$\Gamma_{\lambda c}(E) = 2P_c(E-E_f)\gamma_{\lambda c}^2, \qquad \Delta_{\lambda c}(E) = -(S_c(E-E_f)-B_c)\gamma_{\lambda c}^2 \tag{3.78}$$

Thus, in Fig. 3.22, the energy distribution of the particles emitted from the intermediate resonance E$_\lambda$ is given by equation 3.77, where the width of the state is defined as follows

$$\Gamma = 2P_c(E_{\lambda c}-E_f)\gamma_{\lambda c}^2 \tag{3.79}$$

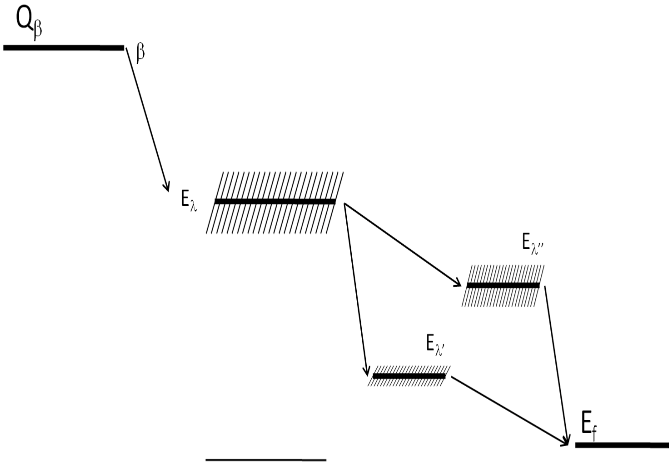

Figure 3.23: Schematic picture of a sequential two-step particle emission. The β precursor feeds a single level in the daughter nuclei which has two decay channels open, each one consists of a broad resonance which emits particles into the final state of energy E_f. The single level multiple channel R-matrix formalism will be used in this case to describe the decay probability.

It is interesting to note that both the penetration factor, $P_c(E - E_f)$, and the Fermi function modify the tranistion probability from a pure Breit-Wigner shape. Specially, the Fermi factor is responsible for the appearance of tails extending to low energies in broad resonances close to the Q$_\beta$ value.

Single level, multiple channel R-matrix formalism

This case is characterized by the β-feeding of a resonance that subsequently decays through several resonances which are unbound themselves, emitting a second particle (see Fig. 3.23). The formalism for β-decay proposed in [Nym90] is based in the simplest, Breit-Wigner like, single level multiple channel R-matrix formalism [LT58].

$$w(E, E') = C f_\beta \sum_c \frac{g^{GT}_{\lambda c} P_c(E - E') \gamma^2_{\lambda c}(E')}{(E_{\lambda c} + \Delta_{\lambda c}(E) - E)^2 + \Gamma^2_{\lambda c}(E)/4} \tag{3.80}$$

where the reduced width is no longer a constant but explicitly depends on the energy E' in the intermediate resonance

$$\gamma^2_{\lambda c}(E') = \gamma^2_{\lambda c} \frac{g^{GT}_{\lambda' c} P_c(E' - E_{fc}) \gamma^2_{\lambda' c}}{(E_{\lambda' c} + \Delta_{\lambda' c}(E') - E')^2 + \Gamma^2_{\lambda' c}(E')/4} \tag{3.81}$$

where $\gamma^2_{\lambda c}$ is the regular reduced width of resonance λ, and the shift factor $\Delta_{\lambda' c}(E)$

and the penetrability $P_{\lambda' c}(E' - E_{fc})$ are defined in the usual way. Thus the expressions of the shift function and penetration factor in equation 3.80 are modified by the energy dependence of the reduced width

$$\begin{aligned}\Delta_{\lambda c}(E) &= -\sum_c \int dE(S_c(E - E') - B_c)\gamma^2_{\lambda c}(E') &(3.82)\\ \Gamma_{\lambda c}(E) &= 2\sum_c \int dE' P_{\lambda c}(E - E')\gamma^2_{\lambda c}(E') &(3.83)\end{aligned}$$

From equation 3.81 we see that the second step resonances in Fig. 3.23 follow the same formalism that in the case of the single level single channel formalism, where the width of the resonance is defined from the penetrability. Therefore the particles emitted from this intermediate resonances wil have a similar distribution. However, the particles emitted from the first resonance follow equation 3.80, which explicitly depends on the energy of the second resonance. Thus the width of the resonance E_λ follows the more complicated expression found in equation 3.83.

3.3.3 Angular correlations

Both in the measurement of γ-γ and particle-particle coincidences a correlation between their relative directions of propagation has been experimentally observed. This is a purely quantum mechanical effect. If only one radiation is considered, then the emitted radiation is isotropic, as no direction in space has been singled out. In particular, each magnetic substate of the nucleus emits anisotropically but summing over the substates of equal populations and random relative phases, so that the sum is incoherent, the total intensity is independent of the angle. However, if two subsequent radiations are considered and the angular distribution of of one radiation is observed when the other has a fixed direction defines a direction in space. This effectively makes the propagation vector a projection operator that gives different weights to the various substates. thus, the radiation subsequently emitted will not be isotropic.

The simplest case of angular correlations that can be measured involves the coincidence rate of two nuclear radiation that were emitted in cascade as a function of the angle between them. In this case the information obtainable from this measurement is the angular momenta of the levels and radiations involved.

The following section contains a brief summary of the formalism of angular correlations used in the analysis presented in this work. More information can be found in [BR53]. Biedenharn and Rose show [BR53] that the general probability of observing a certain angle θ between the two radiation is

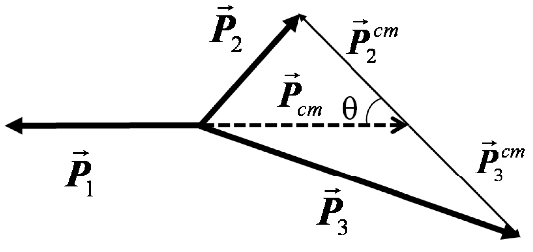

Figure 3.24: Scheme of a sequential three body breakup process, such as those studied in this work. In this case, the angular correlation are observed in the distribution of the angle θ between the direction of propagation of particles 2 and 3 in their reference frame and the direccction of propagation of the first emitted particle.

$$W(\cos\theta) = \sum_{\nu=0}^{\nu_{max}} A_\nu P_\nu(\cos\theta) \tag{3.84}$$

where $P_\nu(\cos\theta)$ is the Legendre polinomia of order ν and A_ν are the correlation coefficients. The value of the A_ν coefficients is determined by the angular momenta of the levels and radiations involved as it will be shown later in this section.

In this work we are interested in sequential multiple particle processes, which involve three particles in the final state (see Fig. 3.24). This implies that the angle θ is not defined simply as the angle between the two detected particles, but as the angle between the first emitted particle and the direction of the two remaining particles in center of mass of the intermediate system.

The step particle emission process is schematically described in Fig. 3.25, where we define j_1, j and j_2 as the spin of the initial, intermediate and final state respectively, and l_1 and l_2 the orbital angular momenta of the emitted particles. The full decay process can be written as $j_1(l_1)j(l_2)j_2$. Of course, angular mometum conservation implies

$$|j_1 - j| \leq l_1 + s_1, \qquad |j_2 - j| \leq l_2 + s_2 \tag{3.85}$$

$$j_1 + j \geq l_1 + s_1, \qquad j_2 + j \geq l_2 + s_2 \tag{3.86}$$

The maximum number of angular correlation coefficients that are involved in a given transition, ν_{max}, is determined by the “triangular conditions” in the Racah coefficients, as they impose

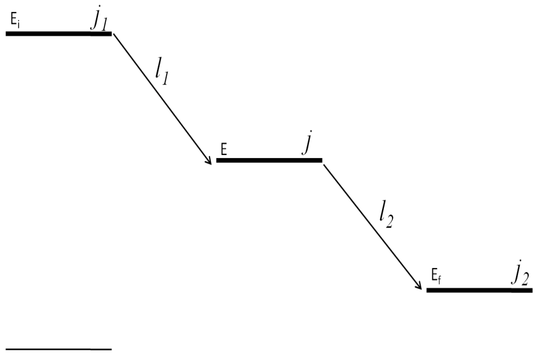

Figure 3.25: General picture of the level scheme associated to the two step process shown in Fig. 3.24. The intial state of angular momentum j_1 emitts a particle of orbital angular momentum l_1 decaying to the intermediate state of angular momentum j. This state decays itself into a final state of angular momentum j_2 by emitting particles of relative orbital angular momentum l_2.

$$\begin{aligned} 0 &\leq \nu_{max} \leq && 2j \\ 0 &\leq \nu_{max} \leq && 2(l_1)_{max} \\ 0 &\leq \nu_{max} \leq && 2(l_2)_{max} \end{aligned} \tag{3.87}$$

where j in the first equation is substituted by $j-1/2$ if j is half integer. One has to take into account that parity conservation and for measurements of non-polarized radiation only even A_ν contribute. Measuring spin 1/2 polarized particles would break the simmetry between right and left-haded reference frames, and then odd A_ν coefficients would have to be used. Finally, if the angular momentum of the intermediate state, j, is equal to 0 or 1/2, or one of the radiation is emitted with $l=0$ (s-wave), then ν_{max}=0, and given that A_0=1, the emission is isotropic.

One has to take into account that equation 3.84 is valid only when the radiations are emitted with single orbital angular momenta l_1 and l_2. In the more general case were the first emitted radiation is a mixture of two orbital angular momenta l_1 and l_2', and the second is just l_2, equation 3.84 can be generalized to

$$W = w_I + \delta^2 w_{II} + 2\delta w_{III} \tag{3.88}$$

where δ is the ratio of the matrix element of the transition of l_1' to the transition of l_1, and

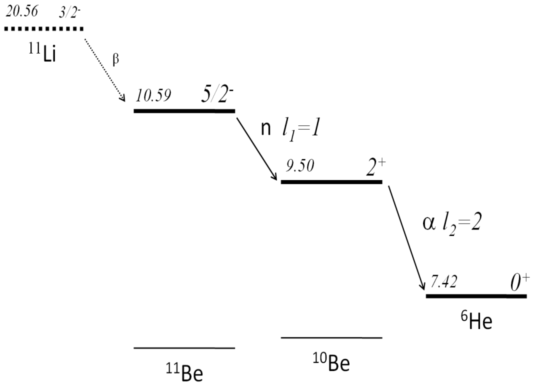

Figure 3.26: Level scheme of the ^{11}Li β-delayed neutron emission from the 10.59 MeV state in ^{11}Be. Energies and spins are taken from [Ajz78, Til04].

$$
\begin{aligned}
w_{I,II} &= \sum_{\nu=0}^{\nu_{max}} A_\nu(\{l_1, l_1'\}, l_2) P_\nu(\cos\theta) && (3.89)\\
w_{III} &= (-1)^{j-j_1-1}[(2j+1)(2l_1+1)(2l_1'+1)]^{1/2} && (3.90)\\
&\quad \times \sum_{\nu} G_\nu(l_1 l_1' j_1 j) F_\nu l_2 j_2 j) P_\nu(\cos\theta)
\end{aligned}
$$

where the coefficients G_ν and F_ν are tabulated in [BR53]. As $l_1' = l_1 + 2$, the angular momentum barrier will make the ratio δ a very small parameter, so the contribution of the higher otbital momentum can be neglected.

In the following sub-sections the calculation of the correlation parameters for the two most relevant cases in this work will be revised:

- The first emitted particle is a nucleon, of spin 1/2. The other two particles have spin zero.
- One of the second emitted particles is a nucleon, of spin 1/2.

The first emitted particle is a nucleon

In this section we discuss the neutron emission from states in ^{11}Be to an intermediate resonance in ^{10}Be. The decay shown in Fig. 3.26 corresponds to the neutron emission from the 10.59 MeV $5/2^-$ state in ^{11}Be [Hir05] through a 2^+ state in ^{10}Be that breaks up in ^{6}He+α.

This sets j_1 to $5/2^-$, j to 2 and j_2 to 0. From equations 3.85,3.86 we see that l_1 can be either 1 or 3, odd to change parity, and l_2 can only be 2. As mentioned above the contribution of l_1=3 is very small and can be neglected.

However, as the particle emitted in the first step carries spin, the angular momentum of the initial state, j_1, does not correspond to the decay channel spin. In this case one has to use the channel spin defined as the sum of the spin of the emitted particle, i, and the initial state angular momentum, $s = j_1 + i$ [BAR51, BR53]. In the ^{11}Be neutron emission case we are studying this implies there are two channels open, $s = 2$ and $s = 3$. The angular correlations in this case will hae to be calculated as the incoherent sum of both spin channels, weighted according to the relative probability for their occurrence.

The maximum index of the angular correlation coefficients, A_ν, is determined for both spin channels by equations 3.87, which is l_1=1 as we neglected $l_1 = 3$. thus we obtain ν_{max}=2. As mentioned above, for non-polarized measurements only even terms contribute, meaning we need to use A_2 and A_4.

The A_ν terms can be calculated using the prescription given by Biedenharn and Rose [BR53]

$$A_\nu = F_\nu(l_1 s j) b_\nu(l_1 l_1) F_\nu(l_1 j_2 j) b_\nu(l_2 l_2) \tag{3.91}$$

where the F_ν coefficients depend on the angular momentum coupling coefficients and the Racah coeffcents. The values of the F_ν coeffcients for even ν index are tabulated in [BR53]. Finally the b_ν coefficients are

$$b_\nu(ll) = \frac{2l(l+1)}{2l(l+1) - \nu(\nu+1)} \tag{3.92}$$

Finally, we can calculate the A_2 coefficient for both spin channels

- **i) Spin channel s=2, 2(1)2(2)0**:
  $A_2 = F_2(122) b_2(11) F_2(202) b_2(22)$, Whith $F_2(122)$=-0.418, $b_2(11)$=-2, $F_2(202)$=-0.597 and $b_2(22)$=2 from [BR53].

$$\boldsymbol{A_2 = -1} \tag{3.93}$$

- **ii) Spin channel s=3, 3(1)2(2)0**:
  $A_2 = F_2(132) b_2(11) F_2(202) b_2(22)$, Whith $F_2(132)$=0.119, $b_2(11)$=-2, $F_2(202)$=-0.597 and $b_2(22)$=2 from [BR53].

$$\boldsymbol{A_2 = 0.287} \tag{3.94}$$

One of the second emitted particles is a nucleon

In this section we discuss the example of the α emission from states in ^{11}Be (fed in the ^{11}Li β-decay) to the intermediate ^{7}He resonance, wich decays into ^{6}He+n (see Fig. 3.27). In this case the selection rules of Gamow-Teller β-decay of ^{11}Li impose

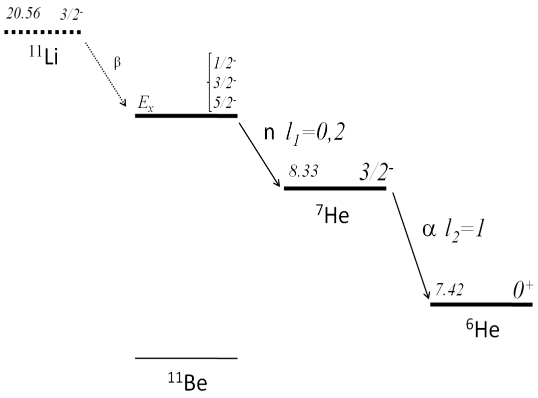

Figure 3.27: Level scheme of the ^{11}Li β-delayed alpha emission from excited states in ^{11}Be. The Gamow-Teller selection rules impose that only 1/2$^-$, 3/2$^-$ and 5/2$^-$ states are populated. Energies and spins are taken from [Ajz78, Til04].

that the states fed in ^{11}Be can have angular momentum j_1=1/2, 3/2 and 5/2, the ground state of the ^{7}He resonance is $j_2 = 3/2$ and the outgoing channel spin is determined in the same way as in the previous section s$_2$=$j_2 + i_2$, where the ground state of ^{6}He is $j_2 = 0$ and the spin of the neutron is $i_2 = 1/2$. In this particular case the only spin channel available is s=1/2, but if more than one is open we should procceed as in the previous section by incoherently adding them.

We are explicitly leaving the angular momentum of the initial state open becouse the angular correlation distribution is going to be used to determine the angular momentum of high energy states in ^{11}Be, thus all three possibilities have to be taken into account.

- **i) j_1=1/2$^-$**:
  As $j_1 = 1/2^-$ and j=3/2$^-$, using equations 3.85,3.86, we obtain orbital angular momenta $l_1 = 2$, no parity change, and $l_2 = 1$. Using equations 3.87 we obtain ν_{max}=2. Therefore

  $$A_2 = F_2(2\frac{1}{2}\frac{1}{2})b_2(22)F_2(1\frac{1}{2}32)b_2(11) \tag{3.95}$$

  with $F_2(2\frac{1}{2}\frac{3}{2})$=-0.5, $b_2(22)$=2, $F_2(1\frac{1}{2}32)$=0.5 and $b_2(11)$=-2 from [BR53].

  $$\boldsymbol{A_2 = -1} \tag{3.96}$$

- **i) j_1=3/2$^-$**:
  In the second possible angular momentum in ^{11}Be, $j_1 = 3/2^-$ and j=3/2$^-$. Thus, using equations 3.85,3.86, we obtain orbital angular momenta $l_1 = 0, 2$,

no parity change, and $l_2 = 1$. We discard the contribution of the $l_1 = 2$ component, as it will be much smaller thant the l_1=0 due to the angular momentum barrier. As the first emitted alpha has a minimum orbital angular momentum l_1=0, this implies ν_{max}=0. Therefore the emission is isotropic and:

$$\boldsymbol{A_2 = 0} \tag{3.97}$$

- **i) $\boldsymbol{j_1}$=5/2$^-$**:
  In the last case, $j_1 = 5/2^-$ and j=3/2$^-$, and using equations 3.85,3.86, the orbital angular momenta are $l_1 = 2, 4$, no parity change, and $l_2 = 1$.This gives us, using equations 3.87, ν_{max}=2. Therefore

$$A_2 = F_2(2\frac{5}{2}\frac{3}{2})b_2(22)F_2(1\frac{1}{2}32)b_2(11) \tag{3.98}$$

with $F_2(2\frac{5}{2}\frac{3}{2})$=0.357, $b_2(22)$=2, $F_2(1\frac{1}{2}32)$=0.5 and $b_2(11)$=-2 from [BR53].

$$\boldsymbol{A_2 = -0.714} \tag{3.99}$$

Chapter 4

Study of the ^{9}Li β-delayed multiple particle emission from the 2.43 MeV state in ^{9}Be

4.1 Introduction

This chapter presents the study of the ^{9}Li β-delayed particle emission from the 2.43 MeV $5/2^{-}$ state in ^{9}Be. The charged particles and neutrons were measured by Double Sided Silicon Strip Detectors and the time of flight neutron detector TONNERRE, respectively.

The multiple particle emission following the β-decay of ^{9}Li is a classical example of three body breakup. The daughter nucleus ^{9}Be, α-α-n is a borromean system, that is, in case one of the particles is removed none of the possible combinations of the remaining two, ^{5}He or ^{8}Be, are bound. Previous studies of the ^{9}Li β-decay indicate that 50% of the β-feeding goes to excited states in ^{9}Be, all of them are above the particle emission threshold. As the three body breakup mechanism will determine the energy distribution of the measured particles, establishing the breakup path is fundamental to properly understand the energy spectrum and calculate the β branching ratios. It has been determined that most of the excited states in ^{9}Be decay sequentially through intermediate resonances in ^{8}Be and ^{5}He. The study of the breakup properties, energy distribution and angular correlations, allowed for the determination of the energies, branching ratios and spins of several high excited states in ^{9}Be. There is however the case of the more controversial breakup of the ^{9}Be $5/2^{-}$ state at 2.43 MeV. This state is located roughly at the same energy as the α particle emission threshold, S_{α}=2460(50) keV [AWT03], and below the first excited state in ^{8}Be (E_{x}=4790(10) keV, Γ=1513(15) keV [Til04]) and the ground state of ^{5}He (E_{x}=2460(50) keV, Γ=578 keV [Til04, AWT03]), both wide resonances.

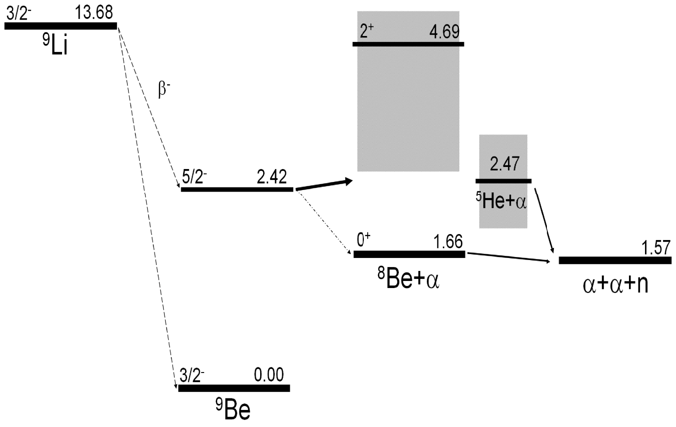

Figure 4.1: Schematic view of the possible sequential breakup channels of the 2.43 MeV ^{9}*Be state. The energies are taken from [Til04, AWT03].*

In this situation the distinction between sequential decay and direct decay becomes less clear.

The aim of the work presented in this chapter is to address the breakup mechanism of the ^{8}Be 2.43 MeV state using a highly segmented coincidence setup, with neutron detection in coincidence provided by the time-of-flight detector TONNERRE.

4.2 Summary of the experiment and goals

The β-delayed particle emission of ^{9}Li has been extensively studied previously [Lan81, Nym90, Pre03, Pre05], allowing for the determination of the breakup mechanism [Nym90, Pre03, Pre05], branching ratios [Nym90, Pre03, Pre05] and spin [Pre05] of the states in ^{11}Be fed in the β-decay of ^{9}Li, except for the breakup mechanism of the 2.43 MeV $5/2^{-}$ state. The 2.43 MeV state is close to both the ground state of ^{5}He, E_x=2460(50 keV and Γ=578 keV [Til04], and not far from the very broad, Γ=1513(15) keV [Til04], first excited state of ^{8}Be, E_x=4790(10) keV and Γ=1513(15) keV [Til04]. As the energy separation between the ^{9}Be state and the two possible intermediate resonances is similar to the width of these resonances, the distinction between sequential decay and direct decay becomes less clear. This makes the breakup mechanism of the 2.43 MeV ^{11}Be state still a controversial subject in the literature.

The first experimental and theoretical efforts to understand the breakup mechanism by Bochkarev et al. [Boc89] and Vasil'ev et al. [Vas89] used a direct decay

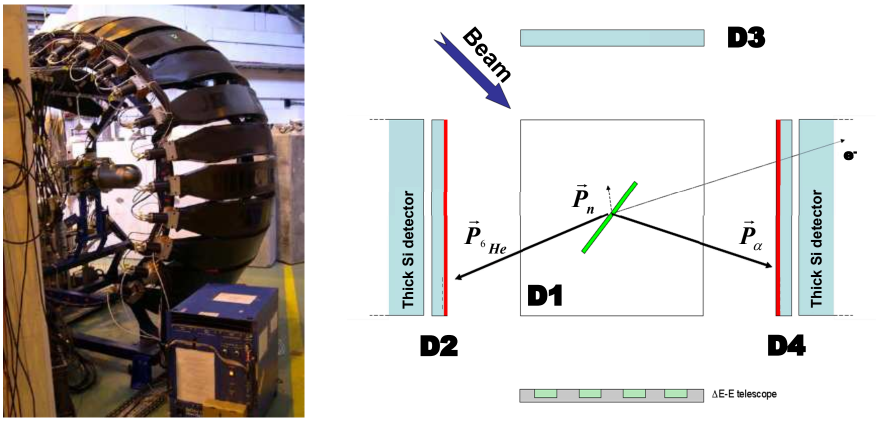

Figure 4.2: Left: photograph of the detector array TONNERRE surrounding the 2003 experimental setup at the ISOLDE hall. The vacuum chamber was the cone-shaped aluminum tube at the end of the beamline, seen at the middle of the picture. Right: Schematical view of the relative positions of the particle telescopes in 2003 experiment. Detector D1 is placed on the surface of the page. The ΔE-E telescope in the bottom is an experimental monolithic solid state telescope, which was placed for testing purposes More information on this type of detector can be found in Amorini et al [Amo08].

approach named "democratic decay", based in the conservation of the total angular momentum after the breakup. The measured alpha singles spectrum was well reproduced by the"democratic" model with a contribution of 20% of breakup through the ground state of ^{8}Be. This picture of the direct breakup of the ^{9}Be is supported by an S-matrix analysis by Grigorenko and Zhukov [GZ05] and the study of ^{9}Be structure and breakup modes using a three body n-n-α model by Alvarez-Rodriguez et al. [Alv08]. The sequential decay model is supported by a recent experiment [Pap07], studied the breakup of the 2.43 MeV state with a highly segmented setup to measure alpha-alpha coincidences and study the kinematics and the angular correlations in the breakup. They propose that the breakup occurs mainly through the first excited state of ^{8}Be, $86.5^{+4.5}_{-2.0}$%, with a contribution of the ground state of ^{8}Be, 11(2)%. This results are in line of the theortical calculations by Descouvemont [Des01], predicting contributions of 92.7% and 0.8% from the the ^{8}Be 2^+ and ground states respectively.

In this thesis work I present the results of a study of the ^{9}Li β-delayed charged particle emission. The 30 keV ^{9}Li ions were implanted in a 60 μg/cm^2 carbon foil, in order to measure the decay at rest. We used a highly segmented setup for charged particle coincidences consisting of four DSSSD's and the neutron time-of-flight detector TONNERRE for neutron detection (see Fig. 4.2). The setup allowed for the coincidence measurement of the two alphas and of alpha particles with neutrons. For more details on the setup see Chapter 2.

The goal of this study was to determine the breakup mechanism of the ^{9}Be 2.43 MeV $5/2^-$ state. Our approach consisted in the determination of the ^{9}Be 2.43 MeV state energy spectrum in both singles, α-α and n-α coincidence measurements, and the comparison of those spectra with Monte-Carlo simulations of the breakup. The two models used are: sequential breakup through either the first excited state of ^{8}Be or the ground state and/or the ground state of ^{5}He; "democratic decay" as described in the works of Bochkarev et al. [Boc89] and Vasil'ev et al. [Vas89]. Thus, the analysis can be divided in the following steps

- Singles spectrum: The first step is the study of the alpha spectrum recorded in each DSSSD without imposing any condition in the others. Because of the proximity of the ^{9}Be 2.43 MeV state to the charged particle thresholds, most of the alphas from its breakup will be emitted at low energies. Thus, the determination of the efficiency of the detectors at low energies is crucial to have a reliable spectrum.

- α-α coincidence spectrum: Measuring the two emitted alphas in coincidence, and recontructing the neutron energy, allows for the determination of breakup Q value, which corresponds to the the excitation energy of the ^{9}Be state fed in the β-decay. This allows to select events corresponding to the breakup of the ^{9}Be state, of interest in order to obtain a much cleaner energy spectrum.

- α-n coincidence spectrum: We measured the ^{9}Li β-delayed neutron time-of-flight spectrum. By imposing a coincidence with an alpha particle detected in one of the DSSSD's, we were able to select the neutrons emitted exclusively in the breakup of the ^{9}Be 2.43 MeV state.

- Simulations: We performed a Monte-Carlo simulation of the breakup of the ^{9}Be 2.43 MeV state that included both the kinematics of the breakup and the geometrical constrains and the efficiency of the experimental setup. Two models of the breakup were contemplated, sequential through a resonance in either ^{8}Be or ^{5}He, and direct decay following the "democratic decay" model. Both simulations were compared to the singles, α-α and α-n spectra mentioned before.

4.3 Analysis

In this section I discuss the method and conditions used to obtain the alpha and neutron energy spectra of the breakup of the ^{9}Be 2.43 MeV state. All measurements

Table 4.1: Thickness, deadlayer and low energy cut offs for the DSSSD detectors used in the analysis of ^{9}*Li* β*-delayed charged particle emission*

Detector	Thickness (μm)	Deadlayer (nm)	Low energy cut off (keV)
D2	60	100	159.4
D3	60	630	167.8
D4	60	100	285.5

were performed without any restriction on time after proton impact on the target. As ^{9}Be is a β-stable nuclei, thus there is no daughter decay contamination. All the alpha spectra are corrected for energy losses in the carbon-foil and the detector dead-layers as described in Chapter 3.

4.3.1 Study of the singles spectra

We start the analysis by looking at the alpha spectrum recorded in the DSSSD's without any coincidence condition. All data in the experiment were recorded in coincident mode, with a common trigger consisting of the four DSSSD's triggers combined using a logical OR. This implies that detectors were self-triggered in the majority of the events, thus the spectrum will be close to a real singles spectrum except for the possible cut-off of the time signal of the detector at low energy due to noise.

Figure 4.3 shows the "quasi"-singles specta for detectors D2, D3 and D4 in 2003 experiment. At high energies the spectra overlap, but at lower energies the differences in the detectors thresholds are appreciable. As the threshold for DSSSD D2 is lower than the thresholds of the other two detectors, we chose D2 for the singles study. The thickness, deadlayer and low energy cuts of the detectors are shown in Table 4.1

The most noticeable feature of the spectrum is the low energy peak at $\sim$ 270 keV, which corresponds to the break-up of the ^{9}Be 2.43 MeV state [Lan81, Nym90]. The "singles" spectrum of D2 in Fig. 4.3 is comparable with the previously published in [Lan81, Nym90, Pre05], although in the case of the singles obtained by Langevin et al. [Lan81], they do not show the low energy peak due to the high β-background at low energies. The singles spectrum from [Pre05], shown Figure 4.4, is similar our "singles" in Fig. 4.3 as it was obtained using a DSSSD detector similar to those used in the experiment presented in this work.

As we are interested in the analysis of the $\sim$270 keV peak, it is important to carefully verify the low energy efficiency of the detector. The response of our detector to low energy alphas was checked by comparing our spectra with the singles energy

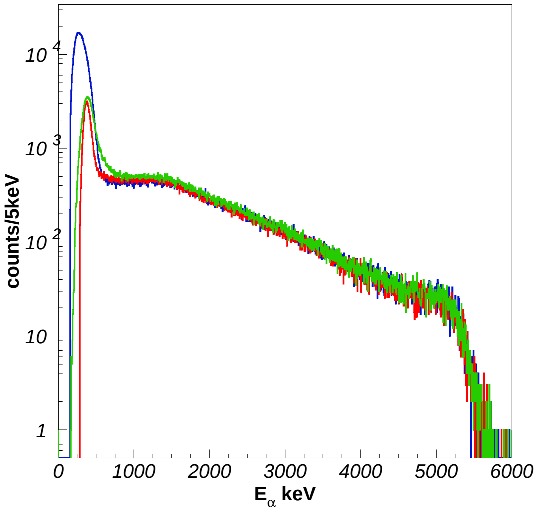

Figure 4.3: The figure shows the "quasi"-singles energy spectrum of the Double Sided Silicon Strip Detectors: D2 spectrum displayed in blue line, D3 spectrum in green line and D4 spectrum in red line. Although the spectra agree well at high energies, the different detection thresholds become apparent at lower energies. The peak corresponds to α particles emitted in the decay of the ^{9}Be 2.43 MeV state.

spectrum measured in a previous experiment with a Si surface barrier detector.

Low energy response of the DSSSD's

In general the charged particle efficiency of a Si detector is 100% above a certain threshold, which is mainly determined by the physical response of the electronics to low voltage pulses. In dedicated low energy experiments, one normally would use a pulse generator to determine the response of the system as the energy decreases (*e.g.* [Raa08], the efficiency was observed to vary from 75% at 200 keV to 100% at 300 keV). Another way of estimating the low energy efficiency is to obtain the singles ^{9}Li β-delayed α-spectrum with a detector whose response at low energies is well known.

In a previous experiment in 2002, a Si surface barrier detector, 40 μm thick and 100 mm^2 area, was mounted 16 cm away from the carbon-foil (to avoid beta summing). Fig. 4.5 shows the α energy spectrum recorded in the 40 μm thick detector. The inset shows a zoom to the first 1000 keV. The tail of the electronic noise can be observed at the low end of the spectrum. If we want to compare the spectrum from D2 detector to the singles from the 40 μm we need to subtract the noise. We fitted the tail to a linear and a exponential function, as shown in the

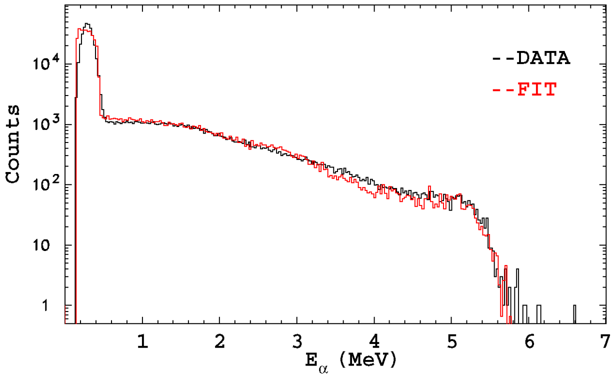

Figure 4.4: Singles spectrum taken from [Pre05]. The Monte-Carlo simulation of the breakup of the different states in ^{9}Be is shown in red. The low energy ∼300 keV peak corresponds to the breakup of the 2.43 MeV state, which was modeled using the same "democratic" decay model of direct breakup presented in this work. Therefore, the simulation of the peak is similar to that shown in Fig. 4.17(a)

inset of Fig. 4.5. In general one expects the noise to decrease exponentially with the energy, thus we anticipate that the exponential fit will better reproduce the actual shape of the noise.

The fits of the noise were subtracted from the 40μm thick detector α spectrum in order to compare them with the D2 α energy spectrum. Fig. 4.6 shows the α spectrum recorded in D2 compared to the singles α spectrum, and the inset displays the first 1000 keV of the spectrum with the noise subtracted with both the linear and exponential fit. The "quasi"-singles recorded in D2 compares well with the 40 μm detector singles. Moreover, the centroid energy and low energy threshold of the D2 energy spectrum (shown in the inset) are close to the ones observed in the singles spectrum once the exponential noise is subtracted, as anticipated. We are confident that we can use the α spectrum recorded in D2 and compare it with simulations of the breakup.

4.3.2 Study of α-α coincidences

By measuring the energy and impinging position of the two emitted alphas in coincidence one can deduce the momentum of the two alphas, and applying energy and momentum conservation calculate the momentum of the missing neutron. Thus one can obtain the excitation energy in ^{9}Be from the sum energy of the two alphas and the reconstructed energy of the neutron.

Figure 4.7 shows the scatter plot of the individual α-α-n energy plot in the x-axis against the sum energy of the three particles plot in the y-axis, for any possible two particle coincidence. The neutron energy is obtained from the alpha energies using

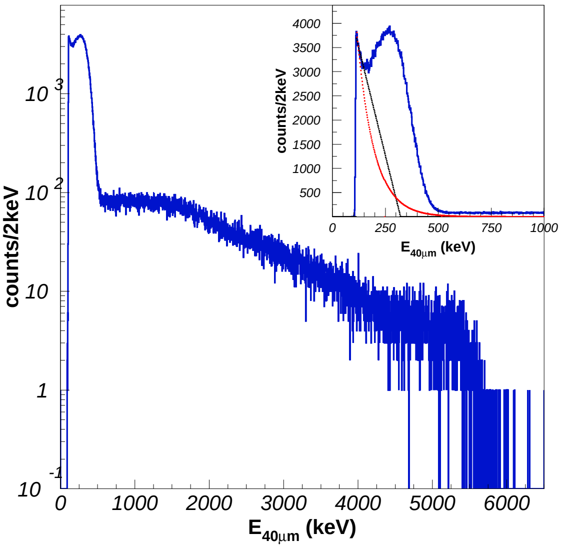

Figure 4.5: Singles α spectrum recorded in the surface barrier 40 μm thick silicon detector in an experiment in 2002. The inset shows the first 1000 keV, with the linear and exponential fits used to simulate the noise contribution overlaid.

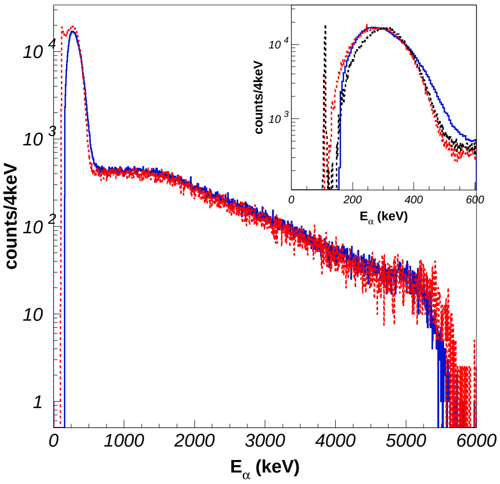

Figure 4.6: D2 alpha spectrum (blue) compared to the singles recorded in the 40 μm detector. The inset shows the first 600 keV compared to the singles spectrum with the noise subtracted using the linear fit (black line) and the exponential fit (red line). The difference at energies aropund 550 keV between the singles spectrum of the 40 μm detector situated at 16 cm and the detector D2 spectrum, located at 5 cm, is understood as due to different β-summings.

momentum and energy conservation (see section 6.3.1). The excitation energy in ^{9}Be is calculated by adding the neutron separation energy, S$_n$=1.6653(4) MeV, to the sum energy of the three particles. The black lines indicate the fingerprints corresponding to the first emitted particle in sequential breakup through the ^{8}Be(gs), ^{8}Be(2^+) first excited state and ^{5}He(gs), with the Full Width Half Maximum (FWHM) of each resonance marked by dashed lines.

As mentioned before, the advantage of working with coincidences resides in the possibility of calculating the excitation energy in ^{9}Be from the sum energy of the two detected alphas and the reconstructed neutron. This allows us to single out events from the ^{9}Be 2.43 MeV state breakup by selecting those of sum energy equal or lower than 0.9 MeV ($E_{^9Be}\leq$2.47 MeV). The condition is shown by the red dashed line in the inset of Fig. 4.7. The resulting E_α-$E_{\alpha'}$ spectrum (Fig. 4.8) shows two peaks at approximately 250 and 360 keV. This double peak structure is an effect of the different detections thresholds of D2 and D4. Inspecting the singles D4 spectrum shown in Fig. 4.3, one can see that the α spectrum peaks at ~360 keV, as expected.

4.3.3 Study of the neutron time-of-flight spectrum

Thanks to the presence of the neutron time-of-flight detector TONNERRE, we were able to directly study the neutron time-of-flight distribution. Fig. 4.9 shows the neutron time-of-flight spectrum recorded in TONNERRE without any condition on other detectors. The large peak at ~4 ns corresponds to the β prompt from the decay. The time distribution of the 12 pads were aligned by setting the β peak for each pad at 4 ns, acting as starting time of the spectrum (for details on TONNERRE see sections 2.5.2 and 3.1.5). The peak at negative time corresponds to the γ transition from both the $1/2^-$ first excited state in ^{11}Be and the β-delayed gammas from ^{10}Be. Apart from the beta prompt peak the spectrum shows other two features, a bump at ~100 ns and a peak at ~240 ns.

We studied the coincidences with the four DSSSD individually, in order to clean the neutron spectrum. Fig 4.10(a) shows the neutron time-of-flight spectrum in coincidence with trigger in D1, and Fig 4.10(b) in coincidence with a trigger in D2 (blue line), D3 (black line) and D4 (red line). The 240 ns peak it observed only in coincidence with D1, detector whose trigger was problematic during the experiment. This indicates the 240 ns peak does not come from real physical events. By looking at the coincidences with the remaining detectors we see that in both D3 and D4 the 100 ns bump is narrower and lower in time, indicating higher energy neutrons. This is a consequence of the higher energy thresholds of both detectors (see Table 4.1). Therefore, we will have better opportunities to study the breakup of the ^{9}Be 2.43 MeV by concentrating in coincidences with D2. Besides, this detector allows to better detect the low energy α particles.

In order to study the neutron spectrum from the 2.43 MeV state in ^{9}Be we select

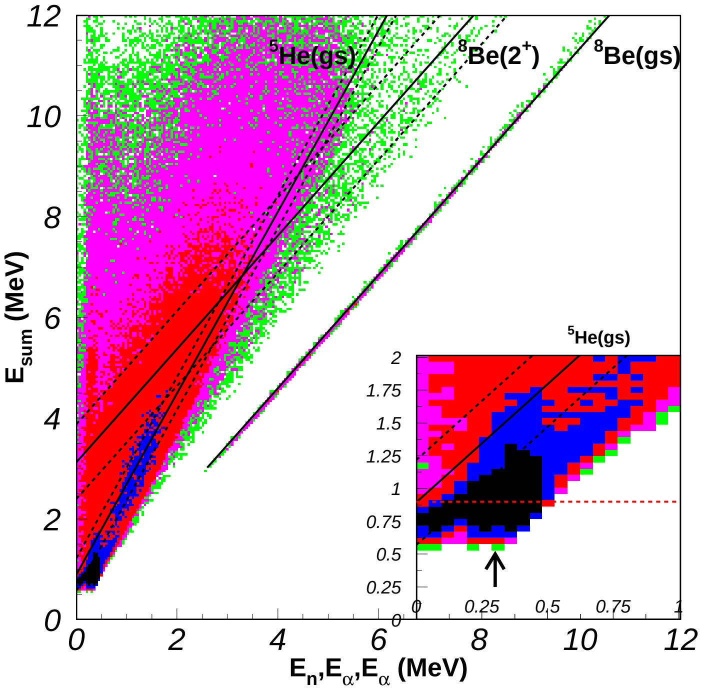

Figure 4.7: Individual energy of the two detected α particles and the reconstructed neutron is compared with the suim energy of the three particles in the y-coordinate. This scatter plot is designed to highlight sequential decay through intermediate resonances, as the first emitted particle will lay on a line of slope and offset determined by the mass ratio of the resonance to the original nucleus and the resonances energy, respectively. The lines indicate the three main intermediate resonances in the sequential breakup of ^{9}Be states,^{8}Be(gs), ^{8}Be(2^{+}) and ^{5}He(gs), with their FWHM marked by dashed lines. The inset shows a zoom to the region near the ^{9}Be 2.43 MeV state. The red dashed line shows the E_{sum}=0.9 MeV gate we used to select events corresponding to ^{9}Be(5/2^{-}). The black line associated to decay through the ground state of ^{5}He is close to the state, indicating a possible contribution to the breakup. The arrow marks the energies of the two alpha particles.

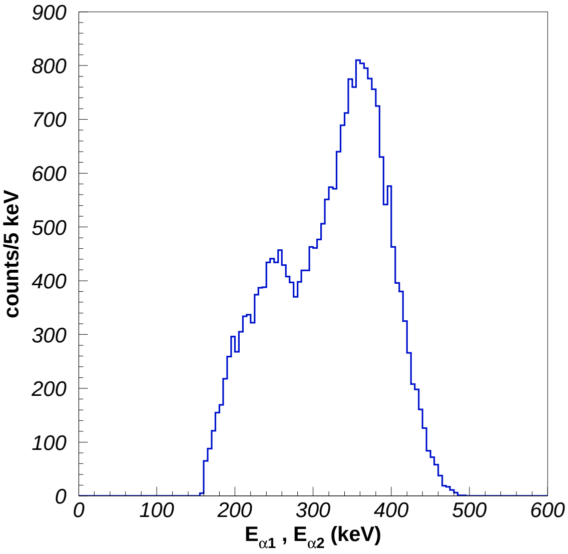

Figure 4.8: Energy spectrum of the two detected alphas in coincidence, two points per evetn, imposing that E_{sum} is lower than 0.9 MeV (see Fig. 4.7).

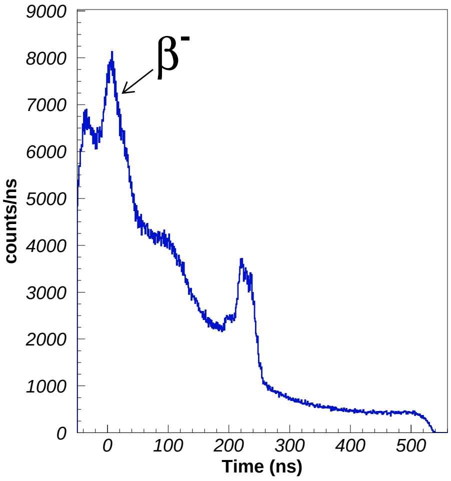

Figure 4.9: Neutron time of flight spectrum recorded in 2003 experiment. The most prominent features are the β-prompt peak (set as starter at 4 ns) marked by the arrow, the γ peak at negative times (mainly the 320 keV $^{11}Be(1/2^-)\rightarrow^{11}Be)(gs)$ γ-transition), the bump at 100 ns and the peak at ~240 ns.

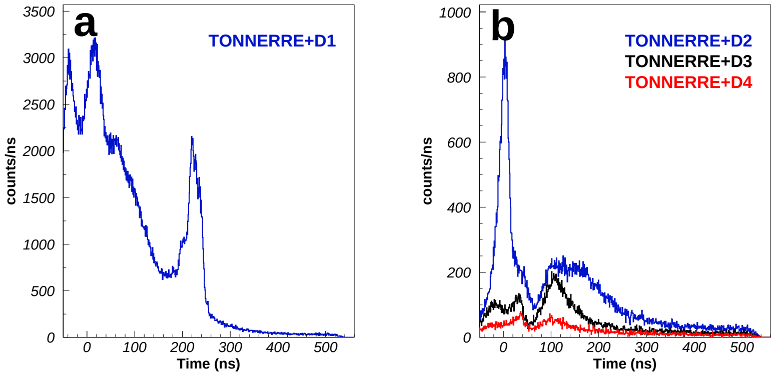

Figure 4.10: Left: (a) neutron time of flight spectrum recorded in coincidence with a trigger in D1. The spectrum shows the peak at ∼240 ns as in Fig. 4.9. Right: the same as in (a) but in coincidence with D2 (blue line), D3 (black line) and D4 (red line). The 240 ns peak does not appear in this figure, indicating it is due to the poor performance of D1 during the experiment. The 100-200 ns bump is broader in coincidences with D2 because its lower energy threshold.

neutrons in coincidence with alpha particles in the peak energy region of D2, between 200 and 350 keV. The gate does not include the upper part of the low energy peak in D2 in order to avoid as much contribution from the ^{9}Be state at 2.78 MeV as possible (Γ=1.08(11) MeV [Til04]) The resulting neutron spectrum is shown in Fig. 4.12(a).

We chose a higher energy gate (760 keV $< E_{sum} <$ 5650 keV) in D2 for comparison, shown in Fig. 4.12(b). The neutron peak appears at shorter times, corresponding to higher energy neutrons. Moreover, there is a clear neutron peak at ∼35 ns, corresponding to neutron energies between 4 and 9 MeV, which fits well with neutrons from the breakup of high energy states in ^{9}Be through the ground state of ^{9}Be. The reconstructed neutron spectrum of Fig. 4.7 confirms the emission of neutrons in the 4 to 9 MeV range. Therefore, we can assign the 160 ns peak of Fig. 4.12(a) to the breakup of the ^{9}Be 2.43 MeV state. The neutron energy for a neutron travelling 1.2 m (TONERRE radius) in ∼160 ns is ∼280 keV. This compares well with the low energy bump in the neutron spectrum of [Nym90], at around 300 keV, see Fig. 4.11. The 680 keV neutron peak in [Nym90] corresponds to the breakup of the 2.43 MeV state through the ground state of ^{8}Be, which should be observed at around 110 ns in our neutron spectrum. However, the alpha particles from the ^{8}Be(gs) breakup channel are emitted with energies lower than our thresholds (E_{α} ∼60 keV, see the sequential breakup discussion below), therefore the peak will not appear in the neutron spectrum in coincidence with a DSSSD.

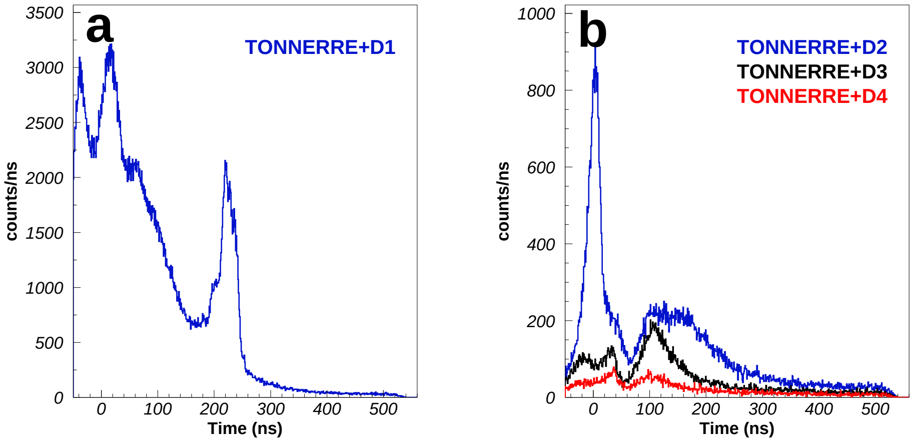

Figure 4.11: The ^{9}Li β-delayed neutron energy distribution obtained by G. Nyman et al. [Nym90]. The two peaks at energies at around 300 keV and 680 keV to the breakup of the ^{9}Be 2.43 MeV state. The 680 keV neutron peak corresponds to the ^{8}Be ground state secuential channel.

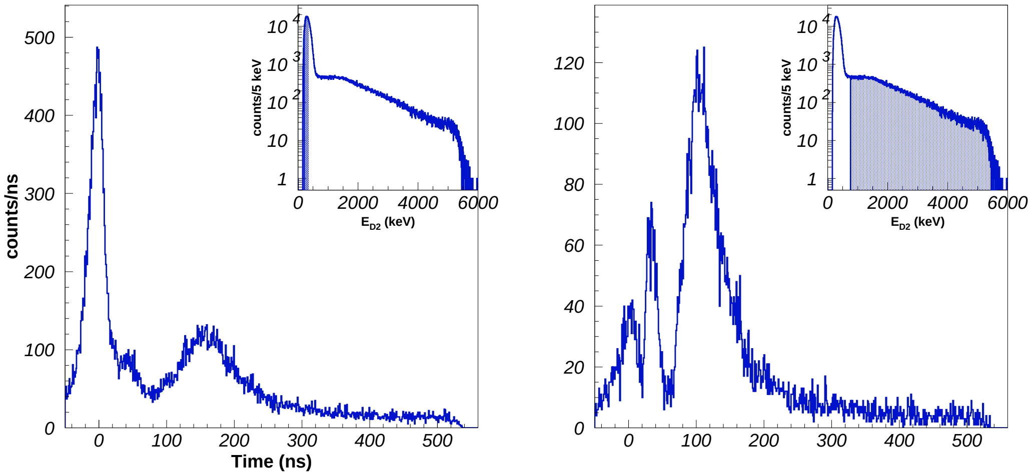

Figure 4.12: Left: (a) neutron time of flight spectrum recorded in coincidence with an alpha detected in D2 with energies in the range 200 keV < E_{D2} < 350 keV. The inset shows the condition set in the D2 alpha spectrum in blue. Right: the same as in (a) but in coincidence with D2 in the range 760 keV < E_{sum} < 5650 keV. The peak in the time-of-flight spectrum appears at lower times, indicating higher energy. The inset shows the condition set in the alpha spectrum in D2 in blue.

4.4 Simulations of the breakup of the ^{9}Be 2.43 MeV state

The singles and coincidence alpha spectra and the neutron time of flight spectrum shown before does not help individually in understanding the breakup mechanism of the ^{9}Be 2.43 MeV state. We need to performed Monte-Carlo simulations of the different proposed breakup mechanism models, sequential decay through the ^{5}He(gs) and/or the ^{8}Be(2^{+})resonances and direct breakup into the n2α continuum, and compared them to the data.

All Monte-Carlo simulations presented in this section included the effects of the experimental setup by explicitely incorporating the angular acceptance of the detectors, the energy losses on the carbon-foil stopper and the detectors dead-layer, and the energy threhsolds. Furthermore, the simulation is filetered with the same code used for the data.

4.4.1 Sequential decay

Assuming sequential breakup of the 2.43 MeV state in ^{9}Be, the energies and momenta of the emitted particles are defined by the energy distributions of the original state in ^{9}Be and the possible intermediate states: ^{8}Be(gs), ^{8}Be(2^{+}) or ^{5}He(gs) (see Fig. 4.1).

- (1) ^{9}Be*(2.43)$\rightarrow$n+^{8}Be(gs)$\rightarrow$n+2α
- (2) ^{9}Be*(2.43)$\rightarrow$n+^{8}Be(2^{+})$\rightarrow$n+2α
- (3) ^{9}Be*(2.43)$\rightarrow\alpha$+^{5}He(gs)$\rightarrow\alpha$+n+α

The sequential decay through the ground state of ^{8}Be is very difficult to measure in a β-decay experiment, as the ground state resonance is 91.8 keV above the $\alpha+\alpha$ breakup threshold [Til04]. The laboratory energy of the alpha particles is determined by the momentum boost due to the recoiling neutron (see Fig. 4.13),

$$\overrightarrow{P}_{\alpha} = \overrightarrow{P}_{\alpha}^{cm} + \frac{m_{\alpha}}{m_{^{8}Be}}\overrightarrow{P}_{^{8}Be} = \overrightarrow{P}_{\alpha}^{cm} - \frac{m_{\alpha}}{m_{^{8}Be}}\overrightarrow{P}_{n} \tag{4.1}$$

where, fixing the energy of the ground state ^{8}Be ground state to 91.8 keV and to 2.43 MeV of the ^{9}Be state

$$\left|\overrightarrow{P}_{\alpha}^{cm}\right|^{2} = 2m_{\alpha}\frac{91.8 \text{ keV}}{2} \tag{4.2}$$

$$\left|\overrightarrow{P}_{n}\right|^{2} = 2m_{n}\frac{m_{^{8}Be}}{m_{^{9}Be}}\cdot)(2.43 - 1.6654) \text{ MeV} \tag{4.3}$$

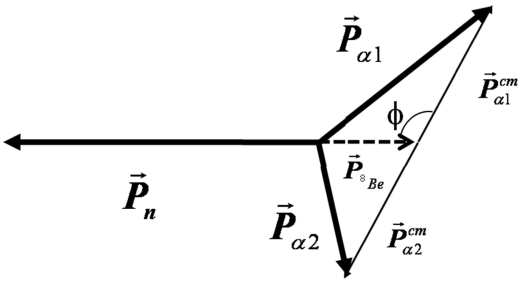

Figure 4.13: schematical view of the momentum relations in the sequential breakup of ^{9}Be through a resonance in ^{8}Be.

Both levels are narrow, Γ=5.57(25) eV for the ground state of ^{8}Be [Til04] and Γ=0.78(13) keV [Til04] for the ^{9}Be 2.43 MeV state, therefore fixing their energies is a good approximation. We calculated the alpha energy distribution from a Monte-Carlo calculation of random angular distribution of the neutron and of the alphas. Fig. 4.14(a) shows the resulting alpha energy distribution. The sahdowed area in the picture represents the events where one of the alphas has an energy above 160 keV, the software threshold of detector D2. The shadowed area in Fig. 4.13(b) corresponds to 14% of the alpha distribution in the simulation. If we assume a 11.4% β branching ratio to the 2.43 MeV state [Pap07], the total contribution of the ^{8}Be(gs) channel to the singles spectrum in D2 will be ~1.6%. Fig. 4.14(b) shows the energy of one of the alphas against the energy of the other for the same Monte-Carlo calculation of sequential decay through the ground state of ^{8}Be. It clearly indicates that this channel cannot be observed in α-α coincidences, as if one of the alphas is above the detector threshold the other will be below it.

We see that the contribution of the decay through the ground state of ^{8}Be to the singles is small, ~1.6% and it does not contribute to the coincidences due to the higher threshold of detectors D3 and D4. We can go further and test the possibility of sequential decay through the 2^{+} first excited state of ^{8}Be and/or the ground state of ^{5}He. We performed a Monte-Carlo simulation of the breakup, including the experimental acceptance. The resonances were described in the Monte-Carlo simulation using the non-interfering single-channel multiple-level R-Matrix formalism as described in [Nym90], see section 3.3.2. In this approximation, the R-matrix formalism intrinsically depends on two variables, as the probability distribution, *w*($E_{^9Be}$,*E'*), depends simultaneously on the energy of the first resonance $E_{^9Be}$ and of the energy of the intermediate resonance *E'* as follows

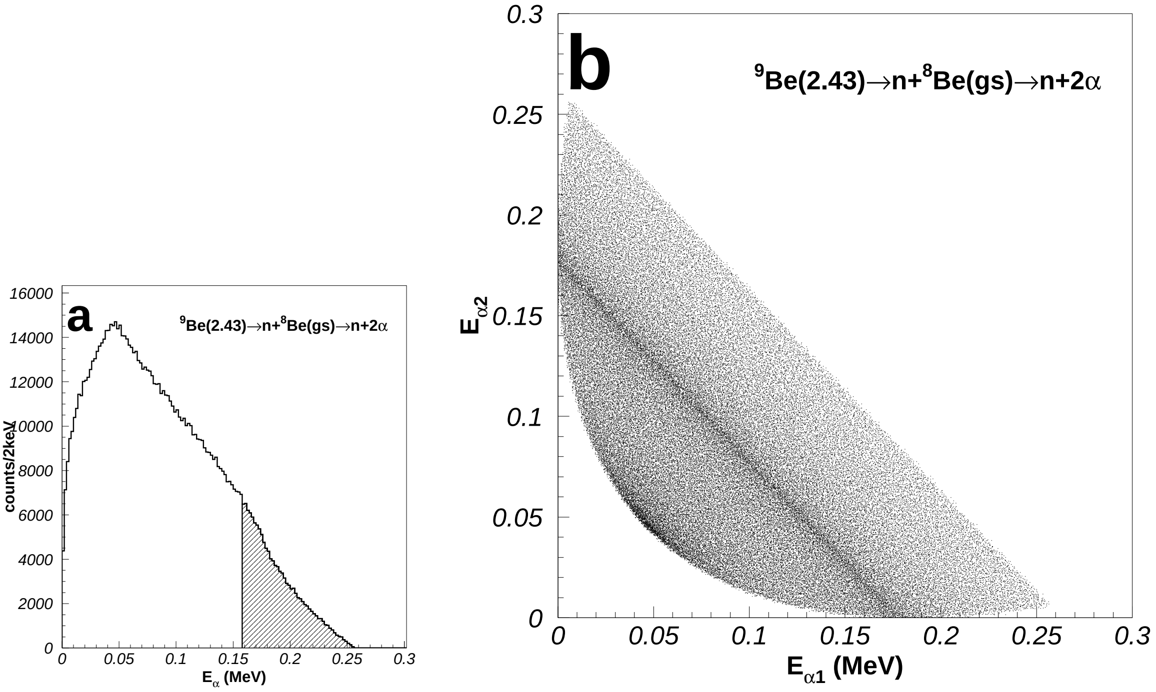

Figure 4.14: Left: (a) the alpha singles energy spectrum following the sequential breakup of the ^{9}Be(2.43) MeV state through the ground state of ^{8}Be is shown. The shadowed area marks the regionof the decay through the ^{8}Be ground state that could be detected in D2. Right: energy of one of the alphas against the other for the same decay of (a). The figure shows it is not possible to observe this channel in α-α coincidences, as if one of the particles is above the detection threshold the other will be below it.

$$w(E_{^9Be},E') = f_\beta(E_{^9Be})\frac{P_\alpha(E_{^9Be}-E')}{(E^0_{^9Be}-E_{^9Be})^2+(\Gamma_{^9Be}/2)^2}\cdot\frac{\Gamma_{E'}}{(E'_0-E')^2+(\Gamma(E')/2)^2} \tag{4.4}$$

where $f_\beta(E)$ is the fermi function, $\Gamma=2\gamma^2P(E)$ is the level width (γ is the reduced width and P(E) is the penetrability), E' refers to either energy in ^{8}Be or ^{5}He, and E^0 is the level centroid. As noted in [Nym90], the $\Gamma_{^9Be}$ width varies slowly with the excitation energy in ^{9}Be, so we fixed the width in the denominator to the tabulated value. The following table lists the parameters of the different resonances included in the simulation.

	E_0 (MeV)	γ^2 (keV)
^{9}Be(2.43)	2.43	$\Gamma_{^9Be}$=0.78
^{8}Be(2^+)	4.7^a	1500
^{5}He(gs)	2.47^a	500

^{a}Above the ^{9}Be ground state

This approximation of the R-matrix formalism explicitly relates the energy of the first emitted particle with the probability distribution of both the original and the intermediate resonance, *$E_{^9Be}$-E'*. Therefore, it is a reliable model of the breakup over the single level single channel approximation. In the single channel R-matrix formalism both resonances are described using independent *w(E)* shapes, which implies that only the centroid of the intermediate resonance plays a role in the distribution of the ^{9}Be resonance.

There is an extra computational cost if the more complex multiple-level formalism is used, as one has to obtain pairs of emitted energies *(e,e')* distributed according to the probability density given by the R-matrix formalism *w(e,e')*. We chose to use the Monte-Carlo Von-Neumann approach to this problem. This technique relies in generating random pairs of energies *e,e'* in a given range and assign them a random probability weight *p*. To increase the speed of the calculation the maximum value of the random weight *p* is the maximum value of the desired function in the energy range of interest, $w(e_o,e'_o)$. Only pairs of random weight *p* lower than the value of the distribution we want to reproduce for that pair, *w(e,e')*, are accepted, theerefore the probability distribution of *(e,e')* will follow the desired function. Thus, for a random *(e,e')* pair we impose

$$x \times w(e_o,e'_o) < w(e,e') \tag{4.5}$$

where x is a random number between 0 and 1. Once the energies of both resonances *($E_{^9Be}$,E')* are obtained from the Monte-Carlo, it is trivial to calculate the energy of the three emitted particles, 2α and a neutron, from energy and momentum conservation. The alpha energies in the ^{8}Be(2$^+$) channel are obtained from eqs. 4.1 and 4.3, substituting $Q_{\alpha\text{-}\alpha}$=91.8 keV in 4.3 by ($E'_{^8Be}$-1.5736 MeV), and the Q_n=(2.43-1.6654) MeV by ($E_{^9Be}$-1.6654). In the case of sequential breakup through the ground state of ^{5}He, the cinematics are a bit different. In Fig. 4.13 one should substitute the first emitted neutron for one of the alphas, and viceversa. This means that the second emitted alpha particle will have a momentum depending on the recoil boost due to the first emitted alpha

$$\overrightarrow{P}_{\alpha 2} = \overrightarrow{P}^{cm}_{\alpha 2} + \frac{m_\alpha}{m_{^5He}} \overrightarrow{P}_{^5He} = \overrightarrow{P}^{cm}_{\alpha} - \frac{m_\alpha}{m_{^5He}} \overrightarrow{P}_{\alpha 1} \tag{4.6}$$

where

$$\begin{aligned} |P^{cm}_{\alpha 2}|^2 &= 2m_\alpha \frac{m_n}{m_{^5He}} (E_{^5He} - Q_{2\alpha\text{-}n}) & (4.7)\\ |P_{\alpha 1}|^2 &= 2m_\alpha \frac{m_{^5He}}{m_{^9Be}} (E_{^9Be} - E'_{^5He}) & (4.8) \end{aligned}$$

where $Q_{2\alpha\text{-}n}$=1.5736 MeV is the 2αn breakup threshold.

However, it is not enough to simply obtain the energy and momentum distribution of the particles in the laboratory frame, as the setup has an intrinsic acceptance that has to be taken into account. The experimental conditions were included in the Monte-Carlo as the detection thresholds, the solid angle covered by the DSSSD's and the relative angles between the detectors. Figures 4.15(a) and (b) and Fig. 4.16 show the simulations for sequential decay compared to the α singles spectrum in D2, the α-α coincidences from Fig 4.8 and the neutron time-of-flight spectrum from Fig. 4.12(a). The sequential decay simulations fail to reproduce both the α singles and coincidence spectrum, as they peak at higher energies than the data. In the neutron time-of-flight spectrum case the sequential decay through ^{5}He(gs) is unable again to reproduce the data, although the decay through ^{8}Be(2$^+$) compares fairly well to the data.

4.4.2 Direct decay

The previous section shows that the simulations of the sequential breakup of the 2.43 MeV state fail to reproduce both the singles and coincidence α spectra and the neutron time-of-flight spectrum, except for neutron ToF spectrum from the simulation of the breakup through the ^{8}Be(2$^+$) resonance, which agrees reasonably well with the data. This lead us to consider a Monte-Carlo simulation of the other possible breakup mechanism, direct breakup into the three body, 2αn, continuum. In this case, the simulation needs to model the energy sharing between the three emitted

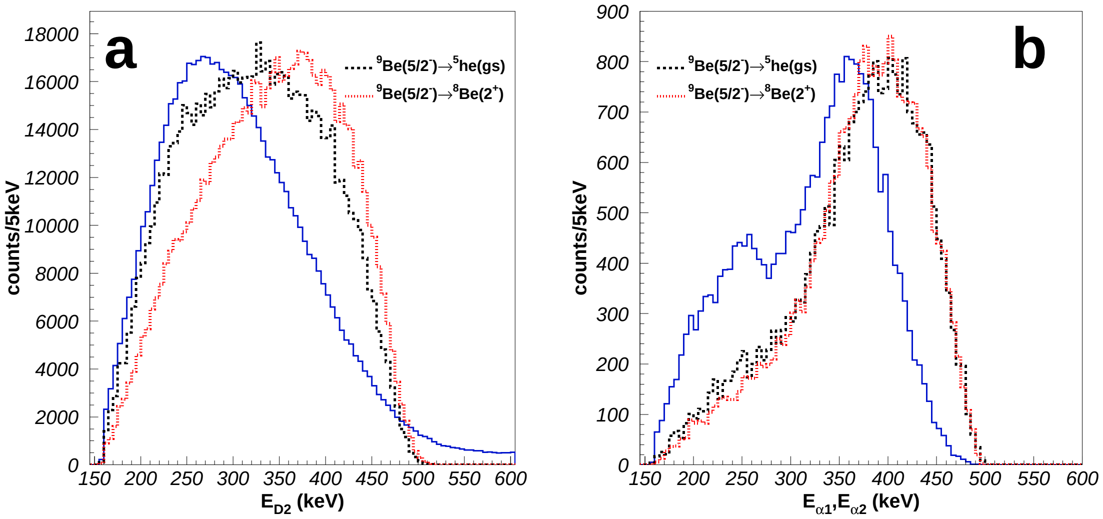

Figure 4.15: Left: (a) the α *energy spectrum from DSSSD D2 inblue compared to the simulation of the sequential breakup of the* ^{9}Be *2.43 MeV state though the* $^{5}He(gs)$ *(black dashed) and* $^{8}Be(2^{+})$ *(red dotted) resonances. Both simulations fail to reproduce the shape of the 270 keV peak, as they consistently appear at higher energies. Right: (b) the* α *coincidence energy imposing* $E_{sum}<0.9$ *MeV (in blue) compared to the same simulations of (a). The simulations of sequential decay, through* $^{5}He(gs)$ *in black dashed and through* $^{8}Be(2^{+})$ *in red dotted, fail to reproduce the low end of the spectrum.*

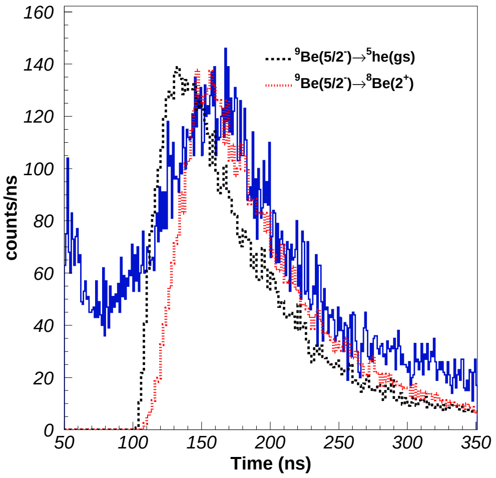

Figure 4.16: Neutron time-of-flight spectrum, gated on the 270 keV peak of D2 alpha spectrum, compared to a Monte-Carlo simulation of sequential decay through the ^{5}*He(gs) (black dashed) and* ^{8}*Be(2*$^{+}$*) (red dotted) resonances.*

particles. The simplest case would be described by phase space energy sharing (see section 3.3.1). However phase space by itself neglects the role of interactions between the emitted particles. A model was derived by Bochkarev et al. [Boc89] by observing that in some cases the direct decay resulted in momentum and spatial focusing of the emitted particles, indicating that the decay may be described by a good quantum number, the hypermoment K. In the case of the decay of the ^{9}Be $5/2^{-}$ 2.43 MeV state, conservation of orbital angular momentum imposes that the minimum value of K is 3, and taking into account that K=L+2n, where n=0,1,2,..., the total orbital momentum L of the $2\alpha n$ final system can be 2 and 3. In this formulation, the probability of α particle emission with a certain momentum $\mathbf{P}$ is given by the sum of hyper-spherical harmonics of K=3

$$\left[\frac{d^{3}\mathbf{P}}{dyd\Omega_{\alpha}d\Omega_{\alpha N}}\right]_{Bochkarev} = a\frac{2^{3}}{\pi^{3}}y^{3/2}(1-y^{5/2})\sin^{2}\phi + b\frac{2^{4}}{7\pi^{3}}y^{3/2}(1-y)^{5/2}(2+\cos^{2}\phi) \tag{4.9}$$

where the first term corresponds to total orbital momentum L=2 and the second term to L=3. The constants a and b define the weight of L=2 and L=3 components, thus a+b=1. The variable y is related to the energies of the emitted particles as $y=\frac{9E_{\alpha}}{5(E_{^{9}Be}-1.57)}$. Finally ϕ is the angle between the relative momentum of the α-α pair and that of the recoiling neutron (see Fig. 4.13).

From a practical point of view, the direct decay was implemented in the Monte-

Carlo code using the same Von-Neuman technique as in the previous section. A breakup event described by phase space energy sharing was generated using the GENBOD code from CERNLIB (for more details on phase space see section 3.3.1), a random probability weight p was assigned to the event, its actual weight was obtained using equation 4.9 and again only events whose p was lower than the actual weight were accepted. In order to explore the best composition of L=2 and L=3 components we performed a Monte-Carlo simulation varying their mixture, first L=2 and L=3 components alone and finally a 50% mixture of both. In order to determine which simulation is favored by the data we performed a χ^2 test over the α singles and coincidence spectra and the neutron ToF spectrum. The results are shown in the following table

	χ^2 (α singl., N$_{free}$=45)	χ^2 (α coin., N$_{free}$=120)	χ^2 (n-tof, N$_{free}$=120)
L=2	9293.6	3437.2	3561.6
50% mix	8391.5	3125.1	3346.2
L=3	11025.0	3519.7	3250.18

Although the results of the tests are far from χ^2/N$_{free}\approx$1, one should note in this approximation of the simulation that one should expect qualitative agreement, rather than quantitative. Regarding the mixture of L=2 and L=3 components, the α spectra tests favor the 50% mixture. In the neutron time-of-flight spectrum case, the 50% mixture simulation and the L=3 simulation are similar, being the L=3 slightly favored. In previous studies of the breakup of the ^{9}Be 2.43 MeV state using the democratic formalism [Boc89, Vas89] a 50% mixture of L=2 and L=3 components was proposed, in agreement with our results.

Figures 4.17(a) and (b) show the Monte-Carlo simulation with 50% mixture of L=2 and L=3 components compared to the α singles and coincidence spectra, respectively. They show an improvement over the Monte-Carlo simulation of sequential break-up (Figure 4.15 (a) and (b)), although there is still a lack of low energy alphas in the coincidence spectrum 4.17 (b). Figure 4.18 shows the same Monte-Carlo simulation compared to the neutron time-of-flight spectrum. In this case the simulation fails to reproduce the neutron distribution.

Before dismissing the "democratic" decay model of direct breakup one should take into account an observation on the model by Bochkarev [Boc89], that the model does not take into account the centrifugal and Coulomb barriers the particle needs to overcome when emitted. A simple solution proposed in [Boc89] would be to add the penetrability formula from the standard R-Matrix model of sequential breakup (see section 3.3.2). The penetrability explicitly depends on the final channel, thus we used, following the sequential simulation that showed the best agreement with the neutron data in Figure 4.16, the penetrabilities of ^{8}Be+n breakup and α-α breakup.

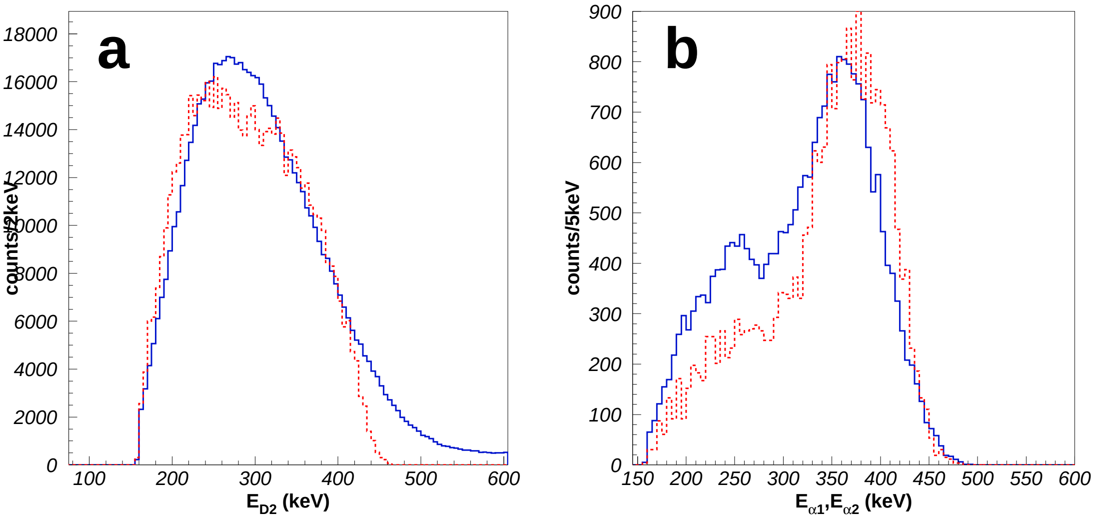

Figure 4.17: Left: (a) the α energy detected from DSSSD D2 compared to the simulation of direct breakup the ^{9}Be 2.43 MeV state using the "democratic" decay model, with a 50% mix of L=2 and L=3 components. Right: (b) the α-α coincidence energy spectrum, two points per event, imposing E_{sum}<0.9 MeV compared to the same direct breakup simulation of (a). The area of the simulation is normalized to the experimental area.

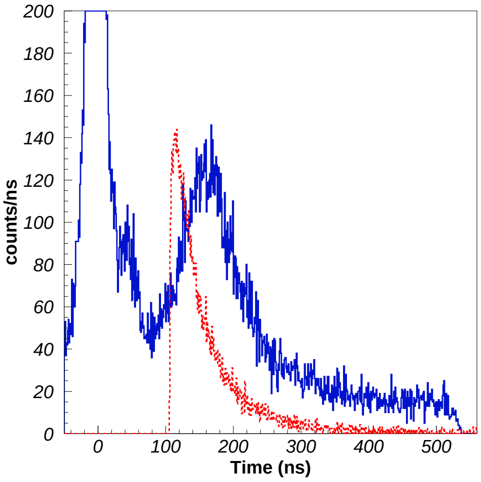

Figure 4.18: Neutron time-of-flight spectrum, gated on the 270 keV peak of D2, compared to a Monte-Carlo simulation of direct breakup assuming the "democratic" model for the breakup and using a 50% mix of L=2 and L=3 components.

$$\frac{d^3\mathbf{P}}{dyd\Omega_\alpha d\Omega_{\alpha N}} = \left[\frac{d^3\mathbf{P}}{dyd\Omega_\alpha d\Omega_{\alpha N}}\right]_{Bochkarev} \times P_{\alpha\alpha}(l=2)P_{n^8Be}(l=1) \tag{4.10}$$

where the orbital angular momentum of both breakups, l=2 for the alphas and l=1 for the neutron, is determined by the spin of the initial state in ^{9}Be, $5/2^-$ and of the intermediate resonance, in this case assuming that it is the ^{8}Be 2^+ state. The ground state of ^{8}Be is not a good candidate, as it is thin enough (Γ=5.57(25) eV [Til04]) to dominate the breakup mechanism into sequential decay. Again we used the Von-Neumann technique to implement the breakup in the code and performed three different simulations with the L=2 and L=3 components alone, and a 50% mixture of both. The resulting χ^2 tests of the simulations are

	χ^2 (α singl., N$_{free}$=45)	χ^2 (α coin., N$_{free}$=120)	χ^2 (n-tof, N$_{free}$=120)
L=2	7180.6	1086.3	688.0
50% mix	7053.77	714.5	698.6
L=3	18962.0	2506.9	734.8

Now, the values of the χ^2 tests are lower than in the regular "democratic" case, three times lower in the case of the coincidence spectrum and 5 times lower in the case of the neutron time-of-flight spectrum. Again a 50% mixture of L=2 and L=3 is favored by the alpha singles and coincidences. Figures 4.19(a) and (b) show the Monte-Carlo simulation of the breakup with 50% mixture of L=2 and L=3 components compared to the alpha singles and coincidence spectra, respectively. Now the simulation of the coincidence spectrum is fairly similar to the data, thus the great reduction in the χ^2 test, from 3125 to 714. Figure 4.20 shows the same 50% mixture simulation compared to the neutron time-of-flight spectrum. Comparing Figure 4.18 with Figure 4.20 we see the positive effect of taking into account the penetrability, as the new simulation reproduces well the neutron data.

4.5 Summary and conclusions

We have analyzed the singles α and α-α and α-n coincidence spectra following ^{9}Li β-decay to study the decay mechanism of ^{9}Be($5/2^-$). Monte-Carlo simulations of the different proposed decay mechanism were performed, "democratic" decay with and without including the particles penetrabilities and sequential decay through ^{8}Be(2^+) or ^{5}He(gs) described by R-matrix theory.

Comparing the Monte-Carlo simulations with the three spectra studied, alpha singles and coincidences and the neutron time-of-flight spectrum consistently favor

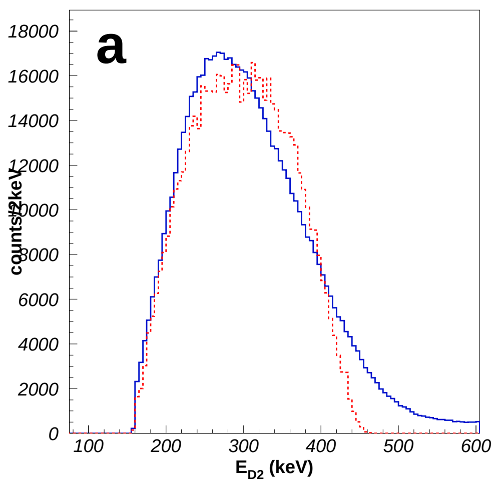

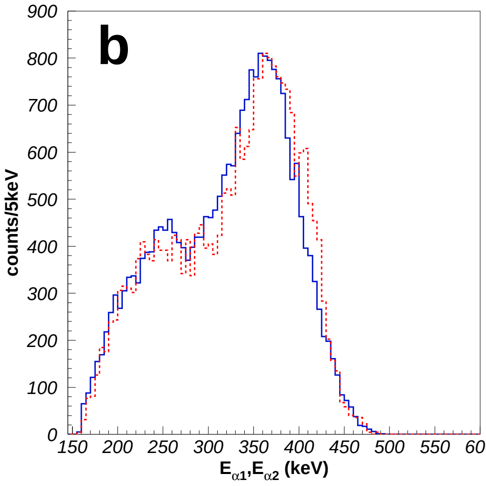

Figure 4.19: Left: (a) the α energy spectrum from DSSSD D2 (in blue) compared to a simulation (in red-dashed line) of direct breakup of the ^{9}Be 2.43 MeV state using the “democratic” model (50% mix of L=2 and L=3) folded by the penetrabilities. Right: (b) the α coincidence (blue) energy imposing E_{sum}<0.9 MeV compared to the same simulation as in (a) (red-dashed).

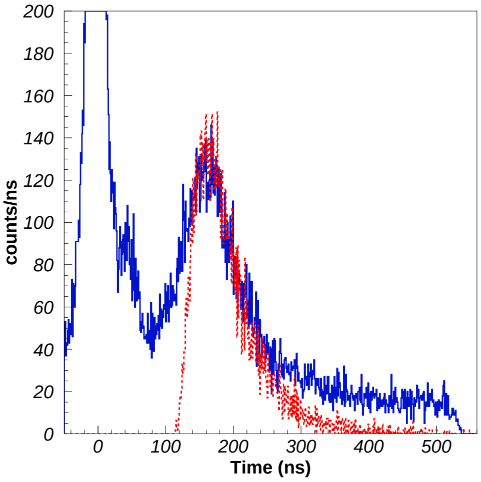

Figure 4.20: Neutron time-of-flight spectrum (in blue), gated on the 270 keV peak of D2 α-spectrum, compared to a simulation of the breakup (red-dashed) using the “democratic” model (50% mix of L=2 and L=3) folded by the penetrabilities.

the “democratic” description prescribed by Bochkarev [Boc89] over the sequential decay. However the neutron time of flight spectrum shows that the neutron and α-α penetrabilities have to be taken into account to properly match the experimental shape. The modified “democratic” decay excellently reproduces all three spectra, specially the α-α coincidences and neutron time-of-flight spectra. The α-α coincidence specrum is the most reliable, as we selected events with the sum energy corresponding to the breakup of the ^{9}Be 2.43 MeV state, thus cleaning from contributions from the decay of other states.

Not only the simulations favor the “democratic” decay model of the breakup, but they reproduce so well the coincidence and neutron time-of-flight spectra that there is little room for sequential breakup branches. This is in agreement with the recent results of Alvarez-Rodriguez et al. [Alv08], where they expect the breakup to occur directly into the 2αn continuum, with no role in the breakup for the ^{5}He(gs) and ^{8}Be(2^{+}) resonances.

Our result of a breakup dominated by direct decay into the continuum contradicts the experimental results obtained by Papka et al. [Pap07] and the theoretical predictions by Descouvemont [Des01] that indicate that the breakup occurs mainly thorugh the 2^{+} state of ^{8}Be, with small contributions of the ground state resonances of ^{8}Be and ^{5}He.

Regarding the calculation of the reaction rate of the ^{4}He(αn,γ)^{9}Be radiative capture, our results does not support that 2.43 MeV level should be included in the calculation of reaction through the ground state of ^{5}He, which was suggested by Buchmann et al [Buc01]. Our results do not mean, however, that the state cannot play role in the radiative capture process of ^{9}Be through a three-body reaction mechanism.

Chapter 5

Study of the ^{11}Li β-delayed charged particle channels

Part I: 2003 experiment

This chapter presents the study of the multifragmentation channels following ^{11}Li β decay. This channels involve the breakup of ^{11}Be states fed in ^{11}Li β-decay in neutrons, α particles and ^{6}He, involving several intermediate resonances in ^{10}Be and ^{A}He isotopes.

The ^{11}Li β-decay is characterized by its large Q_β value (20.557(4) MeV [Smi08, Bac05]) and low particle separation energy in the daughter ^{11}Be, making the ^{11}Li the nucleus with the largest number of decay channels reported [Roe74, Azu79, Azu80, Lan81, Lan84, Muk96]. These include, ordered by threshold energy, β-γ, β-$n\gamma$, β-nα^{6}He, β-2α3n, β-t and β-d. The first two channels have been recently used to study the low lying states in ^{11}Be [Mor97, Hir05, Fyn04, Sar04]. On the other hand, the high energy charged particle channels have been mainly studied by either indirect methods, two and three neutron detection [Azu79, Azu80, Bjo81, Bor97b], or using a single detector set-up [Muk96, Bor97a], which not provides kinematical information. There is only one previous experiment which used a set-up able to detect two charged particles in coincidence. They deduced the breakup mechanism of the two states at the highest energy ^{11}Be [Lan81, Lan84]. Detection in coincidence is crucial, as it provides kinematical information necessary to determine the reaction mechanism, sequential or direct, and in the case of sequential decay, the intermediate resonances involved. The work presented in this chapter summarizes two experiments using several segmented detectors for detection in coincidence.

From here on I am going to concentrate in the analysis of the ^{11}Li data. The experimental setups used are described in detail in Chapter 2 and the calibrations and thresholds used are detailed in Chapter 3.

5.1 Introduction and goals

The β-decay of ^{11}Li has been extensively studied in experiments capable of β-n detection [Mor97], β-γ coincidences [Det80, Bor97b, Fyn04, Sar04] and β-γ-n coincidences [Hir05]. All the information determined on these experiments has led to a detailed knowledge of which states in ^{11}Be (below the charged particle thresholds) are fed in the β-decay of ^{11}Li, their spin and parities and their β-feedings. However, there is a much limited knowledge of the ^{11}Li β-decay to states in ^{11}Be above the charged particle thresholds, i.e. 7.913 MeV. Four decay channels involving charged particles have been reported: three body nα^6He channel and five body 2α3n channel [Lan81], and the two 2-body channels ^{8}Li+t [Lan84] and ^{9}Li+d [Muk96, Bor97a, Raa08]. The only previous study of charged particle coincidences [Lan81] proposed from energetics that the nα^6He and 2α3n channels are involved in the breakup of two states in ^{11}Be, one previosly established at 10.6 [Ajz78] and a new high energy state at 18 MeV (see Fig. 5.1), although the lack of angular resolution to study the kinematics prevented to obtain a definitive answer. The study, with particle identification provided by a gas-Si telescope, of the triton channel confirmed the role of the 18 MeV state [Lan84, Muk96, Bor97a], and indicated that the β-feeding to the 18 MeV state is rather large, in line with what was observed in the β-decay of other halo nuclei [Bor91]. Finally, a recent measurement of the deuteron energy spectrum in the ^{9}Li+d channel [Raa08] indicates that the deuteron is emitted directly into the continuum, without the involvement of any state in ^{11}Be, suggesting that the β-decay occurs directly to the continuum.

This series of experiments studying the ^{11}Li β-delayed charged particle emission show the challenges of studying these channels, as only two states in ^{11}Be separated by ∼8 MeV have been identified to contribute. This indicates that most likely a fraction of the β-stregth goes to states in ^{11}Be not yet identified. This has been already sugested by the study of the neutron recoil-broadened ^{10}Be γ transitions in the β-decay of ^{11}Li [Fyn04], where up to 6% of the β-feeding is assigned to states in ^{11}Be between 10.6 and 18 MeV. On the theoretical side, a calculation of Gamow-Teller transitions in ^{11}Li [SO97] indicates that there is significant β-strength in the unkown region, peaking at 16 MeV excitation energy in ^{11}Be.

Finally, there has been significant interest in obtaining a complete picture of the ^{11}Li β-decay strength distribution to understand the role of the halo structure in the β-decay. It has been already stablished that the observed β strength in the feeding of the first excited stated in ^{11}Be [Det80, Mor97, Bor97b] can only be succesfuly reproduced in shell model calculations by using a wave function of the ground state of ^{11}Li composed of a ∼50% mixture of $p_{1/2}$ and $s_{1/2}$ neutron

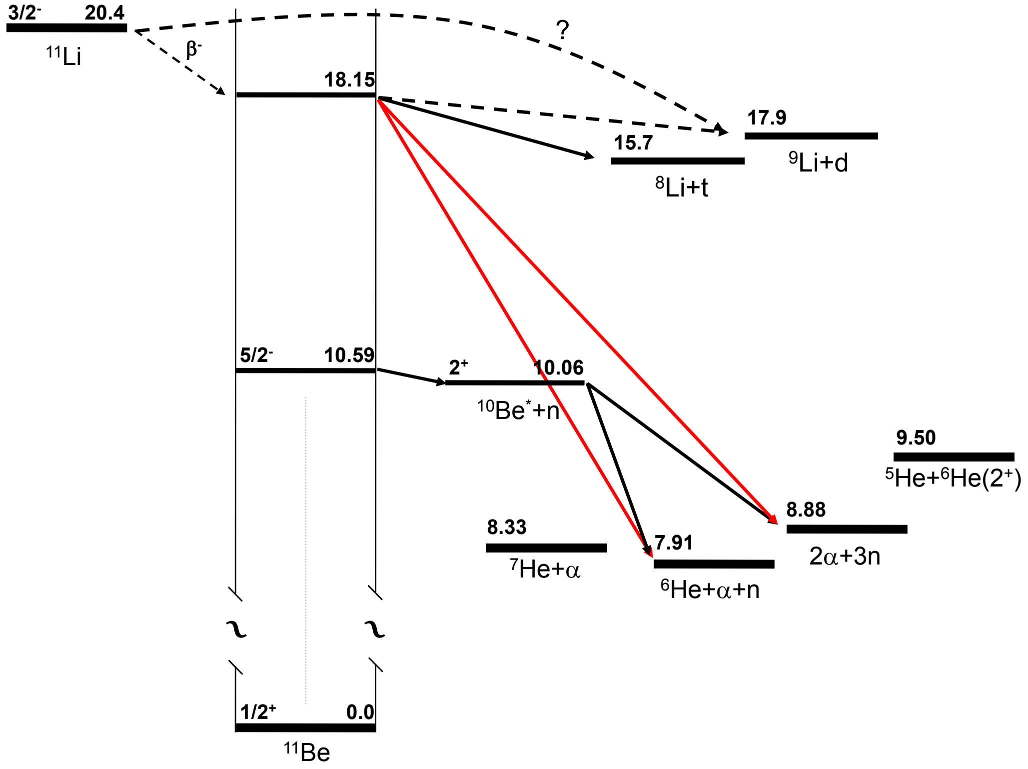

Figure 5.1: *Partial* ^{11}Li β*-decay scheme of the* ^{11}Be *levels above the charged particle threshold. The decay channels shown are taken from [Lan81, Bor97a, Til04].*

single particle states [SO94, Bor97b]. This theory dependent result of the misture of two s and p single particle states for the ^{11}Li ground state was later confirmed by studying the neutron momentum distribution in the stripping experiment by Simon and colaborators [Sim99].

More generally, it has been proposed [Bor91, NNR00] that the β-decay operator might affect independently the halo and core wavefunctions, giving rise to specific patterns in the β-decay strength distribution. This stresses the importance of obtaining a complete picture of the ^{11}Li β-decay strength distribution.

The main aims of this work presented in the two chapters that describe the analysis of the ^{11}Li β-delayed charged particle emission can be summarized in:

- **To improve the description of the breakup mechanism β-delayed branches including two charged particles.** This is essential to correctly determine the branching ratios, as the breakup mechanism determines the shape of the states contributions to the overall intensity distribution.

- **To determine which states in ^{11}Be above the charged particle thresholds are fed in the ^{11}Li β-decay.** The study in full kinematics of the three body nα^6He and two-body βt channels allows for a direct reconstructionof the excitation energy and spin and parity of the states in ^{11}Be involved in these breakup channels.

- **To obtain the branching ratios to these states and the correponding B(GT) values.** The complete β strength distribution will be compared to that of its core nucleus ^{9}Li to look for patterns indicating the effect of direct core β-decay. Finally the strength distribution will be compared to a shell model calculation. This part belongs to the following chapter.

5.2 Brief description of the experimental setup.

The experimental setup consisted in four particle telescopes, each one consisting of a DSSSD backed by a Si pad, mounted on the surfaces of a cubic aluminum frame. The ^{11}Li ions were stopped in a carbon foil situated in the geometrical center of the cube. Thus, each detector center was 5 cm away from the decay source, which defines the angular coverage of each telescope at ∼4% of 4π.

From Fig. 5.2 we see that there are three types of coincidence geometries for the three DSSSD, D2, D3 and D4. Hits in D2 and D4 were classified as *180^o* coincidences, and covered angles from 127^o to 180^o between the detected particles. Hits in D3 and either D2 or D4 were classified as *90^o* coincidences and covered angles from 37^o to 143^o between the detected particles. Finally, coincidences detected in the

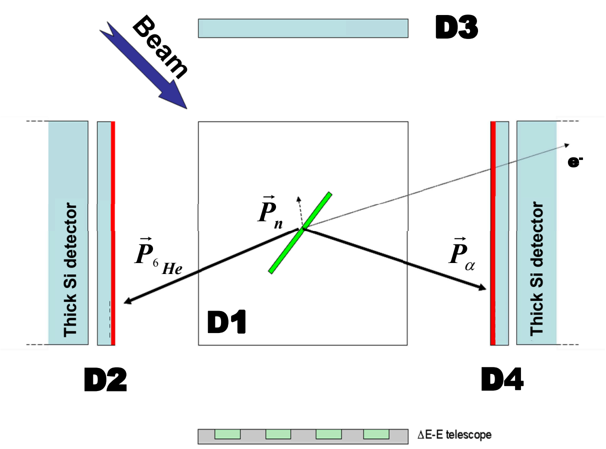

Figure 5.2: Schematical view of the relative positions of the particle telescopes in the 2003 experiment. Detector D1 is placed on the surface of the page. The ΔE-E telescope in the bottom is an experimental solid state telescope, which was placed for testing purposes.

same detector, classified as *0º* coincidences, covered angles from 0^o to 50^o between the detected particles.

The experimental conditions necessary to clean the data were applied (see Chapter 3, Sections 3.1.1 and 3.1.4). Low energy thresholds were imposed to remove the electronic noise present in the low energy end of the raw data. The energy losses in the carbon-foil and detectors dead-layers were reconstructed, and the DSSSD front and back spectra were energy matched to ensure that the data belong to physical events.

5.3 Study of charged particle emission

We concentrate in this section on the analysis of ^{11}Li β-delayed charged particles detected in the DSSSD's. The ^{11}Li β-delayed events are enhanced over daughter activities by gating on the first 40 ms after the proton impact on the target, as described in section 2.3. Figure 5.3 show the recorded events for detectors DSSSD D2 (red-dashed histogram), D3 (black-dotted histogram) and D4 (blue histogram). The very complicated nature of the different decay channels of ^{11}Li makes the charged particle spectrum rather featureless. The main observed feature is a low energy peak, which appears at different energies for each detector. The main reason for the differences between the peaks energies is the low energy acceptance of each detector due to different thresholds.

More information can be obtained from the analysis of charged particles de-

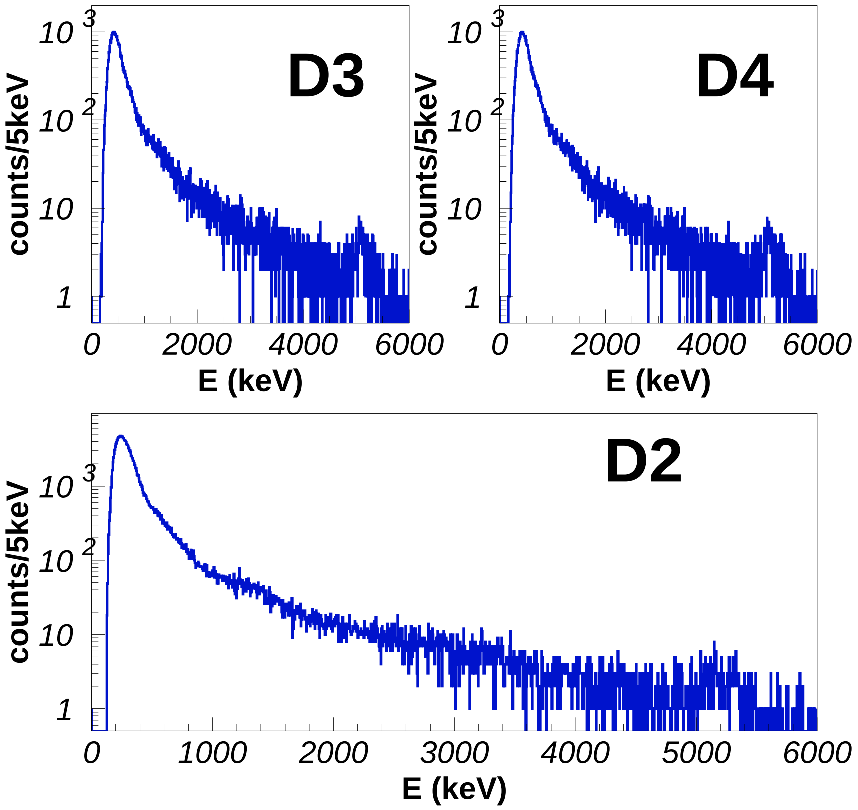

Figure 5.3: Top Left: singles energy spectrum detected in DSSSD D3. Top right: singles energy spectrum in DSSSD D4. Bottom: Singles energy spectrum detectied in DSSSD D2. Although the three histograms fit well at energies above 1 MeV, the different threshold conditions for each detector modify the shape of each spectrum at lower energies.

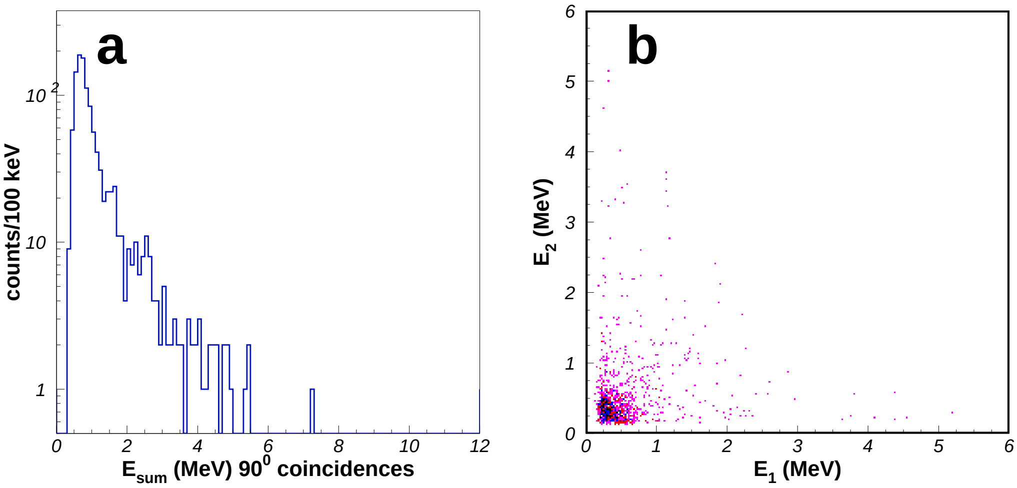

Figure 5.4: Left: a the energy sum spectrum collected in the first 40 ms after the proton impact with the condition of coincidences in detectors either D2 and D3, or D3 and D4. Right: energy-vs-energy Scatter plot corresponding to 90^o *coincidenceevents.*

tected in coincidence, as described in the several experimental techniques detailed in Chapter 3. Figures 5.4a and 5.4b show the sum energy spectrum and scatter plot corresponding to *90*^{0} coincidences. The scatter plot is rather featureless and the only feature of the sum energy plot is a low energy peak, indicating the absence of nuclear structure playing a role in these coincidences. Similarly, *0*^{o} coincidences sum and scatter spectra, shown in Figs. 5.5a and 5.5b, lack of any distinct features but a low energy peak.

On the other hand, the *180*^{o} coincidences, Figs. 5.6a and 5.6b, show several interesting features. There are two peaks at 0.7 and 2.2 MeV in the sum energy spectrum, corresponding to the low energy grouping and the transverse line in Fig. 5.6b respectively. Moreover, the continuous distribution at higher energies, which looks rather plain in the sum energy spectrum, corresponds to the high energy events that tend to group along two lobes in Fig 5.6b. All these structures observed in the *180*^{o} coincidences indicate rich underlying nuclear mechanisms governing the emission of charged particles. Thus, from here on we are going to concentrate in the analysis of *180*^{o} coincidences.

The particle emitting channels following ^{11}Li β-decay that include the emission of two charged particles simultaneously are the 5-body 2α3n, 3-body nα^6He, 2-body ^{8}Li+t and ^{9}Li+d. The low recoil energy of the ^{9}Li ions, $Q_{\beta d}$=2.638 MeV [AWT03, Bac05], makes the contribution of the ^{9}Li+d channel negligible. Our detection threshold, including the effects of energy losses in the carbon foil and the detectors

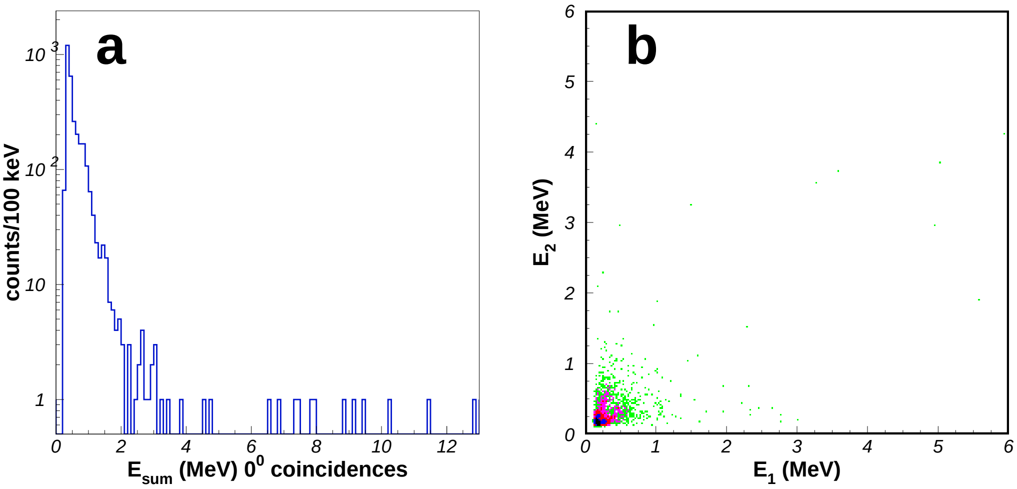

Figure 5.5: Left: (a) the coincidence energy sum spectrum collected in the first 40 ms after the proton impact collected in detectors either D2, D3 or D4, corresponding to 0° coincidences. Right: energy versus energy scatter plot corresponding to 0° coincidence events.

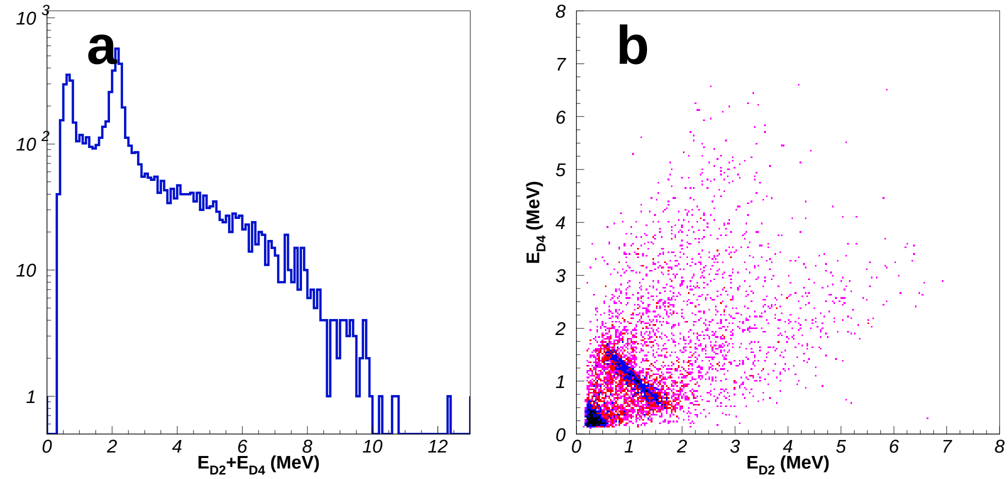

Figure 5.6: Left: the energy sum of ^{11}Li β-delayed coincidence spectrum collected during the first 40 ms after the proton impact. Right: Fig. b shows the energy versus energy scatter plot for charged particle coincidences between the D2 and D4 opposite detectors for t<40 ms. The major features of the plot are: (1) the intensity at low energy and the transverse line at low energies (corresponding to peaks at 0.7 and 2.2 MeV in figure a); (2) the scatter events at high energy form two lobes (at around 30 and 60 degrees).

dead layers, was ∼160 keV for α particles, that is a center mass energy of the ^{9}Li+d system ∼0.9 MeV. From the energy distribution given in [Raa08] we see 95% of the deuteron center of mass energy is below 1 MeV, thus we were not able to detect it. In the case of the ^{8}Li+t channel, however, the greater energy window, $Q_{\beta t}$=4.832(4) MeV [AWT03, Bac05], makes its detection in coincidence possible.

Contribution of the ^{8}Li+t channel to the charged particle coincidences

The ^{8}Li+t channel is sorted out from the data by kinematics. In order to look for the contribution of this channel in our experiment we can take advantage of the fact that the triton and the ^{8}Li in this channel are purely emitted in 180°. Imposing to the corresponding *180°* coincidences that the angle between the two detected particles is 7° or less (corresponding to two pixels separation, see section 3.1.2) will enhance this channel over the other ^{11}Li delayed particles. Moreover, we can identify the triton from ^{8}Li by kinematics, as the tritons must have more energy than the ^{8}Li. Figure 5.7 shows the triton spectrum obtained this way. By comparing to the previous spectrum by Borge et al. (see Figure 2 of [Bor97a]) we see that it should peak at around 1.5 MeV and not extend over 3 MeV. The blue highlighted area in the spectrum corresponds to the region where we expect to see the tritons, while the black highlighted area was used to estimate the background from other ^{11}Li decay channels. Both regions contain the same number of bins. Finally, we removed the area of 1 MeV peak above 20 counts, to take into account events from the 2.2 MeV sum energy peak (see Fig. 5.6a, and Section 6.4 of this thesis). The total number of events obtained is 224.

A more detailed study of the ^{8}Li+t channel was possible due to the enhanced statistics in the analysis of the 2007 data, presented in the next chapter, section 6.4.

5.3.1 Study of the breackup channels in coincidences in opposite detectors

The study of charged particle coincidences greatly enhances the 5-body $2\alpha3$n and 3-body nα^{6}He channels over the two body ^{8}Li+t and ^{9}Li+d channels. Thus, we will describe the charged particle coincidences using the three and five body channels. The first step would be to consider the previous decay modes suggested in [Lan81]. This includes the breakup of two states at 10.59 and 18.15 MeV in ^{11}Be fed by the β-decay into the three-body and five-body channels, shown in Fig. 5.1 . The nα^{6}He and $2\alpha3$n breakup of the 10.6 MeV was proposed to occur through an intermediate state at 9.5 MeV in ^{10}Be, whereas the three and five body breakup of the 18.15 MeV state was modeled using phase space energy sharing.

In order to test this model of the breakup of states in ^{11}Be we performed a Monte-Carlo simulation and compared the resulting spectra with the data. Monte-

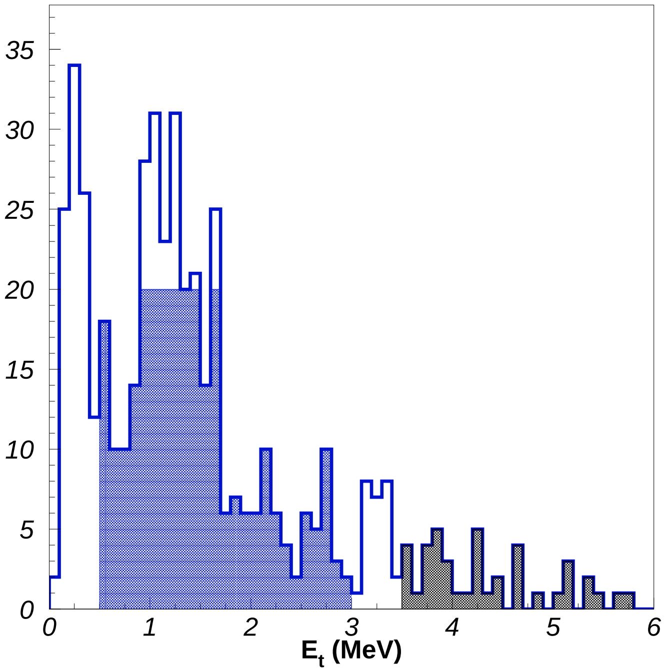

Figure 5.7: Determination of of the βt branching ratio detected in the 180° coincidences where the angle θ between the two detected particles is in the region 173° $< \theta <$180°. The blue region indicates the region we used to calculate the triton area. This region is taken from the triton energy spectrum of Borge et al. [Bor97a], which ends at 3 MeV, although the tritons can have energy above 3 MeV from the Q_β=4.832(4) MeV [AWT03, Bac05]. The peak counts above the blue area (37 counts) were subtracted, as we consider they correspond the ^{6}He+α breakup of ^{10}Be(9.5 MeV). The black region (43 counts) corresponds to an area of equivalent number of channels as the blue region used to estimate the background. This results in 224 counts assigned to the ^{8}Li+t channel.

Carlo simulations of the breakup channels are needed to take into account the effect of the angular acceptance and analysis cuts into the bare energy spectrum given from the breakup kinematics. Thus Monte-Carlo simulation included the different factors that account for the acceptance of the setup and the analysis:

- Energy losses in the carbon-foil stopper.
- Angular acceptance of the detectors.
- Detectors energy thresholds.
- Analysis filters, as described in Chapter 3.

Figures 5.8a and 5.8b show the result of a Monte-Carlo simulation of these channels. Although the simulation in Fig. 5.8a reproduces rather well the sum energy spectrum, the high energy part of the scatter plot in figure 5.8b is very different from the data in Fig. 5.6b. The simulation components show that the low energy part is dominated by the breakup of the 10.59 MeV state in ^{11}Be, whereas the high energy part corresponds to the breakup of the 18.15 MeV state in ^{11}Be. This indicates that the breakup of the 10.59 MeV state in ^{11}Be is correctly described as occurring through an intermediate state in ^{10}Be, but the democratic energy sharing model is not enough to explain the features observed in the breakup of the 18.15 MeV state in ^{11}Be. Let us take an individual look into the breakup of each state.

5.3.2 Breakup of 10.59 MeV state in ^{11}Be

The 10.59 MeV state in ^{11}Be has been suggested to break up into the $2\alpha 3$n and n$\alpha ^6$He channels through an intermediate state in ^{10}Be [Lan81]. This state in ^{10}Be was assumed from energetic calculations to be the previously observed state at 9.4 MeV and with a width of 290(20) keV [And74]. In order to test that hypothesis we studied the ^{6}He-α relative energy in the n$\alpha ^6$He channel. We selected events in this channel by gating events whose $E_{D2}+E_{D4}$ energy is between 1.82 and 2.5 MeV (see figure 5.8a). Figure 5.9 shows the resulting ^{10}Be excitation energy, where the α separationenergy in ^{10}Be is added $Q_{^6He+\alpha}$=7.413 MeV, showing the presence of a ^{10}Be resonance at approximately 9.5 MeV and 300 keV wide.

A recent study of the Li(^{7}Li,$\alpha ^6$He)α reaction experiment found a level in ^{10}Be at 9.56(2) MeV excitation energy and 141(10) keV width [Cur01]. We performed a Monte-Carlo simulation of the breakup of the ^{11}Be 10.59 MeV state using the multiple-level single-channel R-matrix formalism to describe the resonances (see Chapter 3), with the parameters of the ^{10}Be resonance taken from the experiment mentioned before. The χ^2 test of the simulation results in 321 for 12 degrees of freedom, unacceptable high. We optimized the Monte-Carlo simulation by minimizing

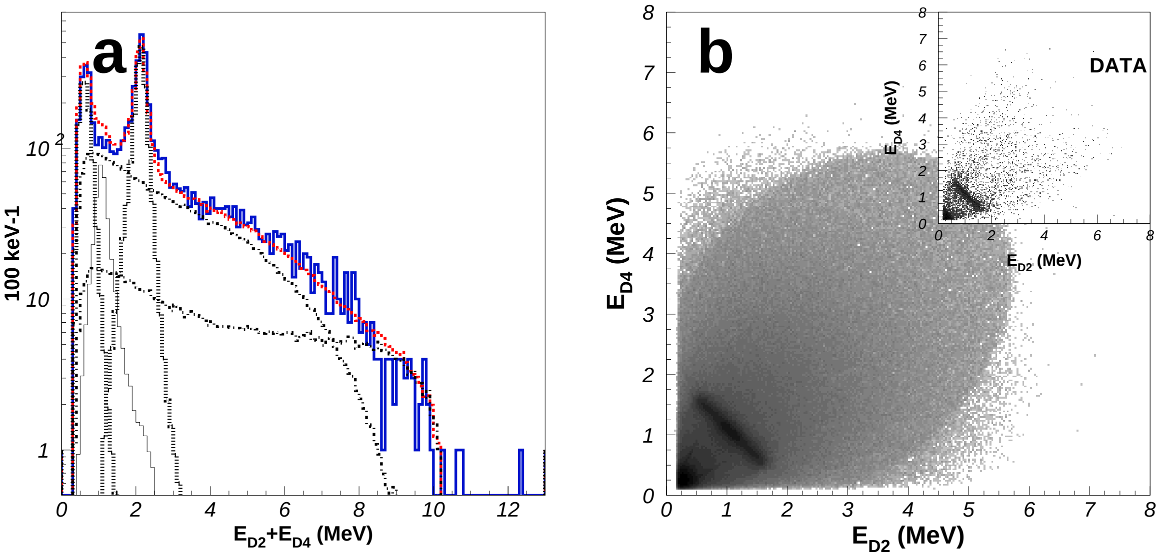

Figure 5.8: Left: the sum energy of the charged particle coincidences is shown in blue. The red dashed histogram is the result of a Monte-Carlo simulation of the charged particle decay channels as described in the literature [Lan81, Bor97a]. The black-dotted histograms correspond to the breakup of the 10.59 MeV state in ^{11}*Be, to* $2\alpha 3n$ *and* $n\alpha^6$*He. The black dash-dotted histograms correspond to the breakup of the 18.15 MeV state, again to* $2\alpha 3n$ *and* $n\alpha^6$*He. Right:Monte-Carlo simulation of the expected* E_{D2} *vs* E_{D4} *scatter plot of the* ^{11}*Li* β*-delayed charged particles assuming the decay channels proposed in Refs. [Lan81, Bor97a], and schematically shown in Fig. 5.2. The main features are reproduced. However, the high energy distribution, modeled as phase-space of the* ^{11}*Be(18.15 MeV) level breaking into 3-body and 5-body particles, is very different from the experimental distribution shown in the inset. In particular the shape of the high energy part does not follow the structure observed in Fig 5.6(b) .*

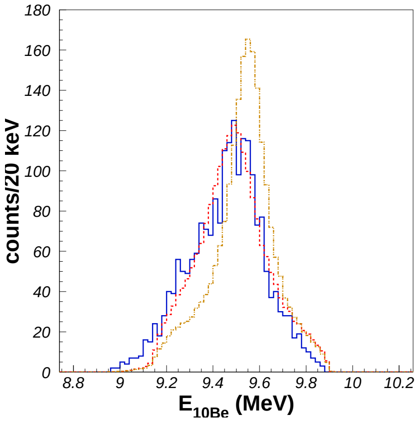

Figure 5.9: Ihe calculated excitation energy in ^{10}*Be for events gated in the n*α^6*He breakup of the state at 10.59 MeV in* ^{11}*Beis shown in blue. The red histogram corresponds to a Monte-Carlo simulation of the breakup using the best fit parameters,* E_0*=9.52 MeV and* γ^2*=0.21 MeV, while the gold histogram corresponds to a Monte-Carlo simulation of the breakup using the parameters of Curtin et al,* E_x*=9.56(2) MeV and* Γ*=141(10) keV [Cur01]. Both simulations are normalized to the area of the data.*

the χ^2 test of the ^{10}Be spectrum. We performed the simulation with 5 different ^{10}Be level centroids and widths, and calculated the χ^2 value of each simulation. The resulting points were fitted to a parabola (shown in figs 5.10a and 5.10b), the expected behavior of the χ^2 squared distribution, and the minima of E_0 and γ^2 obtained were 9.52(2) and 0.21(4) MeV respectively (Γ=0.30(4) MeV). This result is not compatible with the reaction study mentioned above, specially due to the different FWHM of the resonance. Therefore, we cannot conclude that the resonance we see is the same as the one in the two experiments. Table 5.1 shows the parameters of the ^{10}Be resonance obtained in this work with the results of states observed in this energy region in reaction experiments.

In order to describe the ^{11}Be resonance at 10.59 MeV we used the literature values of E_0 and FWHM taken from [Ajz78]. In principle, it is possible to calculate the excitation energy in ^{11}Be from the three body nα^6He channel by calculating the neutron energy from momentum and energy conservation in the detected α plus ^{6}He and summing the energies of the three particles. However, the neutron energy reconstruction depends on the identification of the ^{6}He from the α, which is not possible in our setup. Even using a naive approximation as assuming that the highest energy particle detected is the alpha, it is not perfect, as our simulations of the breakup of the 10.59 MeV state in ^{11}Be indicate that in 20% of the events the energy of the ^{6}He is higher than that of the alpha particle.

Table 5.1: Resonances in ^{10}Be around 9.5 MeV observed in reaction experiments and the value obtained in thsi work.

E_x (MeV)	J^π	Γ (keV)	Ref.
9.52(2)		0.21(4)	this work
9.27	(4^-)	150(20)	[Ajz88, Ham94a, Soi96]
9.4	$(2)^+$	291(20)	[Ajz88]
9.64(20)		[Ham94a]	
9.56(2)		296(15)	[Cur01]

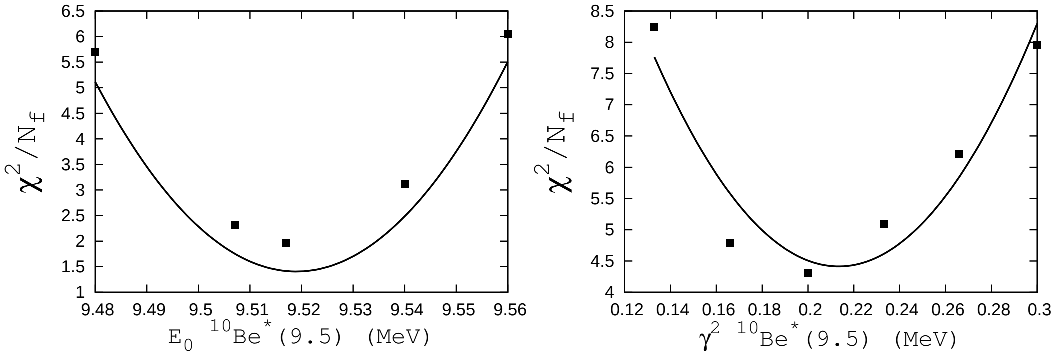

Figure 5.10: Left: The squares indicate the normalized results of a χ^2 test for five different centroid energies E_0 in a Monte-Carlo simulation of the ^{6}He+α breakup of the 9.59 MeV state in ^{11}Be. The parabolic fit minimum is at 9.52 MeV, and shows a width of 0.02 MeV at points of the minimum ±1 normalized χ^2. Right: normalized results of χ^2 test of five different γ^2 in a Monte-Carlo simulation of the same ^{6}He+α breakup of figure a. The parabolic fit minimum is at 0.21 MeV, with a width of 0.04 MeV at points of the minimum ±1 normalized χ^2. All individual χ^2 fits are listed in Table 5.2

Table 5.2: Results of the χ^2 tests performed to eleven different Monte-Carlo simulations of the ^{11}Be(10.6)→n+^{10}Be(∼9.5)→n+α+^{6}He channel. Five E_0 and six γ^2 parameter values were used in the calculation of R-matrix for the ^{10}Be ∼9.5 MeV state.

E_0 (MeV)	χ^2/n_{free} (n_{free}=17)	γ^2 (MeV)	χ^2/n_{free} (n_{free}=17)
9.48	5.692	0.133	8.25
9.507	2.306	0.166	4.79
9.517	1.957	0.2	4.31
9.54	3.108	0.233	5.085
9.56	6.057	0.266	6.207
		0.3	7.962

Finally the five-body 2α3n breakup of the 10.59 MeV state in ^{11}Be was described in a Monte-Carlo simulation using the same R-matrix parameters as in the three-body channel, shown in Table 5.4. The 2α+2n breakup of the state at 9.52 MeV in ^{10}Be was simulated using phase space energy sharing via the GENBOD code from CERNLIB. The simulated sum energy spectra of the three-body and five-body channels are shown as the two dotted peaks in the energy spectrum of Fig. 5.8a, the peak at 0.7 MeV corresponding to the the five-body channel and the peak at 2.2 MeV to the three body one. In the scatter plot of Fig. 5.8b they correspond to the low energy grouping and the transverse line, which reproduce very well the experimental features of Fig. 5.6b.

5.3.3 Breakup of the 18 MeV state in ^{11}Be

In the previous work of Langevin and colaborators [Lan81] it was proposed that the ^{11}Be 18 MeV state decays only by the five body 2α3n channel, and that the kinematics of the breakup are governed by phase space energy sharing. Assuming a resonance energy of 18.5 MeV [Lan81] (and assuming the state is narrow), and taking into account that the 2α3n channel is 8.88 MeV above the ^{11}Be ground state, the Q value of the five body breakup of this state is 9.62 MeV. Therefore, the energy distribution of the charged particles emitted from the ^{11}Be 18 MeV state corresponds to the high energy wide distribution of events in Fig. 5.6(b), as previously proposed by Lagevin et al. [Lan81], and confirmed by the simulation presented in Figs, 5.8(a) and (b). However, if we compare in detail the experimental scatter plot of Figs. 5.6b and the Monte-Carlo simulation, shown in Fig. 5.8b indicates that the shape of the distribution of the high energy coincidence events is not well reproduced by phase

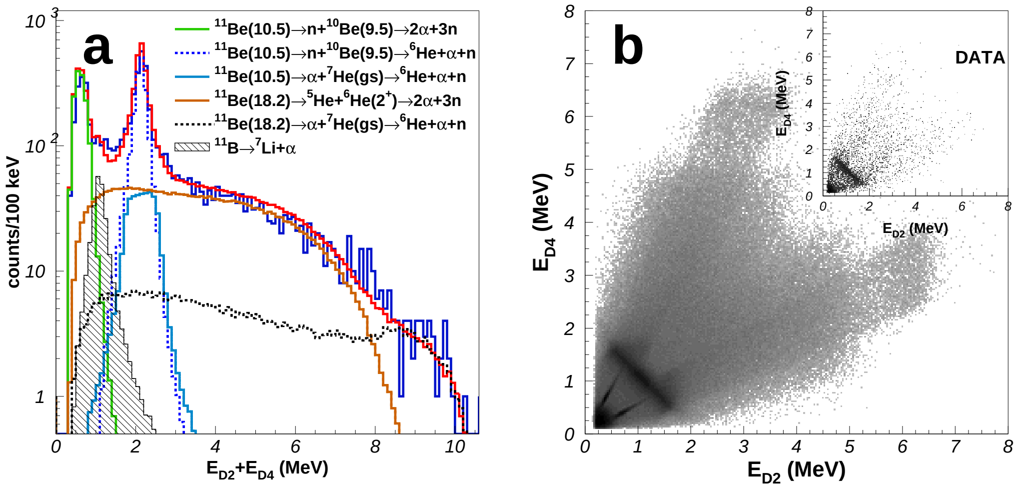

Figure 5.11: Left: Sum energy spectrum in blue, Monte-Carlo simulation including the ^{A}He channels in red. The different breakup channels are also shown, with color code according to the legend. Right: Fig. b shows the E_{D2} vs E_{D4} scatter plot of the Monte-Carlo simulation of the ^{11}Li β-delayed charged particle breakup including the new channels through He isotopes listed in Table 5.5. The shape of the simulation is close to the experimental distribution, shown in the insset.

space energy sharing. Careful inspection of the high energy region reveals that the coincidences are not evenly distributed, they rather form two elongated bumps or lobes, which are not present in the smooth simulation. This is not a surprise, as the 5-body and 3-body breakup of the 18.15 MeV state in ^{11}Be are simulated using a phase space momentum distribution, which neglects the role of possible structure effects.

As just noted, the slope of the lobes in the scatter plot of Fig. 5.6b corresponds to lines of slope 7/4 and 4/7. This structure corresponds to a mass-asymmetric two-body breakup where the initial state is broad. The only mass 4 and mass 7 isobars energetically allowed for ^{11}Li β-decay are ^{7}He+α. This comes naturally, as alpha emission is common to all Be isotopes. Furthermore, the ^{7}He(gs) is the only resonance in ^{7}He below the α+3n threshold, see Fig. 5.2, thus it is a natural choice as intermediate state in the 3-body breakup of ^{11}Be, *i.e.* ^{11}Be(18.15 MeV)→ α+^{7}He(gs)→n+^{6}He+α. The energy distribution of this decay channel appears as two body breakup because it keeps memory of the first step if this Q value is much larger than the second one. It is known that the ^{7}He(gs) is situated 445 keV above the ^{6}He+n threshold [Til04], therefore the recoil energy given by the emission of the neutron will be low. The ^{6}He energy in the laboratory frame is given by the center of mass energy from the ^{7}He→^{6}He+n breakup plus the recoil boost due to the ^{7}He+α breakup, in the form

$$\overrightarrow{P}_{^6He} = \overrightarrow{P}^{CM}_{^6He} + \frac{m_{^6He}}{m_{^7He}} \overrightarrow{P}_{^7He} \tag{5.1}$$

where

$$\left|\overrightarrow{P}^{CM}_{^6He}\right|^2 = 2m_{^6He}(\frac{m_n}{m_{^7He}} 0.445 \text{ MeV}) \tag{5.2}$$

$$\left|\overrightarrow{P}_{^7He}\right|^2 = 2m_{^7He}E_{^7He} \tag{5.3}$$

where E$_{^7He}$ is the recoil energy value, $\frac{4}{7}$E$_\alpha$. As the center of mass energy is small, 64 keV, the ^{6}He momentum is dominated by the second term. Therefore, the ^{6}He energy will follow the 4/7 ratio to the alpha energy, as observed in the scatter plot, and will necessarily be lower than the alpha energy. Thus, the distribution of the two detected charged particles, α and ^{6}He, in the scatter plot will kinematically be very close to a two body breakup, but broadened by the recoiling neutron, which have very low energy. Other possible intermediate steps involving the ground state of ^{6}He and the ^{5}He(gs) resonance would also end up in the 3-body nα^6He channel, but in this case the slope of the two bands would be 6/5 and 5/6, quite different from the experimental distribution.

It is important here to point out that the 3-body breakup of the 18.15 MeV state in ^{11}Be through the ground state of ^{7}He cannot be the only decay channel, as in previous experiments a factor of roughly 5 α particles per ^{6}He ion was determined for the decay of the ^{11}Be 18 MeV state [Lan84]. This implies that the majority of the high energy events correspond to the 2α3n channel. However, the phase space description of the 2α3n channel is not able to explain the energy distribution of coincidence events. On the contrary, if sequential decay is assumed, the first step could be ^{6}He(2$^+$)+^{5}He(gs), as both states are above the α+2n and α+n thresholds, resulting in the 2α3n final channel. This channel is a very good candidate, as the states are broad, widths of 0.113 and 0.648 MeV respectively [Til04], spreading the coincidence data in a similar way as the 5-body phase space distribution, but with a dip in the central part, E$_{D2}$ $\simeq$ E$_{D4}$, as observed in the scatter plot of Fig. 5.6b.

We performed a Monte-Carlo simulation of the two breakup channels, three-body through ^{7}He and five body through ^{6}He(2$^+$)+^{5}He(gs), where the resonances were described by single channel R-matrix formalism. This simulation, plus the other two channels discussed in the breakup of the 10.59 MeV state are shown in Fig. 5.11. Furthermore, the breakup of the 10.59 MeV state into α+^{7}He(gs) was considered as a possible contributing channel, as the fingerprint of this channel was seen near the transverse line (see Fig. 5.6*b*). Although this channel is expected to

Table 5.3: Results of the χ^2 tests of the energy difference plot, with $4.5<E_{D2}+E_{D4}<6$ MeV. The ^{A}He breakup of the state at 18.15 MeV in ^{11}Be is favored over the phase space description of the breakup, although a 20% mixture of ^{A}He breakup and phase space cannot be statistically distinguished from the pure ^{A}He breakup.

Breakup channel	χ^2	N_{free}
^{A}He	20.0	24
Phase space	39.5	25
$0.8\times(^A\text{He})+0.2\times$(phase space)	22.65	23
$0.5\times(^A\text{He})+0.5\times$(phase space)	27.87	23
$0.25\times(^A\text{He})+0.75\times$(phase space)	31.27	23

contribute with ten times less intensity than the decay through ^{10}Be, the normalized χ^2 fit of the sum energy spectrum improves by 20% if this channel is included.

In order to check the goodness of the breakup through ^{A}He isotopes model against the phase space sharing description we studied the energy difference spectrum, defined as

$$E' = \frac{1}{\sqrt{2}}(E_{D2} - E_{D4}) \tag{5.4}$$

This is the best parameter to enhance channels where the decay kinematics group the events across the scatter plot instead of scattering them evenly, as expected from pure phase space kinematics. We selected two regions in Fig. 5.11a to project the energy difference spectrum. In the region for $E_{D2}+E_{D4}>8.2$ MeV we expect the ^{7}He+α breakup of the state at 18.15 MeV in ^{11}Be to dominate. We selected the region $4.5<E_{D2}+E_{D4}<6$ MeV to maximize the contribution of the $2\alpha3n$ breakup of the state at 18.15 MeV in ^{11}Be. The resulting energy difference spectrum are shown in Figs. 5.12a and 5.12b, with the Monte-Carlo simulations of both breakup models. In the case of Fig. 5.12b we see that the ^{A}He breakup is clearly favored over the democratic phase space energy sharing. However, in Fig. 5.12b, were the ^{6}He(2^+)+^{5}He(gs) dominates, the results were not clear, so we performed a χ^2 test of both simulations.

The χ^2 tests were performed to Monte-Carlo simulations of the breakup of the 18.15 MeV state in ^{11}Be fully described by either decay through ^{A}He intermediate resonances or democratic phase space sharing. Furthermore we checked the possibility of a mixture of ^{A}He decay and democratic phase space in different percentages. The results of the tests, shown in table 5.3 indicate that the ^{A}He decay is favored, but up to a 20% of democratic phase space is statistically indistinguishable from the ^{A}He decay only.

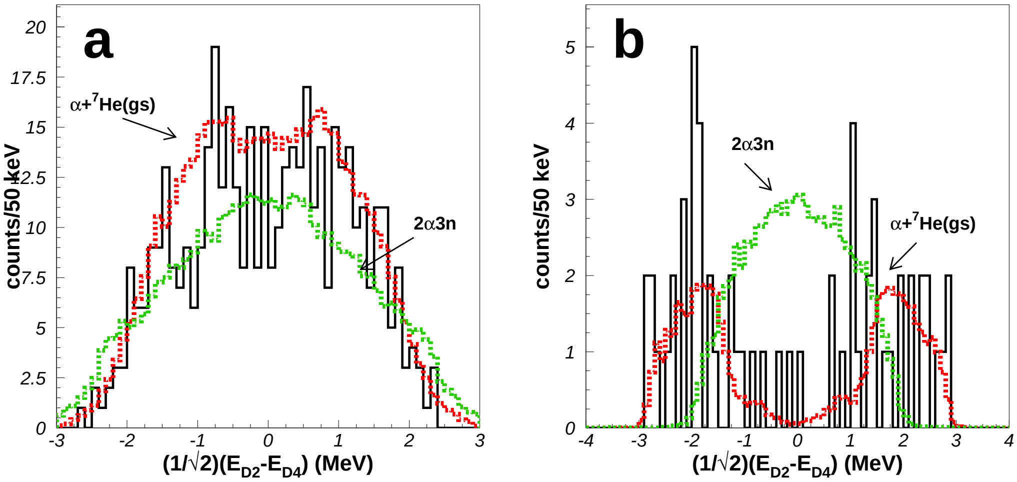

Figure 5.12: Left: energy difference spectrum of coincidence evet) for events with $4.5 \leq E_{sum} \leq 6$ MeV (black line) compared to two Monte-Carlo simulations: in red the one including the ^{7}He(gs) and in green the one corresponding to the 5-body phase-space breakup channel. Right: b shows the spectrum of the energy difference for events with $8.2 \leq E_{sum} \leq 10$ MeV, with the same simulations as in a. The contribution of the ^{7}He(gs) channel is necessary to successfully reproduce the central dip in the experimental distribution.

Table 5.4: The level centroid and reduced widths used in the R-Matrix description of the states modeled in the Monte-Carlo code. The Γ was obtained from a gaussian fit of the R-matrix peak directly.

	E_0 (MeV)	γ^2 (MeV)	Γ (MeV)	Ref.
^{11}Be(10.59 MeV)	10.59	0.21	0.227	[Ajz78]
^{11}Be(18.15 MeV)	18.15	0.07 (3−*body*) 0.06 (5−*body*)	0.8	[Bor97a]
^{10}Be(9.5 MeV)	9.52(2)	0.21	0.30(4)	This work
^{7}He(gs)	$0.43^{\dagger}$	0.4	0.148(1)	[Til04]
^{6}He(2^{+})	1.8	0.113	0.117(1)	[Til04]
^{5}He(gs)	$0.895^{\ddagger}$	2.5	0.658(4)	[Til04]

† above the ^{6}He+α threshold.

‡ above the α+n threshold.

Table 5.5: β-fed states in ^{11}Be above the charged particle thresholds and their breakup channels.

Decay channels proposed previously.	Decay channels from this work.
$^{11}\mathrm{Be}(10.59) \xrightarrow{n} {}^{10}\mathrm{Be}(9.5) \xrightarrow{\alpha} {}^{6}\mathrm{He}$ [Lan81] $\rightarrow 2\alpha 3\mathrm{n}$ [Lan81]	$^{11}\mathrm{Be}(10.59) \xrightarrow{n} {}^{10}\mathrm{Be}(9.5) \xrightarrow{\alpha} {}^{6}\mathrm{He}$ $\rightarrow 2\alpha 3\mathrm{n}$ $\xrightarrow{\alpha} {}^{7}\mathrm{He(gs)} \xrightarrow{n} {}^{6}\mathrm{He}$
$^{11}\mathrm{Be}(18.15) \longrightarrow 2\alpha 3\mathrm{n}$ [Lan81] $\rightarrow \mathrm{n}\alpha{}^{6}\mathrm{He}$ [Bor97a]	$^{11}\mathrm{Be}(18.15) \longrightarrow {}^{6}\mathrm{He}(2^{+}) + {}^{5}\mathrm{He(gs)} \longrightarrow 2\alpha 3\mathrm{n}^{\dagger}$ $\xrightarrow{\alpha} {}^{7}\mathrm{He(gs)} \xrightarrow{n} {}^{6}\mathrm{He}$

† Up to a 20% admixture of the ^{11}Be(18.15)$\rightarrow 2\alpha 3$n direct channel cannot be excluded (see text).

5.3.4 Summary of the study of the breakup mechanism

We have studied the *180°* charged particle coincidences, determining the breakup channels of the states at 10.59 and 18.15 MeV in ^{11}Be using Monte-Carlo simulations. The ^{11}Be resonances were described using the non-interfering R-matrix formalism, with parameters listed in Table. 5.4. All parameters were obtained from the literature, except for the parameters of the 9.5 MeV state in ^{10}Be, which were obtained from a χ^2 minimization of the Monte-Carlo simulation.

We confirm the two decay channels of the 10.59 MeV state in ^{11}Be, $2\alpha 3$n and n$\alpha{}^6$He through an intermediate state at 9.5 MeV in ^{10}Be [Lan81]. On top of these two previously known channels we propose the breakup of the state at 10.59 MeV in ^{11}Be through the ground state of the ^{7}He resonance, which improves the overall fit of the sum energy spectrum. In the case of the breakup of the 18.15 MeV state in ^{11}Be, we propose that the $2\alpha 3$n and n$\alpha{}^6$He final states from the breakup of the 18.15 MeV state occurs through intermediate steps involving ^{6}He(2^+)+^{5}He(gs) and ^{7}He(gs)+α. The study of the energy difference spectrum, which is related to the degree of assimetry of the scatter plot in Fig. 5.6b, favors this interpretation against the democratic phase space description of the breakup. Table 5.5 summarizes the decay channels studied in this work, compared to those previously known.

5.4 Determination of the Branching Ratios.

In β-decay studies the branching ratios are normally obtained by observing all decay channels and normalizing the intensities to 100%. However, in our case, we can only normalize the charged particle channels, so we had to find a way to normalize the

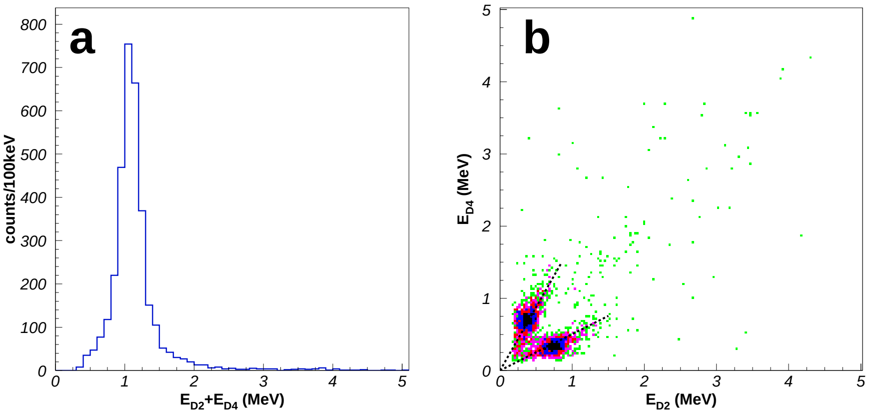

Figure 5.13: Left: 180° *sum energy spectrum for events gated in a time window 0.15 ⩽ t < 4 s. The ∼1 MeV peak corresponds to the* ^{11}*Be βα channel. Right:* E_{D2} *versus* E_{D4} *scatter plot for events selected in the same time window as in (a). The two point-like regions correspond to the ∼1 MeV peak in (a). The two dotted lines of 7/4 and 4/7 slope indicate the phase space region (see section 6.3.1) where a two body breakup of masses 4 and 7 occurs.*

channel intensities.

In order to normalize the results we calculated the number of ^{11}Li β-decays during the experiment from the β-delayed ^{7}Li+α activity from the decay of the daughter nucleus ^{11}Be ($T_{1/2}$=13.81(8)s [Ajz88]), measured for a time window of 0.15 $\leqslant$ t $<$ 4 s after the proton impact, where after 4 s the clock reset. We chose a time window after 150 ms to clean the spectrum from the contribution of ^{11}Be β-decay events ($T_{1/2}$=8.5 ms [Ajz88]), altohugh there is tradeoff in that we do not measure the full activity of ^{11}Be β-decay. From the analysis of the background in the time spectrum (see section 2.3) we estimate $\lesssim$2% of the total ^{11}Be activity appears in the first 150 ms. Figure 5.13(a) and (b) show *180^0* sum energy and scatter plot for the selected time window. The ∼1 MeV peak in the sum energy region is identified as the β-delayed ^{7}Li+α breakup of the daughter ^{11}Be nucleus from the associated two point-like regions in the scatter plot. The two regions are identified as coming form the $\beta\alpha$ channel due to them laying on lines of 7/4 and 4/7 slope, corresponding to asymmetric two body breakup of mass ratio between the two fragments of 7/4 (see section 6.3.1). The area of the 1 MeV peak, $N_{\beta\alpha}$, the $\beta\alpha$ activity, is 3069. We determine the number of ^{11}Li decays, A(^{11}Li) from this number as

$$A(^{11}Li) = \frac{N_{\beta}\alpha}{BR_{\beta\alpha}BR_{1/2^{-}\epsilon}} \tag{5.5}$$

Table 5.6: Branching ratios of the channels determined in this work following ^{11}Li β-decay. The total branching ratio to charged particle emitting channels obtained in [Lan81] is 3.1(9)%, compared to the value of 1.73(2)%. in our work. The ^{11}Li activity was deduced from the branching of the β-(^{7}Li+α) decay channel of the daughter.

Channel	β-feeding (%)	β-feeding (%)§
^{11}Be(10.59)$\rightarrow$n+^{10}Be(9.5)$\rightarrow$2α+3n	1.1(2)	1.4(2)
^{11}Be(10.59)$\rightarrow$n+^{10}Be(9.5)$\rightarrow$n+α+^{6}He 0.23(4)	0.29(4)	
^{11}Be(10.59)$\rightarrow$ α+^{7}He$\rightarrow$n+α+^{6}He 0.035(6)	0.044(7)	
^{11}Be(18.15)$\rightarrow$^{6}He(2^{+})+^{5}He$\rightarrow$2α+3n	0.34(5)	0.43(7)
^{11}Be(18.15)$\rightarrow$ α+^{7}He$\rightarrow$n+α+^{6}He	0.057(9)	0.072(10)

§ Assuming a 2% feeding to the ground state in ^{11}Be, stated as upper limit in previous works [Bjo81].

$BR_{\beta\alpha}$, 2.9(4)%, is the value for ^{11}Be β-decay branching ratio to the 9.8 MeV state in ^{11}B [AMW81]. Finally, $BR_{1/2^-}$ is the ^{11}Li β-decay branching ratio to the first excited state in ^{11}Be(1/2$^-$). We used 7.4(3) %, which is the weighted average of the values from [Bor97b, Bjo81, Aoi97, Mor97, Det80].

Finally, the contribution of each channel was obtained from the Monte-Carlo simulation, rather from the direct experimental data, as the experimental coincidence efficiency is difficult to determine. The values shown in the second column in Table 5.6 were obtained assuming negligible β-feeding to the ^{11}Be ground state. The third column shows the branching ratios obtained assuming 2% β-feeding to the ^{11}Be ground state. A possible source of uncertainty in the estimation of the β-feeding values is the presence of ^{11}Be ions in the incoming ^{11}Li beam. Direct production of ^{11}Be up to a few percent of the ^{11}Li beam has been observed previously at ISOLDE [Bor97b]. If this is the case, the branching ratios will increase in the same few percent as the direct production of ^{11}Be.

Chapter 6

Study of the ^{11}Li β-delayed charged particle channels

Part II: 2007 experiment

In order to confirm the results of the 2003 experiment shown in the previous chapter, in particular the decay through the ^{5,6}He resonances for the 2α3n channel and a the new breakup channel involving the ground state resonance of ^{7}He, $^{11}\text{Be}^{*}\rightarrow\alpha+^{7}\text{He(gs)}\rightarrow\text{n}+\alpha+^{6}\text{He}$, we performed a new experiment in 2007 with the purpose of characterizing the latter channel. The type of setup presented in this study is ideal to study the breakup of states in ^{11}Be that ends in a three body system. We use the analysis techniques of the breakup kinematics described in section 6.3.1 to determine the excitation energy and the spin of the states that contribute to the breakup. The study of the ^{7}He+α channel allowed for the identification of two states at 16 and 18 MeV decaying through the ^{7}He channel. Moreover we determined that their spin and parity is $3/2^{-}$ by studying the breakup angular correlations in the ^{7}He+α channel.

Furthermore, we also studied the ^{11}Li β-delayed ^{8}Li+t channel, using a new selection method based on kinematics. As the βt channel is a two body breakup, the two particles are emitted strictly at 180° between them. Thus, we selected from the two particle coincidences those detected in opposite pixels, scanning through the 256 possible pairs. Moreover, as the energy ratio between the two emitted particles corresponds to their mass ratio, we were able to select specifically triton events from the remaining events detected in opposite pixels. The analysis of the triton spectrum allowed us to confirm that the βt channel occurs through the 18 MeV state in ^{11}Be and obtain a new value of the channel branching ratio.

With this two complimentary approaches, and the study of the charged particle emission from the ^{11}Be 10.59 MeV state presented in the previous section, we obtained the ^{11}Li β decay branching ratios to states above the charged particle thresholds, except for the ^{9}Li+d channel. This a crucial step to study the ^{11}Li B(GT) distribution, as the study of the β-decay of other even neutron rich nuclei in the region terminating the A=6,8,9 series, ^{6,8}He and ^{9}Li [Bor91] show strong feeding to states close to the Q_{β}. In fact, the B(GT) we obtained for the ^{11}Be 18 MeV state is large compared to its neighbour states, as previously observed in the β-decay of ^{6,8}He and ^{9}Li. We also compared the B(GT) distribution to a shell model calculation of ^{11}Be, described in the full *p* and *sd* shells. The calculated B(GT) of $3/2^{-}$ states above the charged particle thresholds is remarkably similar to the experimental B(GT) distribution, further supporting the spin assignment from angular correlations.

Following the points described above, the analysis of the 2007 experiment is divided in three sections:

- **Study of the ^{11}Li β-delayed ^{7}He+α channel.** We studied the kinematics of the channel in order to determine which states in ^{11}Be decay through this intermediate state. From the angular correlations in the breakup we deduced their spins and parities. We also determined the five body $2\alpha 3$n and three body nα^{6}He partial branching ratios of these states.

- **Kinematical identification of the ^{8}Li+t channel.** We used the kinematical properties of a two body breakup, strict 180° angle between the emitted particles and relative energies given by the fragments masses to identify the ^{8}Li+t in the charged particle coincidence spectrum. We obtained the branching ratio of this channel.

- **Study of the ^{11}Li B(GT) distribution.** We calculated the B(GT) distribution from the branching ratios obtained from both the three body and five body channels and from the ^{8}Li channel. We compared the ^{11}Li β-strength distribution to that of its core ^{9}Li. Finally, the ^{11}Li B(GT) distribution was compared to a calculation using the shell model.

Before entering in detail of the analysis let us summarize the experimental setup used in the 2007 experiment.

6.1 description of the experimental setup

The ^{11}Li ions selected using the General Purpose Separator (GPS) were implanted in a 50 μg/cm^{2} thin carbon foil, located in the center of the setup (see Fig. 6.1), in order to measure the decay at rest. We measured the activuty of the $\beta\alpha$ decay

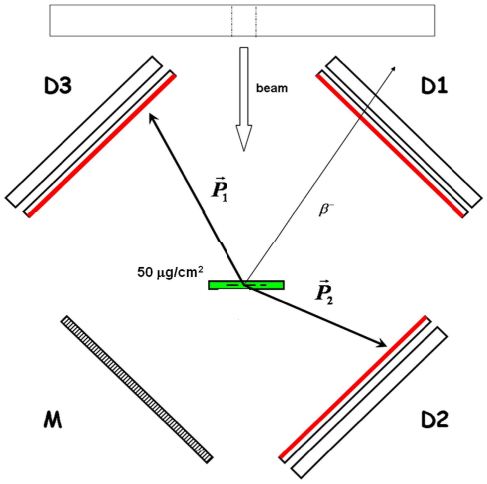

Figure 6.1: Schematic view of the 2007 experiment. Detector M corresponds to a prototype monolithic telescope mounted for testing purposes [Amo08].

channel of the daughter nuclei ^{11}Be, and assuming no direct production of ^{11}Be, we estimate a production of ∼800 ^{11}Li ions in our experimental setup. The GPS transmission efficiency was estimated to be 50%, indicating a production of 1.6×10^3 Li/s

The charged particle detection was provided by three particle telescopes, all of them with new ultrathin DSSSD stacked with 1.5 mm thick Si pads for beta signal and veto. The angular acceptance of the detectors was given by their distance to the carbon foil. Detectors D1 and D3 (see Fig. 6.1) were placed 5 cm away from the carbon foil, thus covering ∼4% of 4π, whereas detector D2 was placed 3.7 cm away from the foil, covering ∼7% of 4π. We can make a rough estimate of the improvement over the 2003 experimental run by using the angular acceptance of measuring two isotropically emitted particles in coincidence, $2\Omega_1\Omega_2$. In 2003 we obtained a 0.3% of 4π whereas in 2007 we obtained a 0.6% of 4π, i.e. a factor of 2 increase.

The experimental cuts and conditions necessary to clean the data, as described in Chapter 2, were applied. The noise present in the low end of the raw spectra was eliminated by applying the thresholds obtained from the α-calibration sources to the low energy data. The energy losses in the carbon-foil and detectors dead-layers were reconstructed, and the DSSSD front and back spectra were energy matched to ensure that the data belong to physical events.

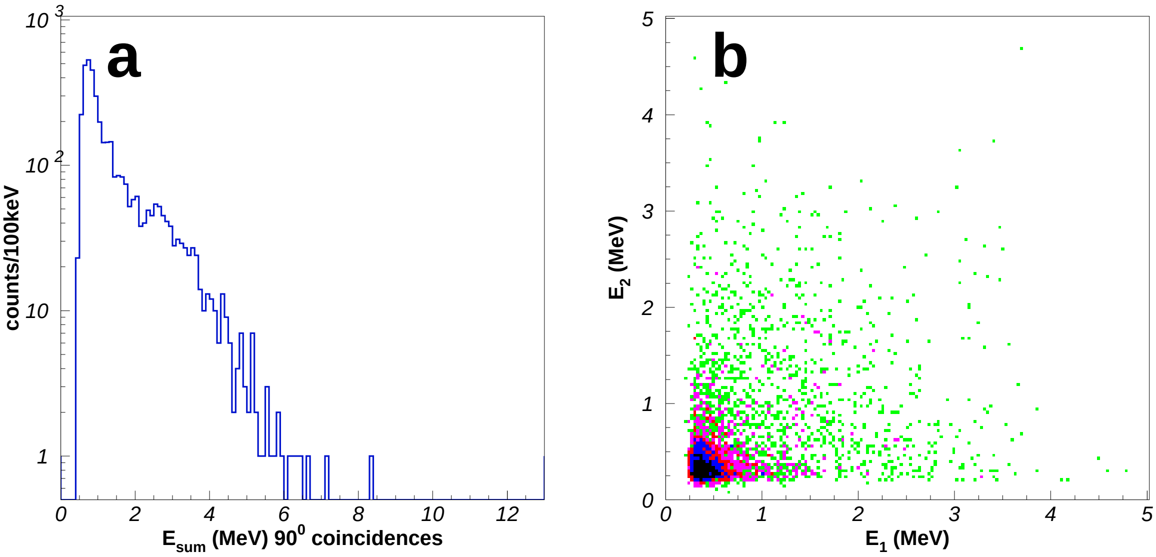

Figure 6.2: Left: sum energy spectrum corresponding to 90° *coincidences of 2007 experiment. Right: scatter plot for the 90° coincidences. Notice the substantial increase of statistics compared to the data from the 2003 experiment in Figs. 5.4.*

6.2 Analysis of charged particle coincidences

As indicated in the section corresponding to the 2003 experiment, the singles charged particle spectra do not contain the relevant information in the study of the ^{11}Li β-delayed charged particle emission. Because of this, in the analysis of the data belonging to the 2007 experiment we started directly our analysis studying the charged particle coincidences, where the three body nα^6He and five body channel 2α3n channels were previously identified by Langevin and colaborators [Lan81] and the work presented in this Thesis in the previous section.

The geometry of the setup defines three types of two particle coincidences defined by the detectors hit (see Fig. 6.1). Detectors D1 and D3 were 5 cm away from the carbon foil stopper, while detector D2 was 3.7 cm away. This makes some differences in the angle covered depending if detector D2 was hit or not. Detectors D2 and D3 are opposite to each other, thus defining *180°* coincidences, which correspond due to the size of the detectors and closer distance of D2 to the carbon foil to particles detected with angles between 120° and 180°. Hits in D1 and either D2 or D3, classified as *90°* coincidences, covered angles from 31° to 149° between the detected particles. Finally, coincidences detected in the same detector, classified as *0°* coincidences, covered angles from 0° to 50° between the detected particles for

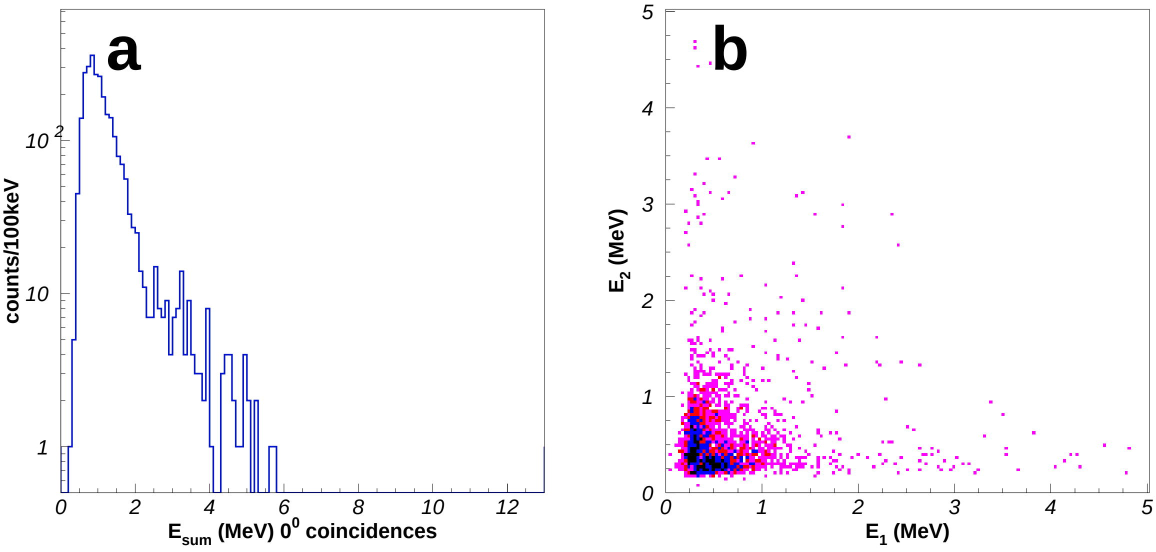

Figure 6.3: Left: sum energy spectrum corresponding to 0° *coincidences of 2007 experiment. Right: scatter plot for the 0° coincidences.*

detectors D1 and D3 and between 0° and 68° for D2.

Figures 6.2(a) and (b) show the sum energy and scatter plot spectrum for charged particles in coincidence in detectors at *90°*, and ocurring during the first 60 ms after the proton impact. The time interval is chosen in order to enhance ^{11}Li activity ($T_{1/2}$=8.5(2) s [Ajz88]) over the decay of the daughter ^{11}Be ($T_{1/2}$=13.81(8) s [Ajz88]). Similarly to the spectra from the 2003 experiment, the data consists in a low energy peak, corresponding to a point-like distribution in the low energy end of the scatter plot. The lack of distinctive structures indicates that nuclear structure does nor play a role in the breakup mechanism.

The *0°* coincidences are shown in Figs. 6.3(a) and (b). In the *0°* coincidences case the low enegy peak appears as two lobes in the scatter plot, which (as seen in section 6.3.1), indicates the presence of a two-body breakup mechanism. Following this idea, and assuming that both particles are alphas, we calculated their energy in the center of mass system, shown in Fig. 6.4. The spectrum shows a peak at E_0=90.5(7) keV, with Γ=31(2) keV full width half maximum, obtained from a fit of the peak using a Lorentzian function, as shown in the figure. The ground state of ^{8}Be has a Q value of 0.0918 MeV above the $\alpha+\alpha$ continuum [Til04], which corresponds rather well to our fit. The full width half maximum of the state in the literature is 5.57×10^{-3} MeV, which is around 6 times thiner than our fit. One should keep in mind, though, that the intrinsic energy resolution of our DSSSD is ~30 keV.

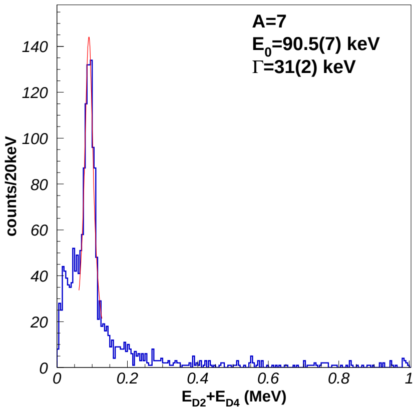

Figure 6.4: Center of mass relative energy between the two detected particles, assuming they are alphas. The red line corresponds to a fit of the peak using a Lorentzian function. A energy centroid of E_0*=90.5(7) keV and a FWHM of* Γ*=31(2) keV is obtained. The parameter A corresponds an the arbitrary normalization constant. The energy centroid value indicates that this peak corresponds to the ground state resonance of* ^{8}*Be of* Q_α*=91.8 keV [Til04].*

The presence of the ^{8}Be ground state resonance corroborates the previously proposed [Lan81] breakup of the 10.59 MeV state into the five body 2α3n channel through intemediate states in ^{9}Be and the ground state of ^{8}Be.

6.3 Study of the ^{7}He+α channel

The kinematical fingerprint of the ^{7}He+α channel was observed in the analysis of coincidences detected in opposite detectors in the 2003 experiment, so from here on we concentrate on the charged particle coincidences in this geometry, so called *180°* coincidences. Figures 6.5(a) and (b) show the sum energy spectrum of the two detected particles in coincidence and the scatter plot one versus the other, corresponding to *180°* coincidences. Both spectra are very similar to the ones from the 2003 experiment, but with larger statistics. The most interesting feature in the scatter plot is the presence of two clear bands of 7/4 and 4/7 slopes, corresponding to decay through the ^{7}He(gs)+α channel. The two bands are similar to the groupings of data observed in the 2003 experiment, although the increased statistics allow for a much clearer definition of the boundaries. We can compare the new scatter plot in Fig 6.5(b) with a simulation using the breakup channels deduced from the study of the 2003 experiment. The two bands at high energy in the 2007 data correspond

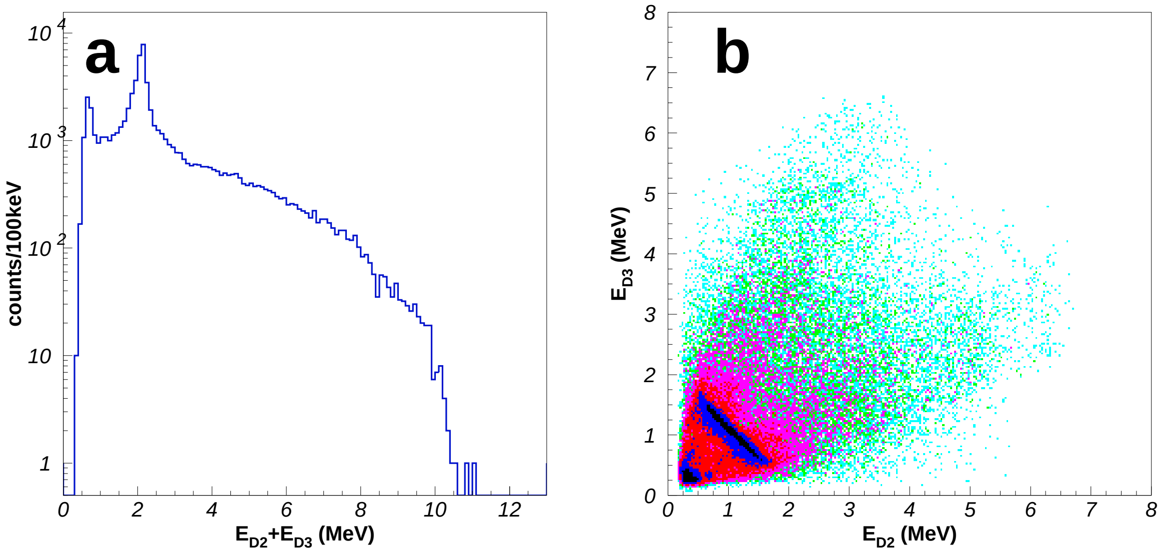

Figure 6.5: Left: sum energy spectrum corresponding to 180° coincidences in the 2007 experiment. Right: scatter plot of the energy detected in D2 versus the energy detected in D3 for the 180° coincidences.

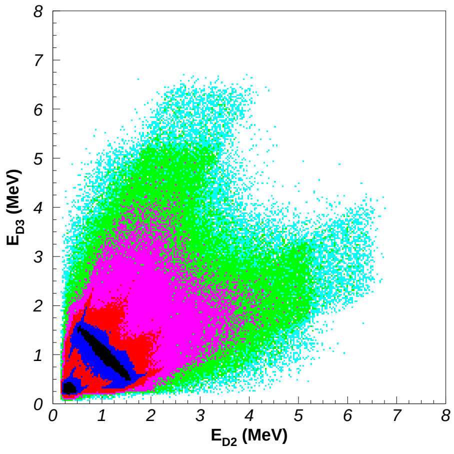

Figure 6.6: Monte Carlo simulation of the breakup channels proposed in the study of 2003 experiment, including the experimental acceptance of the 2007 setup. The two bands at high energy, due to the ^{7}He+α channel, correspond remarkably well with two bands observed in Fig. 6.5b.

remarkably well with the simulation of the breakup through the ^{7}He+α channel.

Not only we study the scatter plot, but we can take advantage of the increased statistics to use the scatter plot constructed as the individual energy of the particles against their sum energy, as explained in section 6.3.1. We demonstrated that in case of sequential decay the first emitted particle will be grouped along a line of slope and offset determined by the intermediate resonance mass ratio to ^{11}Be and energy

$$E_{sum} = Q_R + \frac{M_{^{11}Be}}{m_R} E_1 \tag{6.1}$$

where Q_R and m_R are the Q value and the mass of the resonance in the first step of the breakup channel studied. In this work we are interested in the three body nα^{6}He channel, thus the sum energy is defined as $E_{^6He}+E_\alpha+E_n$, and we can obtain the excitation energy in ^{11}Be by simply adding to this sum energy the channel $Q_{n\alpha^6He}$ value of 7.920(4) MeV [Bac05, AWT03], $E_{^{11}Be}=E_{sum}+Q_{n\alpha^6He}$. This certainly introduces a problem. The plot is designed to highlight events from the three body nα^{6}He channel, but the majority of the events in *180°* coincidences are five body 2α3n breakup. From the branching ratios obtained in the 2003 experiment (see section 5.4) we see that 82% of the charged particle intensity corresponds to the 2α3n channel. As the neutron energy can only be obtained from energy and momentum conservation, we are making a mistake each time we calculate a the neutron energy from the charged particles energies for an 2α3n event, thus these events will act as a background in the scatter plot of individual particles energy vs total energy.

Figure 6.7 shows the individual energy vs ^{11}Be excitation energy scatter plot for *180°* coincidences in 2007 experiment. There are two distinct features of the plot associated to three body nα^{6}He decay channels. First, a horizontal line at 10.6 MeV ^{11}Be excitation energy, with an associated line of 11/10 slope and 10 MeV offset (marked by red dashed lines in Fig. 6.7). The slope and offset of the line indicates it corresponds to neutron emission to the ^{10}Be 9.5 MeV resonance, which appears at 10 MeV in relation to ^{11}Be by adding the 0.5 MeV ^{11}Be neutron separation energy. Both the horizontal line, which is therefore assigned to the ^{6}He and alpha energies and the neutron line, imply they are associated to the breakup of the $5/2^-$ state [Lan81, Hir05] explored in the previous section. Second, a grouping along the line, marked by the black dashed line, of 11/7 slope and with 8.35 MeV offset [Bac05, AWT03]. The slope naturally indicates the role of ^{7}He, following eq. 6.1. The ^{7}He resonance (8.35 MeV offset) is 0.430 MeV above the 7.920 MeV nα^{6}He channel Q value [Bac05, AWT03], indicating that the ^{7}He resonance is the ground state. The black dashed line of 11/4 slope indicates the theoretical line the ^{7}He will follow in this plot. As the ^{7}He breaks into a ^{6}He ion and a neutron, we expect both particles to be scattered around that line, as in fact happens in the plot. It is interesting to perform kinematical analysis of the breakup in this region,

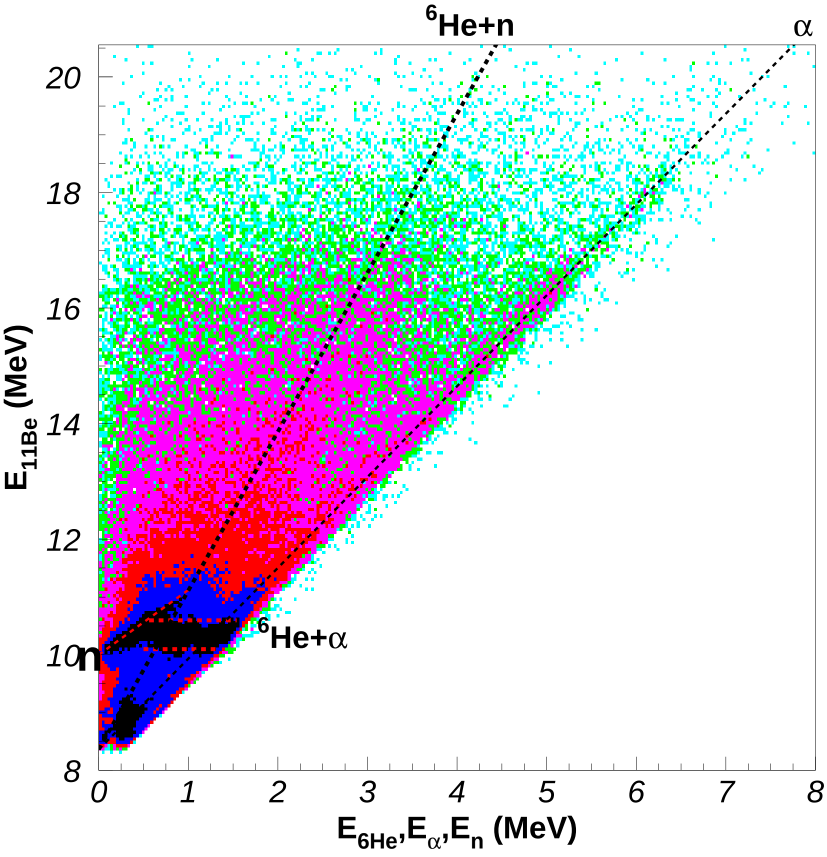

Figure 6.7: Scatter plot of the individual n, α and ^{6}He energies plotted versus the ^{11}Be excitation energy, recorded in opposite detectors and within the first 60 ms after the proton impact. The thin red dashed line marks the neutron energy (the 11/10 line with 10 MeV offset) emitted in the breakup of the ^{11}Be 10.59 MeV state. The two thick red dashed lines indicates the energies of alpha and ^{6}He of the subsequent breakup of the ^{10}Be 9.5 MeV state (10 MeV adding the 0.5 MeV neutron separation energy). The black dashed lines indicate the α (the alpha energy is the 11/7 line with 8.33 MeV offset, set by the kinematics of the ^{7}He+α breakup channel), ^{6}He and neutron energies of the breakup of ^{11}Be states through the ground state of ^{7}He.

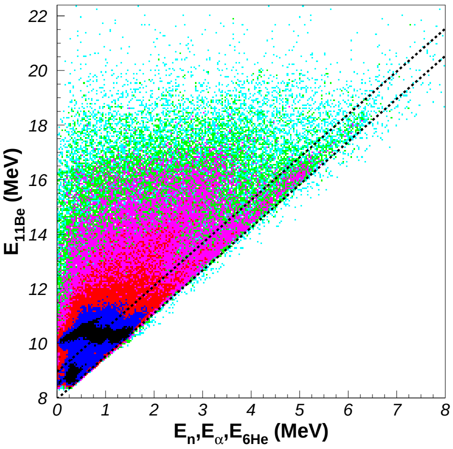

Figure 6.8: Scatter plot of the excitation energy in ^{11}Be versus the individual energies of the neutron, α and ^{6}He, the same shown in Fig.6.7. The ^{7}He+α channel correponds to events where the energy of the alpha particle lies in the line of 11/7 slope and 8.35 MeV offset. The two dashed lines indicate the boundaries of the gate imposed to the alpha energy select events in the ^{7}He+α channel.

as the angular correlations of the breakup in the ^{7}He+α channel will modify the ^{6}He and neutron distribution. Inspecting the intensity along the 11/7 line we see that there are two accumulations of events in this line at around 16 MeV and 18 MeV in ^{11}Be, indicating the presence of states in ^{11}Be at these energies decaying through the ^{7}He+α channel.

The advantage of plotting the individual energies versus the sum energy is evident here. We can individually study the ^{7}He+α channel by imposing that the detected alpha particle is on the 11/7 line. Particle identification is given by kinematics, as demonstrated in the 2003 experiment section 5.3.3, the ^{6}He energy is dominated by the ^{7}He+α breakup, and thus is 4/7 of the alpha energy. Once we have determined the alpha energy, the ^{7}He+α gate is defined from the alpha energy as follows: we require that the calculated excitation energy in ^{11}Be, obtained according to eq. 6.1 from the charged particle of higher energy, the α. The Q$_R$ offsets of the two limits of the gate are obtained by adding 0.6 MeV for the upper one and subtracting 0.4 MeV for the lower one. This limits define an interval for the energy of the α particle

$$E_\alpha \geq \frac{11}{7} \cdot E_{^{11}Be} + 7.93 \text{ MeV} \tag{6.2}$$

$$E_\alpha \leq \frac{11}{7} \cdot E_{^{11}Be} + 8.93 \text{ MeV} \tag{6.3}$$

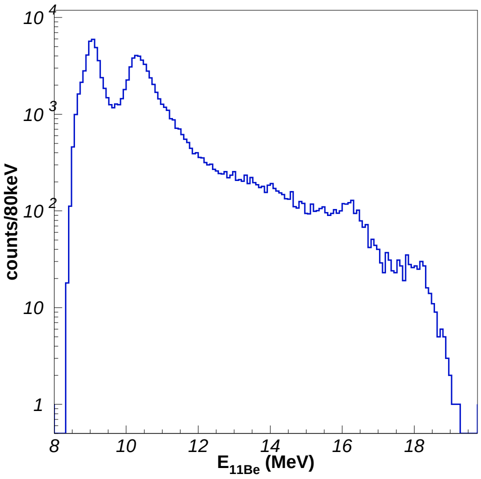

Figure 6.9: Excitation energy spectrum for events where the charged particle of higher energy lies between the two lines shown in Fig 6.8, assumend, in this work, to correspond to the ^{7}He+α channel.

where the two dashed lines in Fig. 6.8 correspond to the lines that define the boundaries of the gate.

The ^{11}Be excitation energy spectrum for these events, obtained from the sum of n, α and ^{6}He energy plus $Q_{n\alpha^6He}$=7.920(4) MeV [Bac05, AWT03], is shown in Fig. 6.9. As expected from Fig. 6.8, the ^{11}Be excitation spectrum below 12 MeV is dominated by events from the nα^6He and 2α3n breakup of the ^{11}Be 10.59 MeV state through the ^{10}Be 9.5 MeV state, as the gate overlaps with both regions. This does not directly means that the breakup of the ^{11}Be 10.59 MeV state occurs through the ^{7}He(gs)+α channel, but that the breakup through the ground state of ^{7}He is kinematically indistinguishable from the rest of the channels. In the high energy part of the ^{11}Be excitation energy spectrum we see a sharp peak at 16 MeV and a bump at around 18 MeV, which corresponds to the contribution of the wide state at 18 MeV, as proposed from the analysis of the 2003 experiment.

We concentrate our interest in the analysis of the ^{11}Be excitation energy region above 13 MeV, where we are free of the contribution of the ^{11}Be 10.59 MeV state. However, as mentioned above, we cannot avoid the contribution of the 2α3n channel acting as a background in the excitation energy plot, as evidenced by the flat distribution of intensity between the 10 and 16 MeV peaks. Therefore, analysis of the events in the ^{7}He+α channel gate, we must take into account the effect of the 2α3n as background. Previous studies by Langevin et al. [Lan81] and Borge et al. [Bor97a], and the analysis of the 2003 data presented in this Thesis, assigned the

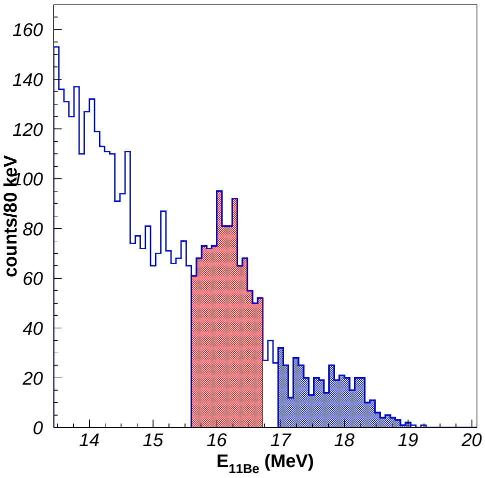

Figure 6.10: Regions in the ^{11}Be excitation energy, calculated as the sum of the reconstructed neutron, and detected charged particles assumed to be alpha and ^{6}He. The χ^2 tests of the Monte-Carlo simulations to the data were done varying the resonances parameters. The blue filled area corresponds to the area of the fit of the ^{11}Be 18 MeV state and the red filled area the region of the fit of the ^{11}Be 18 MeV state.

statistics observed at high energy as due to the $2\alpha3$n channel of the decay of the ^{11}Be 18 MeV state. However, the newly observed ^{11}Be 16 MeV state can be considered to decay through the five body $2\alpha3$n channel as well, and we will include it, along with the five body breakup of the 18 MeV state, in the Monte-Carlo simulations shown in the next section. For a more detailed discussion on the five body $2\alpha3$n breakup of the 16 MeV state see section 6.3.3.

6.3.1 Characterization of the 16 and 18 MeV states observed in the ^{7}He+α channel

Once we have determined which decay channels contribute to the sum energy spectrum shown in Fig. 6.5(a) and that the ^{11}Be excitation energy spectrum gated on the ^{7}He+α channel indicate the contribution to this channel of two states at 16 and 18 MeV excitation energy, we can proceed with the R-matrix formalism. The two ^{11}Be states were described using the single channel single level R-Matrix approximation (see section 3.3.2), which implies we do not take into account possible interferences between the levels. We set the interaction radius to $1.4(A_1^{1/3}+A_2^{1/3})=4.9$ fm and the orbital angular momentum of the neutron to $l=1$. The alpha orbital angular

Table 6.1: Energy centroid and width of the ^{11}Be 18 MeV state compared to the values in the literature.

this work		Borge et al. [Bor97a]		
E$_0$ (MeV)	Γ (MeV)	E$_0$ (MeV)	Γ (MeV)	
18.4(3)	1.6(6)	18.2(2)	1.25(15)	from the ^{9,10}Be spectrum
		18.0(1)	0.8(1)	from the ^{4,6}He spectrum
		18.15(15)	1.3(3)	from the triton spectrum

momentum depends on the spin and parity of the ^{11}Be state, which was determined to be $3/2^-$ for both states from angular correlations (see below). This leaves two parameters to be determined, the centroid and reduced width, which can be obtained from a fit to the ^{11}Be excitation energy spectrum in Fig. 6.13. We performed χ^2 tests of the simulation varying the centroid and width parameters and the χ^2 tests were done in two regions of the ^{11}Be excitation energy, one for each state as shown in Fig. 6.10. We first studied the 18 MeV state, as by being at the high energy end of the spectrum there are no other channels overlaping in its region. We modified the centroid energy and reduced width independently several times and fitted the resulting χ^2 tests to a parabola, the expected behavior of the χ^2 function, shown in Figs. 6.11(a) and (b). The resulting minima of the parabolas for the centroid and reduced width are E$_0$=18.4(3) MeV and γ^2=0.11(4), which corresponds to a full width half maximum, Γ, of 1.6(6) MeV, for the second.

The energy and width of this state were previously determined in [Bor97a] from the fit of the singles spectra where the various β-delayed fragments were identified with a gas-Si telescope. The gas-Si telescope allows to separate the contribution from d+t, α+^{6}He and recoils. An E$_0$=18.2(2) MeV and Γ=1.25(15) MeV were obtained from the ^{9,10}Be spectrum, E$_0$=18.0(1) MeV and Γ=0.8(1) MeV from the ^{4,6}He spectrum and E$_0$=18.15(15) and Γ=1.3(3) from the triton spectrum [Bor97a]. The resonance parameters for this state in ^{11}Be coincide within error bars with the previously published parameters, although are more in line with the values obtained from the ^{9,10}Be spectrum. The slightly larger error bars of the ^{11}Be 18 MeV state obtained in this work are due to the shallow profile of the χ^2 tests on the ^{11}Be excitation energy. This effect is expected, as the excitation energy is obtained from the reconstructed neutron energy, which depends on the angular resolution of the coincidence measurement of the two other charged particles (see section). This effect is implemented in the Monte-Carlo simulation, thus indirectly taken into account in the χ^2. from the limited angular resolution. The advantage of this experiment over the previous one is that the coincidence detection allows to indentify and separate the different decay channels.

The fits for the second state, shown in Figs. 6.12(a) and (b) were a little more

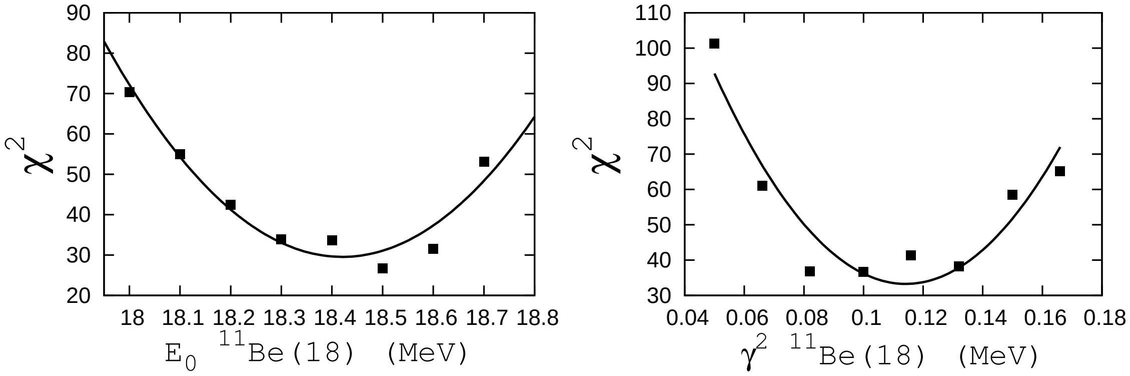

Figure 6.11: Variation of the χ^2 values with the centroid energy (left) and reduced width (right) of the 18 MeV state in ^{11}Be. The χ^2 values were fit to a parabola to obtain the minimum.

complicated due to the effect of the $2\alpha3$n background and the tail of the ^{11}Be 18 MeV state below the 16 MeV level, specially in the case of the fit of the reduced width. We see in Fig. 6.12(b) that the reduced width stops increasing above 0.06 MeV. Due to this effect we did not used the points above 0.06 MeV for the parabola fit. The resulting energy centroid and width are E$_0$=16.3(1) MeV and γ^2=0.05(1) MeV, which corresponds to a full width half maximum, Γ=0.7(1) MeV.

The Monte-Carlo simulation where the ^{11}Be 16 and 18 MeV state are described in the R-matrix formalism with the parameters obtained from the fits is shown in Fig. 6.13. The ^{7}He+α breakup of the two states is shown in black hatched histogram and the five body $2\alpha3$n breakup of the 16 and 18 MeV states is shown in black and brown lines respectively.

6.3.2 Determination of the spin of the 16 and 18 MeV states

The β-decay selection rules restrict the spin and parities of the states in ^{11}Be that are fed. In the case of the Fermi β-decay transition, it populates the Isobaric Analog State (IAS) in the daughter nucleus, of equal spin and isospin of the parent nucleus, just different T$_z$. However, ^{11}Li is a β^- emitter, therefore the IAS is above the Q$_\beta$ value, due to the Coulomb repulsion of the extra proton. This leaves only Gamow-Teller β-decay transitions available. The selection rules of Gamow-Teller β-decay forbid parity changing transitions, and set the variation of total angular momentum, ΔJ, to 0,1. As the ground state of ^{11}Li is a $3/2^-$, the β-decay will populate states in ^{11}Be of spin and parity $1/2^-$, $3/2^-$ and $5/2^-$.

In order to determine which of the three possible spins are assigned to each state

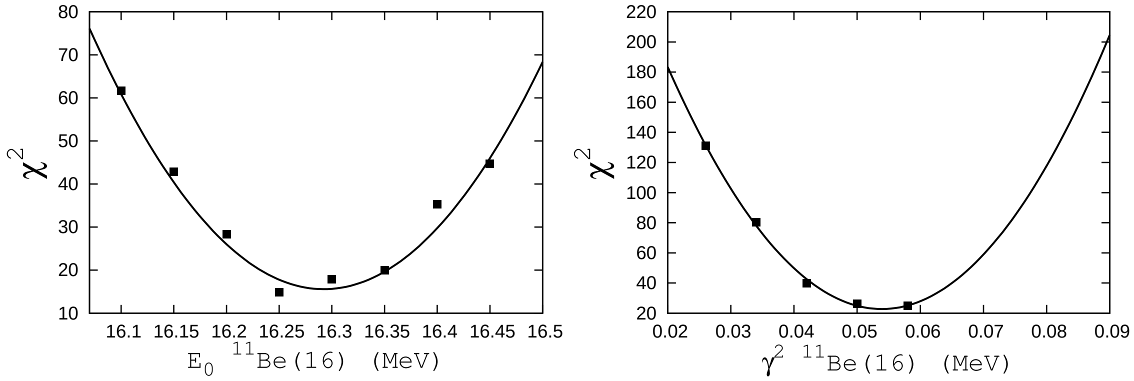

Figure 6.12: Result of the χ^2 tests and fits to obtain the energy centroid and reduced width of the ^{11}Be 16 MeV state. In the parabola fit of the χ^2 results of reduced width we did not use the test points above γ^2=0.06 MeV, as they are insensitive to the level width.

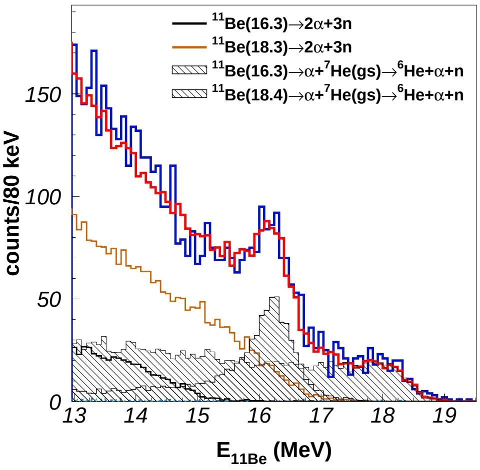

Figure 6.13: Excitation energy in ^{11}Be for events inside the interval corresponding to the ^{7}He(gs) channel, shown in Fig 6.7. The Monte-Carlo simulation of thecontribution of the different breakup channels is shown superimposed in red, with the different channels color coded according to the legend.

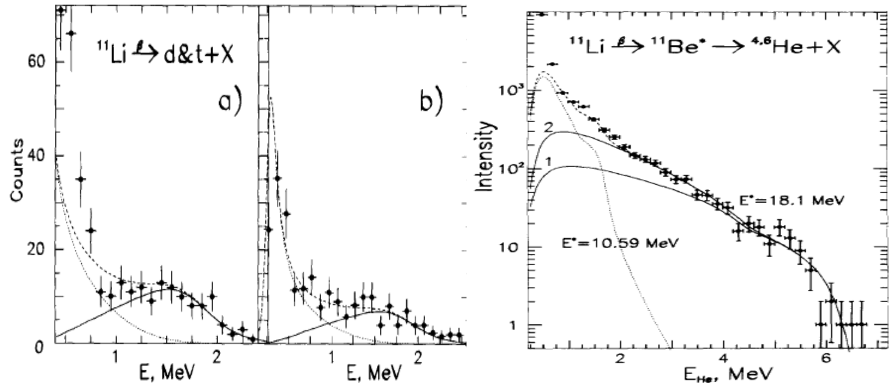

Figure 6.14: Left: β-delayed energy spectrum of deuterons and tritons identified using a gas-Si telescope (from [Bor97a]). The R-matrix fit to the data is shown in continuos line. The two figures in the left panel correspond a two differnt experiments. Right: α and ^{6}He energy spectrum indetified with a ga-Si telescope (from [Bor97a]). The continious lines 1 and 2 are the contribution of the $n\alpha^{6}$He and $2\alpha 3n$ channels respectively. The dashed line is the contribution of the ^{1}Be 10.6 MeV state. The R-matrix fits to this spectra were used to determine the paramters of the ^{11}Be 18 MeV resonance discussed in the text.

in ^{11}Be we used two complimentary analysis,

- (1) the angular correlations between the first emitted alpha and the center of mass breakup of ^{7}He
- (2) the energy distribution of the ^{6}He and neutron.

In order to choose events in each of the states we want to study both their angular correlations and the ^{6}He and neutron energy distribution, we defined two ranges on the ^{11}Be excitation energy spectrum, previously gated in the ^{7}He+α channel. These energy ranges were optimized to maximize the contribution of the ^{7}He+α channel of each state over the remaining channels present. They correspond to energies from 15.66 to 16.635 MeV for the ^{11}Be 16 MeV state and from 17.37 to 18.6 MeV for the ^{11}Be 18 MeV state. Fig. 6.16 show the selected ^{6}He and neutron regions in individual energy versus total energy spectrum-

The ^{6}He and neutron energy distribution can be immediately obtained from Fig. 6.16, as it is just the events inside the two regions. The angular correlations take advantage of the fact that in sequential decay through and intermediate state, where the spin of this intermediate state is different than 0 or 1/2, there is a correlation between the angle of emission of the second breakup and the first emitted particle (see section 3.3.3 for details). Although both breakups occur isotropically in their

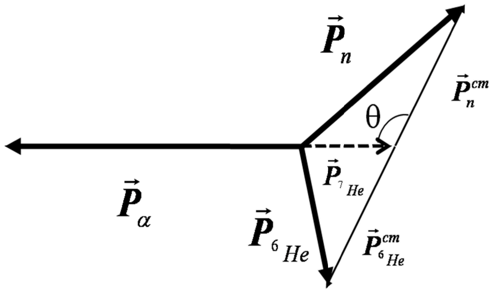

Figure 6.15: Schematic view of the momentum relations in the sequential breakup of ^{11}*Be through a resonance in* ^{7}*He.*

respective center of mass references frame, if we have determined the direction of the first emitted alpha in the laboratory frame, this will define a preference direction for the second breakup (see figure 6.15). In the case of breakup of ^{11}Be states through the ground state of ^{7}He, which is a $3/2^-$ [Til04], the Racah inequalities impose that the maximum coefficient is A$_2$, so the angle will be distributed according the equation

$$W(\cos\theta) = 1 + A_2(2\cos^2\theta - 1)/2 \tag{6.4}$$

where the A$_2$ coefficient depends on the spin of the initial state in ^{11}Be. Using the formalism given in section 3.3.3 the A$_2$ parameter for the alpha particle emitted with the lowest orbital angular momentum possible is

Spin	A$_2$
1/2	1
3/2	0
5/2	-0.714

Certainly, in the case of spin 3/2 and 5/2 in ^{11}Be a second orbital angular momentum is possible, l=2 and l=4 respectively, which would end up in A$_2$ equals to 0 and 0.714. Biedenharn and Rose [BR53] suggest a way of combining both W correlations weighted by the probability of emission in each orbital angular momentum. In general we can assume the emission with an angular momentum 2 units higher is really small and discard the second term (see 3.3.3).

From a practical point of view, the study of angular correlations require obtaining the angle θ. It can be calculated from the momentum of the alpha, the ^{6}He and the neutron in the laboratory frame as

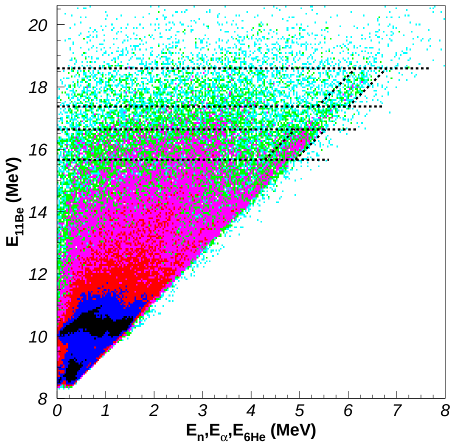

Figure 6.16: The horizontal doted lines indicate the boundaries of the two regions in the ^{11}Be excitation energy used to select events corresponding to the breakup of the ^{11}Be 16 and 18 MeV states. Of course, this two regions are applied to events previously identified as coming from the ^{7}He+α channel, as indicated by the tilted dashed lines around the 11/7 line corresponding to alphas from the ^{7}He ground state channel.

$$\theta = \arccos \frac{\overrightarrow{P}^{CM}_{6He} \cdot \overrightarrow{P}_\alpha}{\left|\overrightarrow{P}^{CM}_{6He}\right| \left|\overrightarrow{P}_\alpha\right|} \tag{6.5}$$

where the complimentary angle, 180°-θ, corresponds to the angle calculated from the neutron momentum. The ^{6}He momentum in the center of mass system can be obtained from the laboratory momentum

$$\overrightarrow{P}^{CM}_{^6He} = \overrightarrow{P}_{^6He} - \frac{m_{^6He}}{m_{^7He}}\overrightarrow{P}_{^7He} = \overrightarrow{P}_{^6He} + \frac{m_{^6He}}{m_{^7He}}\overrightarrow{P}_\alpha \tag{6.6}$$

We performed a Monte-Carlo simulation of the breakup of both ^{11}Be states at 16 a 18 MeV respectively for the 9 possible combinations of spin of each state, according the angular correlations in the ^{7}He+α channel, and performed a χ^2 test on the θ spectrum and the spectrum of the individual n-α-^{6}He energies (we denote E$_i$, where i=n,α or ^{6}He). As mentioned in the determination of the centroid and width, we startedn by the determination of the spin of the ^{11}Be 18 MeV state because of the absence of other contributions to the intensity in its region (see Fig. 6.13). The results of the simulations are shown in Figs. 6.17 and 6.18. the results of the χ^2 tests were:

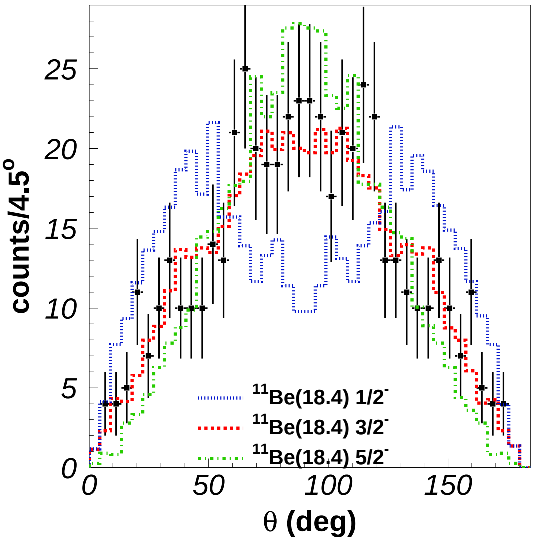

Figure 6.17: Angular distribution, θ, for events gated on the 18 MeV state (see Fig. 6.16) in ^{11}Be shown in black dots. The Monte-Carlo simulations for the three possible spin assignments of the state are shown on top and color coded according to the legend. By visual inspection we can disregard an assigment of spin 1/2 for the ^{11}Be 18 MeV state. The χ^2 analysis favors a spin assigment of 3/2.

^{11}Be(18) Spin	$\chi^2(\theta)$ N$_{free}$=19	χ^2(E$_i$) N$_{free}$=49
1/2	67.54	158.24
3/2	16.61	54.70
5/2	30.61	63.83

We see that results of both χ^2 tests of the angular correlations and the E$_i$ spectrum support a 3/2 assignment. In the case of angular correlations the difference with the next spin-value of the χ^2-value is almost the number of degrees of freedom, strongly indicating a **3/2** assignment.

In the case of the n-α-^{6}He spectrum, E$_i$, the difference between the 3/2 and 5/2 is lower than in the angular correlations case. However, the probability of the energy spectrum χ^2 test for spin 5/2, of value 63.83, to be correct is less than 10% [chi], so we reject it on that basis.

In the case of the ^{11}Be 16 MeV state we calculated the χ^2 test to both the angular correlations spectrum and the energy spectrum for the three possible spins in combination to the three possible spins in the ^{11}Be 18 MeV state, as a quarter of the intensity in the 16 MeV state gate comes from the tail of the 18 MeV state.

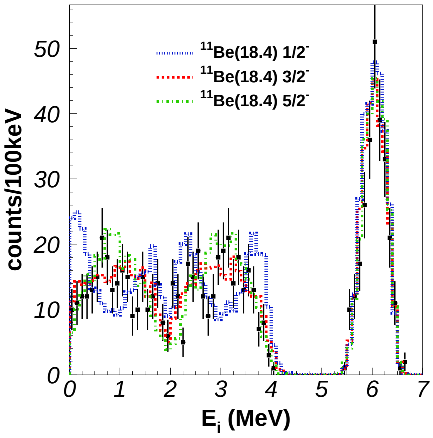

Figure 6.18: The black dots correspond to the individual alpha, neutron (reconstructed) and ^{6}He energies (E_i, three points per event) for events gated on the 18 MeV state (see Fig. 6.16). The 6 MeV peak corresponds exclusively to the alpha particles. The simulations of the three possible spins in ^{11}Be are shown overlaid, color coded according to the legend. As for the angular correlations, the χ^2 analysis favors an assigment of 3/2.

^{11}Be(16) Spin	^{11}Be(18) Spin	$\chi^2(\theta)$ N$_{free}$=19	χ^2(E$_i$) N$_{free}$=49
1/2	1/2	132.65	336.43
1/2	3/2	70.49	268.80
1/2	5/2	44.154	195.32
3/2	1/2	24.20	157.08
3/2	3/2	20.56	151.94
3/2	5/2	29.48	157.38
5/2	1/2	27.57	165.59
5/2	3/2	58.68	200.68
5/2	5/2	77.83	233.05

Once the spin of the ^{11}Be 18 MeV state to be 3/2 is determined, it is easier to sort through the 9 combinations of spins, as only the three results where the χ^2 test of the 16 MeV state is calculated with 3/2 for the 18 MeV state should be considered (highlighted in grey in the table). Again an assignment of 3/2 is strongly supported by the angular correlations, as the minimum χ^2 is less than half of the closest value, for spin of 5/2. In the case of the fit of the E$_i$ spectrum, the three individual energy spectrum of α,n and ^{6}He, we see all three results are high, indicating that the simulation poorly reproduces the E$_i$ spectrum. This is not a surprise, as the

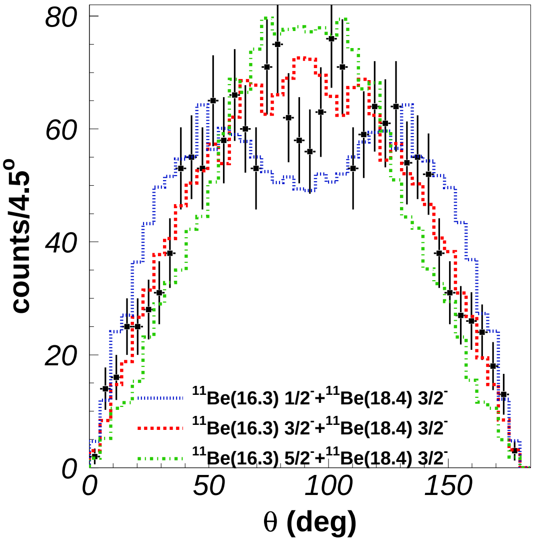

Figure 6.19: The black dots show the angular distribution, θ, for events gated on the 16 MeV state in ^{11}*Be, as seen in Fig. 6.16. The Monte-Carlo simulations for the three possible spin assignments of the state are shown on top and color coded according to the legend. An assigment of spin 1/2 is vissually discarded by comparing the suimulations to the data. Again, the* χ^2 *analysis favors a spin assigment of 3/2.*

E_i spectrum is sensitive to the background from the energy distribution of the five body 2α3n breakup of the ^{11}Be 16 and 18 MeV channels. Nevertheless, the difference between the results of the χ^2 test for spin assignments of 3/2 and 5/2 for the ^{11}Be 16 MeV state is the number of degrees of freedom, which supports the assignment of 3/2. Figures 6.19 and 6.20 show respectively the angular correlations and E_i spectra for the ^{11}Be 16 MeV state.

In summary, have been able to determine the energy centroid and width of the ^{11}Be 16 and 18 MeV states by fitting the Monte-Carlo simulation to the excitation energy spectrum calculated from α-^{6}He events gated in the ^{7}He+α channel. For the previously unknown state at 16 MeV we obtain E_0=16.3(1) MeV and γ^2=0.05(1) MeV, which corresponds to a full width half maximum Γ=0.7(1) MeV. For the ^{11}Be 18 MeV state we obtain E_0=18.4(3) MeV and γ^2=0.11(4), which corresponds to Γ=1.6(6) MeV. Finally, the spin-parity assignment of both states was determined to be $3/2^-$ from the analysis of the angular correlations and the n,α,^{6}He energy spectrum.

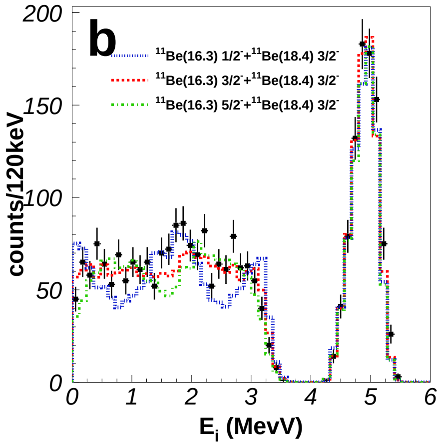

Figure 6.20: The black dots correspond to the alpha, neutron and ^{6}He energiesd distribution (E_i) for events gates in the ^{11}Be 16 MeV state, see Fig. 6.16. The 4.9 MeV peak corresponds exclusively to the alpha particles. Again, the simulations of the three possible spins in ^{11}Be are shown on top and color coded according to the legend. The χ^2 analysis once again favors an spin assigment of 3/2.

6.3.3 Determination of the branching ratios to the ^{11}Be 16 and 18 MeV states

The presence of a new state decaying into the three body nα^{6}He and five body 2α3n channels implies that we need not only to calculate its branching ratio but re-evaluate the branching ratio of the ^{11}Be 18 MeV state. This is due to the fact that part of the intensity of the *180°* coincidences which was assigned to the ^{11}Be 18 MeV state is now assigned to the 16 MeV state. In the previous section we have studied the breakup of the ^{11}Be 16 MeV state in the three body nα^{6}He channel by selecting events with the appropriate kinematical fingerprint. It was indicated that, for completitude, the 16 MeV state will decay into the five body 2α3n decay channel as well.

In order to obtain the contribution of the 2α3n channel of the ^{11}Be 16 MeV state we cannot rely in the intensity as observed gating on the ^{7}He channel. In this case we need to study the sum energy coincidence spectrum of Fig. 6.5(a). We performed a Monte-Carlo simulation including all the breakup channels proposed in the analysis of the 2003 experiment (listed in Table 6.2), that is the 2α3n and nα^{6}He breakup channels of the ^{11}Be 10.59 MeV state through the ^{10}Be 9.5 MeV state, the ^{5}He+^{6}He(2^{+})→2α3n and ^{7}He(gs)+α→nα^{6}He breakup of the ^{11}Be 18 MeV state plus the breakup of a 16 MeV state through the ground state of ^{7}He, as suggested from

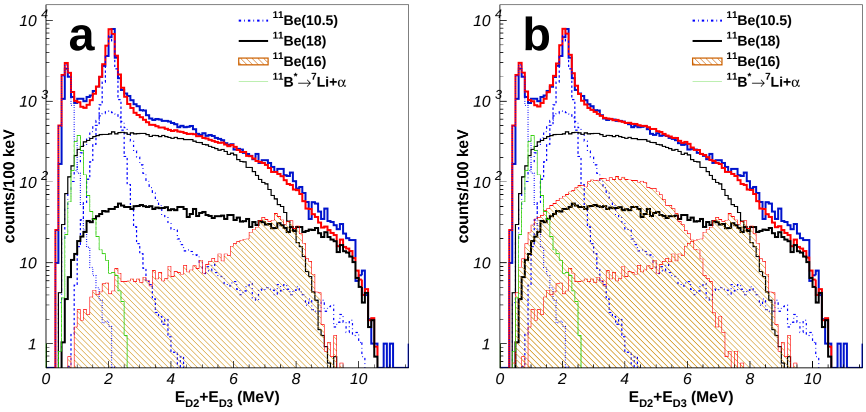

Figure 6.21: Left: the two charged particle sum energy spectrum in coincidence in opposite detectors is compared to a Monte-Carlo simulation including the different breakup channels as listed in Table 6.2, sum shown in red . All channels of a given state in ^{11}Be are the same color, according to the legend. (a) without the $2\alpha3n$ channel of the 16 MeVstate (b) including $2\alpha3n$ breakup of the ^{11}Be 16 MeV state. The simulation reproduces now better the sum energy region between 3 and 6 MeV.

Table 6.2: β-fed states in ^{11}Be above the charged particle thresholds and their breakup channels.

Decay channels from this work.

$^{11}\mathrm{Be}(10.59)$	$\xrightarrow{n}{}^{10}\mathrm{Be}(9.5)$	$\xrightarrow{\alpha}{}^{6}\mathrm{He}$ $\longrightarrow 2\alpha3\mathrm{n}$
	$\xrightarrow{\alpha}{}^{7}\mathrm{He(gs)}$	$\xrightarrow{n}{}^{6}\mathrm{He}$
$^{11}\mathrm{Be}(16)$	$\longrightarrow{}^{6}\mathrm{He}(2^{+})+{}^{5}\mathrm{He(gs)}$	$\longrightarrow 2\alpha3\mathrm{n}^{\dagger}$
	$\xrightarrow{\alpha}{}^{7}\mathrm{He(gs)}$	$\xrightarrow{n}{}^{6}\mathrm{He}$
$^{11}\mathrm{Be}(18)$	$\longrightarrow{}^{6}\mathrm{He}(2^{+})+{}^{5}\mathrm{He(gs)}$	$\longrightarrow 2\alpha3\mathrm{n}^{\dagger}$
	$\xrightarrow{\alpha}{}^{7}\mathrm{He(gs)}$	$\xrightarrow{n}{}^{6}\mathrm{He}$

Fig. 6.9. In principle, we did not include the five body $2\alpha3$n breakup of the 16 MeV state in ^{11}Be. However, the resulting simulation sum energy spectrum for the *180°* coincidences shows a dip between 3 and 6 MeV, as seen in Fig. 6.21(a). We included the five body decay of the ^{11}Be 16 MeV state assigning it an intensity following the same ratio as deduced from the ^{11}Be 18 MeV state, where the five body channel is ∼10 times more intense than the three body decay. The resulting simulation including thenew channel is shown in Fig. 6.21(b). A χ^2 test of the simulation to the region between 3.5 and 5.5 MeV in the sum energy spectrum drops from 313 to 36 for 24 degrees of freedom, an indication of the excellent fit obtained including the $2\alpha3$n breakup of the ^{11}Be 16 MeV state and shown in Fig. 6.21(b). One might note that there is a discrepancy between the experimental sum energy intensity above 9 MeV and the simulation. The intensity of the ^{7}He+α breakup channel of the ^{11}Be 18 MeV state, which dominates in this region, is fixed to reproduce the intensity observed in the ^{11}Be excitation spectrum (see Fig. 6.13). Therefore, the discrepancy of the sum energy spectrum above 9 MeV with the simulation indicates a breakup channel which has not been accounted for.

In order to obtain realistic energy spectrum, the Monte-Carlo simulation included the kinematics of the breakup channels and the different factors that account for the acceptance of the setup and the analysis:

- Energy losses in the carbon-foil stopper.
- Angular acceptance of the detectors.
- Detectors energy thresholds.
- Analysis filters, as described in Chapter 3.

In order to obtain the absolute branching ratios we followed the same procedure as in the analysis of the 2003 experiment. The β-decay branching ratios to the ^{11}Be were obtained from the Monte-Carlo simulations, rather than directly from the area of the coincidence data. This is due to the difficulty in determining the experimental coincidence efficiency for the different channels discussed, as it depends on the kinematics of the channel in question.

In order to normalize the Monte-Carlo simulations we used the same procedure as in the analysis of the 2003 experiment, see section 5.4. We measured the *180°* coincidences in a time window of 0.07 s $\leqslant$ t $<$ 4 s after the proton impact. The selection of events at times larger or equal than 70 ms cuts parts of the ^{11}Be activity, estimated to be small, $\lesssim$2%, from the time distribution. Figure 6.22(a) and (b) show the *180⁰* sum energy spectrum and scatter plot for the selected time window. The ∼1 MeV peak in the sum energy spectrum is identified as the $\beta\alpha$ channel of the daughter ^{11}Be nucleus, and corresponds to the two point-like regions in the scatter plot. The

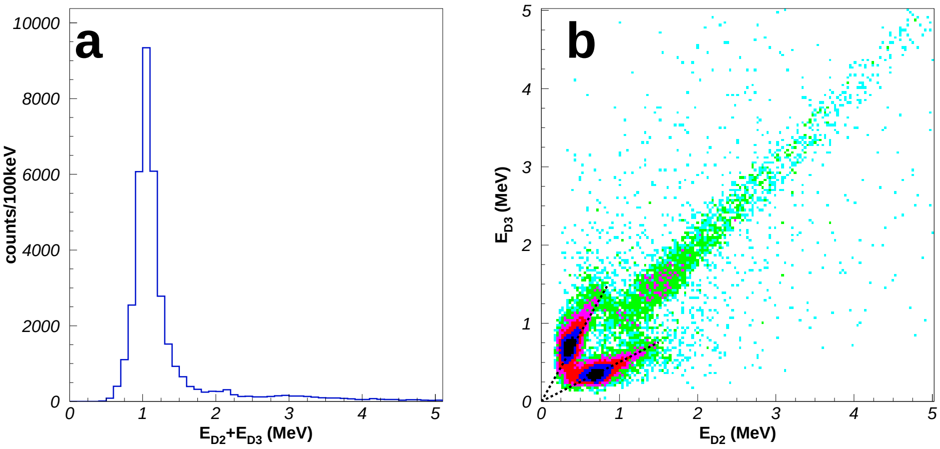

Figure 6.22: Left: the 180° *sum energy spectrum for events gated in a time window* $0.07 \leqslant t < 4$ *s. The* ∼*1 MeV peak corresponds to the* ^{11}*Be* $\beta\alpha$ *branch. Right: energy in detector D2 versus energy in detector D3 scatter plot for events selected in the same time window as in (a). The two point-like regions correspond to the* ∼*1 MeV peak in (a).*

two dotted lines of 7/4 and 4/7 slope indicate the kinematical locus(see section 6.3.1) where a two body breakup of masses 4 and 7 occurs. We see that the region corresponding to ^{7}Li+α breakup is mainly free from other channels contributions. The diagonal line corresponds to the ^{8}Li β-delayed 2α emission, and the transverse line corresponds to the same transverse line in Fig. 6.5(b).

The area of the ∼1 MeV peak, $N_{^7Li+\alpha}$, is 32250 counts. We determine the number of ^{11}Li decays, A(^{11}Li) from this number as

$$A(^{11}Li) = \frac{N_{\beta}\alpha}{BR_{\beta\alpha}BR_{1/2^-\epsilon}} \tag{6.7}$$

where the $BR_{\beta\alpha}$ is the ^{11}Be β-delayed branching ratio of the ^{7}Li+α channel and $BR_{1/2^-}$ is the ^{11}Li β-feeding to the $1/2^-$ 320 keV first excited state in ^{11}Be. The 320 keV state is the only bound state in ^{11}Be, thus, assuming we can discard direct feeding to the ground state, it is the only state that can feed the ground state. The first term, the ^{11}Be β-delayed branching ratio of the ^{7}Li+α channel has only been measured once and its value is 2.9(4)% [AMW81]. The second term, the feeding to the 320 keV state in ^{11}Be is taken as the weighted average of the values from [Mor97, Bor97b, Bjo81, Aoi97, Det80], resulting in 7.4(3)%. The deduced branching ratios are shown in the following table. The sum of the branching ratios to both ^{11}Be 16 and 18 MeV states, 0.31(5)%, is comparable to the branching ratios obtained in the 2003 experiment, 0.39(7)%, and the previously published values of β-feeding to the 18 MeV state in ^{11}Be, 0.30(5)% [Lan81].

Channel	β-feeding (%)
$^{11}Be^{*}(16.3)\rightarrow 2\alpha+3n$	0.042(7)
$^{11}Be^{*}(16.3)\rightarrow \alpha+^{7}He\rightarrow n+\alpha+^{6}He$	0.006(1)
$^{11}Be^{*}(18.4)\rightarrow 2\alpha+3n$	0.24(4)
$^{11}Be^{*}(18.4)\rightarrow \alpha+^{7}He\rightarrow n+\alpha+^{6}He$	0.020(3)

6.4 Kinematical identification of the ^{8}Li+t channel

In the previous sections we have studied the three body nα^{6}He and five body 2α3n decays of the high excited states in ^{11}Be. However, as mentioned in the introduction of this chapter, this two channels are not the only possible decay mechanism for these high excited states in ^{11}Be, as the channels βt (^{8}Li+t), $Q_{\beta t}$=4.832(4) MeV [AWT03, Bac05, Smi08] (see below), and βd (^{9}Li+d), $Q_{\beta d}$=2.638(6) MeV [AWT03, Bac05, Smi08] (see below), are also open to states below the Q_{β} value, and have been previously observed [Lan81, Muk96]. As previously stated, one of the goals of this experiment is to determine the B(GT) values of the β-decay of ^{11}Li into high excited states in ^{11}Be, which of course depend on determining the total branching ratios to these levels, including the possible contribution of the βt and βd channels.

First, we have to consider which levels in ^{11}Be might decay through the βt and βd channels is the triton and deuteron separation energies. The triton and deuteron separation energies can be calculated from the ^{11}Be, ^{8,9}Li and ^{3,2}H mass excesses (ΔM):

$\Delta M(^{11}Be)$	20171(4) keV	[Bac05]
$\Delta M(^{8}Li)$	20946.84(9) keV	[AWT03]
$\Delta M(^{9}Li)$	24954.3(19) keV	[AWT03]
$\Delta M(^{2}H)$	13135.7216(3) keV	[AWT03]
$\Delta M(^{3}H)$	14949.8060(23) keV	[AWT03]

where the separation energyies are calculated as

$$S_t(^{11}Be) = \Delta M(^{8}Li) + \Delta M(^{3}H) - \Delta M(^{11}Be) \qquad (6.8)$$

$$S_d(^{11}Be) = \Delta M(^{9}Li) + \Delta M(^{2}H) - \Delta M(^{11}Be) \qquad (6.9)$$

This results in separation energies of $S_d(^{11}Be)$=17919(4) keV and $S_t(^{11}Be)$=15724.8(4) keV. From the separation energies we immediately see that both the ^{11}Be 16 and

18 MeV states can in principle decay through the βt channel, buy only the 18 MeV state can decay through the βd channel. The ^{11}Li energy windows in the triton and deuteron channels, $Q_{\beta t}$ and $Q_{\beta d}$ are calculated as

$$Q_{\beta t} = Q_{\beta}(^{11}Li) - S_t(^{11}Be) \tag{6.10}$$

$$Q_{\beta d} = Q_{\beta}(^{11}Li) - S_d(^{11}Be) \tag{6.11}$$

where $Q_{\beta}(^{11}\mathrm{Li})$=20.557(4) MeV [AWT03, Bac05] and $S_t(^{11}\mathrm{Be})$ and $S_d(^{11}\mathrm{Be})$ are listed above, resulting in Q values of $Q_{\beta t}$=4.832(4) MeV and $Q_{\beta d}$=2.638(6) MeV.

Let us start with the βd channel. As stated above, the high deuteron separation energy makes this channel open only for the ^{11}Be 18 MeV state. However, a recent measurement of the deuteron energy spectrum [Raa08], where the ^{11}Li beam was impanted in the middle of a pixelated Si detector and the decay channels identified via temporal correlations, does not support the role of the 18 MeV state. Instead, the deuteron spectrum aindicates that the emission occurs directly to the continuum. This implies that the βd channel does not contribute to theβ-feeding to the ^{11}Be 18 MeV state and its corresponding branching ratio. With our setup, it is really difficult to study the βd channel with setup. The setup in 2007 experiment lack detectors capable of particle identification (see section 2.4.2). A possible way of studying the channel would be to use the kinematical identification technique presented in this section. However, that would require detecting the ^{9}Li in coincidence with the deuteron. As our detection threshold is ~160 keV for charged particles, meaning that a ^{9}Li detected with that energy will correspond to a center of mass energy of the system of $\frac{m_{^{11}Be}}{m_d}\times$0.160 MeV~0.9 MeV. Although the $Q_{\beta d}$ is 2.638(6) Mev, we see in the energy spectrum published in [Raa08] that 95% of the deuteron channel lies below 1 MeV. We thus conclude we do not expect to see the deuteron channel in the coincidence spectrum.

The βt channel, on the other hand, has a $Q_{\beta t}$ value of 4832.2(6) keV, and taking into account that the minimum center of mass energy detectable in coincidence with a ^{8}Li is $\frac{m_{^{11}Be}}{m_t}\times$0.160 MeV~0.6 MeV, we expect to be able to measure it in the coincidence spectrum. Moreover, the lower triton separation energy might allow both the ^{11}Be 16 and 18 states to decay through the βt channel. The problem, however, is to select events of this channel out of the bulk of α-α and α-^{6}He coincidences, as the expected branching ratio, ~$1.0(4)\times10^{-4}$ is two orders of magnitude lower than the combined contribution of the three body and five body decay channels to the tow charged particle coincidence spectrum.

6.4.1 Identification of the ^{8}Li+t channel

The method proposed in this work takes advantage of the kinematical characteristics of the ^{8}Li+d breakup in order to filter it out of the rest of two charged particles

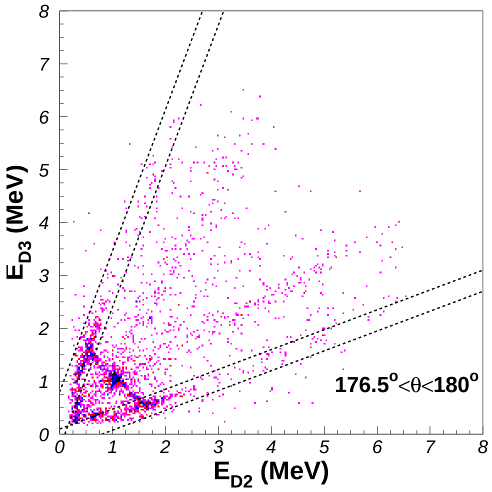

Figure 6.23: energy vs energy scatter plot for particles detected with angles 176.5° < θ < 180°. The dotted lines indicate the two intervals where we selected events corresponding to the ^{8}Li+t channel.

coincidences. Momentum conservation in a two-body break-up imposes that, in the center of mass reference frame, the breakup occurs strictly along one direction. This indicates that the βt channel can only be detected in coincidences strictly detected at 180°. The first filter used selects events detected in opposite pixels within the coincidences detected in opposite detectors, fulfilling the condition of being detected along one direction. As the pixels in our DSSSD's are 3×3 mm^2 wide, and the detectors are 5 and 3.7 cm away respectively, the minimum angular resolution is 3.5° and 4.6° respectively. In order to simplify the analysis, we selected coincidence events whose angle between the detected particles was cut to the minimum resolution of detector D3 of 3.5°, thus between $176.5^o < \theta < 180°$.

Figure 6.23 shows the energy versus energy scatter plot for events recorded within the first 60 ms after the proton impact on target (time interval used in general in the study of ^{11}Li β-decay events see Fig. 6.5(b)) and detected in strictly opposite pixels. The main features of the plot are the two lines with slopes of $8/3$ and $3/8$, and a grouping of data in the same line of Fig. 6.5(b), thus related to the breakup of the state at 10.59 MeV in ^{11}Be. The two lines correspond to a mass asymmetric, with $8/3$ mass ratio, two body breakup, thus easily assigned to the ^{8}Li+t channel. We ssume that the ^{9}Li+d channel does not appear in the scatter plot, as it is really difficult to observe in ^{9}Li and d coincidence events. The fact that the two observed lines have precisely slopes of $8/3$ and not $9/2$ comfirms that our experimental threshold

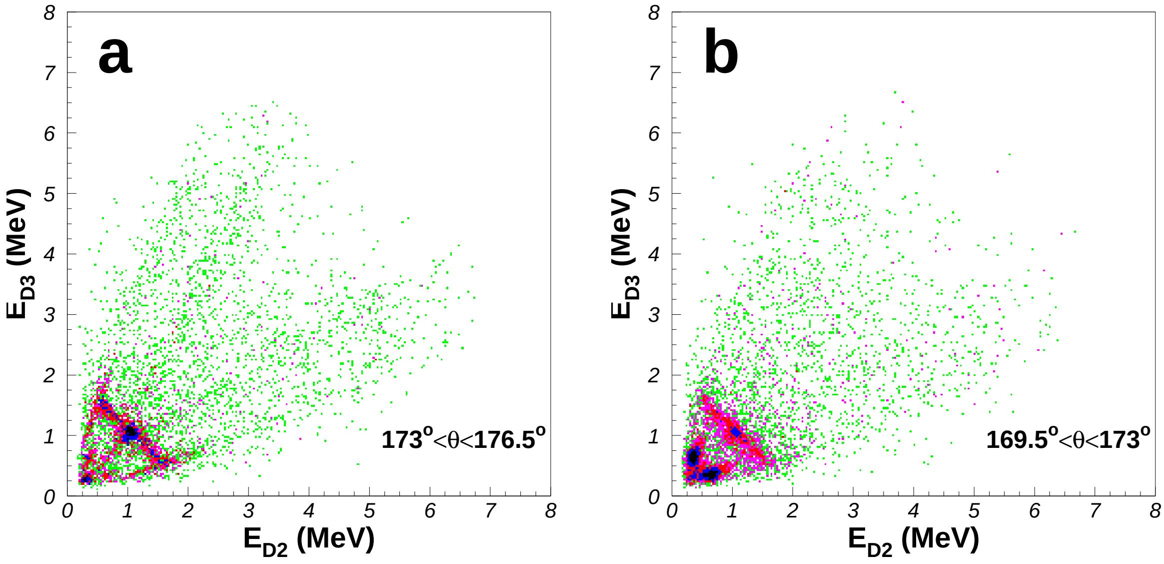

Figure 6.24: Left: charged particle energy versus energy scatter plot for coincidence particles detected with angles $173° < \theta < 176.5°$. *There is still a contribution from the two bands corresponding to* $^{8}Li+t$ *breakup events, although less intense than the region* $\Theta > 176.5°$ *in Fig. 6.23. This can be attributed to the fact that detector D2 was closer to the carbon foil stopper, thus having an angular coverage of 4.6°, greater than the 3.5° cuts we used. Right: energy versus energy scatter plot for particles detected with angles* $169.5° < \theta < 173°$. *Now the contribution of the* $^{8}Li+t$ *has completely dissappeared.*

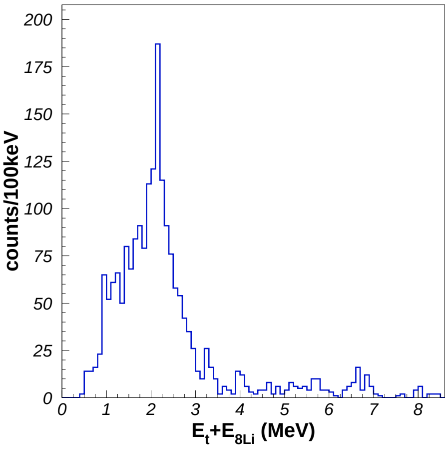

Figure 6.25: Triton energy plus ^{8}Li energy for events gated in the intervals shown in Fig. 6.23.

prevents the observation of the βd channel. The lines at higher energies correspond to strictly back-to-back events of the three body breakup of the ^{11}Be 16 and 18 MeV states through the ground state of ^{7}He (see previous section).

In order to be sure that the assignment of the two bands to the ^{8}Li+t channel is correct, we studied the *180°* coincidences imposing different angular conditions. Fig 6.24(a) and (b) show the coincidence events with detected angles between 173° and 176.5° and between 169.5° and 173° respectively. We see how there is still some residual of the two bands visible, which dissappear completely for angles between the particles lower than 173°. This supports that the two bands correspond to true back-to-back events. The fact that the angular resolution of one pixel in detector D2, 4.6°, is larger than the resolution of D3, 3.5°, as detector D2 was closer to the carbon foil, meaning thy do not fully overlap, is likely the reason why strict back-to-back coincidences, as the two bands, appear in both Fig. 6.23 and 6.24(a).

We selected the events within the two bands shown in Fig. 6.23. These intervals correspond to lines of 8/3 and 3/8 slope, and $\pm^{0.1}_{0.3}$ MeV offsets, in order to include data associated to the ^{8}Li+α channel. At this point in the reconstruction of energy we take into account pulse height effects for both tritons and ^{8}Li, correcting the energy calibration from the alpha sources by a factor of $\epsilon_t/\epsilon_\alpha = 1.012$ and $\epsilon_{^{8}\mathrm{Li}}/\epsilon_\alpha = 0.987$, taken from [Len86]. In order to increase the precision of the energy reconstruction the energy losses in the detector deadlayers and the carbon-foil stopper were calculated using SRIM tables for tritons and ^{8}Li ions.

Fig. 6.25 shows the sum energy spectrum for events selected within these two

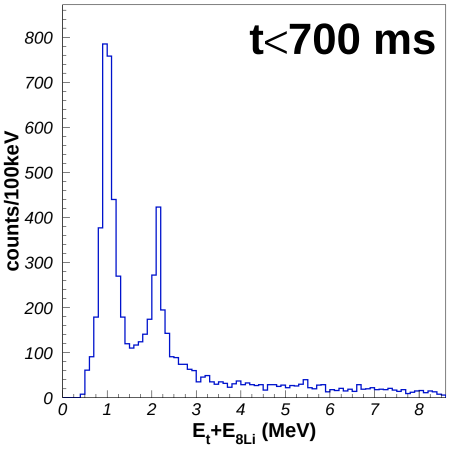

Figure 6.26: Triton and ^{8}Li sum energy spectrum for events within the first 700 ms after the proton impact. The longer time window, compared to the typical 60 ms used to study events from the ^{11}Li β-decay, increases relatively the intensity of the 1 MeV peak, indicating that it comes from the $\beta\alpha$ background of the daughter ^{11}Be.

bands. Fig. 6.25 includes decay channels beyond the ^{8}Li+t spectrum, a peak at 2.2 MeV and an increase of statistics at 1 MeV, hidding an unresolved peak. The 2.2 MeV peak corresponds to the transverse line in Fig. 6.23, indicating the presence of the nα^{6}He channel. The increase of statistics at 1 MeV can be interpreted from a careful inspection of the scatter plot in Fig. 6.23. We see that the contribution of the ^{11}Be daughter $\beta\alpha$ activity is present as the usual two groupings at low energy. In order to confirm the presence of the ^{11}Be $\beta\alpha$ activity in the ^{8}Li+t sum energy spectrum we increased the time window up to 700 ms after the proton impact, instead of the usual 60 ms, see Fig. 6.26. Now, the 1 MeV peak appears clearly defined and much more intense than the 2.2 MeV peak associated to the ^{11}Li β-delayed events.

Once we have characterized the decay channels contributing to the events gated on the ^{8}Li+t channel we proceed to characterize the state or states decaying through the triton emission channel.

6.4.2 Characterization of the state(s) decaying through triton emission

First, we have to consider which level or levels contribute to the βt channel. Both the ^{11}Be 16 and 18 MeV states are above the triton separation energy, $S_t(^{11}\text{Be})=15724.8(4)$ keV. If the ^{11}Be 16 MeV state were to contribute (E_0=16.3(1) MeV), the Q value for

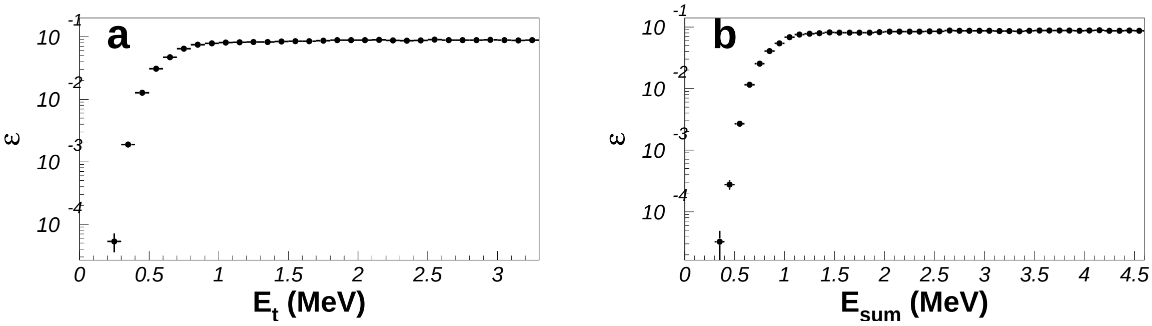

Figure 6.27: Left: Detection efficiency in the ^{8}Li+t channel function of the triton energy. Right: Detection efficiency in the the ^{8}Li+t function of the triton plus ^{8}Li sum energy .

the ^{8}Li+t breakup would be centered at ∼0.6 MeV, which would correspond to a broad peak in the low end of the triton plus ^{8}Li sum energy spectrum in Fig. 6.25, which does not appear. However, before ruling out the involvement of the ^{11}Be 16 MeV state we should note that the expected Q value is low enough to be affected by a reduction of the coincidence detection efficiency at low energy.

We estimated the coincidence detection efficiency from a Monte-Carlo simulation of the ^{8}Li+t breakup. In order to obtain the distribution of the detection efficiency as a function of the center of mass energy of the ^{8}Li+t system, we performed the Monte-Carlo simulation for all energies in the $Q_{\beta t}$ window. The resulting detection efficiency from the simulation, function of both the triton energy and the triton plus ^{8}Li sum energy, is shown in Figs. 6.27(a) and (b). The absolute detection efficiency we obtain for tritons is a fairly constant 8.8(1)% above 1.5 MeV (2 MeV sum energy). The efficiency decays linearly and slowly at energies lower than 1.5 MeV, with 7% detection efficiency at 800 keV (1.1 MeV sum energy). At energies lower than 800 keV the efficiency drops dramatically. The detection efficiency drops to 0.8% at 430 keV triton energy, corresponding to 600 keV sum energy, which is the expected energy for the decay of 16 MeV state through the ^{8}Li+t channel. In summary, because of the coincident detection efficiency we do not expect to observe the decay of the ^{11}Be 16 MeV state through triton emission.

Thus, this indicate that only one known state, the one at 18 MeV, contribute significantly to the ^{8}Li+t channel threshold energy. As there are no indications, such as extra peaks, in the triton plus ^{8}Li sum energy spectrum, we work with the hypothesis that only one state in ^{11}Be is involved. A Monte-Carlo simulation of the ^{8}Li+t breakup of a highly excited state in ^{11}Be was performed. The two other channels present in Fig. 6.25, the low energy ^{7}Li+α channel and the nα^{6}He breakup of the state at 10.59 MeV in ^{11}Be were also considered. The ^{11}Be resonances were described using the non-interfering single channel R-matrix formalism (see section 3.3.2). The triton penetrability was calculated using l=1 orbital angular momentum, which is the lowest value for the $3/2^{-}$ spin of the ^{11}Be 18 MeV state (see previous sections) and the 2^{+} and $1/2^{+}$ ground states of ^{8}Li and the triton, respectively. The intensity of the nα^{6}He and $\beta\alpha$ channels were fixed to reproduce the coincidence spectrum observed in opposite detectors, corresponding to the values given in section 5.4 of the 2003 experiment.

In order to obtain an accurate model of the ^{11}Be state decaying through the βt channel it is important to include the background from the $\beta\alpha$ and nα^{6}He channels. The channels that contribute to the spectrum in 6.25 are

- (1) $^{11}\text{Li} \rightarrow \beta + {}^{11}\text{Be}^{*} \rightarrow \text{t} + {}^{8}\text{Li}$.
- $^{11}\text{Li}\rightarrow \beta+{}^{11}\text{Be}^{*}(10.6)\rightarrow\text{n}+\alpha+{}^{6}\text{He}$ ($\Theta <176^{\circ}$)
- $^{11}\text{Be}\rightarrow \beta+\alpha+{}^{7}\text{Li}$

The nα^{6}He channel ws described using the parameters from the breakup of the ^{11}Be 10.6 MeV state as discussed in the analysis of the 2003 experiment. On the other hand, to reproduce the ^{11}Be daughter $\beta\alpha$ channel as accurately as possible we described the center of mass energy distribution using a Lorentz resonance shape

$$w(E) = \frac{0.5}{\pi}\frac{\Gamma}{(E-E_0)^2+\Gamma^2/4} \tag{6.12}$$

whose centroid and width were fitted to the D2 and D3 sum energy spectrum of events detected in opposite pixels. In order to enhance the conrtibution of the daughter $\beta\alpha$ instead of analysing events in the first 60 ms after proton impact, see Fig. 6.28(a), we studied events for a time interval 0.12<t<4 s (see Fig. 6.28(b)). The parameters of the Lorentzian resonance obtained from the fit are E_0=1.10(5) MeV and full width half maximum Γ=0.28(1) MeV. The literature [Ajz88] Q value and width of the reaction are 1.212(8) MeV and 0.110(15) MeV, respectively, which deviate from the parameters obtained from the fit. However, the results of the fit, overlaid in red in Fig. 6.28, are remarkably good.

We evaluated the energy centroid and reduced width of the resonance decaying into ^{8}Li+t via a χ^2 test of the Monte-Carlo simulation of the triton plus ^{8}Li sum energy spectrum, shown in Fig. 6.25. We tested a series of Monte-Carlo simulations modifying the value of the centroid of the state between 18.25 and 18.55 MeV and γ^2 between 0.15 and 0.45 MeV pairs, trying every combination possible in steps of 0.1 MeV. We performed a χ^2 test of the Monte-Carlo simulation to the triton plus ^{8}Li sum energy spectrum between 1.6 MeV and 3.1 MeV, in order to minimize the

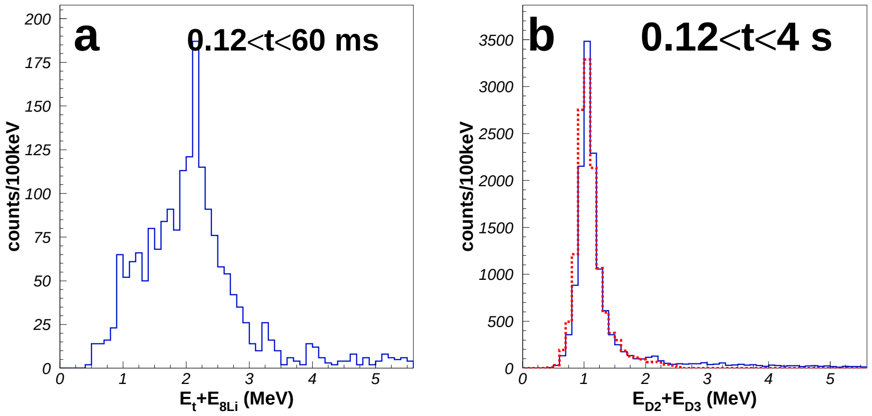

Figure 6.28: Left: (a) the ^{8}*Li+t energy spectrum for events selected in between the bands in Fig. 6.23, for events within the first 60 ms after the proton impact, is shown. Right: (b) the detectors D2 and D3 sum energy spectrum for events gated in between the bands of Fig. 6.23 and within the difference time interval* $0.12 \leq t < 4$ *s, in order to increase the intensity of the* ^{11}*Be daughter* $\beta\alpha$*decay. The red dashed histogram shows the result of the fit of the* ^{11}*Be daughter* $\beta\alpha$ *channel.*

effect of the daughter $\beta\alpha$ channel. Fig 6.29 shows the result of the 16 χ^2 tests. The distribution along the energy centroid axis shows that the χ^2 is fairly insensitive to the centroid. The χ^2 curves for the different γ^2 for centroid at 18.35 MeV and 18.45 MeV are similar, but the curve for the E_0=18.35 is somewhat lower. This puts the minimum at E_0=18.35(3) MeV and γ^2=0.25(7) MeV, with a χ^2 value of 17.3 for 13 degrees of freedom. The error in the energy centroid is a conservative value, taking into account that the χ^2 test is not sensitive to E_0. These values agree within error bars with the previously published E_0=18.15(15) MeV and Γ=1.3(3) MeV [Bor97a].

The Monte-Carlo simulation of the triton plus ^{8}Li sum energy spectrum and the triton energy spectrum, compared with the data, are shown in Figs. 6.30(a) and (b) respectively, with the different channels involved color coded according to the legend. The triton component of the simulation in the triton energy spectrum in Fig. 6.30(b) compares well to the triton component in [Bor97a].

One should note that the result of the χ^2 test for the minimum, 17.3 for 13 degrees of freedom, is small, indicating that we have a good fit. In order to have an idea of the goodness of a χ^2 fit, the χ^2 0.1 critical value is defined as the limit where a χ^2 result greater than the limit would only have a 10% probability of being correct even being high. The 0.1 critical value for 13 degrees of freedom is 19.81 [Bar89]. Our χ^2 results is lower than this critical value, indicating that the R-matrix model

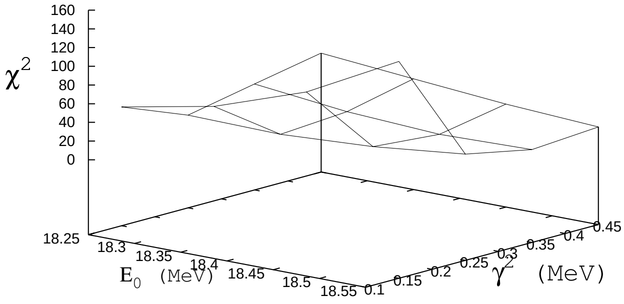

Figure 6.29: Result of the χ^2 tests performed by changing the energy centroid and reduced width of the state decaying through the ^{8}Li+t channel.

including one resonance reproduces well the experimental features in the selected range, and we do not need to include the contribution of other states.

6.4.3 Determination of the βt branching ratio

After the determination of the parameters of the state decaying through triton emission, we can obtain the channel branching ratio. By inspecting Fig. 6.24(a) we see that the two lines signature of ^{8}Li+t breakup are still present for detection angles in the range $173^o < \theta <176.5°$, thus we increased the acceptance to 7°, two pixels, to include the full βt channel statistics.

We follow the procedure explained in the previous section, used to determine the nα^6He and 2α3n branching ratios. We determine the total ^{11}Li activity, to normalize the Monte-Carlo simulations, from the the daughter ^{11}Be $\beta\alpha$ activity. Eq. 5.4 shows the activity as function of the ^{11}Li β-decay branching ratio to the first excited state in ^{11}Be of 7.4(3)%, we used the weighted average of the values from [Bor97b, Bjo81, Aoi97, Mor97, Det80], and the branching ratio of the $\beta\alpha$ ^{11}Be decay, obtained from the value of ^{11}Be β-decay branching ratio to the 9.8 MeV state in ^{11}B, 2.9(4) % [AMW81].

Finally, the intensity of the ^{8}Li+t branch was obtained from a χ^2 test of the Monte-Carlo simulation of the ^{8}Li+t sum energy spectrum varying the intensity of the βt channel, see Fig. 6.32. The results of the test were fitted to a parabola, the expected behavior of the χ^2 distribution, to obtain the minimum, resulting in a BR$_t$=$0.93(8)\times10^{-4}$. This value agrees well with the previously published

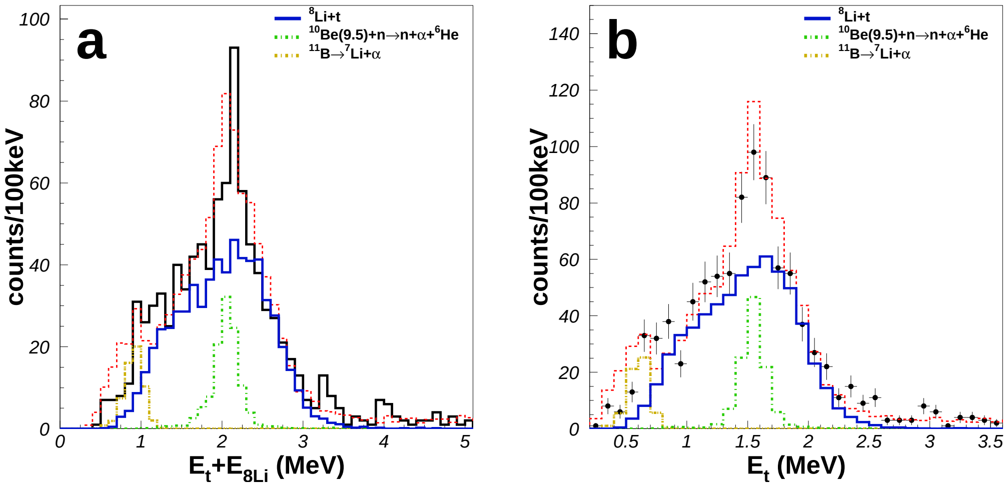

Figure 6.30: Left: the triton plus ^{8}Li sum energy spectrum in black compared to the Monte-Carlo simulation in dashed red, with the different components color coded according to the legend. Right: the triton energy spectrum is compared to the simulation. The triton spectrum matches well to the one obtained in [Bor97a].

branching ratios obtained from the triton spectrum BR$_t$=1.0(4)×10^{-4} [Lan84] and BR$_t$∼ 1.2×10^{-4} [Muk96].

6.5 Determination of the B(GT) values to states in ^{11}Be above the charged particle emission thresholds

Once we have determined the branching ratio of the different breakup channels of the ^{11}Be states above the charged particle thresholds, we are ready to tackle the problem of obtaining their B(GT) values. First let us summarize the branching ratios of the different levels and channels obtained in this work

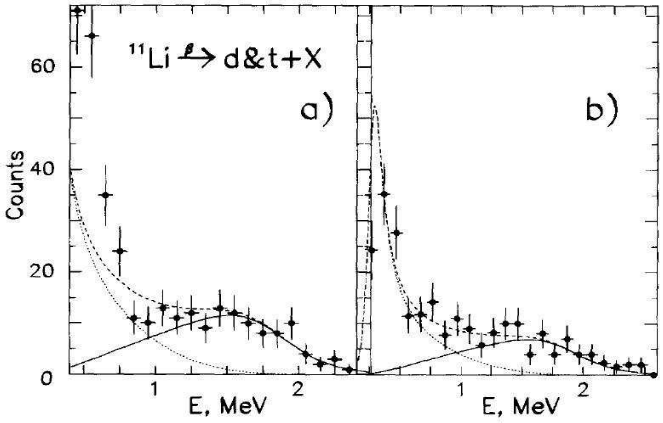

Figure 6.31: Energy spectrum of deuterons and tritons identified using a gas telescope [Bor97a]. The left and right panels correspond to different data sets. The thin dotted line corresponds to the fit deuteron spectrum whereas the thick continous line corresponds to the fit to the triton spectrum. The fitted triton spectrum, and the data above 1.2 MeV corresponds well to the triton spectrum obtained in this work, presented as a thick blue line in Fig. 6.30(a).

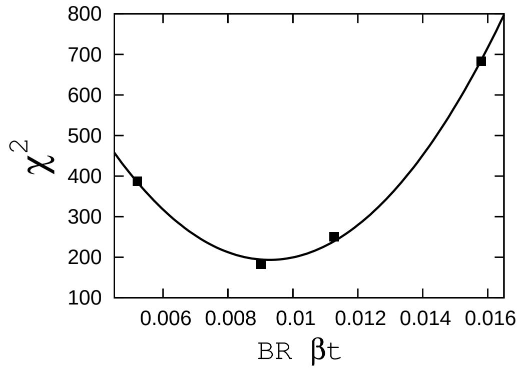

Figure 6.32: Results of the χ^2 tests performed to obtain the intensity of the βt channel. The minimum of the parabola is at 0.93(8)$\times$10^{-4}.

	Channel	BR (%)	Total BR (%)
^{11}Be(10.6)	$2\alpha 3$n†	1.1(2)	1.45(20)
	^{10}Be(9.5)+n†	0.23(4)	
	^{7}He(gs)+α	0.12(2)	
^{11}Be(16)	$2\alpha 3$n	0.042(7)	0.048(7)
	n$\alpha^{6}He$	0.006(1)	
^{11}Be(18)	$2\alpha 3$n	0.24(4)	0.27(4)
	n$\alpha^{6}He$	0.020(3)	
	^{8}Li+t	0.0093(8)	

†taken from the 2003 experiment

And, in the case of the ^{11}Be 18 MeV state, Borge et al. [Bor97a] cite three more decay channels involving the emission of neutrons, thus not detectable in coincidences in our experiment, into states in ^{9}Be and ^{10}Be

	Channel	BR (%)
^{11}Be(18)	^{10}Be+n	$\leqslant$0.0015
	^{10}Be(2^{+})+n	0.15
	^{9}Be+n+n	$\leqslant$0.027

In principle, these three channels should be taken into account in order to calculate the B(GT). However, there is a problem in including the ^{9}Be+n+n channel. The method we used to calculate the B(GT) value relies in the R-matrix resonance shape to normalize the Fermi function over the state (see below), and neither the decay model nor the resonance parameters for the ^{9}Be+n+n channel are provided in [Bor97a]. Thus, we only include the first two decay channels in our calculation.

The determination of the B(GT) values from the branching ratios for broad states is not a trivial matter. The usual decay rate expresion for narrow levels is (see section 1.1)

$$ft = \frac{K/g_V^2}{\mathrm{B_F} + (g_A/g_V)^2\mathrm{B_{GT}}} \tag{6.13}$$

where K/g_V^2=6144.2(13) [HT09] and g_A/g_V=-1.2695(29) [Yao06], and defining B(GT)=$(g_A/g_V)^2\mathrm{B_{GT}}$.

This expression is no longer valid for broad levels. Instead, the branching ratio is given by the integral over the energy in the daughter nucleus of the probability distribution, described by the R-matrix formalism

$$BR = \int_{E_c}^{Q} w(E) \tag{6.14}$$

where E$_c$ is energy of intermediate state after the particle emission, (*i.e.* E$_c$(^{7}He)=8.35 MeV) and $w(E)$ is, in the single-level single-channel R-matrix approach, for the Gamow-Teller transitions, used in this work (see section 3.3.2)

$$w(E) = \frac{ln(2)}{\pi K} f(Q-E) \frac{g_A^2 \mathrm{B_{GT}} P(E-E_c)}{(E_0 + \Delta E - E)^2 + \Gamma^2(E)/4} \tag{6.15}$$

where f(Q-E) is the Fermi factor, $\Gamma = 2P(E-E_c)\gamma^2$ and ΔE and $P(E-E_c)$ are the shift function and penetrability defined in the usual manner (see section 3.3.2). In principle, one should obtain the B(GT) value fitting the channel branching ratio defined in eq. 6.14 to the data. However, there is a technical problem in this approach. In our experiments the coincidence detection efficiency is not trivial, thus the relation between the probability distribution and the experimental distribution is not direct. We solve this problem by performing a Monte-Carlo simulation where the detector efficiency and geometry is explictly implemented.

In the Monte-Carlo method of simulating both the breakup mechanism through R-matrix formalism and the setup efficiency each particle track is studied in an event by event basis, with the total number of events in the simulation of a given decay channel defined by the user. The drawback of this technique is that the R-matrix probability distribution governing the particle energies are normalized to the number of user-defined events, not the proper β-decay normalization. Therefore, **the branching ratio is an intrinsic variable of the Monte-Carlo**, defined as the number of events in the simulation, properly normalized to the experimental area, as we defined in the previous sections dealing with the branching ratios.

Therefore, in our case, we are interested in calculating the B(GT) from the branching ratios directly, using eq. 6.13. Following the method suggested by Nyman et al. [Nym90], the ratio R, which measures the broadness of a state, is defined by dividing eq. 6.14 by eq. 6.13 (for Gamow-Teller transitions (B(F)=0))

$$R = \frac{1}{\pi} \int_{E_c}^{Q} \frac{f(Q-E)}{f(Q-E_0)} \frac{P(E-E_c)}{(E_0 + \Delta E - E)^2 + \Gamma^2(E)/4} \tag{6.16}$$

In our experiment each state has several decay channels, so a single R ratio was calculated for each state, by summing the contribution of each channel weighted by the channel partial branching ratio. Finally, we define an effective Fermi function as

$$f' = R * f(Q-E_0) \tag{6.17}$$

Using the effective Fermi factor we can calculate the B(GT) directly from eq. 6.13. The (g$_A$/g$_V$)^2 term was included in the value of the B(GT), following [Bor97b], in order to compare with the shell model results presented below. We obtain the following R ratios, log(ft) and B(GT)

	R	log(ft)	B(GT)
^{11}Be(10.6)	0.876	4.8(8)	0.09(1)
^{11}Be(16)	1.75	4.9(8)	0.07(1)
^{11}Be(18)	13.03	3.5(6)	1.9(3)

There is only one previous experimental calculation of the B(GT) value of the 18 MeV state [Bor97a], obtaining a B(GT) of 1.6(4) (not counting the deuteron branch), which compared to our value of 1.2(2) (removing the $(g_A/g_V)^2$ term out of the B(GT) value) corresponds within error bands. One should note that they used a technique to calculate the broad level correction to the ft value similar to the one presented in this work, but calculating a partial B(GT) for each individual decay channel. We noticed that the value of R tends to be underestimated for levels close Q_β value, such as the ^{11}Be 18 MeV state, thus overestimating B(GT). Nevertheless, both values correspond rather well.

6.6 Discussion on the B(GT) distribution

The aim of the work presented in this thesis is to study the effects of the halo structure of the ^{11}Li ground state wave function in the distribution of the β-decay strength. In particular, we are interested in two complimentary effects that have been mentioned in the literature:

- If the ground state wave function can be factorized into its core and halo part, it might give rise to similitudes between the B(GT) distribution of ^{11}Li with that of its core ^{9}Li [NNR00].
- Super-allowed like β transitions have been observed to states in the daughter at energies close to Q_β in the decay of the neutron rich ^{6,8}He and ^{9}Li nuclei. The large B(GT) values of this super-allowed transitions are close to the free value (B(GT)=3(N-Z)) of 6 for a di-neutron decaying into a deuteron, indicating they might be linked to the β-decay of one of the halo neutrons [Bor91].

Prior to this work, only the states below the charged particle emission thresholds have been studiedthoriughly and comprehensive way [Fyn04, Hir05]. Now, with the branching ratios and B(GT) values obtained in this work to states above the charged particle thresholds, a more complete picture of the β-decay strength distribution is possible.

Figure 6.33 shows all known states fed in ^{11}Be in the ^{11}Li β-decay. The following table lists the branching ratios, spins and B(GT) values to all known states in ^{11}Be fed in the β-decay of ^{11}Li

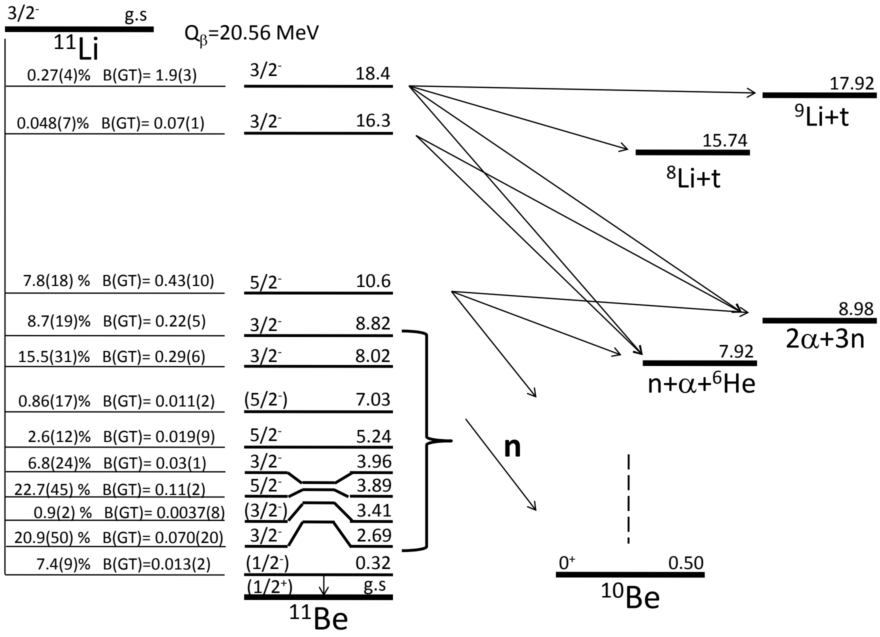

Figure 6.33: Level scheme of the ^{11}Be states fed in the β-decay of ^{11}Li. The open breakup channels are shown for each state by arrows. Please bear in mind that ^{11}Be 10.6 MeV state breaks to the $n\alpha^{6}He$ channel occurs both via neutron emission to $^{10}Be^{*}$ and via alpha emission to the $^{7}He(gs)$, while the breakup of the 16 and 18 MeV states to the $n\alpha^{6}He$ channels occurs via the $^{7}He(gs)$ exclusively.

^{11}Be (MeV)	J$^{\pi}$	BR (%)	B(GT)
g.s.	$1/2^+$	<2	—
0.32	$1/2^-$	7.4(9)	0.013(2)
2.69	$3/2^-$	20.9(50)	0.070(20)
3.41	$(3/2^-)$	0.9(2)	0.0037(8)
3.89	$5/2^-$	22.7(45)	0.11(2)
3.96	$3/2^-$	6.8(24)	0.03(1)
5.24	$5/2^-$	2.6(12)	0.019(9)
7.03	$(5/2^-)$	0.86(17)	0.011(2)
8.02	$3/2^-$	15.5(31)	0.29(6)
8.82	$3/2^-$	8.7(19)	0.22(5)
10.59	$5/2^-$	7.8(18) [1.45(2)]†	0.43(10)[0.09(1)]†
16.35	$3/2^-$	0.048(7)	0.07(1)
18.40	$3/2^-$	0.27(4)	1.9(3)

† contribution of the charged particles channels, obtained in this work.

where, the ground state branching ratio is un upper limit cited by Bjornstad et al [Bjo81], the branching ratios for states below the ^{11}Be 10.59 MeV state are the weighted average of the values in [Fyn04, Hir05], and their B(GT) values were calculated assuming they are narrow states, using eq. 6.13. The spin and parity assigments are taken from the analysis of β-n decay assymetry of Hirayama et al. [Hir05]. The ^{11}Be 10.59 MeV state is a peculiar case, as a mix of one neutron emission and charged particled branches have been measured. A branching ratio of 7.8(18) % is reported in [Hir05], with neutron branches to the ground state of ^{10}Be, the first excited state in ^{10}Be and to a state(s) around 9.5 MeV in ^{10}Be.

	^{10}Be(gs)	^{10}Be(2_1^+)	^{10}Be($\sim$9.5)
^{11}Be(10.59) BR (%)	0.8(1)	0.41(8)	7.2(17)

A 3.4(7) % out of the 7.2(17) % neutron branch to high excited states in ^{10}Be is assigned to the ^{9}Be+2n channel. This leaves a 3.8(18) % for the $2\alpha3$n and nα^6He branches, which were measured in this work. We obtained a 1.45(20) % branch, significantly lower. However, one should take into account the large uncertainty in the neutron transition to the 9.5 MeV state(s) provided in [Hir05], which are due to the difficulty in fitting the low energy neutron peak feeding the $\sim$9.5 MeV state(s) in ^{10}Be, E$_n$ $\sim$1 MeV, which appears as a large time of flight tail of the spectrum. We consider the 7.8(18) % value as an upper value of the branching ratio, thus the B(GT) obtained should be also considered an upper value.

The B(GT) distribution is shown in Fig. 6.34, with the values taken from [Fyn04, Hir05] shown in open bins and the values obtained in this work shown in full bins.

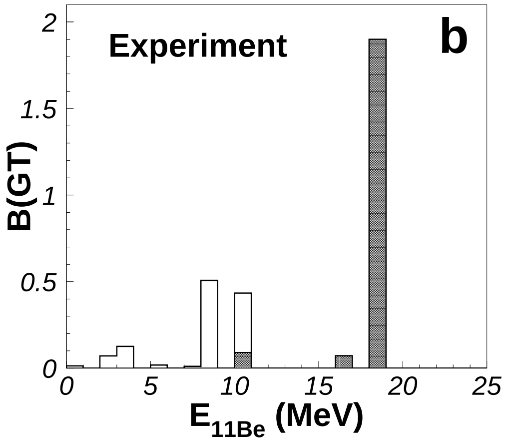

Figure 6.34: B(GT) transition values to excited states in ^{11}Be, corresponding to Table 6.6 . The values obtained in this work are shown in solid bins. The values to states below the charged particle emission thresholds are shown in open bins.

The part of B(GT) value of the ^{11}Be 10.59 MeV state obtained in this work from the $2\alpha 3$n and nα^{6}He channels is shown as the filled part of the 10 MeV bin.

6.6.1 Comparison to the B(GT) distribution of the decay of the ^{9}Li core

As mentioned in the introduction of this section, one of the aims of this work consists in comparing the B(GT) distribution of the beta decay of ^{11}Li with the distribution of its core ^{9}Li. Nilsson and coworkers [NNR00] proposed that the halo structure of ^{11}Li can affect not only to the beta transitions to certain levels, as the reduced strength observed in the transition to first excited state in ^{11}Li [Aoi97, Bor97b], but if the halo neutrons decay more or less independently of the core, this might produce specific patterns in the β-decay strength. This can be understood if we assume we can factorize the halo ground state in its halo and core parts, thus the β-decay operator may act independently on each one

$$\hat{O}_\beta|halo\ state\rangle = \hat{O}_\beta\left(|core\rangle|halo\rangle\right) = (\hat{O}_\beta|core\rangle)|halo\rangle + |core\rangle(\hat{O}_\beta|halo\rangle) \quad (6.18)$$

Both terms on the right hand side are needed to have the correct isospin in the final state. This equation will only describe well the β-decay if the states in the right hand part, to a good approximation, is an eigenstate of the daughter nucleus (or eigenstates if the core β-decay leads to several levels). As both the halo and

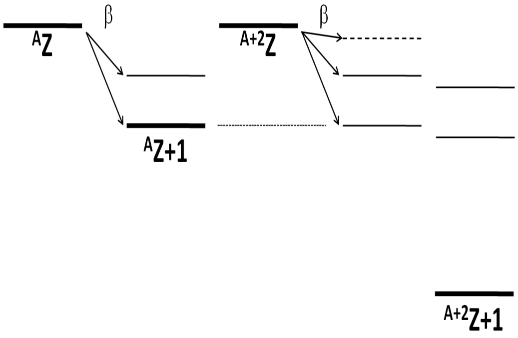

Figure 6.35: Schematic model of the β-decay of a two neutron halo nucleus. If the wave function can be factorized in its halo and core components, the decay of the core (shown on the left) and the halo (the dashed line on the right) contribute to the decay separately. The true eigenstates of the daughter nucleus will have different energies due to the isotopic variation of the core+n potential. Taken from [NNR00].

core parts participate in both terms, partial overlapping between the final state wavefunction and one of the parts will greatly reduce the impact of this model.

Figure 6.35 shows schematically this process. On the other hand, approximations neglecting one of the terms in the right hand side has been studied by Zhukov and coworkers [Zhu95] (neglects core decay) and Timofeyuk [TD96] (neglects halo decay).

Zhukov and coworkers [Zhu95] propose that the decay occurs directly to the halo neutrons, with no effect to the core. The isospin change due to the β-decay in the halo neutrons gives rise to two halo analog states in the daughter nucleus, of halo isospins $T^h = T^h_0$, T^h_0-1 and angular momentum $J^h = J^h_0$, J^h_0+1. These two states in the decay of the halo neutrons of ^{11}Li are calculated, with the $T^h=1$, $J^h=0^+$ state above the ^{9}Li+p+n breakup threshold, and the state with $T^h=0$, $J^h=1^+$ below the ^{9}Li+p+n threshold but above the ^{9}Li+d threshold. Thus, in this approximation of eq. 6.18, the effect of the halo state on the beta decay is local, restricted to the halo-analog states populated in the daughter. In this section we are interested in the overall effect of the halo plus core structure of ^{11}Li on the B(GT) distribution, thus the possible interpretation of this model on the ^{11}Li βd branch will be explored in the next section.

Timofeyuk and coworkers [TD96] explore the opposite approximation, decay of the core with little perturbation of the halo neutrons. This approximation is fairly attractive as the final states populated in the daughter nuclei will match the decay of the core alone (in our case ^{9}Li) and, if the interaction of the valence neutrons and the core is slightly changed after the beta decay, with binding energies respect to the particle emitting thresholds similar to those of the core nucleus itself (see Fig. 6.35). They applied their model to the beta decay of ^{14}Be, and the decay of the ground state of the ^{12}Be core into the 1^+ ground state of ^{12}B. For identical ^{12}Be+n and ^{12}B+n potentials, they calculate the energy of the ^{12}B+n+n like state in ^{14}B at 4.4 MeV. The daughter nucleus ^{14}B is described in a two cluster model, mixing ^{12}B+2n and ^{13}B+n configurations, showing that a 1^+ state is bound only for the ^{12}B+2n configuration. The transition strength obtained is similar to the feeding to the ^{14}B 1.28 MeV 1^+ state, supporting the picture of the core decay.

We compare in our case the β-decay of ^{11}Li with its core ^{9}Li. The following table shows the states populated in ^{9}Be in the β-decay of ^{9}Li, their spins, branching ratios and B(GT) strengths, taken from [Nym90, Pre03]

^{9}Be* (MeV)	J$^{\pi}$	BR (%)	B(GT)
g.s.	$3/2^-$	49.2(9)	0.031(3)
2.43	$5/2^-$	31.9(34)	0.047(5)
2.78	$1/2^-$	11.6(22)	0.011(5)
5.0	$3/2^-$	3.15(40)	—
7.94	$5/2^-$	1.5(4)	<0.403
11.81	$5/2^-$	2.7(2)	8.5(1)

Figure 6.36 upper and lower panels show the B(GT) distribution of the ^{9}Li β-decay and the ^{11}Li β-decay respectively. Both distributions show a similar trend of having the B(GT) strength fragmented along several states, and a trend of increasing strength towards higher energies. but no direct correspondence seems to be possible. Naively, one might disregard the two neutrons binding energy in ^{11}Be and calculate the ^{9}Be $3/2^-$ ground state excitation energy in ^{11}Be as

$$E_x = Q(^{11}Be) - Q(^{9}Be) = 8.824(4)\ \text{MeV[Bac05, AWT03]} \tag{6.19}$$

There is a known $3/2^-$ state at 8.82 in ^{11}Be [Hir05], however its B(GT) is an order of magnitude higher than that of the ground state of ^{9}Be. Of course, we have not taken into account the binding energy of the two neutrons, which will make the excitation energy lower. We can compare the first state fed in the β-decay above the charged particle emission thresholds, which in both ^{9}Be and ^{11}Be corresponds to a $5/2^-$ state. However, again the observed B(GT) strength does not match in the two β decays, being the strength to the ^{11}Be 10.56 MeV state 10 times the strength to the ^{9}Be 2.43 MeV state. This is not surprising, as the ^{11}Be 10.56 MeV state has a strong neutron emission channel, indicating a strong component of a ^{10}Be core plus a neutron.

Although in a superficial way both strength distributions of the ^{9}Li and ^{11}Li β-decays seem to be similar, a direct correspondence between the two decays cannot

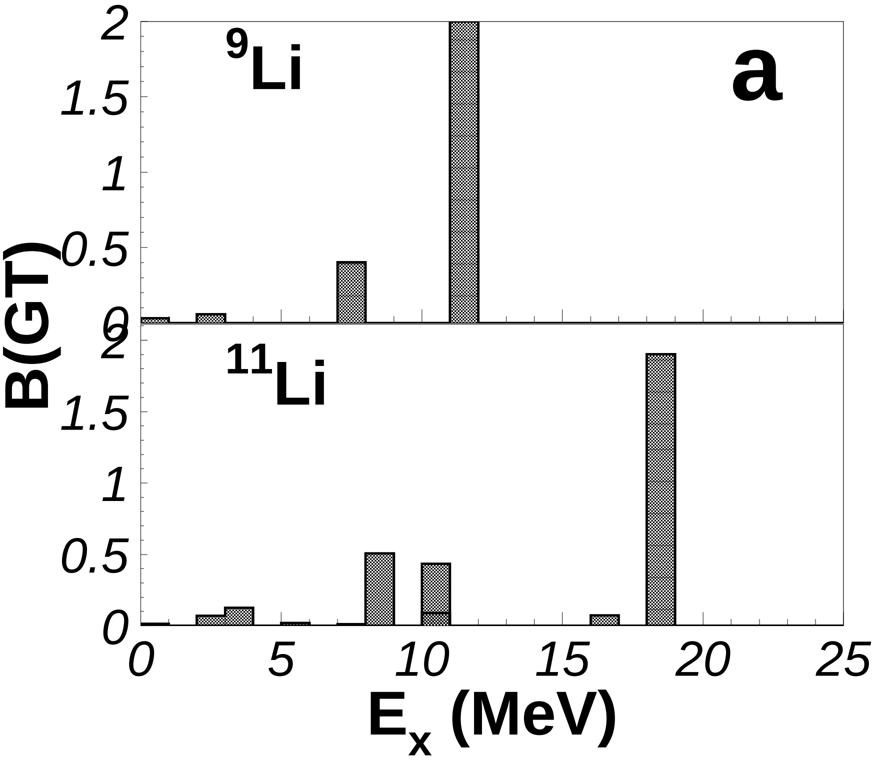

Figure 6.36: B(GT) distribution of the ^{9}Li β decay (upper panel, the strength to the ^{9}Be 11.81 MeV state is truncated) and of the ^{11}Li β-decay (lower panel). The ^{9}Li B(GT) values are taken from [Nym90, Pre03], while the ^{11}Li values below particle emission thresholds are from [Fyn04, Hir05], and the values above the particle emission thresholds are from this work. Both distributions show the same general trend of fragmented intensity increasing as the states get closer to the Q_β value, but no one to one fitting can be done, except for the strong transition present in both nuclei at energies close to the Q_β values of 13.6066(19) MeV and 20.557(4) MeV for ^{9}Li and ^{11}Li respectively.

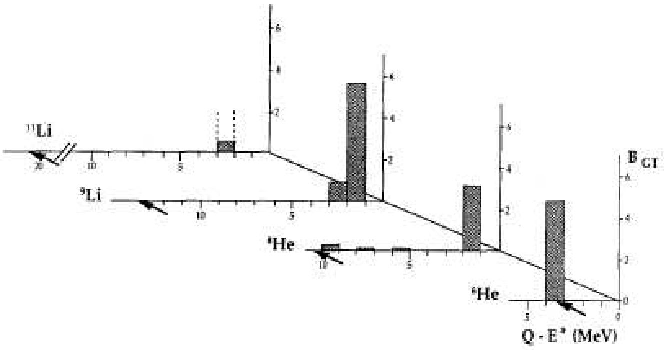

Figure 6.37: B(GT) distribution of the β-decay of light neutron rich isotopes ^{6}He, ^{8}He, ^{9}Li and ^{11}Li. All show a similar strong transition at an energy close to the Q_β value. Figure taken from [Bor91].

be made. This indicates that, in general, the excited states in ^{11}Be have a structure that does not match with a simple ^{9}Be core plus two neutrons picture. Even in the states near the particle emission thresholds, close to where possible ^{9}Be core states might be, there is no direct match possible. This indicates that the underlying structure of the ^{11}Be states is better described as ^{10}Be core plus neutron or more complicated n-α-^{6}He molecular states.

The strong β-feeding to a state close to the Q_β value is an obvious exception to this rule. This transition has been observed in several other light nuclei, and has been linked to the β-decay of the neutrons in the ^{11}Li halo wave-state [Bor91, Zhu95]. In the following section we will discuss more in detail this transition.

6.6.2 Super-allowed transitions

The large B(GT) value, 1.9(3) (B_{GT}=1.2(2)), and low value of the log(ft), 3.5(6), suggests that the β-transition feeding the ^{11}Be 18 MeV state is of the super-allowed type. Transitions of this type have been confirmed for the neutron rich nucleus near the drip-line ^{6,8}He and ^{9}Li

Decay	log(ft)	B_{GT}	Ref.
^{6}He→^{6}Li(gs)	2.910(2)	4.75	[WA74, Rob78]
^{8}He→^{8}Li*(9)	3.09	3.14	[BW88]
^{9}Li→^{9}Be*(11.81)	2.7(2)	5.3(9)	[Nym90, Pre03]
^{11}Li→^{11}Be*(18)	3.5(6)	1.2(2)	This work

We see that the ^{11}Li β-decay transition to the ^{11}Be 18 MeV state follows, although it is not as strong, the same trend observed in these neutron rich nuclei, see fig 6.37.

This leads to a publication by Borge et al. [Bor91] which suggested that these transitions are linked to the β-decay of neutrons in the halo. They argue that the large spatial extension of the halo might favor that the β-decay can occur locally to a neutron in the halo. Besides, they argue that if the nuclear interaction were spin and spin independent, the beta decay would connect states in a Wigner supermultiplet. The effect of spin dependent interactions and Coulomb force is around a few MeV, just affecting the states fed below the Q_β value were it is observed. Moreover, a subsequent work by Poves et al. [Pov94] on the β-decay of the hypothetical double magic ^{28}O supported this picture. They found that the ^{28}O is loosely bound neutron rich nucleus, so they expect the last two neutrons in the fp shell to develop an extended wavefunction, forming a neutron halo. Furthermore, the B(GT) strength distribution indicates that there is a peak in a region at ∼17 MeV, where they expected a large fraction of the overlap with a state in ^{28}F that corresponds to the spin and isospin flip of the two neutrons in the pf shell compared to the ground state of ^{28}O. However, there is recent experimental evidence [Hof09] that ^{24}O is a already a double magic nucleus, and that ^{28}O is not bound. The first excited state was observed at an excitation energy of around 4.7 MeV, indicating that the first excited state is linked to a shell gap. Moreover, the large energy of the first excited state observed in ^{24}O follows the trend of the other known neutron rich oxygen isotopes, indicating that the neutron shell closure moves from N=20 to around 16. This effect of new magic numbers whenmoving away from stability has been observed in N=8, N=20 and N=28 so far.

Alternatively to this attractive interpretation of the B(GT) distribution of the β-decay of light neutron rich isotopes, Sagawa et al. [SHI93] and Hamamoto [HS93, Ham94b] used Hartree-Fock calculations with the random phase approximation to calculate the excited states in series of isotopes with increasing number of neutrons. They found that as the number of neutrons increases in the mother nucleus the single-particle energy of the protons decreases. The reduced single-particle proton energy in the mother nucleus compared to the daughter suggests that the excitation energy of Gamow-Teller giant resonance (GTGR) will decrease relatively to that of the isobaric analog state (see Fig. 6.38). Thus, they argue that the observed super-allowed type β-transitions in nuclei near the drip-lines is due to transitions to the tail of tranistions to the GTGR. They indicate that this effect should be observed as truly super-allowed only for very light nuclei, as, even for nuclei close to the drip lines, for nuclei of Z>8 the GTGR will be above the Q_β [Ham94b].

In the case that concerns this work, the β-decay of ^{11}Li, both interpretations seem to apply. A recent study of the deuteron emission by Raabe et al. supports the interpretation of direct decay of the halo neutrons, as the energy distribution they obtain is not compatible with the emission of deuterons from an intermediate state in ^{11}Be. On the other hand, both the present work and the previous experimental calculation of the ^{11}Be 18 MeV state B(GT) value [Bor97a] indicate that the β^-

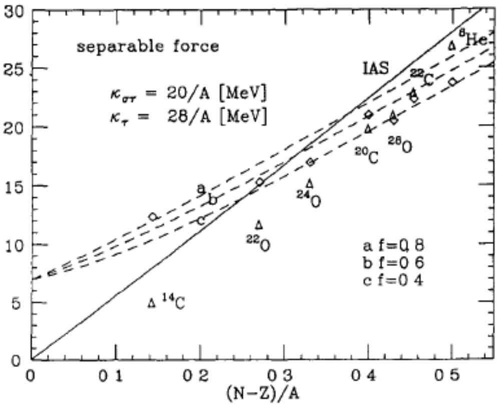

Figure 6.38: Energies of the isobaric analog state (IAS), continuous line, and the gamow teller giant resonance GTGR, the three dashed lines, calculated using a Tamm-Dancoff approximation (TDA) for the nucleon nucleon interaction. Each dashed line corresponds to a different TDA f parameter [Ham94b]. The diamonds represent the calculated GTGR energies for the different nuclei shown, whereas the triangles show the mothers ground state energy. Superallowed beta decay is possible when the diamond lies lower than the triangle of a given nucleus. Figure taken from [Ham94b].

transition to the ^{11}Be 18 MeV state is of the super-allowed type, as expected if the transition occurs to the GTGR.

We finish this discussion section by comparing our experimental B(GT) values with a calculation of the B(GT) from a shell model calculation provided by G.M. Pinedo and A. Poves [MP95, Bor97b]. In this shell model calculation the valence space used consists of the $0p_{3/2}$,$0p_{1/2}$, $0d_{5/2}$ and $1s_{1/2}$ shells, leaving the $0d_{3/2}$ shell out of the calculation as it is located at high energy. The particle occupancy of the different shells of the ^{11}Li and ^{11}Be ground states was adjusted by modifying the calculation with different single-particle energies, in order to reproduce the ^{11}Li half-life, 8.5(2) ms [Til04] and the $\log(ft)$ of the transition to the only bound excited state in ^{11}Be, 5.74 [Bor97b]. They found the best agreement with the data with an occupancy of **0.43** 0.36 0.10 for the $\mathbf{1}s_{1/2}$, $0p_{1/2}$ and $0d_{5/2}$ shells respectively (see figure 6.39), obtaining a $T_{1/2}$=8.29 ms and a decay rate to the first excited state in ^{11}Be with $\log(ft)$=5.73, in excellent agreement with the experimental values. In the calculation they used: effective charges for the protons, e_π=1.2e, and for the neutrons, e_ν=0.2e; free giromagnetic factor; and the oscillator parameter b=1.65. This results, although model dependent, where the first evidence of the a s wave component of the ^{11}Li ground state wave function, as later observed in the experiment by Simon et al [Sim99]

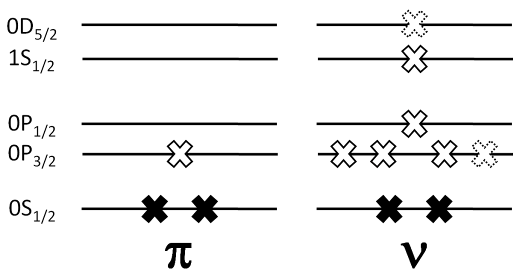

Figure 6.39: Occupation scheme of protons, π, and neutrons, ν, in the shell model calculation of G.M. Pinedo and A. Poves [MP95, Bor97a]. The full crosses indicate the occupancy of the α particle core of the calculation, and the open crosses the valence nucleons. The calculation was performed over the full p and sd shells. The neutron occupancy corresponds to the calculation that best reproduces the ^{11}Li half life 8.5(2) ms [Til04] and the $\log(ft)$ *of the transition to the first excited state in ^{11}Be, 5.74 [Bor97b]. The dashed cross indicates 0.5 occupancy probaility of that single particle state.*

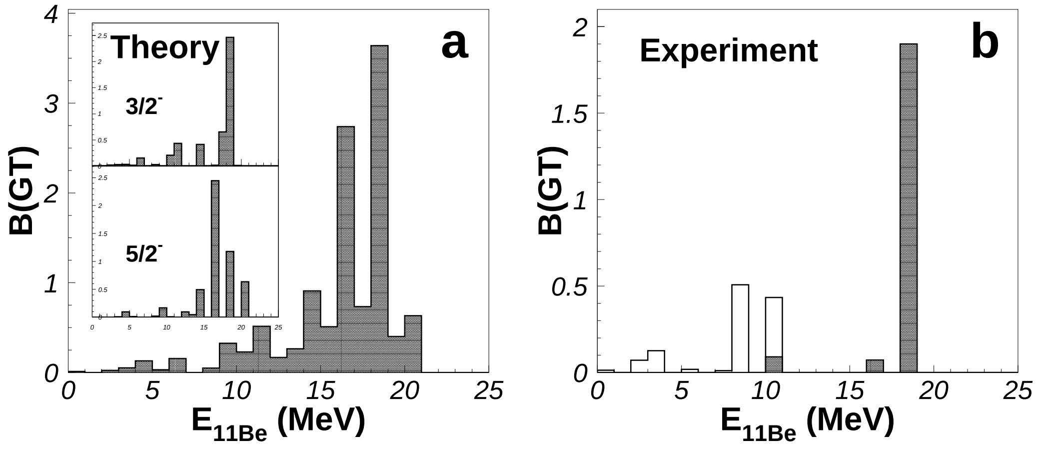

Figure 6.40: Left: B(GT) distribution to excited states in ^{11}Be from the shell model calculation described in the text [MP95]. The upper part of the inset shows the B(GT) distribution for 3/2$^-$ states in ^{11}Be. The lower part shows the distribution for 5/2$^-$ states in ^{11}Be. Right: (b) shows the B(GT) transition values to excited states in ^{11}Be. The values obtained in this work are shown in solid bins. The values to states below the charged particle emission thresholds are shown in open bins.

Fig. 6.40(a) shows the calculated B(GT) strength distribution to excited states in ^{11}Be from the shell model calculation. The inset panels in Fig. 6.40(a) shows the partial B(GT) distribution assuming feeding only to $3/2^-$ or $5/2^-$ states in ^{11}Be, respectively. The B(GT) distribution shows a behavior similar to that observed in the decay of other neutron rich halo nuclei, where a large part of the B(GT) distribution is located at high energy. The interpretation given by Martinez-Pinedo is that this strength corresponds to β-decay transition of the quasi-free neutrons in the halo. However, as they are not able to determine the deuteron emission branching ratio from their wave functions, it cannot be ruled out that the large peak at high energy corresponds to the tail Gamow-Teller giant resonance, as suggested by Sagawa and Hamamoto [SHI93, HS93].

The B(GT) values obtained in this work, are shown in Fig. 6.40(b) in solid bins. The open bins correspond to the B(GT) values to states below the charged particle thresholds, calculated from the weighted average of the branching ratios in [Fyn04, Hir05] and, assuming they are narrow levels, using eq. 6.13 (see Table in the beginning of this section). The shape of the calculated B(GT) distribution to the $3/2^-$ states at high excitation energy in ^{11}Be (E>10.6 MeV) follows the trend of the experimental B(GT) values, supporting the $3/2^-$ spin and parity assignment for these states given in this work. The experimental B(GT) strength for the 16 MeV state in ^{11}Be is very low compared to the shell model calculation including all possible final spins. It should be stressed that the B(GT) values for the high excited levels in ^{11}Be given in this work correspond to decays were at least two charged particles are involved in the breakup. However, one should be aware that there is previous evidence of a feeding of up to 6% to levels in the region between 14-17 MeV excitation energy in ^{11}Be decaying through neutron emission to low energy states in ^{10}Be [Fyn04]. This could explain the difference between the expected B(GT) distribution in this region and the experimental one.

It is interesting to compare the B(GT) value obtained in this work for the ^{11}Be 18 MeV state, 1.9(3) to the one obtained in the shell model calculation at that energy for $3/2^-$ states, B(GT)=2.5. This indicates that the observed transition to the ^{11}Be is close to exhaust the β-strength in that region for $3/2^-$ states. On the other hand, if we look at the B(GT) distribution for all possible final spins in Fig. 6.40, the B(GT) value at 18 MeV goes up to 3.7, corresponding to the remaining strength to $1/2^-$ and $5/2^-$ states. This indicates that there is still unobserved β-decay strength in this energy region. This extra β-strength might be assigned to the deuteron branch, which should have a total B(GT) close to the total sum rule for decay of two neutrons into deuteron, 6, as it has been determined to occur to the quasi-free halo neutrons [Raa08]. It can be explained in a similar picture of that proposed for the decay of ^{28}O, where the final configuration of states in ^{11}Be corresponds to the the same wavefunction of the ^{11}Li core but with the spin and isospin flip of the two neutrons in the *p* and *sd* shells. Following this reasoning, Martinez-Pinedo

[MP95] calculates an upper limit of the deuteron branching ratio from the sum of the transition probabilities of any electron emitted with an energy lower than 2.7 MeV (E(^{11}Be)>17.9 MeV), obtaining 4.42×10^{-4}. The result is fairly good, as it is of the same order of magnitude than the experimental results, 1.2×10^{-4} [Bor97a] and $1.30(13)\times10^{-4}$ [Raa08]. Our value of the ^{11}Be 18 MeV B(GT) matrix element suggests that a more precise value of the deuteron branching ratio might be obtained if one subtracts from the calculation the transition probability corresponding to $3/2^{-}$ states, as neither the ^{11}Be 16 MeV nor the 18 MeV states play a role in the deuteron emission.

Chapter 7

Summary and conclusions

In this work we have studied the β-delayed charged particle emission channels of ^{11}Li and its core ^{9}Li. The goal of this work was to study and compare the β-decay strength distribution of ^{11}Li and its core, to look for specific patterns that would indicate separate decay of the core or the halo. The results obtained can be summarized as:

- In this work we present the results of the analysis of two experiments performed at ISOLDE, CERN in 2003 and 2007. The nuclei of interest, ^{9}Li and ^{11}Li were produced in by spalation in a Ta target, separated from the bulk of reaction products and implanted in a carbon foil to measure the decay at rest. The setups were optimized to measure charged particle coincidences, consisting in 3 double sided silicon detector, each one consisting in 32 individual strips, equivalent to 256 pixels. Morevoer, in the 2003 study of the ^{9}Li decay we had the neutron time of flight detector TONNERRE, in order to detect α-n coincidences.
- **Evidence of the direct breakup to the 2αn continuum of the ^{9}Be 2.43 MeV state.** We studied the breakup mechanism of the $5/2^{-}$ 2.43 MeV state in ^{9}Be fed in the β-decay of ^{9}Li. We obtained the singles alpha energy distribution, the alpha-alpha coincidences energy distribution and the neutron time of flight distribution in coincidence with alpha particles, all gated to the decay of the 2.43 MeV state. We compared the three spectra with simulations of the breakup using three different models: **1)** sequential breakup through the ground state of ^{5}He; **2)** sequential breakup through the first excited state of ^{8}B; **3)** direct decay into the continuum in the "democratic" decay model. The "democratic" model reproduced consistently better than sequential decay all three experimental spectra.
- **Evidence of ^{11}Li beta-delayed decay channels involving ^{A}He reso-**

nances. We studied the charged particle energy correlations following the ^{11}Li beta decay in two experiments in 2003 and 2007 realized at ISOLDE (CERN). The 7/4 or 4/7 ratio between the two charged particles in high sum energy coincidences indicated that the ^{11}Be 18 MeV state breaks-up sequentially in the nα^6He channel through the ground state resonance of ^{7}He. Furthermore, we proposed, from the detailed study of the energy correlations of the two α particles in the 2α3n channel, that the five body breakup occurs through an intermediate step involving ^{5}He(gs)+^{6}He(2^+).

- **Evidence of a new state in ^{11}Be at 16 MeV.** We studied the ^{7}He+α breakup channel in full kinematics. Improved statistics in the 2007 experiment, mainly due to an improved production and a closer geometry of the setup, allowed us to identify the kinematical fingerprint of the ^{7}He+α channel, the energy of the first emitted alpha, from the bulk of alpha-alpha coincidences. By selecting events exclusively in this decay channel we observed the contribution of the previously known ^{11}Be 18 MeV state, and the contribution of a new state at 16.3 MeV.

- **Determination of energy and width of high excited states in ^{11}Be.** By comparing the ^{11}Be excitation energy distribution with Monte-Carlo simulations of the breakup of both states into nα^6He through the ^{7}He(gs), we obtained the energy centroid and width of both states: **1)**for the 18 MeV state we obtained E_0=18.4(3) MeV and Γ=1.6(6) MeV, which coincide within error bars with the values obtained in a previous experiment which used a gas-Si telescope to measure the triton (E_0=18.15(15), Γ=1.3(3)), ^{4,6}He (E_0=18.0(1) MeV, Γ=0.8(1)) and ^{9,10}Be (E_0=18.2(2) MeV, Γ=1.25(15)) emission from this state; **2)** for the 16 MeV state we got E_0=16.3(1) MeV and Γ=0.7(1) MeV.

- **Determination of the spin of the ^{11}Be 16.3 and 18 MeV states.** We studied the angular correlations and the energy distribution of ^{6}He-α coincidence events selected in the ^{7}He+α channel, and compared them with simulations of the breakup assuming the β-transition to the ^{11}Be state is allowed giving possible spin and parities values $1/2^-$, $3/2^-$ and $5/2^-$. The results of both the angular correlations and the energy distribution consistently favor an spin of $3/2^-$ for both states.

- **A new kinematical method to study the βt channel.** We applied the kinematical condition of two body decay to enhance the contribution of the triton channel over the rest of multiple-particle emitting channels. This procedure was applied for the first time to circunvent the lack of Z-identification of the detector system. We selected charged particle coincidences detected in opposite pixels, taking advantage of the fact that the ^{8}Li+t channel, thus the particles are emitted at 180°. The ^{8}Li+t events in the opposite pixels coincidences were identified as those detected with an energy ratio of 8/3. From the resulting triton energy distribution we were able to determine the parameters of the single ^{11}Be resonance involved in the decay, E_0=18.35(3) MeV and Γ^2=1.5(4) MeV, and the βt branching ratio, BR_t=0.93(8)$\times 10^{-4}$.

- **Determination of the B(GT) distribution for states above the charged particle thresholds. 1)** we obtained the beta branching ratios to the 10.6, 16.3 and 18 MeV states (we used the simulations of the different decay channels in order to take into account the experimental acceptance). **2)** The branching ratios were used to calculate the B(GT) distribution. In order to compensate for the large resonances widths, we used a modified Fermi factor, integrated over the full energy distribution of each state.

- **Comparison of the ^{11}Li B(GT) distribution to that of its core ^{9}Li.** Although both ^{11}Li and ^{9}Li distributions show the same general trend of fragmented pattern, no direct state to state comparison was possible. The B(GT) of both states in the β-decay of ^{11}Li is one order of magnitude greater than B(GT) to the ^{9}Be $3/2^-$ ground state and $5/2^-$ excited states observed in the ^{9}Li β-decay. However, the large strength, B(GT)=1.9(2), to the ^{11}Be 18 MeV state indicates it might be of the super-allowed type transition, following the same trend of other halo nuclei as ^{6,8}He and ^{9}Li. The fact that the B(GT) to the 18 MeV state is large, despite the fact that the decay into ^{9}Li+d is not included as it has been proven to occur to the continuum, supports the interpretation of the super-allowed transitions as due to the lowering of the tail of the Gamow-Teller Giant Resonance in light neutron rich nuclei.

- **Comparison of the B(GT) distribution to a shell model calculation.** We compared our B(GT) distribution to a shell model calculation provided by G. Martínez-Pinedo and A. Poves, whose single particle occupancies, 50% of s and p waves , for the ground state de ^{11}Li, were fine-tuned to reproduce the B(GT) to the ^{11}Be 320 keV state. The resulting B(GT) distribution for $3/2^-$ states in the calculation agrees well with the experimental distribution, further supporting the $3/2^-$ assignment from the angular correlations and kinematical analysis of the ^{7}He+α channel.

List of publications

The work presented in this thesis has been published in the following:

- M.Madurga et al., *Multiple particle break-up study of low excited states in Be-9: The ghost peak in the Be-8 excitation energy spectrum visited*, Eur. Phys. J., Spec. Topics, 150 (2007) 138.
- M. Madurga et al., *Study of beta-delayed 3-body and 5-body breakup channels observed in the decay of Li-11*, Nucl. Phys. A, 810 (2008) 1
- M. Madurga et al., *Kinematic identification of the βt branch in the decay of* ^{11}Li Eur. Phys. J. (2009), (online first), DOI 10.1140/epja/i2008-10769-0.
- M. Madurga et al., *Evidence of a new state in Be-11 observed in the Li-11 beta-decay*, Phys. Lett. B 677 (2009) 255

Acknowledgements

My warmest thanks to all the young students and postdocs in the Experimental and Theoretical Nuclear Physics groups at IEM-CSIC. To Raquel, Diego y Susana, whose hearty welcome (and long coffe breaks) made starting at CSIC so much more enjoyable, Ricardo (which shares my love of comics and games), Mario (for being so patient with me in the last months while I was working in my thesis), and to the youngest generation, Mariano and Jose Antonio, whose southern joyfulness is so infectious. My gratitude to Carlos Pascual and Daniel Galaviz, who were allways eager to help with all our problems. I cannot forget to thank all the young people in the Theory group, Armando, Bea, Carolina, Oscar and Raul, for dragging me out of work and reminding me to have fun. Very special thanks to Martin, for all the fruitful physics conversations during coffe (and cigarette) breaks all these years.

My gratitude to Uffe Bergman, for showing me the first steps in the long way of the analysis presented in this work, Fredrik Wenander and Didier Voulot (for making REX experiments possible) and all the people at ISOLDE.

My grateful thoughts to Göran Nyman, Björn Jonson, Elisabeth Tengborn (we shared the longest night-shifts imaginable) and Håkan Johanson (the MBE guru) and all the members of the Subatomic Physics Group at Chalmers.

All my gratitude to Karsten Riisager and Hans Fynbo, for being so kind and welcoming the many times I spent at ISOLDE and Århus, and for the fruitful and exciting discussions that developed. My thanks also to Henrik Jeppessen, Hans Henrik Knudsen, Oliver Kirsebom (allways at the front line in the experiments), Solveig Hyldegaard and the rest of members of the Nuclear Physics group at the University of Århus.

Finally, to Maria Jose and Olof, without their patience, wisdom and pushing me to always give my best, this work would not have been possible.

Bibliography

[AF61] W. P. Alford and J. B. French, Phys. Rev. Lett. **6** (1961), no. 3, 119.

[Ajz78] F. Ajzenber-Selove et al., Phys. Rev. C **17** (1978), 1283.

[Ajz86] F. Ajzenber-Selove, Nucl. Phys. A **460** (1986), 1.

[Ajz88] F. Ajzenber-Selove et al., Nucl. Phys. A **490** (1988), 1.

[Alv08] R. Alvarez-Rodriguez et al., Phys. Rev. Lett. **100** (2008), 192501.

[Amo08] F. Amorini et al., Nucl. Instr. and Meth A **589** (2008), 280.

[Ams08] C. Amsler et al., Phys. Lett. B **667** (2008), 1.

[AMW81] D.E. Alburger, D.J. Millener, and D.H. Wilkinson, Phys. Rev. C **23** (1981), 473.

[And74] RE Anderson et al., Nuclear Physics, Section A **236** (1974), no. 1, 77–89.

[Ang99] C. Angulo et al., Nucl. Phys. A **656** (1999), 3.

[Aoi97] N. Aoi et al., Nucl. Phys. A **616** (1997), 181c.

[Ara96] K. Arai et al., Phys. Rev. C **54** (1996), 132.

[Aum00] T. Aumann et al., Phys. Rev. Lett. **84** (2000), no. 1, 35.

[AW76] D.E. Alburger and D.H. Wilkinson, Phys. Rev. C **13** (1976), 835.

[AWT03] G. Audi, AH Wapstra, and C. Thibault, Nucl. Phys. A **729** (2003), 337.

[Azu79] R.E. Azuma et al, Physical Review Letters **43** (1979), no. 22, 1652–1654.

[Azu80] R.E. Azuma et al., Phys. Lett. B **96** (1980), 31.

[Bac05] C. Bachelet et al., Eur. Phys. J. A **25** (2005), no. s01, 31.

[Bac08] C Bachelet et al., Phy. Rev. Lett. **100** (2008), 182501.

[BAR51] L. C. Biedenharn, G. B. Arfken, and M. E. Rose, Phys. Rev. **83** (1951), no. 3, 586–593.

[Bar89] R.J. Barlow, *Statistics*, John Willey & sons, 1989.

[BB08] B. Blanck and M.J.G. Borge, Progress in Particle and Nuclear Physics **60** (2008), 403.

[Ber01] U.C. Bergmann et al., Nucl. Phys. A **692** (2001), 427.

[BH80] J. P. Biersack and L. Haggmark, Nucl. Instr. and Meth **174** (1980), 257.

[Bjo81] T. Bjornstad et al., Nucl. Phys. A **359** (1981), 1.

[Bla05] B. Blank, et al., Phys. Rev. Lett. **94** (2005), 232501.

[Boc89] O.V. Bochkarev et al., Nucl. Phys. A **505** (1989), 215.

[Boc90] ______, Sov. J. Nucl. Phys. **52** (1990), 964.

[Boc92] ______, Sov. J. Nucl. Phys. **55** (1992), 955.

[Bor91] M.J.G. Borge et al., Z. Phys. **340** (1991), 255.

[Bor93a] ______, Phys. Lett. B **317** (1993), 25.

[Bor93b] ______, Nucl. Phys. A **560** (1993), 664.

[Bor93c] ______, Phys. Lett. B **317** (1993), 25.

[Bor97a] ______, Nucl. Phys. A **613** (1997), 199.

[Bor97b] ______, Phys. Rev. C **55** (1997), R8.

[BR53] L.C Biedenharn and M.E. Rose, Rev. Of Modern Phys. (1953), 729.

[Bro07] T.A.D. Brown et al., Physical Review C **76** (2007), 054605.

[Buc01] L. Buchmann et al., Phys. Rev. C **63** (2001), 034303.

[But00] A. Buta et al., Nucl. Inst. and Methods A **455** (2000), 412.

[BW88] F.C. Barker and E.K. Warburton, Nucl. Phys. A **487** (1988), 169.

[Cab83] M. D. Cable et al., Phys. Rev. Lett. **50** (1983), no. 6, 404–406.

[cer] http://cernlib.web.cern.ch/cernlib/.

[CF88] G. B. Caughlan and W. A. Fowler, At. Data Nucl. Data Tables **40** (1988), 283.

[Che70] Y.S. Chen et al., Nucl. Phys. A **146** (1970), 136.

[chi] *NIST/SEMATECH e-Handbook of Statistical Methods*, http://www.itl.nist.gov/div898/handbook/eda/section3/eda3674.htm.

[Chu97] L.V. Chulkov et al., Phys. Rev. Lett. **79** (1997), 201.

[CK65] S. Cohen and D. Kurath, Nucl. Phys. **73** (1965), 1.

[Cli89] E.T.H. Clifford et al., Nucl. Phys. A **493** (1989), 293.

[CS97] L.V. Chulkov and G. Schrieder, Z. Phys. A **359** (1997), 231.

[Cur01] N. Curtiset al. , Physical Review C **64** (2001), no. 4, 44604.

[CWB93] W.-T. Chou, E. K. Warburton, and B. A. Brown, Phys. Rev. C **47** (1993), no. 1, 163–177.

[Dan87] B.V. Danilin et al., Sov. j. Nucl. Phys. **46** (1987), 225.

[Dat03] U Datta et al., Phys. Lett. B **551** (2003), 63.

[Des01] P. Descouvemont, Eur. Phys. J. A **12** (2001), 413.

[Det80] C. Detraz, J. de Phys. Lett. **41** (1980), 459.

[Dix91] S. Dixit et al., Phys. Rev. C **43** (1991), 1758.

[Dos07] C. Dossat et al., Nucl. Phys. A **792** (2007), no. 1-2, 18.

[Fer34] E. Fermi, Z. Phys. **88** (1934), 161.

[Fir99] Richard B. Firestone, *Table of Isotopes*, John Willey & sons, 1999.

[For99] S. Fortier et al., Phys. Lett. B **461** (1999), 22.

[For08] C. Forssen et al, Phys. Rev. C **77** (2008), 024301.

[Fyn03] H.O.U. Fynbo, Nucl. Instrum. Methods B **207** (2003), 275.

[Fyn04] H.O.U. Fynbo et al., Nucl. Phys. A **736** (2004), 39.

[Gar91] A. García et al, Phys. Rev. Lett. **67** (1991), 3654.

[Gei99] Geithner et al, W., Phys. Rev. Lett. **83** (1999), no. 19, 3792.

[Gio02] J. Giovinazzo, et al., Phys. Rev. Lett. **89** (2002), 102501.

[GK90] K. Grotz and V. Klapdor, *The Weak Interaction in Nuclear, Particle and Astrophysics*, Adam Hilger, 1990.

[GKM51] W.L. Gardner, N. Kable, and B.J. Moyer, Phys. Rev. **83** (1951), 1054.

[Gor95] J. Gorres et al., Phys. Rev. C **52** (1995), 2231.

[Gri00] L. V. Grigorenko et al., Phys. Rev. Lett. **85** (2000), no. 1, 22.

[Gri01] ———, Phys. Rev. C **64** (2001), no. 5, 054002.

[GZ05] L.V. Grigorenko and M.V. Zhukov, Phys. Rev. C **72** (2005), 015803.

[Ham94a] S. Hamada et al., Phys. Rev. C **49** (1994), 3192.

[Ham94b] I. Hamamoto, Nucl.Phys. A **577** (1994), 19c.

[Hir05] Y. Hirayama et al., Phys. Lett. B **611** (2005), 239.

[HM84] F. Halzen and A.D. Martin, *Quarks and Leptons: An Introductory Course in Modern Particle Physics*, John Willey & sons, 1984.

[Hof09] C.R. Hoffman et al, Phys. Lett. B **672** (2009), 17.

[HS93] I. Hamamoto and H. Sagawa, Phys. Rev. C **48** (1993), R960.

[HT09] J. C. Hardy and I. S. Towner, Phys. Rev. C **79** (2009), no. 5, 0555002.

[IT94] M.Z. Zhukov I.J. Thompson, Phys. Rev. C **47** (1994), 1904.

[Jam68] F. James, *Monte carlo phase space*, CERN **68-15** (1968).

[JR98] B. Jonson and K. Riisager, Phil. Trans. R. Soc. Lond. A **356** (1998), 2063.

[JR01] ———, Nucl. Phys. A **693** (2001), 77.

[KEHO95] Y. Kanada-En'yo, H. Horiuchi, and A. Ono, Phys. Rev. C **52** (1995), 628.

[Kno79] Glenn F. Knoll, *Radiation Detection and Measurement*, John Willey & sons, 1979.

[Kob88] T. Kobayashi et al., Phys. Rev. Lett. **60** (1988), 2599.

[Kop60] G. Kopylov, Zh. Eksperim. i Teor. Fiz. **39** (1960), 1091.

[Kor90] A.A. Korsheninnikov, Yad. Fiz. **52** (1990), 1304.

[Kre61] M. Kretzschmar, Ann. Rev. Nucl. Sci. **11** (1961), 1.

[Kug00] E. Kugler, Hyperfine Interact. **129** (2000), 23.

[Kum74] N. Kumar, Nucl. Phys. A **225** (1974), 221.

[Lan81] M. Langevin et al., Nucl. Phys. A **366** (1981), 449.

[Lan84] ______, Phys. Lett. B **146** (1984), 176.

[Len86] W.N. Lennard et al., Nucl. Instr. and Meth A **248** (1986), 454.

[Leo87] William R Leo, *Techniques for Nuclear and Particle Physics Experiments*, Springer-Verlag, 1987.

[LT58] A.M. Lane and R.G. Thomas, Rev. Mod. Phys. **30** (1958), 257.

[LY56] T.D Lee and C.N. Yang, Phys. Rev. C **104** (1956), 254.

[Mac60] M.H. Macfarlane et al., Rev. of Mod. Phys. **32** (1960), 567.

[Mad01] V. Maddalena et al., Phys. Rev. C **63** (2001), 024613.

[Mie07] K. Miernik et al., Phys. Rev. C **76** (2007), 041304(R).

[Mik88] D. Mikolas et al., Phys. Rev. C **37** (1988), 766.

[Mil] D.J. Millener, Private communication.

[Mor97] D.J. Morrissey et al., Nucl. Phys. A **627** (1997), 222.

[Mor02] A.C. Morton et al., Nucl. Phys. A **706** (2002), 15.

[MP95] Gabriel Martínez-Pinedo, *Estudio de procesos debiles y de propiedades colectivas en nucleos ligeros y medios*, Ph.D. thesis, Universidad Autonoma de Madrid, 1995.

[Muk96] I. Mukha et al., Phys. Lett. B **367** (1996), 65.

[MWW69] B.E.F. Macefield, B. Wakerfield, and D.H. Wilkinson, Nucl. Phys. A **131** (1969), 250.

[NNR00] T. Nilsson, G. Nyman, and K. Riisager, Hyperfine Interact. **129** (2000), 67.

[Nym90] G. Nyman et al., Nucl. Phys. A **510** (1990), 189.

[Ohl65] G.G. Ohlsen, Nucl. Inst. and Methods **37** (1965), 240.

[Oza97] A. Ozawa et al., J. Phys. G **24** (1997), 143.

[Pap07] P. Papka et al., Phys. Rev. C **75** (2007), 045803.

[Pfu02] M. Pfutzner, et al., Eur. Phys. J. A **14** (2002), 279.

[Poe96] D.N. Poenaru (ed.), *Nuclear Decay Modes*, Insitute of Physics Publishing, 1996.

[Pos66] A. M. Poskanzer et al., Phys. Rev. Lett. **17** (1966), no. 25, 1271–1274.

[Pov94] A. Poves et al., Z. Phys. A **347** (1994), 227.

[Pre03] Y. Prezado et al., Phys. Lett. B **576** (2003), 55.

[Pre05] ——, Phys. Lett. B **618** (2005), 43.

[Raa08] R. Raabe et al., prl **101** (2008), 212501.

[Rav] H.L. Ravn, *Sources for Production of Radiactive Ion-Beams*, ISOLDE intenal document.

[RG73] S. Raman and N. B. Gove, Phys. Rev. C **7** (1973), no. 5, 1995–2009.

[Rii90] K. Riisager et al., Phys. Lett. B **235** (1990), 30.

[Rob78] R.G.H. Robertson et al., Phys. Rev. C **17** (1978), 4.

[Roe74] E. Roeckl et al., Physical Review C **10** (1974), no. 3, 1181–1188.

[Sar04] F. Sarazin et al., Phys. Rev. C **70** (2004), 031302(R).

[Sau00] E. Sauvan et al., Phys. Lett. B **491** (2000), 1.

[SHI93] H. Sagawa, I. Hamamoto, and M. Ishihara, Phys. Lett. B **303** (1993), 215.

[Sim99] H. Simon et al., Phys. Rev. Lett. **83** (1999), no. 3, 496.

[Sin98] B. Singh et al., Nuclear Data Sheets **84** (1998), no. 3, 487 – 563.

[Smi08] M. Smith et al., Phys. Rev. Lett. **101** (2008), 202501.

[SO94] T. Suzuki and T. Otsuka, Physical Review C **50** (1994), no. 2, 555–558.

[SO97] ______, Physical Review C **56** (1997), no. 2, 847–856.

[Soi96] N. Soic et al., Zadro. Europhys. Lett. **34** (1996), 7.

[SPS91] D.E. Cullen S.T. Perkins and S.M. Seltzer, *Tables and Graphs of Electron-Interaction Cross Sections from 10 ev to 100 Gev Derived from the LLNL Evaluated Electron Data Library (EEDL), z=1,100*, U.S. Department of Energy, 1991.

[SRI92] S. Sundell, H.L. Ravn, and ISOLDE collaboration, Nucl. Instr. and Meth B **70** (1992), 160.

[SS58] P.P. Srivastava and G. Sudarshan, Phys. Rev. **110** (1958), no. 3, 765–766.

[Tan85a] I. Tanihata et al., Phys. Lett. B **160** (1985), 380.

[Tan85b] ______, Phys. Rev. Lett. **55** (1985), 2676.

[TD96] N.K. Timofeyuk and P. Descouvemont, J. Phys. G **22** (1996), L99.

[Ten04] O. Tengblad et al., Nucl. Inst. and Methods A **525** (2004), 458.

[Til98] D.R. Tilley et al., Nucl. Phys. A **636** (1998), 249.

[Til04] ______, Nucl. Phys. A **745** (2004), 155.

[Tim01] Nicolae Timis Cozmin, *Etude de la Decroissance par Neutrons Retardes de Noyaus Legers Riches en Neutrons avec le Multidetecteur TONNERRE*, Ph.D. thesis, Université de Caen, 2001.

[Tur08] M. Turrión et al., Nucl. Inst. and Methods B **(in press)** (2008).

[Vas89] O.Yu. Vasil'ev et al., Pis'ma Zh. Eksp. Teor. Fiz. **49** (1989), 539.

[WA74] D.H. Wilkinson and D.E. Alburger, Phys. Rev. C **10** (1974), 1993.

[WHPF01] William T. Vetterling William H. Press, Saul A. Teulkoski and Brian P. Flannery, *Numerical Recipes in Fortran 77*, Cambridge University Press, 2001.

[Wig46] E.P. Wigner, Phys. Rev **70** (1946), 15.

[WM74] D.H. Wilkinson and B.E.F. Macefield, Nucl. Phys. A **232** (1974), 58.

[Wu 57] C. S. Wu et al, Phys. Rev. **105** (1957), no. 4, 1413–1415.

[Yao06] W.-M. Yao et al., J. Phys. G **33** (2006), 1.

[Zel60] Y.B. Zeld'ovich, Sov. Phys. JETP **11** (1960), 812.

[Zhu95] M.V. Zhukov et al., Phys. Rev. C **52** (1995), 2461.

Resumen en castellano

1.1. Introducción

Uno de los principales objetivos de la física nuclear moderna es el estudio de la materia nuclear en condiciones extremas. Las propiedades de los núcleos cerca de las lineas de goteo, que determinan la frontera de exitencia de isótopos de un cierto elemento, son muy diferentes de las de los núcleos estables, los que forman la materia ordinaria. Lejos de la linea de estabilidad la ordenación de las capas nucleares puede ser distinta, lo que resulta en la aparición de nuevos números mágicos. La progresiva atenuación de la energía de ligadura de los últimos nucleones da lugar a fenómenos como la emisión β retardada de partículas cargadas, ó incluso la emisión directa de protones o neutrones.

Uno de los aspectos más estudiados en núcleos ricos en neutrones es el halo nuclear. El halo nuclear es un fenómeno límite, dado que solo aparece cuando la energía de ligadura de los últimos nucleones es pequeña. A medida que la energía de ligadura decrece los estados de valencia del núcleo se acercan al continuo y la probabilidad de que los últimos nucleones se encuentren, por efecto túnel, en la región prohibida de la barrera de potencial se incrementa. El efecto resultante es que el núcleo se asemeja a un "core" interno de densidad nuclear normal rodeado de un halo de baja densidad.

EL halo fue observado por primera vez por Tanihata y colaboradores en un estudio sistemático del radio de materia nuclear de núcleos radioactivos, en particular, de isótopos de helio ^{6}He y ^{8}He [Tan85a], y poco despues lo observaron también en el núcleo de interés de esta Tesis, ^{11}Li [Tan85b]. Desde entonces, numerosos experimentos de reacciones han estudiado las propiedades del halo nuclear en estos núcleos y otros que también presentan halos, como por ejemplo, ^{11}Be [For99], ^{15,19}C [Dat03, Mad01] y ^{23}O [Sau00].

El estudio de la desintegración β de núcleos cercanos a las lineas de goteo es, gracias a que es un proceso bien conocido, una fuente importante de información de la estructura nuclear de los núcleo padre e hijo. El gran desafío del estudio de la desintegración beta en esta región es que, al disminuir la energía de ligadura de los últimos nucleones y aumentar la energía de la desintegración, Q$_{\beta}$, la probabilidad de emisión retardada de partículas incrementa drásticamente hasta ser igual o mayor que la probabilidad de alimentar estados ligados. Esto hace que en la región abunden canales de desintegración exóticos como la emisión retardada de tritio, [Lan84], deuterio, [Muk96] o la fragementación en 3 o más partículas, como se observa, por ejemplo, en los dos núcleos en estudio en esta Tesis, ^{9}Li [Lan81, Nym90, Pre03, Pre05] y ^{11}Li, [Lan81, Bor97a].

En este resumen en castellano del trabajo presentado en esta Tesis voy a exponer el trabajo de análisis sobre la emisión retardada de partículas en la desintegración β de ^{9}Li y ^{11}Li. Antes, resumiré los conocimientos previos sobre ambos núcleos, expondré el esquema de los dispositivos experimentales usados y presentaré un breve resumen de los métodos requeridos para analizar los experimentos. Este capitulo de resumen se estructura de la siguiente manera:

- Conocimientos previos de la desintegración β de ^{9}Li y ^{11}Li.
- Estudio de la emisión retardada de partículas del estado a 2.43 MeV en ^{9}Be.
- Estudio de los canales de emisión retardada de partículas cargadas en la desintegración β de ^{11}Li.

1.2. Conocimientos previos de la desintegración β de ^{9}Li

El ^{9}Li es un núcleo rico en neutrones con Z=3 y N=6, cuya desintegración β tiene una vida media de 178.3(4) ms [AW76] y Q_β=13.6066(19) MeV [AWT03]. Todos los estados excitados del núcleo hijo ^{9}Be se encuentran por encima de la energía de separación de un neutrón y de alfas, S_n=1665.3(4) keV y S_α=2460(50) keV [AWT03].

La emisión retardada de partículas de ^{9}Li ha sido estudiada extensivamente [Lan81, Nym90, Pre03, Pre05], lo que ha permitido determinar el mecanismo de desintegración [Nym90, Pre03, Pre05], las razones de ramificación [Nym90, Pre03, Pre05] y el espín [Pre05] de los excitados en ^{9}Be alimentados en la desintegración de ^{9}Li, excepto el mecanismo de ruptura del estado de espín $5/2^{-}$ a 2.43 MeV. El estado a 2.43 MeV en ^{9}Be se encuentra cerca del estado fundamental de ^{5}He, E_x=2460(50) keV y Γ=578 keV [Til04], y no muy lejos del primer estado excitado de ^{8}Be, E_x=4790(10) keV y Γ=1513(15) keV [Til04]. Siempre que la energía de separación del estado en ^{9}Be y las posibles resonancias intermedias en ^{5}He y ^{8}Be es comparable con la anchura de estas es complicado distinguir entre la ruptura directa del estado y la ruptura secuencial. Esto hace que el mecanismo de ruptura de este estado sea todavía un tema controvertido en la literatura.

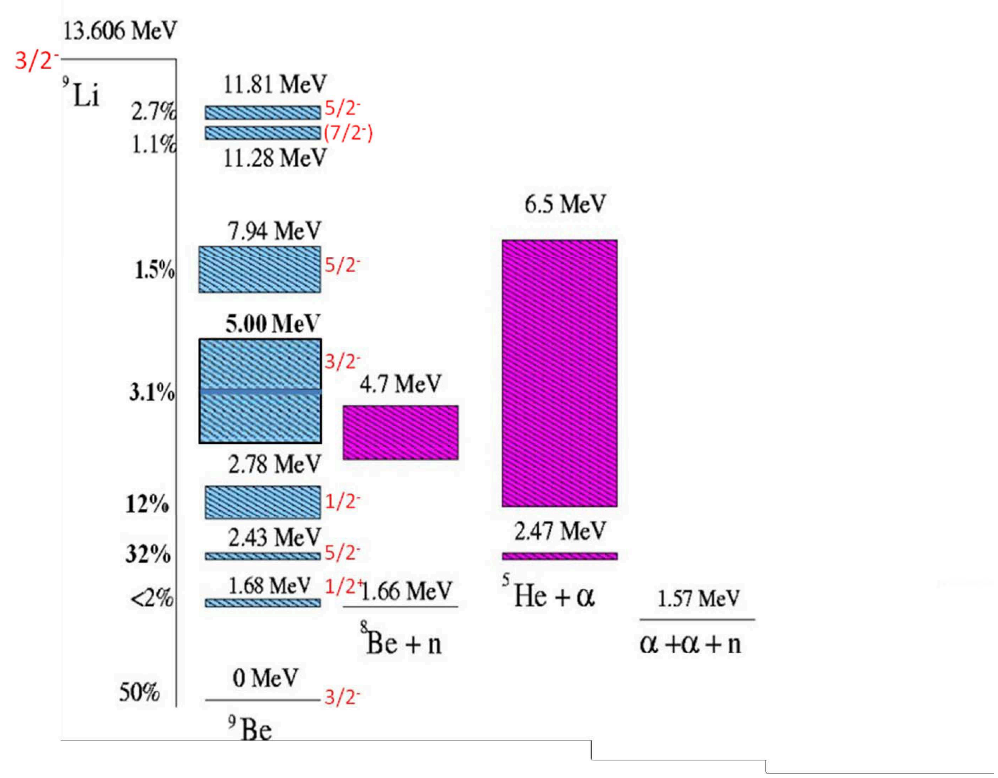

Figura 1.1: Vista esquemática de la desintegración beta de ^{9}Li y de las resonancias intermedias en ^{5}He y ^{8}Be que intervienen en la ruptura de los estados de ^{9}Be. La energía, espín y paridad de los estados pertenecen a [Til04], las razones de ramificación de todos los estados, y los espines y paridades de los estados a 7.94 y 11.81 MeV en ^{9}Be provienen de [Pre03, Pre05]. La energía, anchura, espín y paridad del estado a 5.0 MeV en ^{9}Be se han obtenido de [Pre05].

Los primeros intentos de entender el mecanismo de ruptura de este estado son de Bochkarev et al. [Boc89] y Vasil'ev et al. [Vas89] se basaron en un mecanismo de desintegración directa denominado "desintegración democrática", basado en la conservación del momento angular total del sistema despues de la ruptura del estado. El modelo de "desintegración democrática", añadiendo un 20 % de desintegración a través del estado fundamental de ^{8}Be, se uso para reproducir el espectro de energía alfa observado, con excelentes resultados. Trabajos Posteriores de Grigorenko y Zukhov [GZ05] utilizando la matriz-S, y de Álvarez-Rodríguez et al. [Alv08], mediante un modelo de tres cuerpos α-α-n de ^{9}Be, también favorecen que la desintegración del estado a 2.43 MeV en ^{9}Be ocurre directamente al continuo de tres partículas.

Un experimento reciente [Pap07] en el que se usó un sistema experimental de alta segmentación para medir coincidencias alfa-alfa, y de esta manera estudiar la cinemática de la desintegración y sus correlaciones angulares. Proponen que la desintegración ocurre principalmente a través del primer estado excitado de ^{8}Be, $86.5^{+4,5}_{-2,0}$ %, con una pequeña contribución del estado fundamental de ^{8}Be, del 11(2) %. Estos resultados están de acuerdo con los cálculos de Descouvemont [Des01], ya que este predice contribuciones del 92.7 %, 0.8 % y del 6.5 % de los canales a través del primer estado excitado de ^{8}Be, el estado fundamental de ^{8}Be y el estado fundamental de ^{5}He, respectivamente.

1.3. Conocimientos previos de la desintegración β de ^{11}Li

EL ^{11}Li, Z=3 y N=8, es el último isótopo ligado de Li, con un exceso de masa de 40.72828(64) MeV [Smi08]. Si tenemos en cuenta el exceso de masa de ^{11}Be, 20.171(4) MeV [Bac05], obtenemos una energía de desintegración beta Q_{β}=20.557(4) MeV. La vida media beta es de 8.5(5) ms [Til04]. La desintegración beta de ^{11}Li se ha estudiado extensivamente en experimentos capaces de medir simultaneamente β-n [Mor97], β-γ [Det80, Bor97b, Fyn04, Sar04] y β-γ-n [Hir05]. La información recopilada en estos experimentos ha permitido obtener un conocimiento detallado de razones de ramificación y espines, de los estados en ^{11}Be por debajo del límite de emisión de partículas cargadas de 7.913 MeV (ver Fig. 1.2). Por otra parte, el conocimiento de los estados en ^{11}Be por encima de la energía de separación de partículas cargadas alimentados en la desintegración de ^{11}Li es mucho más limitada. Se han observado cuatro canales de desintegración que incluyen partículas cargadas han sido observados: de tres cuerpos nα^{6}He y de cinco cuerpos 2α3n [Lan81], y dos canales de dos cuerpos ^{8}Li+t [Lan84] y ^{9}Li+d [Muk96, Bor97a, Raa08]. El único trabajo previo capaz de detectar partículas cargadas en coincidencia estableció que los canales de tres y cinco partículas están relacionados con la desintegración de dos estados en ^{11}Be, uno previamente conocido a 10.6 MeV [Ajz78] y otro propuesto a 18 MeV, aunque la falta de resolución angular para estudiar las propiedades cinemáticas de la desintegración impidió obtener un resultado definitivo. Estudios posteriores del canal de desintegración de dos cuerpos ^{8}Li$+t$, usando identificación de partículas mediante un telescopio de gas-Si [Lan84, Muk96, Bor97a], confirmaron la presencia de un estado a 18 MeV, y además indicaron que la razón de ramificación a este estado es grande, al igual que en la desintegración beta de otros núcleos con halo [Bor91]. Finalmente, un experimento reciente ha medido la distribución de energía de los deuterones del canal ^{9}Li$+d$, espectro compatible con la emisión directa del deuterón al continuo, sin la intervención de ningún estado intermedio en ^{11}Be.

La serie de experimentos descritos arriba muestran la dificultad de estudiar la emisión beta retardada de partículas cargadas de ^{11}Li, ya que solo se ha identificado la contribución de dos estados en ^{11}Be separados 8 MeV. Esto implica que muy probablemente una fracción de la fuerza beta alimenta estados en ^{11}Be que aún no han sido observados. De hecho, un estudio del efecto de ensanchamiento Doppler de radiación γ debido al momento del neutrón que alimenta el estado que se desexcita en ^{10}Be indica que hasta un 6 % de la intensidad beta alimenta estados en la región entre 10.6 y 18 MeV. Un cálculo teórico realizado en el modelo de capas [SO97] también predice que una parte importante de la fuerza beta se concentra en la región entre 10.6 y 18 MeV en ^{11}Be.

Por ultimo, es importante obtener una imagen completa de la distribución de fuerza beta de ^{11}Li para poder entender el papel de la estructura del halo en la desintegración beta. Varios trabajos previos [Det80, Mor97, Bor97b] han establecido que la fuerza beta que se observa en la alimentación del primer estado excitado en ^{11}Be solo se puede reproducir en el modelo de capas si la función de ondas del estado fundamental de ^{11}Li es una mezcla al 50 % de los estados neutrónicos de partícula independiente $p_{1/2}$ y $s_{1/2}$. Esta predicción de un estado mezcla $s_{1/2}$ y $p_{1/2}$ del estado fundamental de ^{11}Li fue confirmada en el estudio de la distribución de momento de n + ^{10}Li en un experimento de reacciones en GSI de Simon et al. [Sim99].

De manera general, se ha propuesto [Bor91, NNR00] que el operador de desintegración beta podría afectar de manera independiente a las funciones de onda del halo y del corazón del núcleo, lo que daría lugar a una distribución particular de la distribución de fuerza beta. 1) Por una parte se puede esperar una reducción general de la fuerza beta debido a un menor solapamiento entre la función de onda del padre (f.d.o extensa) y el hijo (f.d.o. concentrada). 2) Si el estado del núcleo padre se factoriza en core$\otimes$halo, la desintegración beta podria afectar de manera independiente a los dos términos.

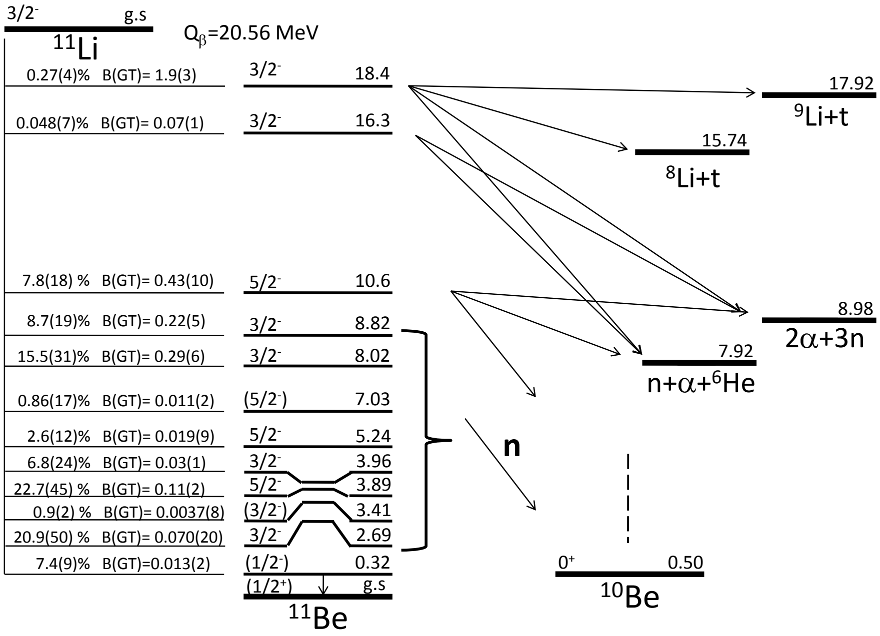

Figura 1.2: Esquema de niveles de los estados en ^{11}Be alimentados en la desintegración beta de ^{11}Li. Las razones de ramificación de los estados por encima del estado 10.6 MeV, incluyendo éste, han sido obtenidos en este trabajo.

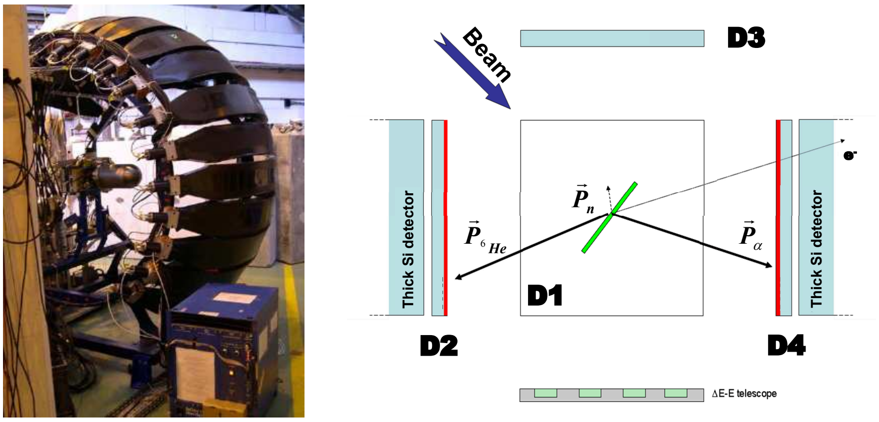

Figura 1.3: Izquierda: Fotografía del detector de neutrones TONERRE en el dispositivo experimentalde 2003 utilizado en este trabajo. La cámara de vacío es el contenedor de aluminio con forma de cono al final de la linea del haz, diseñado para reducir la dispersion de neutrones. Derecha: Esquema de los detectores de partículas cargadas usados en este experimento.

1.4. Estudio de la emisión retardada de partículas del estado a 2.43 MeV en ^{9}Be

El objetivo del trabajo presentado en esta Tesis es determinar el mecanismo de desintegración del estado $5/2^-$ a 2.43 MeV en ^{9}Be. Como se ha mencionado en el resumen de los conocimientos previos sobre este núcleo, la cercanía del estado de 2.43 MeV a las resonancias intermedias el estado 2^+ de ^{8}Be y el estado fundamental de ^{5}He, hace que no se sencillo determinar si la ruptura del estado ocurre a través de estas resonancias [Pap07, Des01], es decir, secuencialmente o directamente al continuo de tres partículas [Boc89, Vas89, Alv08].

El experimento tuvo lugar en ISOLDE, en el CERN. Los iones de ^{9}Li fueron seleccionados del resto de productos de la fisión de un blanco de Ta mediante el separador HRS (High Resolution Separator). Los iones de ^{9}Li una vez separados se implantaron en una lámina de carbono colocada en el centro del sistema experimental, con el objetivo de medir la desintegración β en reposo. Los detectores del sistema experimental encargados en detectar partículas cargadas consistieron en tres detectores DSSSD (Double Sided Silicon Detector), D2, D3 y D4, colocados en la superficie de un cubo de aluminio de dimensiones 10×10×10 cm^{3} (ver Fig. 1.3(b)). Finalmente, el detector basado en el método de tiempo de vuelo TONNERRE se utilizó para detectar neutrones y medir su energía (ver Fig. 1.3(a)).

El mayor desafío a la hora de estudiar la desintegración en multiples partícula del estado a 2.43 MeV en ^{9}Be consiste en saber interpretar los espectros de energía. EL método adoptado en este trabajo consistió en obtener la proyección del espectro de alfas detectados en en un detector, exigiendo coincidencias y el espectro de neutrones detectados en coincidencia con una partícula alfa y compararlos con simulaciones Monte-Carlo de la ruptura usando: 1) un modelo secuencial, en el que la energía de las resonancias es descrita en el teorema de Matriz-R; 2) ruptura directa al continuo, usando el modelo de ruptura "democrática” [Boc89].

En el análisis solo utilizamos el espectro de alfas en singles del detector D2, ya que este tenia el umbral de detección a más baja energía. Como las partículas alfa emitidas en la ruptura del estado a 2.43 MeV en ^{9}Be tienen una energía cercana al límite, $E_\alpha \sim 270$ keV comparado con el límite de 160 keV, es importante controlar la eficiencia del detector a baja energía. Para ello comparamos el espectro del detector D2 con el tomado con un detector de Si en singles de 40 μm de espesor, con buen resultado. El espectro de alfas en coincidencia correspondientes a la desintegración del estado a 2.43 MeV se obtuvo reconstruyendo la energía de excitación en ^{9}Be y seleccionando sucesos de energía de ^9Be menor o igual a 2.47 MeV. Para ello se calculó la energía del neutrón usando el momento de las dos alfas detectadas y aplicando la conservación de momento y energía. Finalmente el espectro de tiempo de vuelo de neutrones se obtuvo en coincidencia con alfas en el pico a ~270keV en D2, para seleccionar neutrones provenientes de la desintegración del estado a 2.43 MeV en ^{9}Be.

1.4.1. Simulaciones de la ruptura secuencial del estado a 2.43 MeV en ^{9}Be

En la simulación Monte-Carlo del proceso de ruptura del estado a 2.43 MeV suponiendo que este sucede de forma secuencial y utilizamos el modelo de Matriz-R para múltiples canales y niveles individuales [Nym90] para describir la distribución de energía de la resonancia de ^{9}Be, $E_{^9Be}$ y la energía de la resonancia intermedia, E', sea esta el primer estado excitado de ^{8}Be ó el estado fundamental de ^{5}He:

$$w(E_{^9Be}, E') = f_\beta(E_{^9Be}) \frac{P_\alpha(E_{^9Be} - E')}{(E^0_{^9Be} - E_{^9Be})^2 + (\Gamma_{^9Be}/2)^2} \cdot \frac{\Gamma_{E'}}{(E'_0 - E')^2 + (\Gamma(E')/2)^2} \tag{1.1}$$

Las simulaciones Monte-Carlo se realizaron incluyendo un modelo realista del dispositivo experimental usado, de manera que tenemos en cuenta el efecto de la apertura angular limitada del experimento. El resultado de las simulaciones, comparado con los datos experimentales de singles, coincidencias alfa-alfa, mostrados en las Figs. 1.4(a) y (b), indica que el modelo de ruptura secuencial reproduce de manera muy pobre los espectros experimentales.

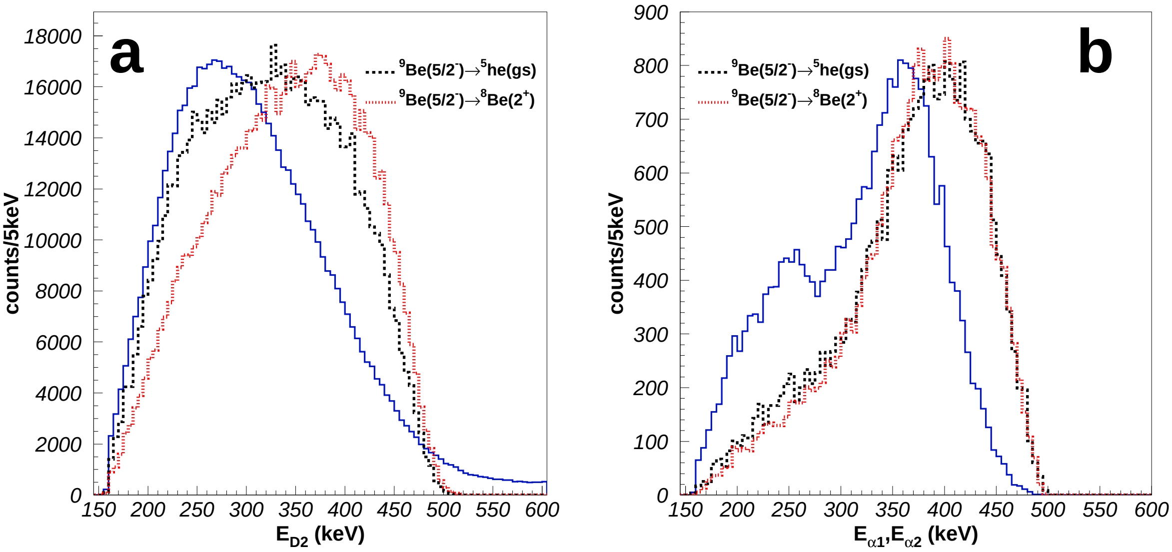

Figura 1.4: Izquierda: (a) Espectro de energía de partículas alfa detectadas en singles en D2 en azul comparado con la simulación de la ruptura secuencial del estado a 2.43 MeV en ^{9}Be a través del estado fundamental de ^{5}He (linea negra punteada) y el primer estado excitado de ^{8}Be (linea roja punteada). Ambas simulaciones muestran un pico cuyo máximo se encuentra a mayor energía que en los datos. Derecha: (b) Espectro de las dos alfas observadas en coincidencia correspondientes a la desintegración del estado a 2.43 MeV de ^{9}Be. De nuevo, los modelos de ruptura secuencial a través del estado fundamental de ^{5}He, linea negra punteada, o del primer estado excitado de ^{8}Be, linea roja punteada, no son capaces de reproducir la distribución de energía experimental.

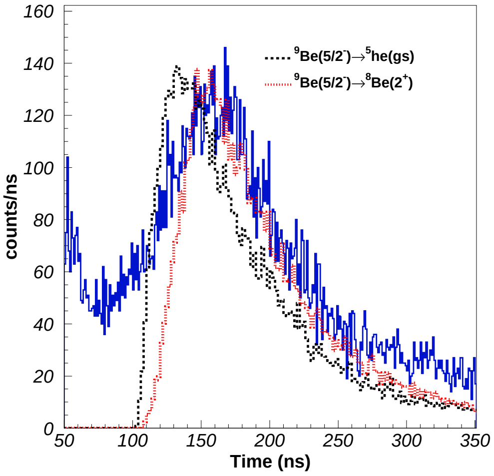

Figura 1.5: Espectro del tiempo de vuelo de neutrones en coincidencia con partículas alfa detectadas en D2 en el pico a 270 keV. La linea negra punteada corresponde con la simulacion de ruptura secuencial a través del estado fundamental de ^{5}*He mientras que la linea roja punteada corresponde a la ruptura a través del primer estado excitado de* ^{8}*Be.*

En el caso del espectro de tiempo de vuelo de los neutrones detectados en TONNERRE, la simulación de la ruptura a través del estado fundamental de ^{5}He es claramente diferente a la distribución experimental, como se muestra en la linea negra punteada en la Fig. 1.5. Por otra parte, la simulación de la ruptura a través del primer estado excitado de ^{8}Be reproduce bastante bien la distribución de tiempo de vuelo de neutrones, como vemos en la linear roja punteada en la Fig. 1.5.

1.4.2. Simulaciones de la ruptura directa al continuo del estado a 2.43 MeV en ^{9}Be

En la simulación Monte-Carlo del proceso de ruptura directa del estado a 2.43 MeV en ^{9}Be, la distribución de momentos de las dos alfas fue obtenida mediante el modelo de desintegración "democrática" de hiper-momento total del sistema K=3 [Boc89]:

$$\left[\frac{d^3\mathbf{P}}{dy\,d\Omega_\alpha d\Omega_{\alpha N}}\right]_{Bochkarev} = a\frac{2^3}{\pi^3}y^{3/2}(1-y^{5/2})\sin^2\phi + b\frac{2^4}{7\pi^3}y^{3/2}(1-y)^{5/2}(2+\cos^2\phi) \tag{1.2}$$

donde el primer término corresponde a momento angular orbital del sistema L=2 y el segundo L=3. Los parametros a y b son los pesos de las dos componentes de momento angular orbital, nomalizados a 1. Probamos diferentes combinaciones de pesos, sólo L=2, sólo L=3 y una mezcla al 50 % de L=2 y L=3. El mejor resultado al comparar con los datos lo obtuvimos para la mezcla al 50 %. La variable y se relaciona con la energía de las partículas emitidas como $y = \frac{9E_\alpha}{5(E_{^9Be}-1{,}57)}$. Y ϕ es el ángulo entre el momento relativo de las dos alfas y el neutrón.

Además, para poder reproducir la distribución de tiempo de vuelo de neutrones, tuvimos en cuenta el efecto de la barrera Coulombiana para la emisión de alfas y de la barrera centrifuga para la emisión del neutrón incluyendo las penetrabilidades para una ruptura donde las alfas se encuentran el la resonancia 2^+ de ^{8}Be y el neutrón es emitido primero:

$$\frac{d^3\mathbf{P}}{dyd\Omega_\alpha d\Omega_{\alpha N}} = \left[\frac{d^3\mathbf{P}}{dyd\Omega_\alpha d\Omega_{\alpha N}}\right]_{Bochkarev} \times P_{\alpha\alpha}(l=2)P_{n^8Be}(l=1) \tag{1.3}$$

donde los momentos angulares de emisión se obtienen partiendo de $j^\pi=5/2^-$ en ^{9}Be, y 2^+ en ^{8}Be. El resultado de las simulaciones comparados con los espectros de alfas en singles y coincidencias, para una mezcla al 50 % de L=2 y L=3 (como se menciona más arriba), se muestra en las Figs. 1.6(a) y (b). La simulación reproduce de manera excelente los dos espectros de energía de alfas, especialmente el espectro de energía de alfas en coincidencia. Finalmente, en la Fig. 1.7 se muestra el resultado de la simulación de la ruptura en el modelo “democrático” comparado con el espectro de tiempo de vuelo de neutrones, donde también observamos un buen acuerdo.

En conclusión, vemos que el modelo “democrático” de la ruptura del estado a 2.43 MeV en ^{9}Be reproduce la distribución de energía de las alfas y de tiempo de vuelo de neutrones, con mejor resultado que la simulaciones de la ruptura en un proceso secuencial, en buen acuerdo con los cálculos de Grigorenko y Zhukov [GZ05] y Álvarez-Rodriguez et al. [Alv08].

1.5. Estudio de los canales de emisión retardada de partículas cargadas en la desintegración β de ^{11}Li

Como hemos descrito más arriba, el conocimiento de los estados en ^{11}Be alimentados en la desintegración β de ^{11}Li por encima de la energía de separación de partículas cargadas esta limitado a dos estados a 10.6 y 18 MeV. El primer estado ha sido observado en un experimento de reacciones [Ajz78], y el segundo, fue propuesto [Lan81] para explicar el espectro de coincidencias alfa-alfa, fue confirmado en un posterior estudio del espectro de energía de tritones [Bor97a]. Es difícil imaginar que ningún estado en ^{11}Be a energías intermedias sea alimentado en la desintegración de

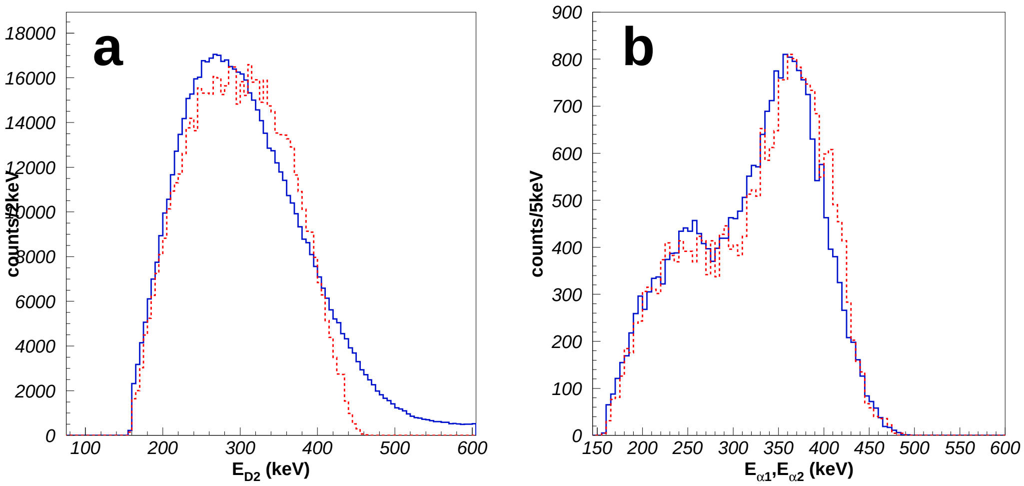

Figura 1.6: Izquierda: (a) Espectro de energía en singles en D2 (linea azul) comparado con la simulación de la ruptura usando del modelo de emisión "democrática" (mezcla al 50 % de L=2 y L=3) que incluye la penetrabilidad para la emisión de las alfas y el neutrón (linea roja punteada). Derecha: (b) Espectro de energía de alfas en coincidencia correspondientes al estado a 2.43 MeV en ^{9}*Be (linea azul),* $E_{\alpha1+\alpha2+n}$ *<0.9 MeV comparada con la misma simulación de (a) en linea roja punteada.*

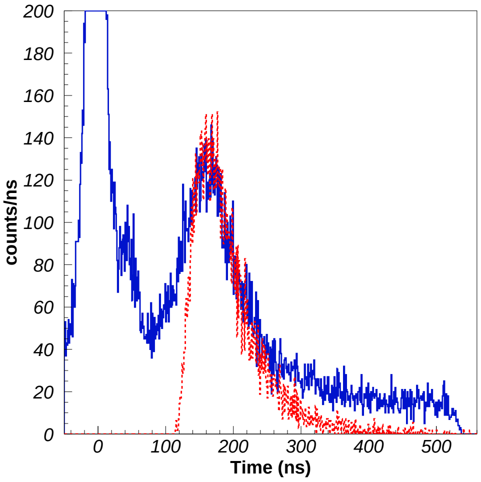

Figura 1.7: Espectro de tiempo de vuelo de neutrones en coincidencia con alfas detectadas en D2 con energía en el pico a ∼270 keV en linea azul, comparado con la simulación de la ruptura usando el modelo democrático, con mezcla al 50 % de L=2 y L=3, e incluyendo las penetrabilidades.

^{11}Li, como de hecho se sugiere en un estudio de coincidencias β-γ y en una cálculo teórico usando el modelo de capas [SO97]. El objetivo de este trabajo es profundizar en el conocimiento de la desintegración beta de ^{11}Li en la región de emisión de partículas cargadas, y los pasos a seguir se pueden resumir en:

- **Mejorar la descripción del mecanismo de desintegración de los canales que incluyen dos partículas cargadas.** Es esencial entender el mecanismo de desintegración, ya que éste determina la contribución de cada estado a la distribución de energía de partículas.
- **Determinar los estados en ^{11}Be por encima de la energía de separación de partículas cargadas alimentados en la desintegración beta de ^{11}Li.** El análisis de la cinemática de desintegración del canal de tres partículas nα^6He y de dos cuerpos ^{8}Li+t permitirá calcular la energía de excitación y el espín de los estados en ^{11}Be que se desintegran en estos canales.
- **Obtener las razones de ramificación y la fuerza beta B(GT) a estos estados.** La distribución de fuerza β de la desintegración de ^{11}Li se comparará con la distribución del núcleo que forma su ”core“, ^{9}Li, para buscar patrones que pudieran indicar la desintegración directa del ”core“.

El estudio de la desintegración de ^{11}Li se realizo en dos experimentos en 2003 y 2007. Este capítulo se divide en los resultados obtenidos en 2003 y los obtenidos en 2007 y finalmente la discusión sobre la distribución de fuerza beta.

1.5.1. Resultados del experimento en 2003

El sistema experimental usado en el experimento en 2003 es el mismo utilizado para el estudio de la desintegración beta de ^{9}Li, aunque en este caso no contamos con el detector de neutrones TONNERRE. El sistema de detección de partículas cargadas consistió en tres detectores DSSSD, D2, D3 y D4 (ver 1.3(b)). En este trabajo nos concentramos en estudiar los espectros de partículas detectadas en coincidencia en detectores opuestos, D2 y D4, que cubrían ángulos entre 127°y 180°.

Las figuras 1.8(a) y (b) muestran el espectro de energía suma y el espectro bidimensional de la energía de una partícula frente a la energía de la otra de partículas detectadas en coincidencia en los detectores D2 y D4. Los dos picos a 0.7 y 2.2 MeV en (a) corresponden con la agrupación de sucesos a baja energía y la linea transversal en (b). Los dos picos a 0.7 y 2.2 MeV fueron asignados por Langevin et al. [Lan81] a la desintegración en el canal 2α3n y nα^6He, respectivamente, del estado a 10.6 MeV en ^{11}Be. La distribución continua de energías por encima del pico a 2.2 MeV, se corresponde con la distribución de sucesos a gran energía en (b). El detalle más interesante de la distribución a alta energía, que corresponde con la desintegració del

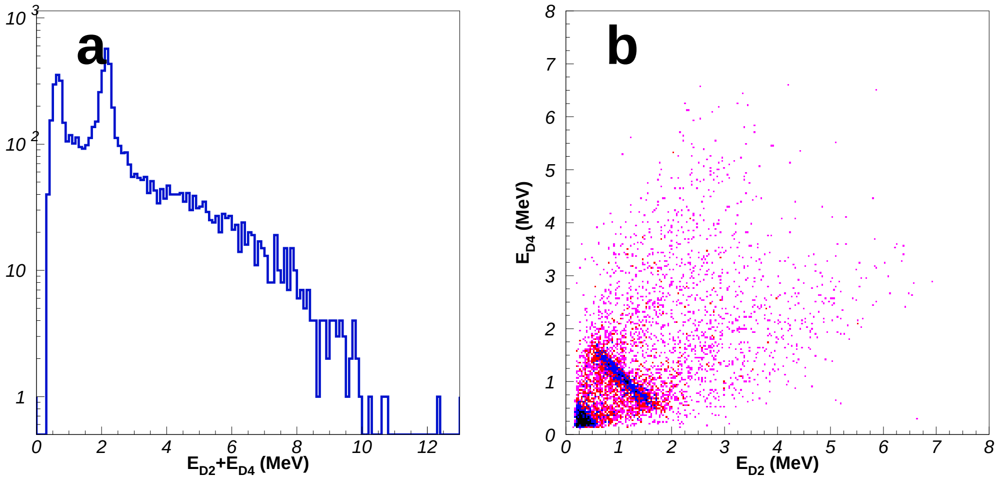

Figura 1.8: Izquierda: espectro de energía suma de dos partículas cargadas detectadas en DSSSD opuestos. Derecha: espectro de energía de una de las partículas en función de la energía de la otra. Las principales características de este espectro son la agrupación de sucesos a baja energía y la linea transversal, que corresponden con los picos a 0.7 y 2.2 MeV en (a), respectivamente.

estado a 18 MeV, es la agrupación en dos lóbulos, que caen aproximadamente sobre las lineas de pendiente 4/7 y 7/4. Esto indica que la desintegración del estado a 18 MeV a través del canal α^6He ocurre secuencialmente emitiendo una partícula alfa a través del estado fundamental de ^{7}He. Por otra parte, Langevin [Lan81] propone que la desintegración del estado a 18 MeV ocurre directamente al continuo simplemente dominado por el espacio de fase. Siguiendo el ejemplo del canal de ^{7}He, en este trabajo proponemos que la desintegración ocurre a través de ^{5}He(gs)+^{6}He(2^+)$\rightarrow 2\alpha+3$n.

Las figuras 1.9(a) y (b) muestran el resultado de la simulación Monte-Carlo, incluyendo los canales de desintegración ^{7}He+α y ^{5}He(gs)+^{6}He(2^+). La tabla 1.1 muestra los canales de desintegración que forman la simulación Monte-Carlo. Vemos que los dos lóbulos en la distribución de energía versus energía experimental se reproducen bien en la simulación.

Las razones de ramificación para los dos niveles a 10.6 y 18 MeV fueron obtenidas de la distribución de la simulación Monte-Carlo, dado que es muy difícil separar las diferentes contribuciones en los datos. La simulación se normalizó al canal $\beta\alpha$ del núcleo hijo ^{11}Be ($T_{1/2}$=13.81(8) [Ajz88]), BR=2.9(4) % [AMW81], suponiendo que todo el ^{11}Be en su estado fundamental fue alimentado desde el primer estado excitado $1/2^-$ en la desintegración β de ^{11}Li, B.R.=7.4(3) % [Bor97b, Bjo81, Aoi97, Mor97, Det80]. La tabla 1.2 muestra las razones de ramificación obtenidas suponiendo que

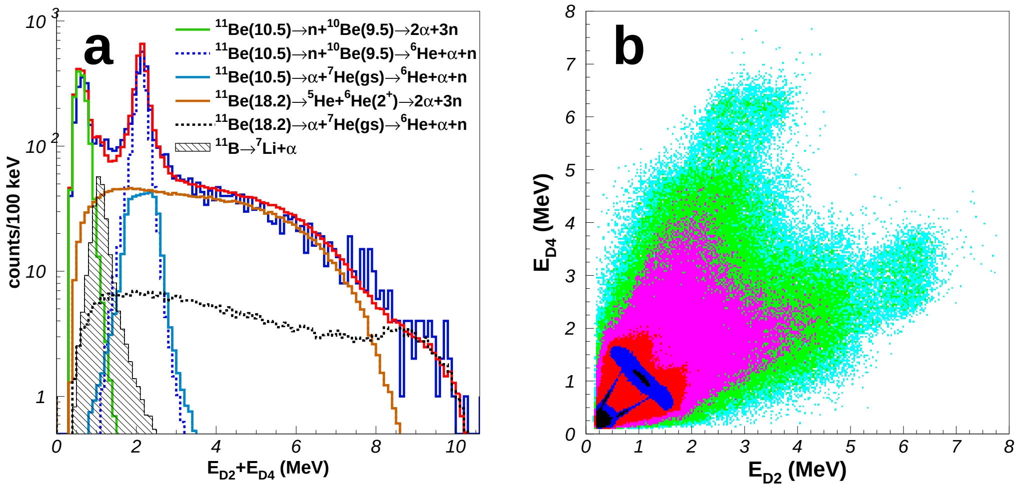

Figura 1.9: Izquierda: Espectro de energía suma en azul, con la simulación Monte-Carlo superimpuesta en linea roja. Los diferentes canales de desintegración se muestran en lineas de colores de acuerdo con la leyenda. Derecha:Plot bi-dimensional de la distribución de energía de una partícula frente a la energía de la otra de la simulación Monte-Carlo.

Cuadro 1.1: Estado en ^{11}Be alimentado en la desintegración beta y sus canales de desintegración.

Canales propuestos previamente	Canales propuestos en este trabajo
^{11}Be(10.59) $\xrightarrow{n}$ ^{10}Be(9.5) $\xrightarrow{\alpha}$ ^{6}He [Lan81] $\rightarrow$ 2α3n [Lan81]	^{11}Be(10.59) $\xrightarrow{n}$ ^{10}Be(9.5) $\xrightarrow{\alpha}$ ^{6}He $\rightarrow$ 2α3n $\xrightarrow{\alpha}$ ^{7}He(gs) $\xrightarrow{n}$ ^{6}He
^{11}Be(18.15) $\longrightarrow$ 2α3n [Lan81] $\rightarrow$ nα^{6}He [Bor97a]	^{11}Be(18.15) $\longrightarrow$ ^{6}He(2^{+})+^{5}He(gs) $\longrightarrow$ 2α3n† $\xrightarrow{\alpha}$ ^{7}He(gs) $\xrightarrow{n}$ ^{6}He

Cuadro 1.2: Razones de ramificación de los canales determinados en este trabajo en la desintegración beta de ^{11}Li.

Canal	Alimentación β (%)	Alimentación β (%)§
^{11}Be(10.59)$\rightarrow$n+^{10}Be(9.5)$\rightarrow$2α+3n	1.1(2)	1.4(2)
^{11}Be(10.59)$\rightarrow$n+^{10}Be(9.5)$\rightarrow$n+α+^{6}He	0.23(4)	0.29(4)
^{11}Be(10.59)$\rightarrow$ α+^{7}He$\rightarrow$n+α+^{6}He	0.035(6)	0.044(7)
^{11}Be(18.15)$\rightarrow$^{6}He(2^{+})+^{5}He$\rightarrow$2α+3n	0.34(5)	0.43(7)
^{11}Be(18.15)$\rightarrow$ α+^{7}He$\rightarrow$n+α+^{6}He	0.057(9)	0.072(10)

§ suponiendo una alimentación del 2 % al estado fundamental de ^{11}Be, el máximo establecido en el trabajo previo [Bjo81].

no hay alimentación al estado fundamental de ^{11}Be, como que hay un máximo de 2 % [Bjo81].

1.5.2. Resultados del experimento en 2007

El principal objetivo del experimento en 2007 fue estudiar el canal de desintegración ^{7}He+α propuesto por primera vez en el experimento de 2003. Queremos determinar los estados que se desintegran en este canal y obtener sus espines y paridades mediante el estudio de la cinemática y las correlaciones angulares de la ruptura. Además estudiaremos el canal de ^{8}Li+t usando un nuevo método basado en las características cinemáticas de la ruptura para identificar los tritones del resto de partículas cargadas.

El dispositivo experimental usado en 2007 consistió en tres detectores de partículas cargadas DSSSD, con dos de ellos D1 y D3 colocados a 5 cm de la lámina de carbono y el tercero, D2 a 3.7 cm (ver Fig. 1.10). La cercanía del detector D2 permitió obtener un factor 2 de mejora respecto al sistema experimental de 2003 para la detección de dos partículas cargadas emitidas isotrópicamente.

Estudio del canal de ^{7}He

Para estudiar el canal de ^{7}He analizamos las coincidencias de partículas cargadas detectadas en detectores opuestos, D2 y D3. En esta ocasión, en vez de estudiar el espectro de energía suma como en 2003, estudiamos un tipo de espectro diseñado para estudiar desintegraciones secuenciales. Para construirlo suponemos que todos los sucesos son de tres cuerpos, nα^{6}He (el canal de cinco cuerpos sera actuara como señal de fondo) y representamos la energía suma de las tres partículas frente a su energía individual (tres puntos por suceso). En este caso la energía de la primera

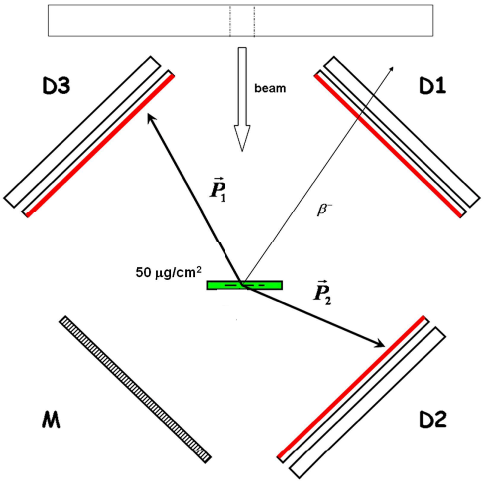

Figura 1.10: Esquema del sistema experimental usado en el experimento de 2007.

partícula emitida desde estados anchos formara una linea de pendiente proporcional al cociente de la masa de ^{11}Li sobre las masa de la resonancia intermedia, ^{7}He, y de "offset" igual a la energía de la resonancia intermedia, ver Fig. 1.11

Seleccionamos sucesos pertenecientes al canal de ^{7}He imponiendo que la energía de la partícula alfa sea mayor que 7.93 MeV y menor que 8.93 MeV, y representamos la energía de excitación de ^{11}Be (ver Fig. 1.12). Vemos que se observa un pico a 16 MeV, correpondiente a un nuevo estado, y una "joroba" a 18 MeV, correspondiente con el estado previamente conocido. Realizamos una simulación Monte-Carlo de la desintegración a través de ^{7}He usando el modelo de matriz-R, en la aproximación de un canal y estado independiente [Nym90], para describir la distribución de energía de las resonancias, e incluimos la ruptura de cinco cuerpos, $2\alpha 3$n, de ambos estados ya que actúan de señal de fondo. Los parametros de las resonancias se obtuvieron realizando un ajuste de χ^2 de los datos, obteniendo E_0=18.4(3) MeV y γ^2=0.11(4) MeV, FWHM Γ=1.6(6) MeV, para el estado a 18 MeV y E_0=16.3(1) MeV y γ^2=0.05(1) MeV, Γ=0.7 MeV para el estado a 16 MeV.

El espín y paridad de los dos estados se obtuvo estudiando las correlaciones angulares, teniendo en cuenta que el espín de del ^{11}Li es $3/2^-$ y por tanto los dos estados solo pueden ser $1/2^-$, $3/2^-$ o $5/2^-$ debido a las reglas de selección de transiciones Gamow-Teller. La distribución de momento del ^{6}He o del neutrón en sistema de centro de masas con respecto al momento de la partícula alfa viene determinada por la expresión [BR53]

$$W(\cos\theta) = 1 + A_2(2\cos^2\theta - 1)/2 \tag{1.4}$$

donde A_2 es 1, 0 y -0.714 para espines de 1/2, 3/2 y 5/2 en ^{11}Be respectivamente.

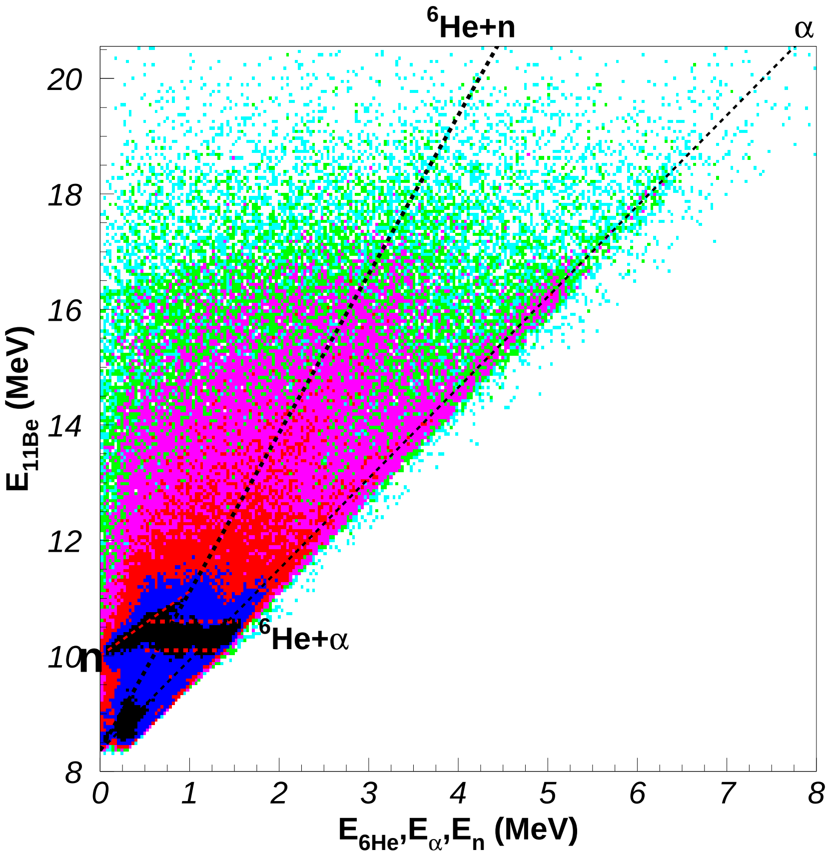

Figura 1.11: Energía de excitación en ^{11}Be frente a la energía individual del neutrón, alfa y ^{6}He, resultando en tres puntos por suceso. Las lineas punteadas rojas indican la energía del neutrón (pendiente 11/10) y de las partículas cargadas en la desintegración del estado en ^{11}Be a 10.6 MeV emitiendo un neutrón al estado a 9.5 MeV en ^{10}Be. La linea negra punteada, de pendiente 11/7 y offset 8.33 indica las partículas alfas en el canal de ^{7}He, mientras que la linea de 11/4 y offset 8.33 indica la región donde se esperan el neutrón y el ^{6}He.

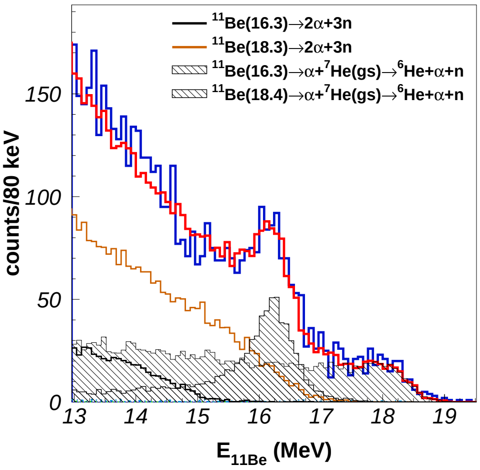

Figura 1.12: Energía de excitación en ^{11}Be seleccionada en el canal de ^{7}He. El resultado de la simulación Monte-Carlo se muestra en linea roja, con los diferentes canales coloreados siguiendo la leyenda.

Para ambos estados obtenemos que el espín 3/2 es favorecido por el test de χ^2 de la simulación.

Las razones de ramificación se obtuvieron normalizando las simulaciones Monte-Carlo al canal $\beta\alpha$ de ^{11}Be, BR=2.9(4) % [AMW81]. Asumiendo que todo el ^{11}Be en su estado fundamental fuera alimentado desde el primer estado excitado $1/2^-$ en la desintegración β de ^{11}Li, B.R.=7.4(3) % [Bor97b, Bjo81, Aoi97, Mor97, Det80]. La suma de las razones de ramificación de los dos estados a 16 y 18 MeV es 0.31(5) %, comparable al valor obtenido por Langevin de 0.30(5) % [Lan81], aunque este lo asigna completamente al estado a 18 MeV por falta de la posibilidad de estudiar los diferentes canales individualmente.

Canal	Alimentación β (%)
^{11}Be*(16.3)→2α+3n	0.042(7)
^{11}Be*(16.3)→ α+^{7}He→n+α+^{6}He	0.006(1)
^{11}Be*(18.4)→2α+3n	0.24(4)
^{11}Be*(18.4)→ α+^{7}He→n+α+^{6}He	0.020(3)

Identificación del canal de ^{8}Li+t

En la secciones precedentes hemos estudiado los canales de desintegración de tres cuerpos, nα^6He, y de cinco cuerpos, 2α3n. Sin embargo, si queremos tener una

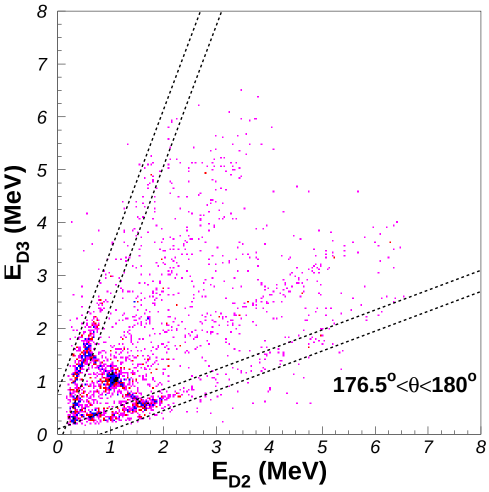

Figura 1.13: Espectro de energía de una de las partículas frente a la energía de la otra, detectadas en píxeles opuestos, es decir, con un ángulo entre 176.5 % y 180 %. Las lineas punteadas indican los intervalos que usamos para seleccionar sucesos en el canal de ^{8}*Li+t*

imagen completa de la alimentación beta de ^{11}Li a estados en ^{11}Be por encima de los canales de emisión de partículas cargadas debemos tener en cuenta los dos canales dos cuerpos, ^{9}Li+d y ^{8}Li+t. El primer canal, βd no se pudo detectar en coincidencia en este experimento, ya que nuestro limite de detección era ~160 keV. Este limite corresponde con ^{9}Li emitidos a 0.9 MeV, un limite que corresponde a menos de 5 % del canal de deuterio de acuerdo con el reciente estudio del espctro de energía realizado por Raabe et al. [Raa08].

En el caso del canal de tritio, nos aprovechamos de que al ser una ruptura de dos cuerpos, las dos partículas has de emitirse con una separación angular de 180°. La Fig. 1.13 muestra el espectro de energía de una de las partículas frente a la otra seleccionando sucesos en píxeles opuestos, es decir con un ángulo entre 176.5 % y 180 %. Vemos dos lineas de pendientes 8/3 y 3/8, como esperabamos para el canal de ^{8}Li+t. También se observa que parte del canal de tres cuerpos a través de ^{10}Be y del canal $\beta\alpha$ de ^{11}Be se cuelan en nuestra ventana.

La Fig. 1.14(a) y (b) muestran la energía suma, tritones y ^{8}Li, y la energía de tritones de sucesos en los dos intervalos mostrados con lineas punteadas, considerados sucesos de ^{8}Li+t. Las energías detectadas fueron corregidas del defecto de amplitud de la calibración de alfas en un factor de $\epsilon_t/\epsilon_\alpha$= 1.012 y $\epsilon_{^{8}\mathrm{Li}}/\epsilon_\alpha$= 0.987, tomados de [Len86]. Los parametros de la simulación usando matriz-R del estado a 18 MeV se

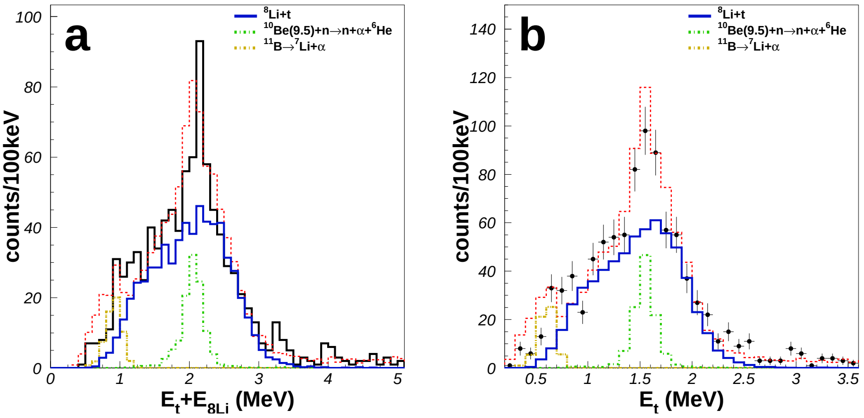

Figura 1.14: Izquierda: Espectro de energía suma del triton y del ^{8}Li, linea negra, comparado con la simulación Monte-Carlo en linea roja, y las componentes coloreadas de acuerdo con la leyenda. Derecha: espectro de energía de tritones, comparado con la simulación en linea roja punteada. El espectro de tritones es similar al obtenido en [Bor97a].

obtuvieron mediante ajustes χ^2 sucesivos de la simulación Monte-Carlo variando el centroide y la anchura, obteniendo un mínimo a E_0=18.35(30) MeV y γ^2=0.25(7) MeV.

La intensidad de simulación Monte-Carlo se optimizó variando la intensidad del canal βt y realizando tests de χ^2 al espectro experimental. Los diferentes tests fueron ajustados a una parábola para obtener el mínimo. El mínimo resultante se normalizo usando el canal $\beta\alpha$ del hijo ^{11}Be, 2.9(4) % [AMW81], suponiendo que el estado fundamental de ^{11}Be solo se alimenta desde el primer estado excitado, 7.4(3) % [Bor97b, Bjo81, Aoi97, Mor97, Det80]. El resultado para el mínimo es BR_t=0.93(8)×10^{-4}, similar a los valores publicados previamente BR_t=1.0(4)×10^{-4} [Lan84] y BR_t ∼1.2×10^{-4} [Muk96] en trabajos donde el uso de telescopios gas-Si permitía distinguir las partículas por su masa. .

1.5.3. La distribución de fuerzas beta B(GT) de la desintegración de ^{11}Li

La intensidad ó fuerza beta B(GT) a los estados por encima del límite de emisión de partículas se obtuvo a partir de sus razones de ramificación obtenidas en este trabajo. En el caso del estado ade ^{11}Be a 18 MeV también incluimos los canales de emisión de neutrones mencionados en Borge et al. [Bor97a]. Dado que los estados de ^{11}Be a 10.5, 16 y 18 MeV son muy anchos la forma habitual de calcular B(GT) debe modificarse. Utilizamos el método propuesto por Nyman et al. [Nym90], basado en estimar el efecto de la anchura del estado integrando la función de Fermi en la anchura completa del estado. Esta técnica se utilizó para calcular los B(GT) para los estados por encima del limite de emisión de partículas cargadas. La siguiente tabla muestra la razón de ramificación y la fuerza B(GT) a todos los estados de ^{11}Be poblados en la desintegración beta de ^{11}Li

^{11}Be (MeV)	J^{π}	BR (%)	B(GT)
g.s.	$1/2^+$	<2	—
0.32	$1/2^-$	7.4(9)	0.013(2)
2.69	$3/2^-$	20.9(50)	0.070(20)
3.41	$(3/2^-)$	0.9(2)	0.0037(8)
3.89	$5/2^-$	22.7(45)	0.11(2)
3.96	$3/2^-$	6.8(24)	0.03(1)
5.24	$5/2^-$	2.6(12)	0.019(9)
7.03	$(5/2^-)$	0.86(17)	0.011(2)
8.02	$3/2^-$	15.5(31)	0.29(6)
8.82	$3/2^-$	8.7(19)	0.22(5)
10.59	$5/2^-$	7.8(18) [1.45(2)]†	0.43(10)[0.09(1)]†
16.35	$3/2^-$	0.048(7)	0.07(1)
18.40	$3/2^-$	0.27(4)	1.9(3)

† contribución de los canales de partículas cargadas,
obtenidas en este trabajo.

donde el limite de un 2 % para la alimentación al estado fundamental de ^{11}Be esta tomado del trabajo de Bjornstad et al. [Bjo81], las razones de ramificación a estados excitados corresponden a la media ponderada de los resultados publicados en [Fyn04, Hir05] y los espines y paridades pertenecen al trabajo de Hirayama et al. [Hir05]. La Fig. 1.15 muestra la distribución de fuerza beta de ^{11}Li, donde las columnas negras corresponden a los valores obtenidos en este trabajo y las columnas blancas a los valores tomados de la literatura [Fyn04, Hir05].

En este trabajo nos interesa estudiar la distribución de fuerza beta de ^{11}Li con especial enfasis en cómo se ve afectada por la peculiar distribución de materia del halo. En concreto, estudiaremos dos efectos complementarios del halo sobre la distribución de fuerza beta:

- 1) La posibilidad de que el halo y el "core" de ^{11}Li se desintegren de manera cuasi-independiente, lo que resultaría en un patrón especifico de la desintegración beta de ^{11}Li similar al de ^{9}Li.

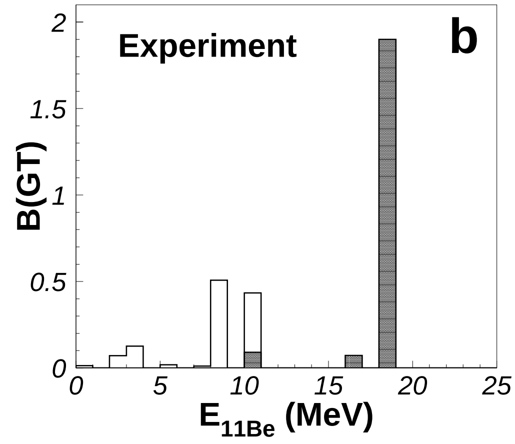

Figura 1.15: Distribución de fuerza beta, B(GT), a estados excitados en ^{11}Be. Los valores obtenidos en este trabajo se muestran en columnas negras. Lo valores para estados por debajo del limite de emisión de partículas cargadas se muestran en columnas blancas. El estado de ^{11}Be a 10.6 MeV se desintegra parcialmente a travé de procesos $n\gamma$ y $2n\gamma$. Estas contribuciones no se han analizado en este trabajo y se han tomado de la literatura [Fyn04, Hir05].

- 2) Las transiciones súper-permitidas a estados cercanos a Q_β observadas en la desintegración beta de núcleos con halo.

La desintegración independiente del ”core“ ^{9}Li

Como vimos en la introducción de este resumen, la gran extensión espacial del estado fundamental de ^{11}Li indica que el núcleo esta formado por un ”core“ de ^{9}Li y dos neutrones poco ligados, los que forman el halo. Si suponemos que la función de onda de los neutrones del halo esta muy poco correlacionada con la del ”core“, por lo que podemos factorizarla en dos términos independientes. El operador de desintegración beta actuaría pues de forma independiente:

$$\hat{O}_\beta|estadodehalo\rangle = \hat{O}_\beta\left(|core\rangle|halo\rangle\right) = (\hat{O}_\beta|core\rangle)|halo\rangle + |core\rangle(\hat{O}_\beta|halo\rangle) \quad (1.5)$$

Si los estados en la parte derecha de la ecuación son autoestados del núcleo hijo, entonces esta ecuación describiría la desintegración beta del ^{11}Li, y se reflejaría en una distribución caracaterística de fuerza beta. El segundo término, la desintegración directa de un neutrón del halo, ha sido estudiada por Zhukov et al. [Zhu95]. En este trabajo se propone que este termino favorecerá la alimentación de estados cuasi-halo en el núcleo hijo. Este efecto se estudiará en detalle en la siguiente sección.

La desintegración independiente de un neutrón del "core" sin afectar al halo fue estudiada por Timofeyuk et al. [TD96]. En este trabajo se aplicó al estudio de la desintegración beta de ^{14}Be, observando que la fuerza beta al estado 1^+ en ^{14}B se corresponde con la fuerza beta observada en la desintegración del "core" ^{12}Be al poblar el estado fundamental 1^+ de ^{12}B. Este caso es muy simple pues la fuerza beta se concentra mayormente en una transición al único estado excitado ligado con razones de ramificación, inferiores a 1 % para βn; β2n.La desintegración de 12Be es mayoritariamente al estado fundamental con logft=3.84 (6) y límite superior para emisión de neutrones de 1 % [Ajz86] En el caso que ocupa esta Tesis, la desintegración del "core" ^{9}Li tiene las siguientes razones de ramificación y fuerzas beta:

^{9}Be* (MeV)	J$^{\pi}$	BR (%)	B(GT)
g.s.	$3/2^-$	49.2(9)	0.031(3)
2.43	$5/2^-$	31.9(34)	0.047(5)
2.78	$1/2^-$	11.6(22)	0.011(5)
5.0	$3/2^-$	3.15(40)	—
7.94	$5/2^-$	1.5(4)	<0.403
11.81	$5/2^-$	2.7(2)	8.5(1)

La Fig. 1.16 muestra la distribución de fuerza β de ^{9}Li comparada con la de ^{11}Li. Vemos que las dos distribuciones se asemejan en su carácter fraccionado. Teniendo en cuenta la diferencia de exceso de masas entre ^{9}Be y ^{11}Be [Bac05, AWT03], y despreciando la energía de ligadura de los dos neutrones extra, el estado fundamental de ^{9}Be se encontraría a 8.824 MeV, pero si comparamos los dos B(GT) vemos que la transición de ^{11}Li es un orden de magnitud mayor que la de ^{9}Li. También podemos comparar el B(GT) del primer estado excitado por encima del limite de emisión de partículas, en ambos casos un estado $5/2^-$. De nuevo, el B(GT) de ^{11}Li es un orden de magnitud mayor que en ^{9}Li. Como vemos, no podemos hacer corresponder de manera directa los B(GT) de ^{11}Li con los B(GT) de ^{9}Li, lo que indica que los estados de ^{11}Be tienen una estructura más complicada que un "core" ^{9}Be y dos neutrones, probablemente un "core" de ^{10}Be y un neutrón o estados moleculares complicados de alfas y neutrones.

Transiciones súper-permitidas

Una característica común de la desintegración beta de núcleos ricos en neutrones que terminan las cadenas isobáricas A=6, 8, 9. es la aparición de una transición beta de tipo súper-permitida a un estado cercano a la venta Q_β [Bor91]

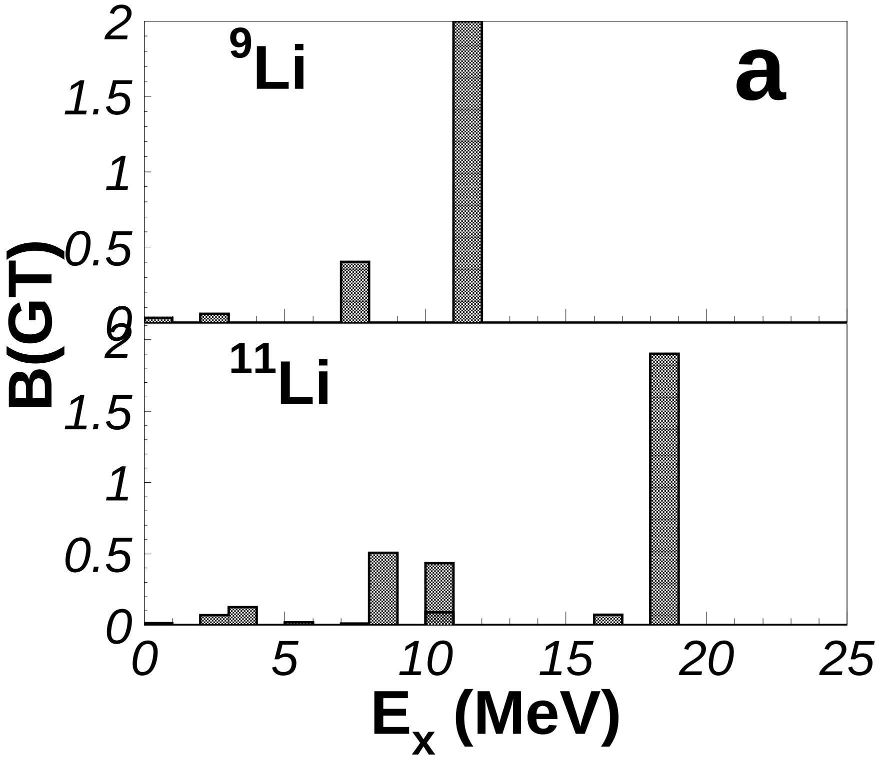

Figura 1.16: Distribución B(GT) en la desintegración de ^{9}Li [Nym90, Pre03], panel superior (el B(GT) del estado a 11.81 MeV esta truncada), comparada con la distribución B(GT) de ^{11}Li, panel inferior. El valor para estados por debajo de 10 MeV pertenece a [Fyn04, Hir05], los valores a estados por encima de 10 MeV a este trabajo. Las distribuciones tienen la misma estructura general, una distribución muy fraccionada con una transición muy intensa a unos 2 MeV del Q_β. La correspondencia entre estas dos distribuciones no es del todo clara excepto en la transición al estado excitado más cercano a Q_β, de carácter súper-permitido en ambos núcleos.

Desintegración	log(ft)	B$_{\mathrm{GT}}$	Ref.
^{6}He→^{6}Li(gs)	2.910(2)	4.75	[WA74, Rob78]
^{8}He→^{8}Li*(9)	3.09	3.14	[BW88]
^{9}Li→^{9}Be*(11.81)	2.7(2)	5.3(9)	[Nym90, Pre03]
^{11}Li→^{11}Be*(18)	3.5(6)	1.2(2)	Este trabajo

Vemos que las desintegración de ^{11}Li al estado a 18 MeV en ^{11}Be sigue la misma tendencia que en el resto de núcleos con halo, aunque de menor intensidad. Dos explicaciones de este fenómeno existen en la literatura. Borge et al. proponen que la gran extensión espacial del halo favorece que uno de los neutrones del halo se desintegre independientemente en un proton, formando un deuterón. En este caso la fuerza B(GT) seria similar al valor de Wigner para la desintegración de un dineutrón, 3(N-Z)=6. El segundo modelo, propuesto por Sagawa et al. [SHI93] y Hamamoto et al. [HS93], sugiere que la evolución de los niveles de partícula independiente de protones en núcleos cercanos a la linea de goteo neutrónico colocan la resonancia gigante de Gamow-Teller (GTGR) por debajo de la estado isobárico análogo (IAS). Por lo tanto, las transiciones súper-permitidas en núcleos ligeros ricos en neutrones se deberían a transiciones a la parte de la GTGR accesible a la desintegración beta.

En el caso de ^{11}Li ambas explicaciones parecen ser validas. Un experimento reciente ha medido la distribución de energía de los deuterones del canal βd, y concluyen que la desintegración ocurre directamente al continuo de ^{9}Li+d, en concordancia con lo esperado si un neutrón del halo se desintegra directamente. Por otra parte, el gran valor de B(GT) para estado a 18 MeV indica que la transición podría ser súper-permitida, como se espera si la transición ocurre a un estado en la GTGR.

Por último, queremos comparar la distribución B(GT) de ^{11}Li presentada en este trabajo con la obtenida mediante un cálculo de modelo de capas por G.M. Pinedo y A. Poves [MP95, Bor97a]. En este cálculo el espacio de valencia consistió en las capas $0p_{3/2}$,$0p_{1/2}$, $0d_{5/2}$ y $1s_{1/2}$. El nivel de ocupación de las capas se ajusto variando la energía de los estados de partícula independiente, de manera que reproduciesen el valor de la vida media, 8.5(3) ms [Til04], y el log(ft) al primer estado excitado de ^{11}Be, 5.74 [Bor97b]. El resultado es una probabilidad de ocupación de **0.43**, 0.36, y 0.1 para los estados $\mathbf{1}s_{1/2}$, $0p_{1/2}$ y$0d_{5/2}$, respectivamente. La Fig. 1.17(a) muestra la distribución de fuerza beta obtenida en el cálculo de modelo de capas, mostrando la contribución de estados de espín $3/2^{-}$ y $5/2^{-}$ en la parte superior e inferior del panel interior, respectivamente. Si comparamos con la distribución experimental, en la Fig 1.17(b) vemos que la distribución de estados de espín $3/2^{-}$ del cálculo es similar a la distribución experimental de los estados a 16 y 18 MeV, lo que apoya el resultado de $3/2^{-}$ obtenido del análisis de correlaciones angulares.

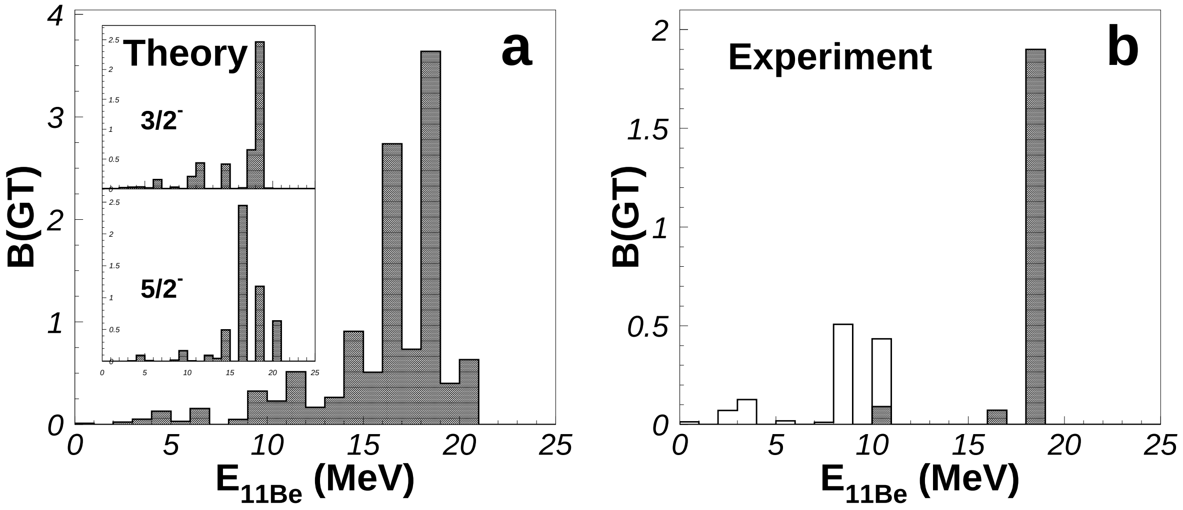

Figura 1.17: Izquierda: Distribución de fuerza beta B(GT) a estados excitados en ^{11}Be obtenida de un cálculo de modelo de capas [MP95]. La figura insertada muestra la distribución para estados de espín $3/2^-$ (panel superior) y estados de espín $5/2^-$ (panel inferior). Derecha: Distribución B(GT) experimental, donde las columnas negras son los valores obtenidos en este trabajo y las columnas blancas corresponden a valores de la literatura [Fyn04, Hir05].

1.6. Resumen y conclusiones

El trabajo presentado en esta tesis comprende el estudio de los canales de emisión retardada beta de partículas cargadas en ^{9}Li y ^{11}Li. El objetivo de este trabajo es obtener y comparar la distribución de fuerza beta de ^{11}Li y su “core”. En particular, queremos buscar patrones en la distribución que indicasen un posible desintegración del ”core“ independiente del halo, o viceversa. Los resultados se resumen en:

- En este trabajo se presentan los resultados del anáÅžisis de dos experimentos realizados en ISOLDE, CERN, en 2003 y 2007. Los núcleos que ocupan este trabajo, ^{9}Li y ^{11}Li fueron producidos por espalacion en un blanco de Ta, separados “on-line” e implantados en una lámina de carbono para medir su desintegración en reposo. El dispositivo experimental consistio en detectores de silicio de doble cara, optimizados para el estudio de particulas cargadas. Además, en el estudio de la desintegración de ^{9}Li en 2003 se instaló el detector de neutrones de tiempo de vuelo TONNERRE, para estudiar coincidencias entre alfas y neutrones.

- **Prueba del la ruptura del estado a 2.43 MeV en ^{9}Be directamente al continuo de 2αn**. Seleccionamos sucesos provenientes de la ruptura del estado a 2.43 MeV y estudiamos la distribución de energías de alfas en singles, la coincidencias alfa-alfa y el espectro de tiempo de vuelo de neutrones en coincidencia con alfas. Los tres espectros se compararon con la simulaciones de la ruptura usando tres modelos:**1)** emisión directa al continuo, usando el modelo de desintegración “democrático”; **2)** ruptura secuencial a través del estado fundamental de ^{5}He; **3)** y la ruptura secuencial a través del estado excitado 2^{+} de ^{8}Be. Cuando comparamos con los espectros experimentales, la simulación del modelo ”democrático“ es sistematicamente mejor que la simulación del modelo secuencial.

- **Prueba de la presencia en la desintegración beta de ^{11}Li de canales de desintegración que involucran resonancias de isótopos de He** Observamos que el ratio entre las dos energías detectadas en coincidencia, en sucesos de gran energía suma, es alrededor de 7/4 y 4/7, lo que indica que el estado a 18 MeV en ^{11}Be se desintegra en tres cuerpos nα^{6}He, a través del estado fundamental de ^{7}He. Además, el estudio de las correlaciones en la energía de las coincidencias de dos alfas en el canal de cinco cuerpos, 2α3n, sugiere que este canal ocurre a través de un proceso intermedio que incluye ^{5}He(gs)+^{6}He(2^{+}).

- **Prueba de la presencia de un nuevo estado en ^{11}BE a 16 MeV**. La mejora en la producción de ^{11}Li., debida al incremento de la produccion de

ISOLDE y que los detectores se encontraban más cerca del punto de implantación, nos permitió estudiar el canal de tres cuerpos, nα^6He en cinemática completa, lo que permitió identifica y seleccionar sucesos en el canal ^{7}He+α. Estudiando la distribución de energía de excitación en ^{11}Be de sucesos seleccionados en el canal de ^{7}He observamos la contribución de dos estados en ^{11}Be, el estado ya conocido a 18 MeV y uno nuevo a 16.3 MeV.

- **Determination of energy and width of high excited states in ^{11}Be.** By comparing the ^{11}Be excitation energy distribution with Monte-Carlo simulations of the breakup of both states into nα^6He through the ^{7}He(gs), we obtained the energy centroid and width of both states: **1)** E_0=18.4(3) MeV and Γ=1.6(6) MeV, which coincide within error bars with the values obtained in a previous experiment which used a gas-Si telescope to measure the triton (E_0=18.15(15), Γ=1.3(3)), ^{4,6}He (E_0=18.0(1) MeV, Γ=0.8(1)) and ^{9,10}Be (E_0=18.2(2) MeV, Γ=1.25(15)) emission from this state; **2)** E_0=16.3(1) MeV and Γ=0.7(1) MeV.

- **Determinamos la energía y la anchura de estados de ^{11}Be a alta energía** Usamos simulaciones Monte-Carlo de la ruptura de ambos estados para caracterizar ambos estados: **1)** para el estado a 18 MeV obtenmos E_0=18.4(3) MeV y Γ=1.6(6) MeV, valores comparables a los obtenidos en un experimento previo en el que, usando un telescopio de gas-Si, midieron la distribución de energía de tritones (E_0=18.15(15), Γ=1.3(3)), ^{4,6}He (E_0=18.0(1) MeV, Γ=0.8(1)) y ^{9,10}Be (E_0=18.2(2) MeV, Γ=1.25(15)); par el estado a 16 MeV obtenemos **2)** E_0=16.3(1) MeV y Γ=0.7(1) MeV.

- **Determinamos el espín de los dos estados a 16.3 y 18 MeV.** Estudiamos las correlaciones angulares y la distribución de energía de sucesos de coincidencias de ^{6}He y alfas en el canal de ^{7}He, y las comparamos con simulaciones del proceso de ruptura en las que se varió el espín de los estados de ^{11}Be entre los tres espines permitidos por las reglas de selección de la desintegración permitida beta, $1/2^-$, $3/2^-$ y $5/2^-$. El estudio de tanto las correlaciones angulares como la distribución de energía apoya que el espín de ambos estados es 3/2.

- **Desarrollamos un nuevo método basado en propiedades cinemáticas para estudiar el canal βt.** EL método se basa en resaltar la contribución del canal de ^{8}Li+t de entre las coincidencias de partículas cargadas. Para ellos seleccionamos sucesos detectados en píxeles opuestos, ya que la emisión de tritio es un proceso puramente de dos cuerpos, por lo que las partículas han de emitirse con 180° de separación. De entre los sucesos detectados en píxeles opuestos identificamos aquellos pertenecientes al canal de ^{8}Li+t como aquellos cuyo ratio de energías era 8/3. El espectro de energía resultando permitió identificar la única resonancia en ^{11}Be involucrada: E_0=18.35(3) MeV y Γ^2=1.5(4) MeV, y una razón de ramificación βt, BR_t=0.93(8)$\times 10^{-4}$.

- **Obtuvimos la distribución de fuerza beta B(GT) a estados por encima del limite de emisión de partículas cargadas. 1)** Determinamos las razones de ramificación de los estados a 10.6, 16.3 y 18 MeV usando simulaciones Monte-Carlo para estimar la eficiencia experimental. **2)** Usando las razones de ramificación calculamos la fuerza beta a estos tres estados. Para tener en cuenta que estos estados son resonancias relativamente anchas, integramos el factor de Fermi sobre la distribución de energía de cada estado.

- **Comparamos la distribución de fuerza beta de ^{11}Li con la distribución del "core" ^{9}Li.** Observamos que, más allá de que en ambos núcleos la distribución de fuerza beta esta fracturada en estados muy separados entre si, no es posible comparar la alimentación de estados específicos en ^{11}Be con sus equivalentes en ^{9}Be. La fuerza beta a los dos estados que energéticamente podrían corresponder con estados en ^{9}Be, el $3/2^-$ a 8.82 MeV y el $5/2^-$ a 10.6 MeV, es 10 veces mayor en ^{11}Li que sus contrapartidas en ^{9}Be. Por otra parte, el gran B(GT)=1.9(2) al estado a 18 MeV sugiere que podría se una transición súper-permitida. Estas transiciones súper-permitidas a estados cerca del Q_β se han observado previamente en núcleos con halo ^{6,8}He y ^{9}Li. El gran valor de B(GT), incluso teniendo en cuenta que no hemos incluido el canal de ^{9}Li+d dado que se ha demostrado que ocuure directamente al continuo, permite apoyar la interpretación de que estas transiciones se deben al efecto de la cola de la resonancia gigante de Gamow-Teller.

- **Comparamos la distribución B(GT) con un cálculo de modelo de capas.** G. Martínez-Pinedo y A. Poves nos proporcionaron un cálculo de la distribución B(GT) de la desintegración de ^{11}Li, en el que la composición del estado fundamental de ^{11}Li, una mezcla al 50 % de onda *s* y onda *p*, se ajusto para reproducir el log(ft) al estado a 320 keV en ^{11}Be. La distribución teórica a estados de espín 3/2 se asemeja a nuestro resultado experimental, lo que apoya nuestro resultado obtenido del análisis de correlaciones angulares.

Bibliografía

[Ajz78] F. Ajzenber-Selove et al., Phys. Rev. C **17** (1978), 1283.

[Ajz86] F. Ajzenber-Selove, Nucl. Phys. A **460** (1986), 1.

[Ajz88] F. Ajzenber-Selove et al., Nucl. Phys. A **490** (1988), 1.

[Alv08] R. Alvarez-Rodriguez et al., Phys. Rev. Lett. **100** (2008), 192501.

[AMW81] D.E. Alburger, D.J. Millener, and D.H. Wilkinson, Phys. Rev. C **23** (1981), 473.

[Aoi97] N. Aoi et al., Nucl. Phys. A **616** (1997), 181c.

[AW76] D.E. Alburger and D.H. Wilkinson, Phys. Rev. C **13** (1976), 835.

[AWT03] G. Audi, AH Wapstra, and C. Thibault, Nucl. Phys. A **729** (2003), 337.

[Bac05] C. Bachelet et al., Eur. Phys. J. A **25** (2005), no. s01, 31.

[Bjo81] T. Bjornstad et al., Nucl. Phys. A **359** (1981), 1.

[Boc89] O.V. Bochkarev et al., Nucl. Phys. A **505** (1989), 215.

[Bor91] M.J.G. Borge et al., Z. Phys. **340** (1991), 255.

[Bor97a] ______, Nucl. Phys. A **613** (1997), 199.

[Bor97b] ______, Phys. Rev. C **55** (1997), R8.

[BR53] L.C Biedenharn and M.E. Rose, Rev. Of Modern Phys. (1953), 729.

[BW88] F.C. Barker and E.K. Warburton, Nucl. Phys. A **487** (1988), 169.

[Dat03] U Datta et al., Phys. Lett. B **551** (2003), 63.

[Des01] P. Descouvemont, Eur. Phys. J. A **12** (2001), 413.

[Det80] C. Detraz, J. de Phys. Lett. **41** (1980), 459.

[For99] S. Fortier et al., Phys. Lett. B **461** (1999), 22.

[Fyn04] H.O.U. Fynbo et al., Nucl. Phys. A **736** (2004), 39.

[GZ05] L.V. Grigorenko and M.V. Zhukov, Phys. Rev. C **72** (2005), 015803.

[Hir05] Y. Hirayama et al., Phys. Lett. B **611** (2005), 239.

[HS93] I. Hamamoto and H. Sagawa, Phys. Rev. C **48** (1993), R960.

[Lan81] M. Langevin et al., Nucl. Phys. A **366** (1981), 449.

[Lan84] ______, Phys. Lett. B **146** (1984), 176.

[Len86] W.N. Lennard et al., Nucl. Instr. and Meth A **248** (1986), 454.

[Mad01] V. Maddalena et al., Phys. Rev. C **63** (2001), 024613.

[Mor97] D.J. Morrissey et al., Nucl. Phys. A **627** (1997), 222.

[MP95] Gabriel Martínez-Pinedo, *Estudio de procesos debiles y de propiedades colectivas en nucleos ligeros y medios*, Ph.D. thesis, Universidad Autonoma de Madrid, 1995.

[Muk96] I. Mukha et al., Phys. Lett. B **367** (1996), 65.

[NNR00] T.Ñilsson, G.Ñyman, and K. Riisager, Hyperfine Interact. **129** (2000), 67.

[Nym90] G. Nyman et al., Nucl. Phys. A **510** (1990), 189.

[Pap07] P. Papka et al., Phys. Rev. C **75** (2007), 045803.

[Pre03] Y. Prezado et al., Phys. Lett. B **576** (2003), 55.

[Pre05] ______, Phys. Lett. B **618** (2005), 43.

[Raa08] R. Raabe et al., prl **101** (2008), 212501.

[Rob78] R.G.H. Robertson et al., Phys. Rev. C **17** (1978), 4.

[Sar04] F. Sarazin et al., Phys. Rev. C **70** (2004), 031302(R).

[Sau00] E. Sauvan et al., Phys. Lett. B **491** (2000), 1.

[SHI93] H. Sagawa, I. Hamamoto, and M. Ishihara, Phys. Lett. B **303** (1993), 215.

[Sim99] H. Simon et al., Phys. Rev. Lett. **83** (1999), no. 3, 496.

[Smi08] M. Smith et al., Phys. Rev. Lett. **101** (2008), 202501.

[SO97] T. Suzuki and T. Otsuka, Physical Review C **56** (1997), no. 2, 847–856.

[Tan85a] I. Tanihata et al., Phys. Lett. B **160** (1985), 380.

[Tan85b] ______, Phys. Rev. Lett. **55** (1985), 2676.

[TD96] N.K. Timofeyuk and P. Descouvemont, J. Phys. G **22** (1996), L99.

[Til04] D.R. Tilley et al., Nucl. Phys. A **745** (2004), 155.

[Vas89] O.Yu. Vasil'ev et al., Pis'ma Zh. Eksp. Teor. Fiz. **49** (1989), 539.

[WA74] D.H. Wilkinson and D.E. Alburger, Phys. Rev. C **10** (1974), 1993.

[Zhu95] M.V. Zhukov et al., Phys. Rev. C **52** (1995), 2461.